ÇUKUROVA UNIVERSITY
INSTITUTE OF NATURAL AND APPLIED SCIENCES

PhD THESIS

Uğur EŞME

EFFECT OF POOL GEOMETRY ON THE QUALITY OF TIG WELDED JOINTS

DEPARTMENT OF MECHANICAL ENGINEERING

ADANA, 2006

ÇUKUROVA ÜNİVERSİTESİ
FEN BİLİMLERİ ENSTİTÜSÜ

EFFECT OF POOL GEOMETRY ON THE QUALITY OF TIG WELDED JOINTS

Uğur EŞME

DOKTORA TEZİ

MAKİNA MÜHENDİSLİĞİ ANABİLİM DALI

Bu Tez 17/07/2006 Tarihinde Aşağıdaki Jüri Üyeleri Tarafından Oybirliği/Oyçokluğu İle Kabul Edilmiştir.

İmza:	İmza:	İmza:
Prof. Dr. Melih BAYRAMOĞLU	Prof. Dr. Necdet GEREN	Doç. Dr. Mustafa Kemal KÜLEKCİ
DANIŞMAN	ÜYE	ÜYE
İmza:	İmza:	
Doç. Dr. Abdülkadir EKŞİ	Yrd. Doç. Dr. Ali KOKANGÜL	
ÜYE	ÜYE	

Bu Tez Enstitümüz Makina Mühendisliği Anabilim Dalında Hazırlanmıştır.

Kod No:

Prof. Dr. Aziz ERTUNÇ
Enstitü Müdürü

Bu çalışma Ç.Ü. Bilimsel Araştırma Projeleri Birimi tarafından desteklenmiştir.

Proje No: MMF.2004.D9

ABSTRACT

PhD THESIS

EFFECT OF POOL GEOMETRY ON THE QUALITY OF TIG WELDED JOINTS

Uğur EŞME

DEPARTMENT OF MECHANICAL ENGINEERING
INSTITUTE OF NATURAL AND APPLIED SCIENCES
UNIVERSITY OF ÇUKUROVA

Supervisor : Prof. Dr. Melih BAYRAMOĞLU

Year: 2006, Pages: 366

Jury : Prof. Dr. Melih BAYRAMOĞLU
: Prof. Dr. Necdet GEREN
: Assoc. Prof. Dr. Mustafa Kemal KÜLEKCİ
: Assoc. Prof. Dr. Abdülkadir EKŞİ
: Assist. Prof. Dr. Ali KOKANGÜL

Across the engineering spectrum, welding is an essential process in the manufacturing of components, assemblies or complete machines. Tungsten inert gas (TIG) welding is the best known and most frequently used method of welding process in food industry, ships, bridges and welding of stainless steels. Basically, TIG weld quality is strongly characterized by the weld pool geometry which has several quality responses such as tensile load (TL), heat affected zone (HAZ), upper width (UW), upper height (UH), penetration (P) and area of penetration (AP). Weld pool geometry plays an important role in determining the mechanical properties of the weld. Therefore, it is very important to select the welding process parameters for obtaining an optimal weld pool geometry. In this study, the effect of TIG welding process parameters (welding speed, welding current, gas flow rate and gap distance) on the weld pool shape and the quality responses were investigated. The mathematical models were developed for optimization and prediction of the weld pool geometry. Also, a neural network (NN) was used to construct the relationships between welding process parameters and weld pool geometry in TIG welding.

Keywords: Tungsten Inert Gas Welding (TIG), Weld Pool Geometry, Central Composite Design (CCD), Response Surface Methodology (RSM), Neural Network (NN)

ÖZ

DOKTORA TEZİ

KAYNAK HAVUZ GEOMETRİSİNİN TIG KAYNAKLI BAĞLANTILARIN KALİTESİNE ETKİLERİ

Uğur EŞME

ÇUKUROVA ÜNİVERSİTESİ
FEN BİLİMLERİ ENSTİTÜSÜ
MAKİNA MÜHENDİSLİĞİ ANABİLİM DALI

Danışman : Prof. Dr. Melih BAYRAMOĞLU
Yıl: 2006, Sayfa: 366
Jüri : Prof. Dr. Melih BAYRAMOĞLU
: Prof. Dr. Necdet GEREN
: Doç. Dr. Mustafa Kemal KÜLEKCİ
: Doç. Dr. Abdülkadir EKŞİ
: Yrd. Doç. Dr. Ali KOKANGÜL

Mühendislik spektrumu kapsamında kaynak, tamamlayıcı parçalar, montaj işlemi ve makine parçaları üretiminde kullanılan temel bir işlemdir. TIG kaynağı, gıda endüstrisinde, gemilerde, köprülerde, paslanmaz çelik kaynağında vb. yerlerde en sık kullanılan ve en iyi bilinen kaynak yöntemidir. Temel olarak TIG kaynağı kaynak kalitesi, çekme yükü (TL), ısıdan etkilenmiş bölge (HAZ), üst genişlik (UW), eriyik derinliği (P) ve eriyik alanı gibi kalite ölçütlerine sahip kaynak havuz geometrisi tarafından nitelendirilmiştir. Kaynak havuz geometrisi, kaynağın mekanik özelliklerini belirlemede önemli bir rol oynar. Bu yüzden kaynak parametrelerinin seçimi, en uygun kaynak havuz geometrisinin elde edilmesinde oldukça önemlidir. Bu çalışmada TIG kaynağı parametrelerinin (kaynak hızı, kaynak akımı, gaz akış oranı ve boşluk mesafesi) kaynak havuz şekli ve kalite ölçütlerine etkisi araştırılmıştır. Kaynak havuz geometrisinin tahmini ve optimizasyonu için matematiksel modeller geliştirilmiştir. Ayrıca, TIG kaynağında kaynak havuz geometrisi ve kaynak parametreleri arasındaki ilişkileri yapılandırmak için yapay sinir ağları (NN) kullanılmıştır.

Anahtar Kelimeler: TIG Kaynağı, Kaynak Havuz Geometrisi, Merkezi Bileşik Dizayn (CCD), Yüzey Tepki Yöntemi (RSM), Yapay Sinir Ağları (NN)

ACKNOWLEDGEMENTS

I am very grateful to my supervisor and first I would like to thank my supervisor Prof. Dr. Melih BAYRAMOĞLU for his guidance, inspiration and encouragement during all my thesis studies.

I also thank my special committee members, Prof. Dr. Necdet GEREN, Assist. Prof. Dr. Ali KOKANGÜL, Assoc. Prof. Dr. Mustafa Kemal KÜLEKCİ and Assoc. Prof. Dr. Abdülkadir EKŞİ for their enthusiasms and many helpful suggestions.

And I would like to thank to, Işın Teknik Machine Construction & Textile and Manufacturing Company, specially Vehbi EŞME, Enis EŞME, Sabahattin EŞME, Hasan EŞME and Sedat EŞME for their interest and support. Also many thanks to Metal Form Company, Ali EŞME for his valuable supports for preparation of the experimental arrangement.

Finally, special thanks to my wife Mehtap EŞME, my family: especially my mother Melahat EŞME, my niece Dilek CÜZDAN for their encouragement, endless supports and just for being there!

CONTENTS **PAGE**

LIST OF TABLES

LIST OF FIGURES

NOMENCLATURE

TIG	Tungsten inert gas welding
GTAW	Gas tungsten arc welding
SMAW	Shielded metal arc welding
GMAW	Gas metal arc welding
SAW	Submerged metal arc welding
EBW	Electron beam welding
TL	Tensile load, (kg)
HAZ	Heat affected zone, (mm)
UW	Upper width, (mm)
UH	Upper height, (mm)
P	Penetration, (mm)
AP	Area of penetration, (mm^2)
ANN	Artificial neural network
NN	Neural network
BPN	Back propagation network
DC	Direct current
AC	Alternative current
SCR	Silicon controlled rectifier
AWS	American welding society
DCEN	Direct current electrode negative
DCEP	Direct current electrode positive
DSAW	Double sided arc welding
V	Welding speed, (mm/s)
I	Welding current, (A)
F	Gas flow rate, (I/min)
G	Gap distance, (mm)
R	Solidification rate

ϕ	Angle between the normal to the solid-liquid interface and the direction of motion of the torch
R'	Growth rate in the preferred direction
ϕ'	Angle between grain growth direction and welding speed
t	Thickness (mm)
w	Width, (mm)
WM	Weld metal
BM	Base metal
E	Voltage, (Volt)
H_n	Heat input, (kJ/mm)
F_1	Heat transfer efficiency
E_t	Total energy input per unit length, (Joule)
E_i	Total energy entering plate, (Joule)
E_m	Energy to melt weld bead, (Joule)
PWHT	Postweld heat treatment
S	Cooling rate, (s)
T_i	Temperature of interest, (°C)
C	Generalized constant
K	Thermal conductivity
ρ	Density, (g/cm^3)
RSM	Response surface methodologu
CCD	Central composite design
SCGC	Subcritically reheated grain-coarsened
ICGC	Intercritically reheated grain-coarsened
SCGR	Supercritically reheated grain-refined
UAGC	Unaltered grain-coarsened
LBZ	Local brittle zones
LOP	Lack of penetration
P_d	Heat source density, ($Watt/cm^2$)
t_m	Melting time, (s)

IWP	Indirect weld parameters
DWP	Direct weld parameters
SA	Simulated annealing
X_n	Input vector
Y_n	Output vector
w	weight
c	Internal offset value
P_n	Normalized output vector
D_n	Desired output value
d_j	Correction factor
e	Error
e_0	Error threshold
η	Correction gain
AVC	Automatic voltage controller
EDD	Extended-delta bar-delta
n	Number of nodes
N	Number of samples
WREF	Desired bead width, (mm)
PREF	Desired bead penetration, (mm)
NLP	Nonlinear programming
LINGO	Language for interactive general optimization

1. INTRODUCTION

Generally, welding can be defined as any process in which two or more pieces of metal are joined together by the application of heat, pressure, or a combination of both. Most of the processes may be grouped into two main categories: pressure welding, in which the weld is achieved by pressure; and heat welding, which is achieved by heat. Heat welding is the most common welding used today.

Arc welding, which is heat-type welding, is one of the most important manufacturing operations for the joining of structural elements for a wide range of applications, including guide way for trains, ships, bridges, building structures, automobiles, and nuclear reactors, to name a few. It requires a continuous supply of either direct or alternating electric current, which create an electric arc to generate enough heat to melt the metal and form a weld.

The most widely used arc welding processes include;

- Shielded metal arc welding (SMAW),
- Gas tungsten arc welding (GTAW or TIG),
- Gas metal arc welding (GMAW),
- Submerged metal arc welding (SAW).

The arc welding process is a remarkably complex operation involving extremely high temperatures, which produce severe distortions and high levels of residual stresses. These extreme phenomena tend to reduce the strength of a structure, which becomes vulnerable to fracture, buckling, corrosion and other type of failures.

The primary goal of any welding operation is to make a weld having the same properties as the base metal. The only way to produce such a weld is to protect the molten puddle from the atmosphere. In gas shielded-arc welding, an inert gas is used as a covering shield around the arc to prevent the atmosphere from contaminating the weld. Gas shielding makes it possible to weld metals that are otherwise impractical or difficult to weld by eliminating atmospheric contamination of the molten puddle.

Tungsten inert gas welding (TIG) is a form of shielded metal arc welding. However, in tungsten inert gas welding, the electrode is used only for creating the arc. The electrode is not consumed in the weld as in the shielded metal-arc process. The basic TIG process involves an intense arc between the base metal and a tungsten electrode. The arc, the electrode, and the weld zone are surrounded by an inert gas (i.e. either helium or argon or a mixture of the two as usual) that displaces the air and eliminates the possibility of weld contamination by the oxygen and nitrogen present in the atmosphere. The high melting point of tungsten electrode made it virtually non-consumable.

Nowadays, TIG welding has become an indispensable tool for many industries since high-quality welds are produced with low equipment costs. The process uses shielding gas without the application of pressure. The process might be used with or without the addition of filler metal as well. The electrode is the cathode and the work-piece is the anode (or vice versa). Primarily electrons obtained by ionization of the inert gas atoms and emitted by the negative electrode carried the arc current. The electrons are attracted towards the positive work-piece where they generate the necessary heat to melt the work-piece edges of the two materials to be joined. Thus, a weld fusion zone containing liquid material is formed and often denoted as weld pool.

Basically, TIG weld quality is strongly characterized by the weld pool geometry which has several quality characteristics as shown in Figure 1.1. These are;

- Upper width,
- Upper height,
- Penetration

of the weld pool.

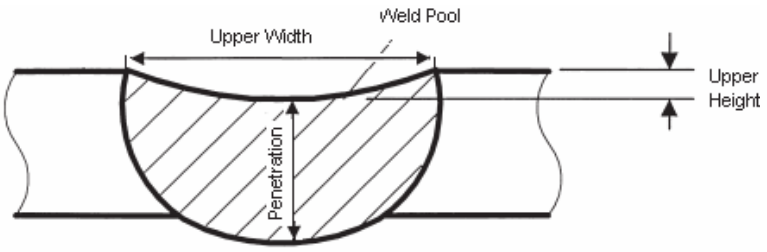

Figure 1.1. Weld pool geometry

Weld pool geometry plays an important role in determining the mechanical properties of the weld. Therefore, it is very important to select the welding process parameters for obtaining an optimal weld pool geometry. Usually, the desired welding process parameters are determined based on experience or from a handbook. However, this does not ensure that the selected welding process parameters can produce the optimal or near optimal weld pool geometry for that particular welding machine and environment.

In the present study, investigations were carried out on the AISI type austenitic stainless steels. The materials selected for the experimental study were;

- To investigate the effect of process parameters on the quality responses of the TIG welded joints 1.2 mm AISI 304 austenitic stainless steel was used. AISI 304 stainless steel is the most versatile and the most widely used in the fabrication of pressure vessels plates, food industry and pipe manufacturing. The difficulties when welding thin steel sheets can be arranged as; sensitive to high heat input, difficult to control heat affected zone and penetration, tearing under high current and slow welding speeds, excessive carbide precipitation under unsuitable welding condition.
- AISI type 5 mm 304 L and 4 mm 304 stainless steels were welded under various electrode tip configurations of 0^o, 15^o, 30^o, 45^o, 60^o, 75^o, 90^o in order to analyze the effect of TIG welding parameters and electrode tip angle on microhardness, tensile load and microstructure of the joints.
- Plates of different thickness are used in the industry and thicker plates are normally joined by multipass welding. In the analyzing of the effect of multipass welding on temperature distribution of the joints, AISI type 304L and 316L stainless steels were used with the thicknesses of 8 mm and 10 mm.

In this study, experimental design based on the statistical principles has been used to achieve the most reliable results. Then, the information obtained has been used to optimize the process and determine the effect of parameters on the quality

responses. A mathematical model of the process has also been developed to determine the optimal values of TIG welding parameters

The following aims had been targeted to study the effect of pool geometry on the quality of austenitic stainless steels:

1. The effect of multipass welding on the temperature distribution of TIG welded joints,
2. The effect of electrode tip angle on the penetration profile, microhardness and transverse tensile load,
3. The effect of process parameters (welding speed, welding current, gas flow rate and gap distance) on the weld pool geometry (tensile load, heat affected zone, upper width, upper depth, penetration and area of penetration), and relationship between the process parameters and responses,
4. Process parameter selection for optimizing the TIG weld pool geometry and quality, i.e. maximizing transverse tensile load (TL), minimizing heat affected zone (HAZ), minimizing upper width (UW), minimizing upper height (UH), maximizing depth of penetration (P) and area of penetration (AP),
5. Developing mathematical formula for predicting the weld pool geometry using MATLAB programming language,
6. Construction and prediction of the relationship between welding process parameters and weld pool geometry by using Neural Network (NN) with Back propagation Network (BPN),
7. Finally, comparison of the results between measured values and predicted values from developed mathematical model and Neural Network.

2. PREVIOUS STUDIES

2.1. Theory of Tungsten Inert Gas (TIG or GTAW) Welding

Welding can be defined as any process in which two or more pieces of metal are joined together by the application of heat, pressure, or a combination of both. Most of the processes may be grouped into two main categories: pressure welding, in which the weld is achieved by pressure; and heat welding, in which the weld is achieved by heat. Heat welding is the most common welding used today.

Arc welding, which is heat-type welding, is one of the most important manufacturing operations for the joining of structural elements for a wide range of applications, including guide way for trains, ships, bridges, building structures, automobiles, and nuclear reactors, to name a few. It requires a continuous supply of either direct or alternating electric current, which create an electric arc to generate heat to melt the metal and form a weld (Awang, 2002).

The arc welding process is a remarkably complex operation involving extremely high temperatures, which produce severe distortions and high levels of residual stresses. These extreme phenomena tend to reduce the strength of a structure becomes vulnerable to fracture, buckling, corrosion and other type of failures.

The most widely used arc welding processes are shielded metal arc (SMAW), gas tungsten arc (GTAW or TIG), gas metal arc (GMAW), and submerged metal arc welding (SMAW) (Teng and et al., 2003).

The TIG welding, also known as Heliarc tungsten inert gas welding process was invented during the Second World War due to the need of the American aircraft industry for a method of joining magnesium and aluminum. Russell Meredith demonstrated the first TIG process for the welding of magnesium using a Tungsten electrode and helium gas in the late 1930's. This joining method replaced riveting as a method of building aircraft with aluminum and magnesium components. The heliarc welding has continued to this day with many refinements and name changes, but with no change in the fundamentals demonstrated by Meredith.

TIG welding uses a non-consumable tungsten electrode protected by an inert gas (Ericsson, 2002). The electrode is either made of pure tungsten or tungsten, mixed with small amounts of oxides (thoriumoxide, zirconiumoxide) improving the stability of the arc and makes it easier to strike. Since the process uses a non-consumable electrode, extra filler material is usually added for thick materials (Wu and et al., 1997). The principle of the process is schematically shown in Figure 2.1.

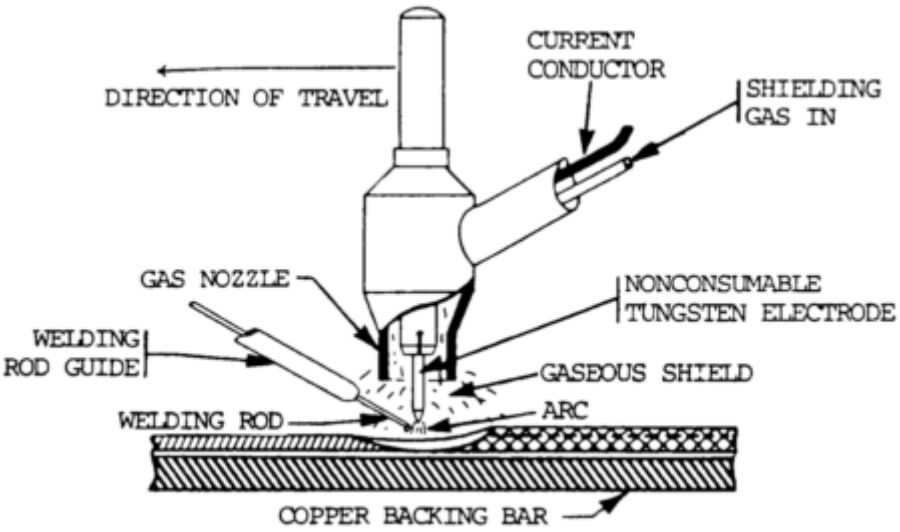

Figure 2.1. Principle of tungsten inert gas (TIG) welding (Ericsson, 2002)

The electrical discharge generates an arc between the electrode tip and the workpiece to be welded. The arc is normally initialized with a power source with a high frequency generator, which produces a small spark that provides the initial conducting path through the air for the low voltage welding current. The frequency of this ignition pulse is large, up to several MHz. This frequency together with a high voltage, produces strong electrical interference around the welding cell, which is a disadvantage when sensors and measuring equipment are used. The arc consists of a high-temperature conducting arc that produces the thermal energy needed to melt the base and filler material. The arc temperature spans between 11700 ^{o}C and 14700 ^{o}C above the pool surface and the temperature of the melted surface spans 1427 ^{o}C to 2500 ^{o}C, dependent on the material (Ericsson, 2002).

Three different alternatives of current can be used namely;

i. Direct current (DC) with a positive electrode,

ii. DC with a negative electrode,

iii. Alternative current (AC).

AC is mainly used for the welding of aluminum and magnesium since cleaning of the oxide layer on the surface can in this way be achieved. DC with a negative electrode is used for most other materials, including thick plates of aluminum. Pulsed and non-pulsed currents can be used. A non-pulsed current is most common. The use of a pulsed current has some advantages, such as increased penetration (Lothongkum and et al., 2001).

Depending on the thickness of the base material, type of joint and certain other factors, extra filler material might be needed. In automatic TIG welding hot or cold wire can be used. Cold wire or Rod is fed in the front of the melted pool as shown in Figure 2.2. Coiled wire may be acquired in small 100 mm spools or 915 mm long as a rod. The coils and rods are manually fed into the leading edge of the weld pool during the cold-wire welding.

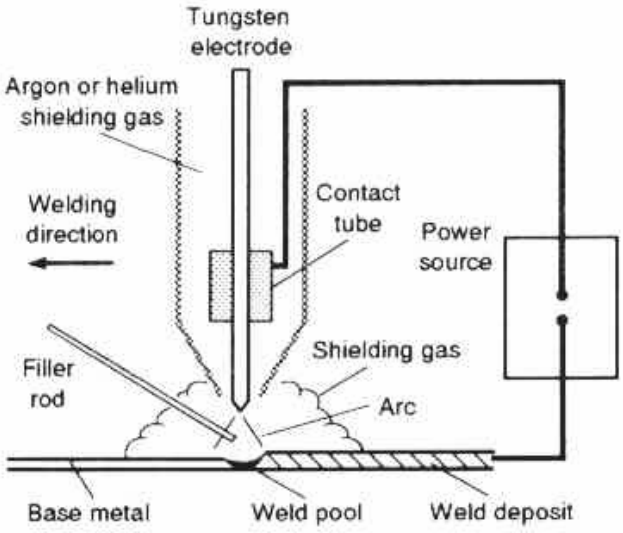

Figure 2.2. Cold-wire TIG welding (Kou, 1987)

Hot wire as shown in Figure 2.3, fed in the back and utilizes a heated filler metal to increase the deposition rate of the process. The wire is resistance heated to near the melting temperature and fed into the trailing edge of the weld pool.

Deposition rates to 29 kg/h are achievable. The higher deposition rates obtained with hot wire make the process competitive for welds and overlays and improve productivity. The filler material is usually the same as the base material (Modenesi and et al., 2000).

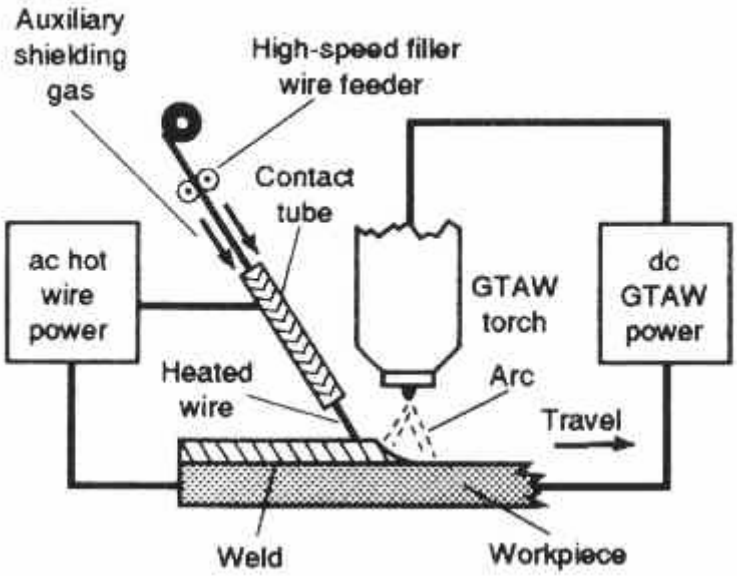

Figure 2.3. Hot-wire TIG welding (AWS, 1991)

An inert gas is used to sustain the arc and to protect the melted pool and the electrode from atmospheric contamination. Depending on the welding parameters and welding materials, either argon, helium or a mix of the two gases can be used. Argon is commonly used in welding unalloyed, low alloyed and stainless steels. However, a mixture of argon and hydrogen or helium can be used for mechanical welding (Tusek and Suban, 2000). For duplex stainless steel, it is common to mix argon with nitrogen to ensure a correct ferrite/austenite balance. Aluminum and alloys are usually welded using argon. The addition of helium can be used to improve the heat transfer and is therefore sometimes used for the welding of thicker parts (Suban and et al., 2001).

Gas tungsten arc welding is used extensively for welding stainless steels, aluminum, magnesium, copper, and reactive materials (for example, titanium and tantalum). The process can also be used to join carbon and alloy steels. In carbon steels, it is primarily used for root pass welding with the application of consumable

inserts or open-root techniques on pipe. The materials welded range from a few thousands of a millimeter to several millimeters in thicknesses.

2.2. Advantages and Limitations

Tungsten inert gas welding has following advantages:

- Produces high quality low distortion welds,
- Free of spatter associated with other methods,
- Can be used with or without filler wire,
- All-position welding,
- The ability to weld most of the metals and alloys,
- The ability to join metals that form refractory oxides, such as aluminum and magnesium,
- Can be used with a range of power supplies,
- Gives precise control of welding heat through pulsing,
- Visible arc and weld pool,
- Filler metal does not cross the arc. The amount added does not depend on the weld current level.

Some limitations of this process are:

- Produces lower deposition rates than consumable arc welding process
- Requires slightly more dexterity and welder coordination than gas metal arc welding (GMAW)
- Slow welding speed
- Problematic in drafty environments because of difficulty in shielding the weld zone properly
- It is not generally used for very low melting metals such as tin and lead,

2.3. Main TIG Welding Equipments

2.3.1. Power Supplies

Power supplies for TIG welding are usually the constant-current type with a dropping (negative) volt-ampere (V-A) curve. Saturable reactors and thyristor-controlled units are the most common. Advances in the electronics industry have readily been accepted in the welding community, resulting in sophisticated, light weight power supplies. Transistorized direct current (DC) power supplies are becoming common and the never rectifier inverter supplies are very compact and versatile.

The inverter power supply consists of three converters:

1. 60 Hz primary alternating current (AC) is rectified to DC
2. Direct current is inverted to high frequency ac
3. Alternating current is rectified to dc (Byrd, 1993).

The inverter supplies can be switched from constant current to constant voltage for TIG welding, resulting in a very versatile piece of equipment. The inverter-controlled power supplies are more stable and have faster response than conventional silicon-controlled rectifier (SCR) power supplies. Figure 2.4 compares the response of an inverter-controlled arc welding machine and a thyristor-controlled welding machine.

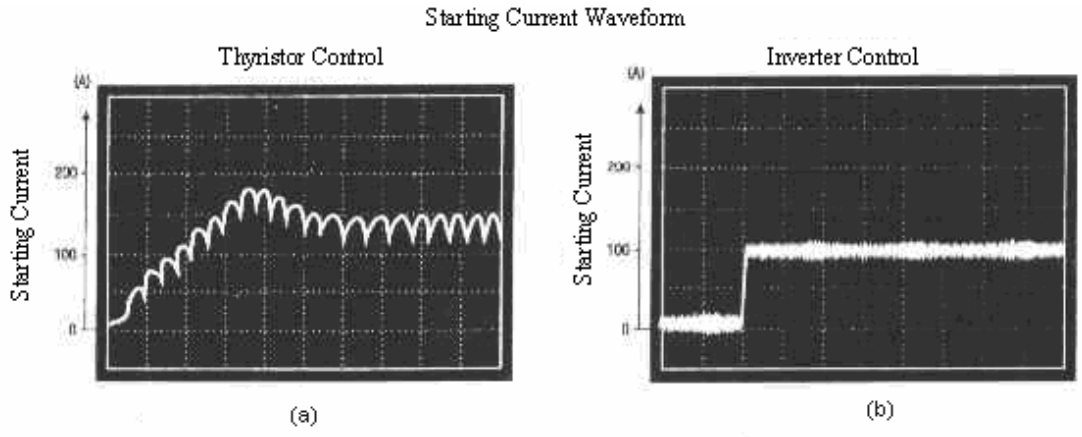

Figure 2.4. (a) Inverter controlled source, and (b) Thyristor controlled source (ASM, 2002)

Li and Zhang (2001), developed robust control to achieve the controlled detachment of the droplet, the welding current was switched from a peak level to a background level to induce droplet oscillation. It is found that the dynamic model of the process depends on welding operational parameters, which vary with applications, and therefore it is unrealistic for operators to provide welding machines these parameters as input.

Lothongkum, Viyanit and Bhandhubanyong (2001), studied the effects of pulsed TIG welding parameters on delta-ferrite content, shape factor and bead quality in orbital welding of AISI 316L stainless steel plate. They showed that increasing nitrogen content in argon gas decreased the pulse current, and increasing the welding speed decreased the weld width.

2.3.2. Torch

The welding torch holds the tungsten electrode that conducts the current to the arc, and it provides a means of shielding the arc and molten metal. The major components of a typical welding torch are shown in Figure 2.5.

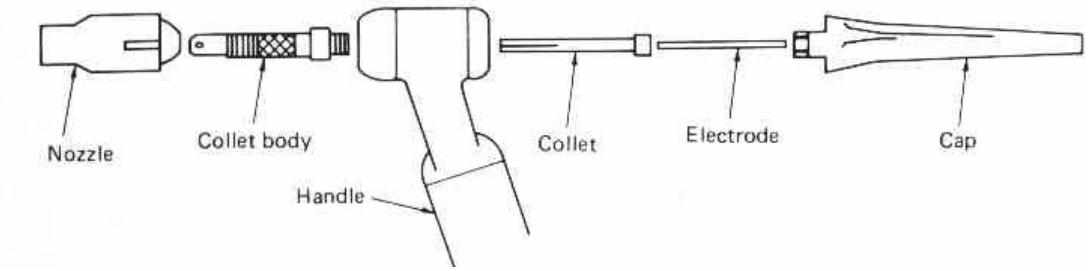

Figure 2.5. Key components of a TIG welding manual torch (ASM, 2002)

Nozzles are made of ceramic, metal, metal jacketed ceramic, fused quartz, or other materials. Ceramic nozzles are the least expensive and most popular, but are brittle and must be replaced often. Fused quartz nozzles are transparent and allow better vision of the arc and electrode. However, contamination from metal vapors from the weld can cause them to become opaque, and they are also brittle (AWS, 1991).

Welding torches rated at less than 200 A arc normally gas-cooled (that is the shielding gas flows around the conductor cable, providing the necessary cooling). Water cooled torches are used for continuous operation or at higher welding currents and are common for mechanized or automatic welding. The cooling water may be supplied to the torch from a recirculating tank that uses a radiator or chiller to cool the water (Myers, 1992).

Zhang and Jiang (2002) developed a new GTA welding process that can increase the weld penetration by using two torches on the opposite sides of the workpiece and connecting them to the power supply in series. This modified welding system achieved good joint penetration, controlled heat input and reduced in the number of passes with the gas tungsten arc process.

2.3.3. Electrodes

The nanconsumable electrodes used in TIG welding are composed of tungsten or alloys of tungsten. The most common electrode is a 2% ThO_2-W alloy (EWTh-2). This material has excellent operating characteristics and good stability. Thoria is radioactive, so care must be taken when sharpening electrodes not to inhale metal dust. The grindings are considered hazardous waste in some states, and disposal may be subject to environmental regulations. Lanthaniated (EWLa-1) tungsten electrodes have the best starting characteristics in that an arc can be started and maintained at a lower voltage. Ceriated tungsten (EWCe-2) is only slightly better than the thoriated tungsten with respect to arc starting and melt-off rate. Any of the aforementioned electrodes produces acceptable welds. The easy starting of the lanthaniated electrode is a result of the lower work function which allows it to emit electrons readily at a lower voltage (AWS, 1991).

Pure tungsten is used primarily in arc welding and has the highest consumption rate. Alloys of zirconium are also used. Tungsten electrodes are classified on the basis of their chemical composition shown in Table 2.1.

Requirements for tungsten electrodes are given in ANSI/AWS A5.12 Specification for tungsten and tungsten alloy electrodes for arc welding and cutting.

The shape of the electrode tip can affect the resulting weld shape (Key, 1980).

Table 2.1. Classification of alloying elements in selected tungsten electrodes for TIG welding applications (AWS, 1991)

AWS Classification	Color	Alloying Element	Alloying Oxide	Alloying Oxide, wt%
EWP	Green	--	--	--
EWCe-2	Orange	Cerium	CeO_2	2
EWLa-1	Black	Lanthanum	La_2O_4	1
EWTh-1	Yellow	Thorium	ThO_2	1
EWTh-2	Red	Thorium	ThO_2	2
EWZr-1	Brown	Zirconium	ZrO_2	0.25
EWG	Gray	Not specified	--	--

Tungsten electrode may have an end profile that is pointed or partly or completely hemispherical. A pointed out end is ideal for welding in restricted locations, and it enables the current density to be maintained at an extremely high level.

The electrode taper angle is the angle that is ground on the end of the tungsten electrode. Taper angles usually range from 30^o to 120^o. Smaller taper angles tend to wear more quickly, especially when the tip of the electrode touches the workpiece. In order to reduce number of times an electrode tip to be ground, a larger taper angle is recommended. Higher current carrying capacity enables thoriated tungsten electrodes to be tapered.

In TIG welding with Direct Current Electrode Negative polarity (DCEN), the taper angle has a significant influence on:

- The voltage-current characteristics of the arc,
- The penetration characteristics and the width of the welding pool,
- The temperature distribution along the length of the electrode.

Once the arc is initiated, the torch is held with the electrode positioned at angle of about 75^o to the welding pool surface for manual feeding of filler metal (Ataman, 2001). Whereas, the filler rod is usually held at angle of about 15^o to the surface of the work and slowly fed into the weld pool as shown in Figure 2.6 (AWS,

1980).

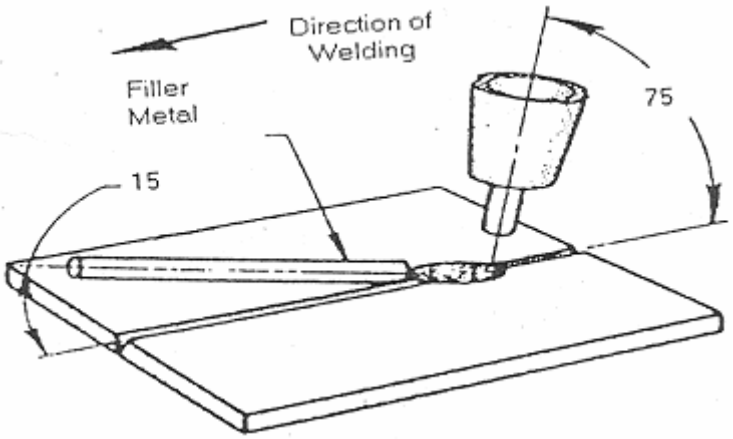

Figure 2.6. Motion of filler metal and nozzle condition for a manual TIG welding

A slight inclination in the forehand position is necessary for good visibility. Yet, an acute angle of filler metal can cause aspiration of air into the shielding gas and thus contaminate the weld. The hot end of the filler metal should always be kept in the protective atmosphere of the shielding gas. Besides, molten pool should be kept as quite as possible to prevent vaporizing the deoxidizing elements.

Goodarzi, Choo, and Toguri (1997) studied mathematical models for the arc and weld pool in TIG welding process and the effect of electrode tip angle on both arc and weld pool. Also they investigated the gas shear stress on the weld pool, anode current density, and heat flux. They showed that for temperatures less than 9730 ^{o}C, some modifications were necessary to take into account the absorption of heat by the cooler parts of the arc. Also, it was found that by increasing the electrode tip angle, the anode spot at the weld pool surface tended to be more localized. This led to a higher maximum heat flux and anode current density.

2.3.3.1. Electrode Extension

Ordinarily, the distance of electrode extend beyond the orifice of the gas nozzle should be equal to one or two times electrode diameters. However, the longer the electrode extension, more danger there is of striking the work metal or filler rod

and of contaminating the electrode. On the contrary, the farther the electrode is extended, the greater must be the volume of gas flow to compensate for the greater distance of the gas nozzle from the workpiece surface (Ataman, 2001).

2.3.4. Filler Metals

In many applications alloy steels with small thickness are welded by TIG welding without filler metal. Selection of filler metal in TIG welding, generally, presents fewer problems than in other arc welding processes. Usually, the choice of the filler metal depends on the type of the base metal being welded. In TIG welding, the filler metal is fed into the welding pool, not into the arc, which is an advantage because it results in more efficient alloy transfer, thus enabling more accurate control over the composition of the weld metal (Modenesi and et al., 2000).

In general, the chemical composition of the filler metal should be similar to the base metal. Besides, the size of the filler metal has also effect on the weld quality. However, if it is too small, it will melt rapidly forming a globule at its end. But on the other hand, if it is too large, the filler metal may cause arc disturbance which will give rise to oxide inclusions in the weld. As well as those, the filler metal and torch must be moved smoothly in order to avoid exposure of the liquid weld metal, the hot filler metal and the hot solidified weld bead to air. In manual welding, the filler metal in the form of wire is continuously fed into groove by the operator.

At the same time, the wire surface must be free of all drawing lubricants and oxides to ensure high quality welding with the correct composition filler metal. Opened packages, dirty gloves, and greasy or dirty welding equipments are all poor workshop practices which may contaminate the filler metal and result in defective welds.

Modenesi and et al., (2000), presented the activated flux TIG welding process for the austenitic stainless steels with fluxes of only one major component. Their results indicated that even the very simple flux that was used can greatly increase the penetration of the weld bead.

Lathabai, Jarvis and Barton (2001), developed a keyhole gas tungsten arc

welding and compared it with a conventional gas tungsten arc welds in commercially pure (CP) titanium. The process enabled single pass, out of chamber welding of 12.7 mm thick CP titanium without excessive filler metal addition or joint preparation.

Ames and Johnson (2003), developed fluxes to increase penetration when used with the gas tungsten arc welding process. This study showed that the high penetration gas tungsten arc welding flux composition could have a significant influence on microstructure evolution in super duplex welds.

2.3.5. Wire Feed Systems

Wire feed systems are made from a number of components and vary from simple to complex. The basic consists of a means of gripping the wire sufficiently (especially in hot-wire TIG welding) to pull it from the spool and push it through the guide tube to the point of welding. Electronic switches and controls are necessary for the electric drive motor. The wire will be fed into the leading edge for cold wire feeds into the trailing edge for hot wire feeds (AWS, 1991).

2.4. TIG welding Process Techniques and Variations

2.4.1. Manual Welding

Manual welding refers to the TIG welding process in which the welder manipulates the welding torch by hand. If a motorized wire feeder is attached to the torch, the process is classified as semiautomatic welding. Product generated by skilled manual welders account for a large proportion of TIG welding applications. The equipment can be quite inexpensive and properly trained welders can join a wide variety of materials. Manual welding is used extensively in stainless steel piping as well as for the root pass in carbon steel pipe welds.

2.4.2. Mechanized Welding

It may require adjustment to welding parameters in response to visual observation of the weld. Machine or mechanized welding requires some specialized accessories. The basic system contains a means for holding and moving the welding torch as well as the workpiece. Because arc voltage is as essential variable in TIG welding and is proportional to the arc length, voltage feedback devices are often used with motorized torch holders to control the arc length (AWS, 1991).

2.4.3. Narrow Groove Welding

Narrow groove welding makes use of the TIG cold wire welding process with a narrowed weld joint. Figure 2.7 shows a typical weld. Narrow groove welding is limited to mechanized welding applications where precise torch location can be maintained (Pfaid, 1990).

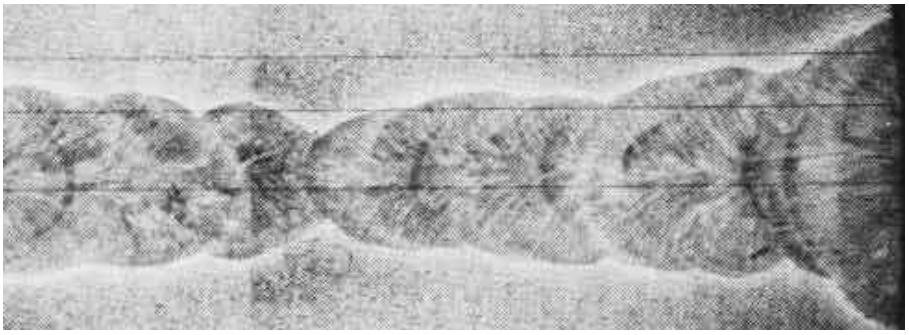

Figure 2.7. Narrow groove weld product in mechanized welding applications (Myers, 1992)

Zhang and Jiang (2002) developed double sided arc welding (DSAW) method to improve the arc concentration for narrow groove welding. They also developed to achieve deep narrow penetration under variations in welding conditions. Their experiments verified that the developed system was capable of achieving deep narrow penetration on a 12.7 mm thick square butt joint in a single pass.

2.4.4. Automatic Welding

It does not require manual parameter adjustment or observation of the weld during the welding process. The most common application of automatic welding is associated with orbiting weld heads used to weld pipe and tubing. The devices attach to the workpieces and move around the circumference fusing the metal. Most systems perform an autogenous weld, others have wire feed and oscillation capabilities. These systems are often used in conjunction with a computer to control the welding variables. Automatic controls utilizing microprocessors and computer numerical control servo drives make it possible to use one welding system to weld a variety of materials and shapes (Pfaid, 1990).

Kodama, Kawano and Iwabuchi (2001), developed TIG automatic welding for use on the raised edges of tank corners, a type of component requiring high-level welding skills. These welds were highly confined, and the joint shape changed in a complex manner.

Li and Zhang (2001), proposed a modified active control of metal transfer in which the droplet starts to oscillate by first moving toward the weld pool. They also concluded that, the detaching pulse can be applied after a very short period of time and combination of increased electromagnetic force and downward momentum is guaranteed.

2.4.5. TIG Arc Spot Welding

Gas tungsten arc spot welding is often done manually with a pistol-like holder that has a vented, water cooled gas nozzle, a tungsten electrode that is concentrically positioned with respect to the gas nozzle, and a trigger switch for controlling the operation as shown in Figure 2.8.

Gas tungsten arc spot welding electrode holders are also available for automatic applications. The configuration of the nozzle is varied to fit the contour of the weldment. Edge locating devices can be used to prevent variations in the distance spot weld locations from the workpiece edge. The nozzle is often used to press

against the workpiece to assure tight fit up of the faying surface. This technique also controls the electrode-to-work distance.

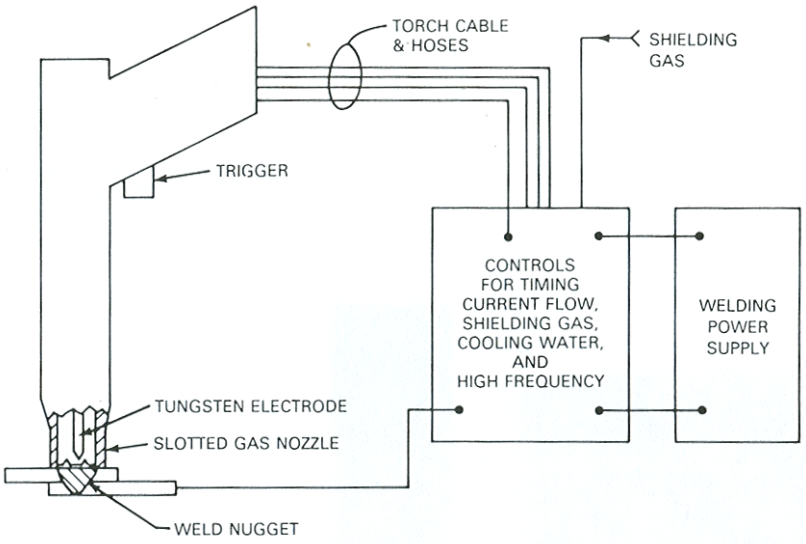

Figure 2.8. Manual tungsten inert gas spot welding (AWS, 1991)

TIG arc spot welding may be done with either AC or DCEN. Automatic sequencing controls are generally used because of the relatively complex cycles involved. The controls automatically establish the preweld gas and water flow, start the arc, time the arc duration, and provide the required postweld gas and water flow.

Penetration is controlled by adjusting the current and the length of time it flows. In some applications, multiple pulses of current are preferred to one long sustained pulse. Variations in the shear strength, nugget diameter, and penetration of the spot weld can be minimized with accurate timers, current monitors, and tungsten electrodes that have precision ground tips. A melted spot on the bottom of the lower workpiece is a positive indication of a good spot weld (AWS, 1991).

2.5. Main TIG Parameters Influencing Joints and Pool Geometry

Welding process variables have effects on the metallurgical changes of the weld metal and the adjoining base plate. Energy input from the welding arc, preheats and interpass temperatures, cooling rate, chemical composition and thermal

properties of the plate and filler metal, joint design of the base metal influence the mechanical, microstructural properties and pool geometry of the steels (Ataman, 2001).

The TIG welding process, which is the most flexible of all fusion welding processes, is limited by the characteristics of the particular metal and joint efficiency requirements. Basically, TIG weld quality is strongly characterized by the welding parameters. This is because the process parameters play an important role on the weld pool geometry and mechanical properties of the weld. As shown in Figure 2.9, three main parameters group can be defined in TIG welding (Ericsson, 2002).

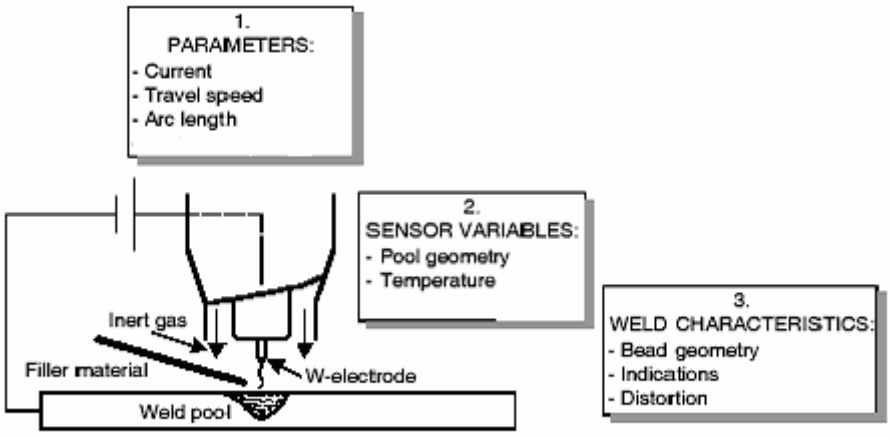

Figure 2.9. Schematic diagram of the TIG process parameters (AWS, 1991)

The following basic variables, that mostly influence the weld pool geometry, can be controlled from the start to the finish with an automatic TIG process:

- Welding current,
- Welding voltage,
- Welding speed,
- Shielding gas flow rate,
- Arc Length,
- Polarity,
- Joint design and production condition of base metal.

2.5.1. Welding Current

Current is the most important variable in TIG since a change in current affects the depth of penetration (pool geometry), welding speed, heat input, deposition rate and quality of the welding.

Fundamentally, there are two choices of welding current. These are:

i. Direct current: Direct current (DC) is an electrical current that flows on one direction only. Most welding power sources are capable of welding with direct current output. They accomplish this with internal circuitry that changes or rectifies the AC into DC. In DC welding, the welding current circuit may be hooked up as either electrode negative (the nonstandard term is straight polarity) or electrode positive (the nonstandard term is reverse polarity). Direct current is generally used for carbon steels, copper and its alloys, stainless steels, nickel and its alloys, titanium, zirconium and its alloys.

ii. Alternating current (AC): The terms electrode positive (reverse polarity) and electrode negative (straight polarity) which were applied to the workpiece and electrode lose their significance. The current is alternating or changing its direction of the flow at a predetermined set frequency and with no control over time or independent amplitude. During a complete cycle of alternating current shown in Figure 2.10, there is theoretically one half cycle of electrode negative and one half cycle of electrode positive (AWS, 1991).

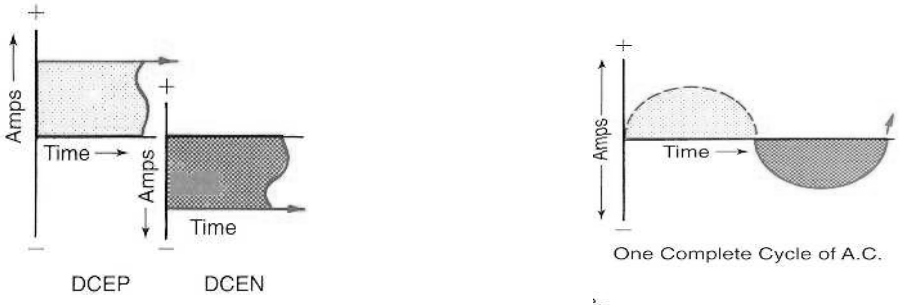

Figure 2.10. Alternating current cycle (AWS, 1991)

Since the heat is evenly distributed at the two ends of the arc as indicated in Figure 2.11, the depth of the penetration is less than that obtained with DCEN, but more than that which would be obtained with DCEP. The profile of the weld lies between by electrode negative and wide, shallow type profile produced by electrode positive. Alternating current is generally used for aluminum and its alloys, magnesium and its alloys.

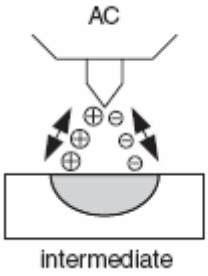

Figure 2.11. Penetration with alternating current (AWS, 1991)

When TIG welding with alternating current is used, it is realized that equal half cycle theory is not exactly true. There are two theories accounting for this. One is the oxide coating on the non-ferrous metals such as aluminum. The surface oxide acts as a rectifier, making it difficult for electrons to flow from the workpiece to electrode, then from the electrode to workpiece. The other theory is that molten, hot, clean workpiece does not emit electrons as easily as hot tungsten. This results in more current being allowed to flow from the hot tungsten to the clean molten weld pool to the electrode. This is referred to as "*arc rectification*". The arc would be unstable and sometimes even go out. To prevent this from happening, it is a common practice to introduce into the welding current a high voltage, high frequency, low power, additional current.

In addition to this, nonpulse or continuous current is the standard for TIG welding. However, there are several advantages to using pulsed current:

- Pulsing produces the maximum amount of penetration while minimizing the total heat applied to the part.
- Pulsing also aids in timing the motion necessary in manual welding and allows the weld pool to cool between pulses.

Lothongkum, Chaumbai and Bhandhubanyong (1999), investigated the effect of pulse current in flat, vertical and overhead positions. The base and pulse currents in all welding positions were adjusted to achieve a weld bead contour corresponding to DIN 8563 class AS. In the vertical and overhead positions, gravitational force made the weld pool fall down, leading to undercut after solidification. With the appropriate welding parameters and pulsed current, the gravitational effect was eliminated.

Lothongkum, Viyanit and Bhandhubanyong (1999), studied the effects of pulsed TIG welding parameters on delta-ferrite content, shape factor and bead quality in orbital welding of stainless steel plate. They have found out that increasing welding speed caused an increase in pulse current and increasing nitrogen contents in argon gas decreased the pulse current. It was also concluded that the delta-ferrite content in the weld ranged from 6 to 10% by volume.

2.5.2. Welding Voltage

The voltage drop which is between the tip of the tungsten electrode and the workpiece is influenced mainly by the type of welding current. As well as current, the arc voltage is proportional to the arc gap length and shielding gas composition (Ataman, 2001). Furthermore, a change in arc voltage will affect the heat input to a lesser extent when working with low voltage values.

2.5.3. Arc Length

Although, in many practices it is stated that arc length should be equal to about 1.5 times the electrode diameter, it can vary depending on the specific applications and particularly on the operator's preference.

The studies made on the effect of arc length showed that the depth/width ratio decreased with increasing arc length. Also, increasing the arc length would have the following effects:

1. Reduction in the arc efficiency when using a constant current,
2. Increase in the arc voltage if the current is maintained constant.

In general, it can be stated that the greater the arc length, the higher is the heat leakage to the surrounding atmosphere which results with inefficient welding. Whereas the opposite is also true (Ataman, 2001).

Mills et al. (1990), found out that increasing the arc length resulted a reduction in the arc efficiency when using a constant current and increase in the voltage if the current is constant.

Li and Wu (1997), analyzed the transport phenomena in the interfacial region between TIG arc length and weld pools. They introduced a three-dimensional model for fluid flow and heat transfer in the interfacial region. This work laid the foundation for developing a comprehensive model of the arc welding process where a dynamic, two way coupling between the welding arc and the weld pool surface is properly represented.

Patricio, F. and et al. (1999), analyzed the effect of welding parameters such as welding current and welding speed on defect and humping formation of very depressed weld pool at high welding speed and current. The conclusions obtained permit to explain the shape of the process envelope for TIG welding observed in experiments, and allow for the analysis of practical alternatives for its expansion.

Li and Zhang (2001), worked on improving the measurement accuracy of arc length using the spectrum of arc light at a particular wavelength during gas tungsten arc welding process with argon shield. They also studied the effect of welding parameters on spectral distribution. Their results showed that spectral lines of argon atoms were determined by arc length, independent of welding parameters other than the current.

2.5.4. Welding Speed

Arc penetration is usually inversely proportional to welding speed. Experimentally optimized welding speed pattern thus minimizes distortions caused by the thermal expansions and contractions during welding.

Alloys prone to thermal cracking cannot be welded at high welding speeds, since the associated steep thermal gradients will contribute to crack formation. So that, fairly low welding speeds are chosen to avoid this cracking problem. Low welding speeds are often used in conjunction with preheating the base metal to further reduce the possibility of thermal shock other than crack formation ability of welding speed. The size of the molten weld pool geometry is also directly influenced by the welding speed (Ataman, 2001).

2.5.4.1. Effect of Welding Speed and Welding Rate on Weld Pool Shape

The velocity of the welding torch affects not only the rate of solidification, but the shape of the weld pool and the propensity to develop centerline hot cracks. The shape of the weld pool is dictated by the velocity, V, at which the welding torch moves and by the rate at which heat can be removed at the solid-liquid interface. To keep a constant shape, the rate of new melting must be exactly balanced by the solidification rate. On the average, this solidification occurs normal to the solid-liquid interface, because this is the direction of the maximum temperature gradient and, thus, the direction of the maximum heat removal shown in Figure 2.12 (Savage, 1980).

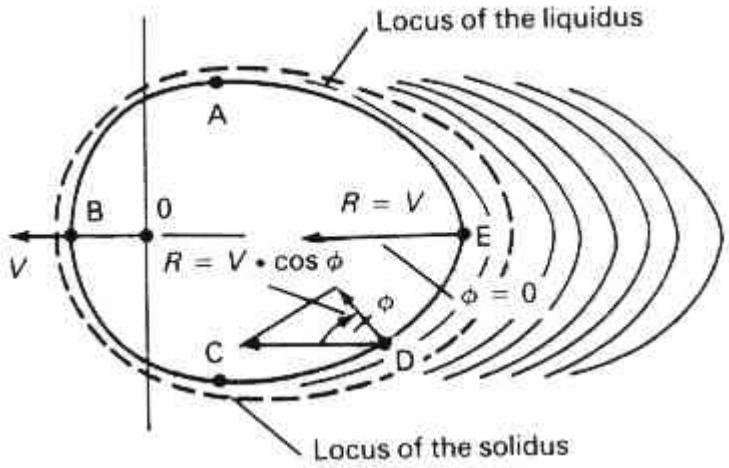

Figure 2.12. A moving weld pool showing the relationship between velocity of travel of welding torch, V, and the rate of solidification, R (Savage, 1980)

Simple geometry requires that for the weld pool shape to remain constant, the solidification rate, R, must be related to the torch velocity by;

$$R = V\cos\phi \tag{2.1}$$

where ϕ is the angle between the normal to the solid-liquid interface and the direction of motion of the torch. At the back of the weld pool, where $\phi = 0, R = V$. If this were not so, then the weld pool would be elongating or shortening. At the side of the weld pool, where $\phi = 90^0$, $R = 0$. If this were not case, then the weld pool would be decreasing in diameter. With a constant weld pool shape, solidification at the side of the weld pool occurs as the region adjacent to where $\phi = 90^0$ sweeps by, rather than by the motion normal to the weld pool velocity.

Equation (2.1) predicts that R will vary around the weld pool. As shown in Figure 2.13, planar solidification is to be expected at the sides of the weld pool, with the extent of the nonplanar solidification increasing towards the center of weld pool (Matsuda, 1969).

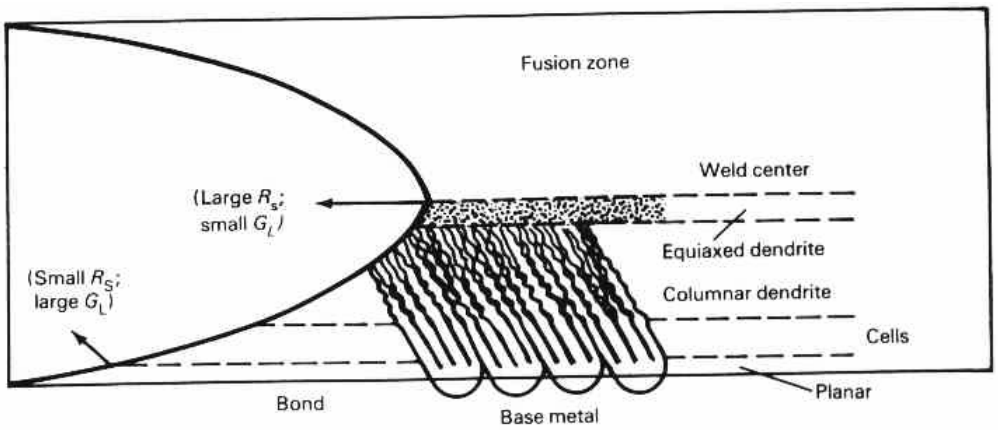

Figure 2.13. Variations of microstructures in response to variation solidification rate around the TIG welded joints (Matsuda, 1969)

The ability of the solid-liquid interface to move at a velocity, V, depends on two factors: maximum solidification rate: Which is a function of the crystallographic orientation of the solid at the point in question, and the ability of the temperature gradient in the solid to remove the heat and establish the appropriate temperature for solidification to proceed (Matsuda, 1969).

The planar growth of grains oriented with the direction normal to the solid-liquid interface is favored. This is shown in Figure 2.13. Grains with the preferred orientation will grow at the expense of adjacent. Because dendrites follow the same preferred growth directions, those with the proper orientation will be favored. The requirement for a constant weld pool size becomes somewhat more complex when the effect of crystallographic orientation is considered (Savage, 1980).

The equation (2.1) can be modified to become:

$$R' = V\cos\phi / \cos(\phi' - \phi) \qquad (2.2)$$

where R' is the growth rate in the preferred direction required to maintain a constant weld pool shape and ϕ' is the angle between R' and V, and $(\phi' - \phi)$ is the angle between the local preferred growth direction R, which is normal to the solid-liquid interface. Figure 2.14 shows the situation at successive points of the

weld pool as it moves in the direction of V (ASM, 2002).

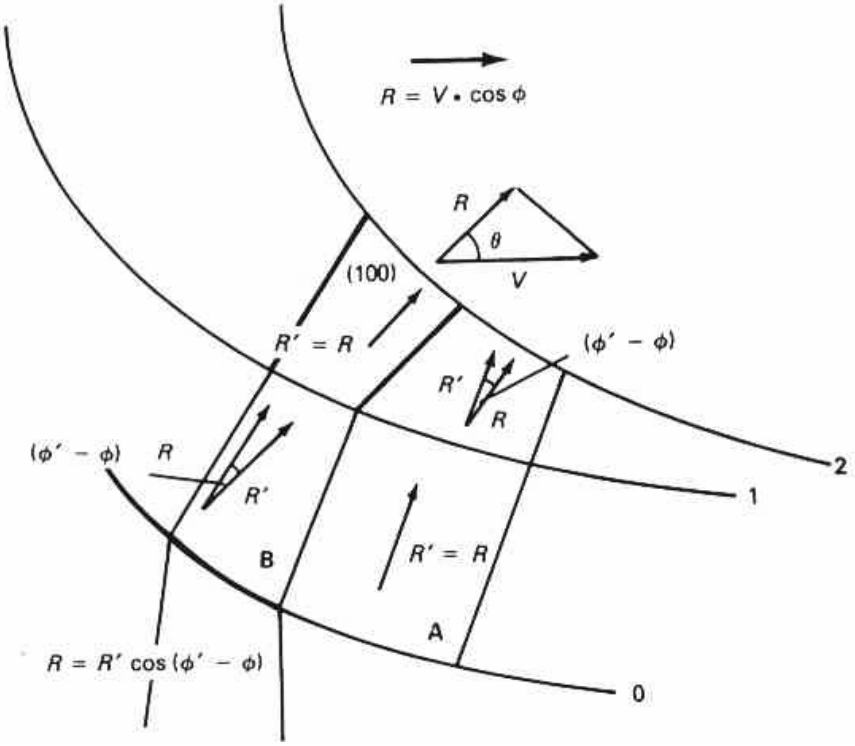

Figure 2.14. Movement of a curved solid-liquid interface for several grains (A and B), and the change in the rapid growth direction relative to the interface position in TIG welding (Savage, 1980)

The weld pool assumed to be elliptical in shape, so that at any point (except at the very back of the weld pool where $\phi = 0$) as the pool moves, the angle between R and V changes. If an adjacent grain becomes oriented such that $R^{'}$ becomes normal to the solid liquid interface (ASM, 2002).

Competitive growth causes grains to try to rotate into the direction of V. Figure 2.15(a) shows how grains rotate in an elliptical weld pool. Dendrites will also try to rotate into the R direction, although the grains or dendrites do not actually rotate.

The second factor is to consider is the ability to extract heat at the solid-liquid interface. Heat is extracted by the temperature gradient of the solid. This gradient is a minimum at the back of the weld pool, where the temperature of the solid is the highest (ASM, 2002). Unfortunately, this is exactly where the solidification rate must be a maximum to keep up with V. The temperature gradient

is a maximum at the side of the weld pool, where the least heat extraction is required, because here $R = 0$. As long as the maximum possible solidification rate, $R_{\max}$, is equal to or greater than V, the weld pool can maintain an elliptical shape. If V is decreased above $R_{\max}$, then the solidification rate at the back of the weld pool can not keep up, and the weld pool elongates. Increasing V decreases the heat input, which shrinks the weld pool volume (ASM, 2002). With the weld elongating, this means that the diameter must decrease as the pool elongates. This causes the weld to take on a tear-drop shape, as shown in Figure 2.15(b).

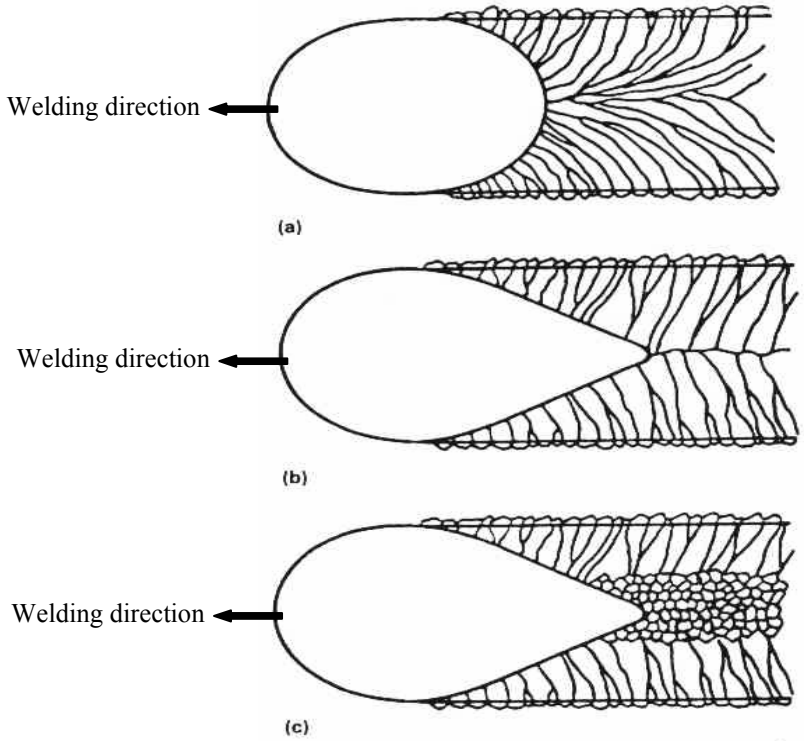

Figure 2.15. Effects of heat input and welding speed variations on weld pool geometry and microstructure. (a) Low heat input and low welding speed producing an elliptical weld pool. (b) Medium heat input and medium welding speed producing a tear-drop shaped welding pool. (c) High heat input and high welding speed producing heterogeneous nucleation at weld pool centerline (ASM, 2002)

The angle at the back of the weld pool will decrease until $\phi_{critical}$ is reached. $\phi_{critical}$ is given by:

$$\phi_{critical} = \cos^{-1}(R_{\max} / V) \tag{2.3}$$

R_{max} is controlled by the thermal conductivity of the solid, the geometry of the part being welded, and the preferred direction growth rate. When there is a shift to a tear-drop weld pool, the grain (or dendrite) rotation is limited to $\phi_{critical}$. When this situation is attained (Figure 2.15(b)), the grains will all grow together at the center of the weld pool. Figure 2.15(b) typifies what is to be expected from a pure material or one with a low solute content.

When R is increased, not only does the weld pool become tear-drop shaped, but the nature of the structure changes. If R is large enough, equiaxed grains can develop from heterogeneous nucleation in the supercooled centerline material as shown in Figure 2.15(c). Such behavior has indeed been observed in aluminum alloys (ASM, 2002).

Norman, Drazhner and Pragnell (1999), studied the effect of TIG welding parameters on the solidification microstructure of autogenous TIG welds in an Al-Cu-Mg-Mn alloy. They observed the finest microstructure at the centre of the weld and was attributed to the higher cooling rates at the weld centre of the weld also increased producing a reduction in the scale of the dendrite secondary arm spacing.

2.5.5. Polarity

2.5.5.1. Direct Current Electrode Negative (DCEN)

In direct current electrode negative polarity (sometimes called as straight polarity), the work would be connected to the positive terminal. In the other words, as shown in Figure 2.16(a), the electrons are flowing from the electrode to the work, concentrating heat at the joint. The electrons carry up to 70 percent of the heat energy in the arc to part. The workpiece tends to melt rapidly since it receives the greater part of the heat. The positive ions are directed toward the negative electrode; the positive electrode experiences only 30 percent of the heat effects. No cleaning action for the removal of oxides from the metal is present with DCEN. With DCEN, higher current may be used on the tungsten electrodes of same size. The increased current density will yield deeper penetration, permits higher speeds, and form a

narrow, deep bead. The narrow bead is due to the small electrode used, while the increased penetration is due to the heat being carried by electrons .The narrower bead also results in a narrower heat affected zone surrounding the weld. Because there are fewer contraction stresses, less trouble with hot cracking of some metals is encountered. The DCEN type of operating current is preferred for welding metals that do not have a refractory oxide such as aluminum or magnesium (Hicken and Jackson, 1966).

2.5.5.2. Direct Current Electrode Positive (DCEP)

It (also called as reverse polarity) is literally the reverse of DCEN. The torch is connected to the positive terminal on the welding of power source and workpiece is connected to negative terminal as shown in Figure 2.16(b). In DCEP welding, the tungsten electrode acquires extra heat because the electrons are flowing toward it instead of work (ASM, 2002).

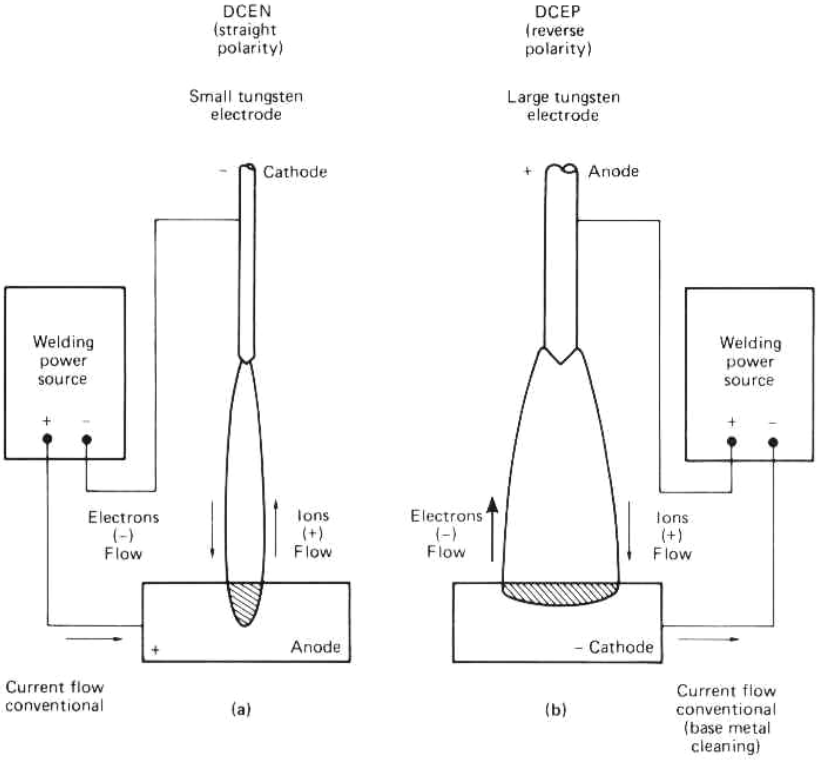

Figure 2.16. Effect of polarity on TIG weld configuration.(a) DCEN, (b) DCEP (Hicken and Jackson, 1966)

Heat tends to melt the tip of electrode. Because of this excess heating of the electrode, a much larger size electrode is required for DCEP than DCEN. Electrodes size limits welding to relatively low current values. Larger diameter electrodes are undesirable because they tend to spread the arc over too large area, cut down the welder's visibility, and increase the instability of the arc. With DCEP the work stays comparatively cool and shallow penetration results. An important characteristic of DCEP welding is oxide cleaning ability. Electrode positive is not generally recommended for TIG because of excess heat it puts into the tungsten. However, it is present during the electrode positive half cycle of ac arc welding. The disadvantage of this polarity is that due to magnetic forces the arc will sometimes wander from side to side when making the fillet weld when two pieces of the metal are at a close angle to one another.

Because, most heat is generated at the anode in the TIG welding process, DCEP is used for welding certain thin sections. Low melting point materials when DCEN would be likely to cause excessive penetration or burn-through.

Besides, DCEN produces a deep and narrow penetration in the base metal. Contrary to DCEN, DCEP results in more heat in the electrode than in the workpiece. Therefore, larger diameter electrodes are necessary with DCEP. The effect of polarity on weld pool shape is shown in Figure 2.17 (ASM, 1988).

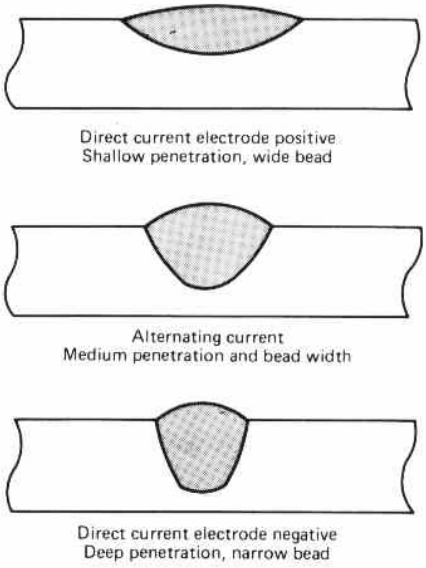

Figure 2.17. Effect of polarity on weld pool geometry (ASM, 1988)

2.5.6. Shielding Gases

The shielding gas used in a welding process has a significant influence on the overall performance of the welding system. Its primary function is to protect the molten metal from atmospheric nitrogen and oxygen as the weld pool is being formed. The shielding gas also promotes a stable arc and uniform metal transfer (Ataman, 2001).

Also, density of the shielding gas has an important influence on the efficiency of shielding the arc and the weld pool against the ambient atmosphere. The values indicating relative density of the shielding gas with regard to air are of primary importance. Argon and carbon dioxide are gases having by far the highest density and therefore, form an efficient gas shielding around the arc. However, the densities of hydrogen and helium are 10–20 times less than that of argon and thus, are prone to turbulent flow at the exit from the blowpipe nozzle due to thermal buoyancy (ASM, 2002).

The shielding gas interacts with the base material and with the filler material, if any, to produce the basic strength, toughness and corrosion resistance of the weld. It can also affect the weld bead shape and the penetration pattern.

Understanding the basic properties of a shielding gas will aid in the selection of the right shielding gas or gases for a welding application. Use of the best gas blend will improve the equality and may reduce the overall cost of the welding operation as well.

Mohandas and et al. (1999), investigated the effect of welding process shielding gas and the addition of grain refining elements on the weld zone tensile properties of a ferritic stainless steel conforming to AISI 430. They found that, the tensile ductility of gas tungsten arc welds was also on an average marginally greater than that of shielded metal arc welds. The addition of titanium and copper led to improved strength over that of the base alloy.

2.5.6.1. Basic Properties of a Shielding Gas

The controlled electrical discharge known as the welding arc is formed and sustained by the establishment of a conductive medium called the arc plasma. This plasma consists of ionized gas, molten metals, slags, vapors, and gaseous atoms and molecules. The formation and structure of the arc plasma is dependent on the properties of the shielding gases used for welding. Basic properties of a shielding gas consist of (Larson and Meredith, 1990):

1. **The ionization potential:** is the energy expressed in electron volts necessary to remove an electron form a gas atom.
2. **The thermal conductivity:** is a measure of how well it is able to conduct heat. It influences the radial heat loss from the center to the periphery of the arc column as well as heat transfer between the plasma and liquid metal.
3. **Dissociation and Recombination:** shielding gases such as carbon dioxide, hydrogen and oxygen are multiatom molecules. When heated to high temperatures within the arc plasma, these gases break down, or dissociate into their component atoms. They are then at least partially ionized, producing free electrons and current flow.
4. **Reactivity/Oxidation potential:** the oxidizing nature of the shielding gas affects both welding performance and properties of the resultant weld deposit. Argon and helium are completely nonreactive, or inert, and thus have no direct chemical affect on the weld metal. Addition of reactive gases such as oxygen or carbon dioxide enhances the stability of the arc and affects the type of metal transfer obtained.
5. **The Surface tension:** it is between the molten metal and

its surrounding atmosphere (shielding gas) has a pronounced influence on weld pool geometry. If the surface energy is high, a convex, irregular bead will result. Low values promote flatter beads with minimal susceptibility for undercutting.

6. **Gas Purity:** Most materials can be welded using a welding grade torch gas with a purity of 99.995% or 50 ppm impurities. However, some reactive materials, such as titanium, molybdenum, and tantalum, require that the contaminant level be less than 50 ppm, which may require certified purity or the use of gas filters and purifiers (Krysrak and Bhaniha, 1990).
7. **Gas Density:** is the weight of the per unit volume. Density is the one of the chief factors that influences shielding gas effectiveness. Basically, gases heavier than air, such as argon and carbon dioxide, require lower flow rates in use than do the lighter gases, such as helium, to ensure adequate protection of the weld puddle.

2.5.6.2. Shielding Gas Selection for TIG

2.5.6.2.1. Argon

The most commonly used gas for TIG welding, argon exhibits low thermal conductivity, which produces a narrow, constricted arc column; this allows greater variations in arc length with minimal influence on arc power or weld bead shape. Its low ionization potential provides good arc starting characteristics and good arc stability using the direct current electrode negative (DCEN) power connection plus superior arc cleaning action and bead appearance when ac power is used. Argon is the most commonly selected gas for DCEN welding of most materials and ac manual welding of aluminum (AWS, 1991).

2.5.6.2.2. Helium

The high thermal conductivity and ionization potential of helium make it suitable for the high current joining of heavy sections of heat-conductive materials such as aluminum. Helium increases the penetration of the weld as well as its width. It also allows the use of higher weld travel speed.

2.5.6.2.3. Argon-Helium Blend

Blends of argon-helium are selected to increase the heat input to the base material while maintaining favorable arc stability and superior arc starting characteristics. Blends of 25, 50, and 75% He in argon are commonly used.

2.5.6.2.4. Argon-Hydrogen Blend

Hydrogen is added to argon to enhance its thermal properties. The slightly reducing atmosphere improves weld puddle wetting and reduces some surface oxides to produce a cleaner weld surface. The addition of hydrogen also significantly increases the volume of molten material in the weld pool due to the higher thermal conductivity of argon–hydrogen mixtures at temperatures at which molecules of hydrogen dissociate. To minimize problems associated with arc starting, additions of hydrogen are generally limited to 5 to 15%. These blends are primarily used to join some stainless steels, nickel and nickel alloys. These mixtures should not be used to join alloy steels; delayed weld cracking may result. Argon/2-5H_2 is used in manual welding applications on materials thicker than 1.6 mm. Additions of 10 to 15 H_2 are used in mechanized applications, such as these found in the manufacture of stainless steel tubing (AWS, 1991).

Mee, Meelker and Schelde (1999), investigated the control of hydrogen level in duplex stainless steel weldments. They made the welds under varying conditions to evaluate the weld susceptibility to hydrogen-induced cracking. The heat input was varied by using different travel speeds. They have found that,

hydrogen in the weld metal appeared to be more dependent on welding procedure rather than moisture content of the shielding gases. Also, they measured the lower hydrogen levels at the higher heat inputs due to a longer time the weld metal was in delta ferrite phase, giving the hydrogen time to diffuse.

Tusek and Suban (2000), analyzed the effect of hydrogen in argon as a shielding gas in arc welding of austenitic stainless steel. The studies showed that hydrogen addition to argon changes the static characteristic of the welding arc. The hydrogen addition to argon increases arc power and, consequently, the quantity of the material melted. In TIG welding a 10% addition of hydrogen to argon increases the quantity of the parent metal melted by four times. The hydrogen addition increases thermal and melting efficiencies of the welding arc too. The process stability in TIG welding in the mixture of hydrogen and argon is very good.

Suban, Tusek and Uran (2001), used hydrogen as a combustible or shielding gas in welding. They determined that, hydrogen addition to argon and/or helium in TIG welding process increased the process efficiency.

Durgutlu (2004), studied the effect of hydrogen in argon as shielding gas for tungsten inert gas welding of 316L austenitic stainless steel. He examined the microstructure, penetration and mechanical properties of the welded joints. It was concluded in his study that, the highest tensile strength was obtained from the sample which was welded under shielding gas of 1.5%H_2+Ar. Also, mean grain size in the weld metal increased with increasing hydrogen content. Additionally, weld metal penetration depth and its width increased with increasing hydrogen content.

Anderson and Wiktorowicz (1999), reported that the depth of penetration in TIG welding can be significantly increased by using an activated flux. Also, it is widely acknowledged that joint completion rates can be increased by using argon-helium or argon-hydrogen shielding gas mixtures.

2.5.6.3. Gas Flow Structure

Shielding gas is used to displace reactive gases in the atmosphere from the vicinity of the weld. Inert gases, as explained above, are preferred for the TIG welding process, because they minimize unwanted gas-metal reactions with the workpieces. A uniform laminar flow of gas from the gas cup would be ideal and, in fact, is usually achieved as long as there is no welding arc. However, the arc discharge rapidly heats the gas in the arc column, and thermal expansion causes plasma jets. The lower temperature near the cathode tip in Figure 2.18 is an indication of a jet pumping in cooler gas (Jackson, 1980 and Glickstein, 1985).

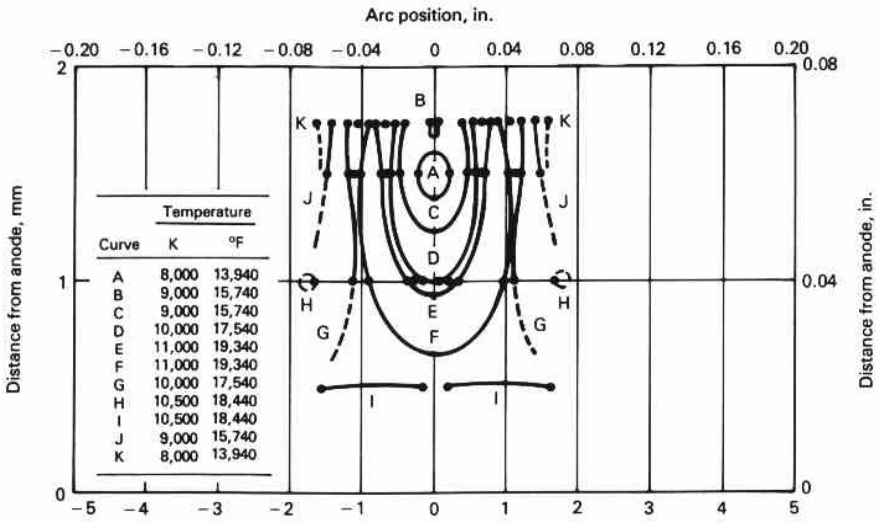

Figure 2.18. TIG welding arc column temperature distribution relative to anode distance and arc position (Jackson, 1980)

This becomes an important factor at high currents, because these jets can depress the surface of the weld pool and alter heat transfer to it. The rapid gas expansion can cause the flow to deviate from laminar and, in extreme cases, the flow can become turbulent (Key, 1980). Turbulence tends to mix atmospheric contaminants into the arc, often where they can do the most harm: at the surface of the molten weld pool (Key, 1982).

Figure 2.19 shows examples of laminar and turbulent gas flow around the nozzle of TIG welding. Laminar flow occurs where the fringes are generally straight and parallel.

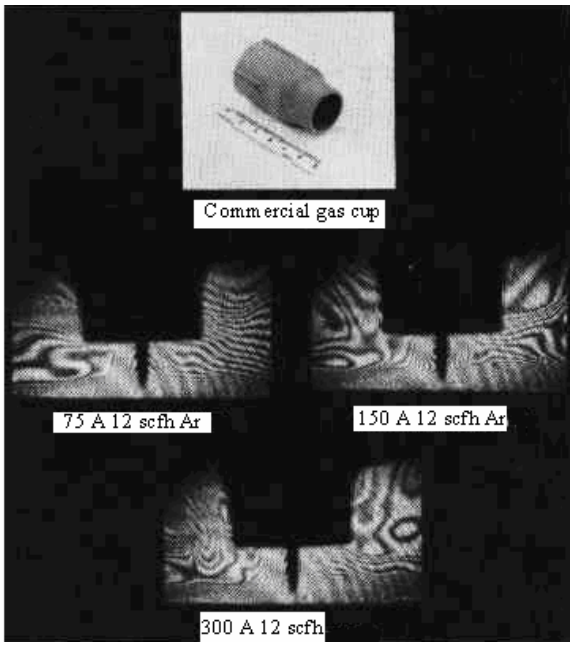

Figure 2.19. Effect of commercial nozzle gas cup geometry on shielding flow characteristics (Smart, 1986)

Turbulent flow is indicated by very wavy or circular fringes. Increasing current tends to make the laminar region somewhat broader and thicker, effectively increasing the area shielded from atmospheric contamination.

Figures 2.20 and 2.21 show gas cup shapes for improved gas flow. Figure 2.20 shows that a converging cone would be a very poor choice for the TIG welding process, as indicated by very small area of laminar flow and extreme turbulence in the surrounding region.

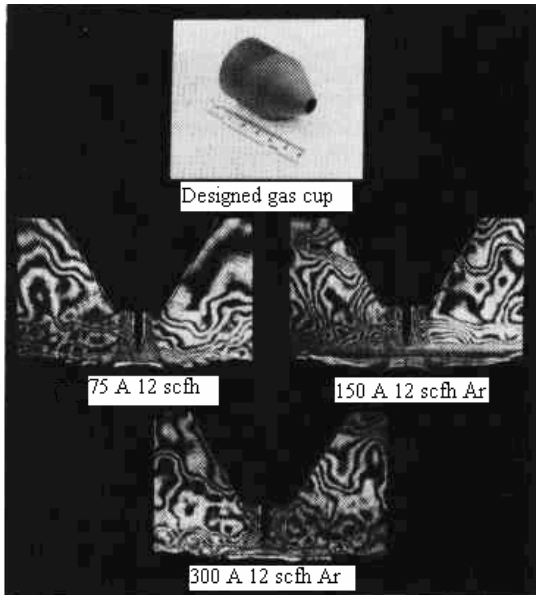

Figure 2.20. Effect of converging cup geometry on shielding flow characteristics (Smart, 1986)

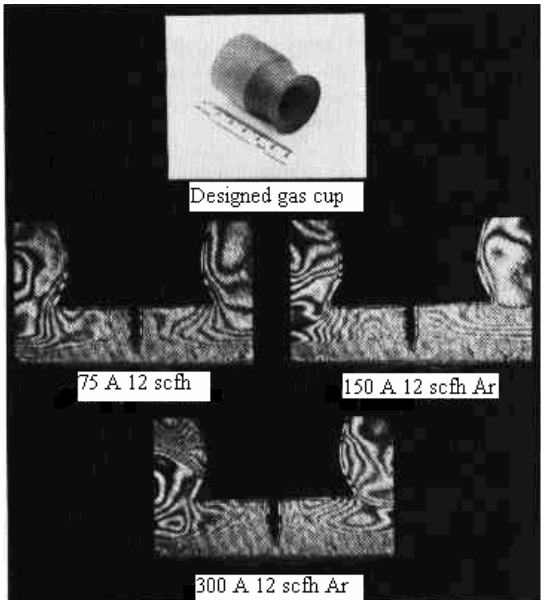

Figure 2.21. Effect of venture gas cup geometry on shielding flow characteristics (Smart, 1986)

2.5.7. Joint Design and Production Condition of Base Metal

Due to the variety of base metals and their individual characteristics (such as surface tension, flowability, melting temperature, etc.), joint geometries or designs that provide optimum welding processes should be selected for TIG welding. Factors affecting the joint design include metal thickness, weld penetration and joint efficiency requirements along with the metals' characteristics.

The required exactness of joint preparation also depends upon whether the TIG welding process is to be carried by manually or automatic means. Due to its tolerance to greater irregularities in joint fit up, manual TIG welding process is less sensitive to narrow joint preparation tolerances than automatic TIG welding.

Moreover, beveling is generally not required for butt joints less than 3.2 mm; whereas base metals higher than this thickness should be beveled to form V-, J- or U-groove in order to minimize erratic penetration that causes crevices and voids (AWS, 1980).

Initially, this is the most widely used joint design for thin plates when complete joint penetration is required from one side only. It also provides the most economical welding, because minimum filler metal, preparation and set up time are required. There are three variables of this joint design; root opening (B), thickness of root face (C) and angle of bevel (A) as shown in Figure 2.22. The amount of root opening and thickness of the root face depend upon whether the TIG welding process is to be manual or automatic, filler metal is to be added during the root pass and a backing is going to be employed. The amount of bevel angle and thickness of root face depends on the thickness of the metal and the clearance needed for arc movement to assure adequate fusion on both sides of the joint (Ataman, 2001).

Generally, bevel angles of 60° to 90°, root face thickness of 2.4 mm or less and root opening of 1.6 mm or less are mainly used for materials having thickness of 3.2 to 12.7 mm (AWS, 1980).

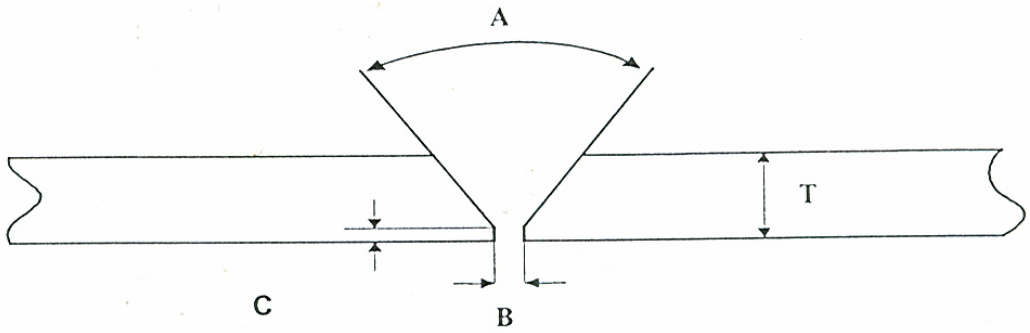

Figure 2.22. Schematic diagram for a single V-groove butt joint (Ataman, 2001)

Since TIG welding process is quite susceptible to contamination during welding, the workpiece must be carefully cleaned. Contaminants such as grease, oil, markings, paints, dirt, oxides, and fingerprints have to be removed from the welding surface area. Basically, ordinary degreasing is sufficient to remove contaminants except oxides. However, grinding or abrasive blasting is necessary for removing tenacious oxides. Finally, a minimum area of cleaning should exceed 15 mm from the joint on each side (AWS, 1980).

Teng and Lin (1998), studied on the effect of weld and joint design conditions on residual stresses due to butt welds. In this work, they predicted the residual stresses during one-pass arc welding in a steel plate using ANSYS finite element techniques. They showed the residual stresses distribution in a butt weld, the middle weld bead was in tension and the magnitude of this stress equals the yield stress. The ends of the weld were in compression. The peak transverse residual stresses in the central region decreased with an increasing specimen length. Also, the magnitude of the residual stresses with a restrained joint was larger than that estimated with an unrestrained joint.

Birch and Alves (2000), established the experimental work to examine the simple dynamic failure of the joints in thin sheet materials that are used extensively in vehicle construction. They made a comparison with similar bolted type joints.

Lebacq and et al. (2002), presented a methodology for the selection of joining in design, implemented in software. The method captures important coupling between the process options, material, joint type and design detail, using

databases assembled by discussion with experts on mechanical fastening, welding and adhesives. The approach first eliminates solutions that are not technically feasible, with reasons, and then ranks the remaining solutions on the basis of the degree of agreement with the set of design requirements.

2.6. Arc Physics of TIG Weld Pool

The TIG process is performed using a welding arc between a nonconsumable tungsten-base electrode and the workpieces to be joined. The physics of TIG arc fundamental to all arc processes and are more straightforward, because the complications of materials transferred through and interacting with the arc can be avoided. Geometrically, the arc discharge in TIG is between a rod-shaped tungsten electrode and a planar shaped electrode, that is, the workpiece.

Analysis of the arc discharge is separated into electrode regions and the arc column. The electrode regions are confined to very small distances from the electrode surfaces, have very high electrical and thermal fields, and have much higher current density, because of the contraction of the arc to a small spot. As a result, electrode regions for both the cathode and the anode are difficult to analyze by diagnostic measurement and theoretical computation. This situation must be remedied for a through understanding of the process, because the process parameter controls the arc discharge at the cathode, with the anode serving as the connection to ground. The arc column, on the other hand, is relatively easy to analyze, but is important primarily as a means to deduce arc characteristics at the electrodes (Key, 1982).

Wendelstorf and et al. (1996), studied on the survey modeling of the TIG and plasma arc welding. They modeled the arc column using finite element modeling. Their results showed a good agreement with the actual results.

Fenggui and et al. (2004), established integral mathematic model of fluid flow and heat transfer of TIG arc and weld pool. They used finite element model analysis and ANSYS software to analyze the behaviour of welding arc and weld pool including welding arc temperature field, current density distribution, fluid

flow in weld pool and effects of a few forces on weld pool shape. They proved calculated results by experiments.

2.6.1. Electrode Regions

The cathode and anode are similar in several respects. Both exhibit a voltage drop caused by a space charge that covers a very thin region over their surfaces, and the arc is significantly contracted on the surface. Figure 2.23 shows that the total arc voltage is partitioned between the electrode drops and arc column. The relative magnitude of these drops depends on welding parameters and electrode material.

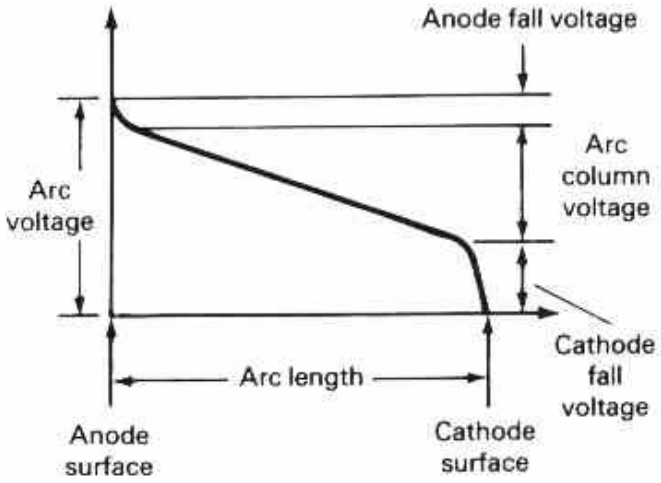

Figure 2.23. Arc voltage versus Arc length distribution between electrodes (Key, 1982)

The arc discharge requires a flow of electrons from the cathode through the arc column to the anode, regardless of polarity or whether ac or dc is used. There are two cases of electron discharge at the cathode (Lancaster, 1988):

1. Thermionic emission
2. Nonthermionic emission

2.6.1.1. Thermionic Emission

Thermionic emission results from joule heating (resistance) of the cathode by the imposed welding current until the electron energy at the cathode tip exceeds the work function (energy required to strip off an electron). This ease applies to the general case DCEN, where the tungsten electrode is the emitter, or cathode. Pure tungsten electrodes have to be heated to their melting point to achieve thermionic emission. Once molten, the equilibrium tip shape becomes a hemisphere and a stable arc results from uniform emission over this surface. Thoria (ThO_2), zirconia ($Zr\ O_2$), or ceria (CeO_2) are added to pure tungsten in amounts up to 2.2 wt% ThO_2, 0.4wt% $Zr\ O_2$, and 3.0 wt% CeO_2 to lower the work function, which results in thermionic emission at lower temperatures and avoids melting the cathode tip. These electrodes typically have a ground conical tip, and thermionic emission is localized to a cathode spot. Thermionic emission creates a cloud of electrons, called a space charge, around the cathode. If a second electrode at a higher potential is nearby, then the electrons will flow to it, thus establishing the arc (Lancaster, 1988).

2.6.1.2. Nonthermionic (Field) Emission

It creates an electron discharge with a very high electric field, typically exceeding 10^9 V/m. This intense electric field literally pulls electrons out of a relatively cold or unheated cathode. This would not appear to be applicable to welding until one considers that for reverse polarity or DCEP, a condensation of positive ions from the arc column can build up in a very thin layer over the cathode surface creating a very high localized electric field even though the cathode voltage drop may only amount to several volts.

An oxide layer, which is always present on the cathode surface in an actual weld, facilitates this discharge with a source of lower work function electrons. When the oxide layer is very thin, emission occurs via a tunneling mechanism through the film to an emitting site. Thicker oxide films exhibit locally conducting

spots at the end of filamentary channels through the oxide.

The cathode cleaning action, which is one of the principal reasons to use DCEP or ac, results from stripping away the oxide film at the emitting sites by very small and intense jets of metal vapor and debris. It becomes obvious that a practical implication of the short lifetime of these cathode spots is a generally unstable arc that is due to the necessity of continual movement of the cathode spot to undepleted regions or oxide film. Arc instability is undesirable and DCEP or ac is only used when cathodic cleaning or the minimizing the heat input to the workpiece is a higher priority than optimizing weld bead shape and location (Lancaster, 1988).

2.6.2. Arc Initiation Methods

2.6.2.1. Scratch or Touch Start

With the power supply energized, and the shielding gas flowing from the cup, the torch is lowered toward the workpiece until the tungsten electrode makes contact with the workpiece. The torch is quickly withdrawn a short distance to establish the arc.

The advantage of this method of arc initiation is its simplicity of operation for both manual and machine welding. The disadvantage of touch starting is tendency for the electrode stick to the workpiece, causing electrode contamination and transfer of tungsten to the workpiece (Key, 1982).

2.6.2.2. High-Frequency Start

It can be used with DC or AC power sources for both manual and automatic applications. High-frequency generators usually have a spark-gap oscillator that superimposes a high-voltage ac output at radio frequencies in series with the welding circuit. The circuit is shown in Figure 2.24.

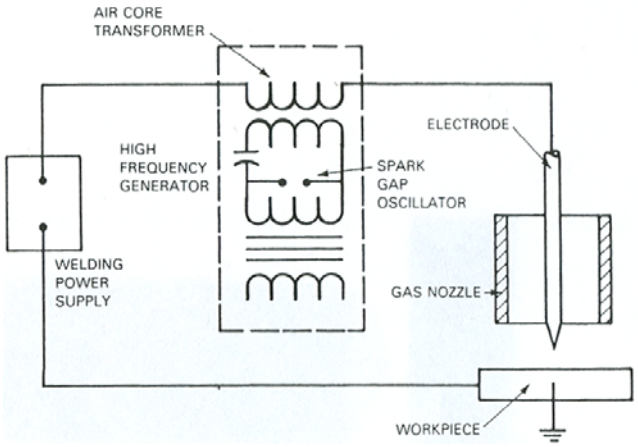

Figure 2.24. High frequency arc starting (Key, 1982)

2.6.2.3. Pulse Start

Applications of a high voltage pulse between the tungsten electrode and the work will ionize the shielding gas and establish the welding arc. This method is generally used with DC power supplies in machine welding operations.

2.6.2.4. Pilot Arc Start

Pilot arc starting may be used with dc welding power sources. The pilot arc is maintained between the electrode and the torch nozzle. The pilot arc supplies the ionized gas required to establish the main welding arc as shown in Figure 2.25.

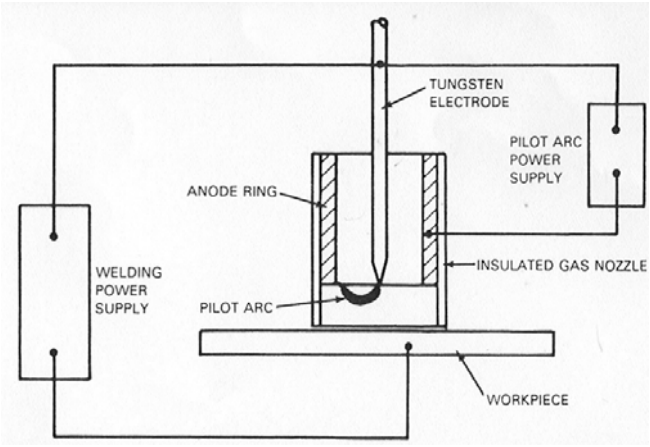

Figure 2.25. Pilot arc starting circuit used for TIG arc spot welding (Key, 1982)

2.6.3. Effect of Cathode Tip Shape on Arc Path

When the arc is used in a weld groove, the relative shapes of the cathode tip and anode groove become more important. The arc discharge from the cathode will seek a path to ground with the lowest electrical resistance. For a stable arc properly centered in the groove (i.e. a root passes), the shortest path to ground should be between the cathode tip and the bottom of the groove, as shown in Figure 2.26 (Lancaster, 1988).

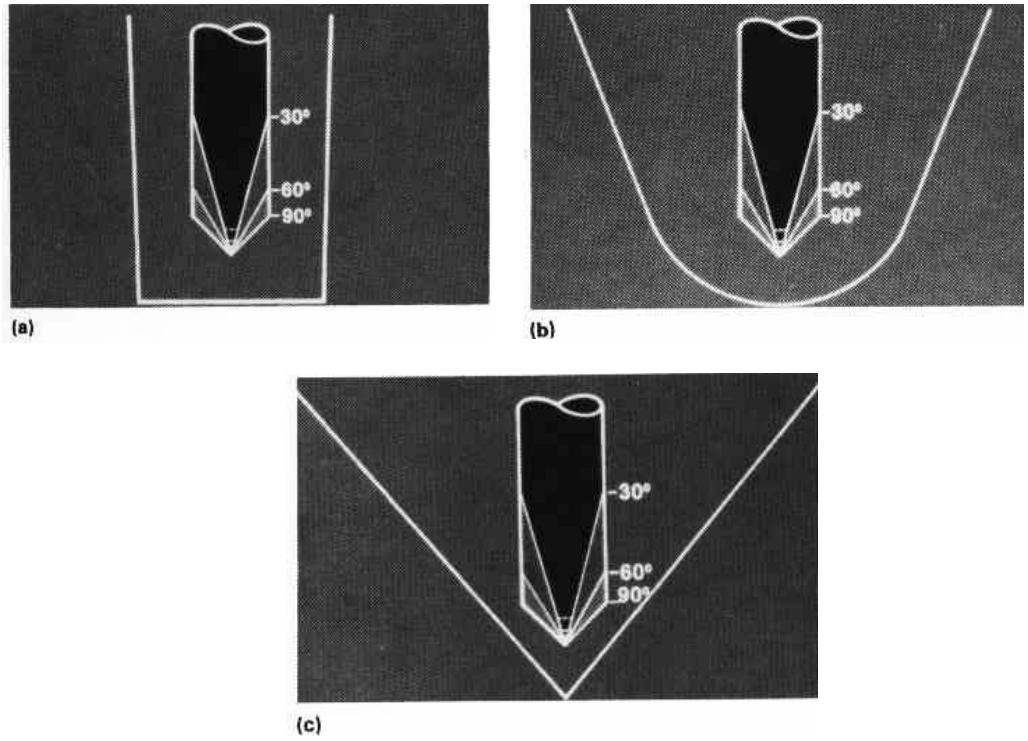

Figure 2.26. Effect of cathode tip geometry on the arc path length. (a) 75° V-groove, (b) 40° U-groove, (c) 10° narrow groove (Lancaster, 1988)

This will require the cathode vertex angle to be somewhat less than included angle of the groove and/or a sufficiently wide groove to ensure that the shortest path to ground is from the cathode tip to the groove bottom and not from the electrode shoulder to the groove wall, as the case would be with a 90° electrode in a 10° narrow groove. Welding in a groove places a higher priority on arc

stability and location than on maximum penetration (Smart, 1986).

2.6.4. Arc Column

The electron discharge between the electrodes partially ionizes the shielding gas in its path, thus making the arc column a conductor, or plasma. Overall, the arc column is neutral and is composed of electrons, positive gas and possibly metal ions, and neutral gas atoms.

Fundamental measurements of arc properties are most easily made in the arc column, although the actual effect of these properties on the electrode region of an actual weld must still be inferred. Nevertheless, it is useful to understand fundamentals of the arc that relate essential welding variables (current, voltage, electrode gap, and electrode shape) to arc temperature, current density distribution and gas flow structure at the anode surface.

Shielding gas composition has a rather strong effect on arc column temperature distribution and arc voltage. Figure 2.27 shows how shielding gas affects arc voltage (ASM, 2002).

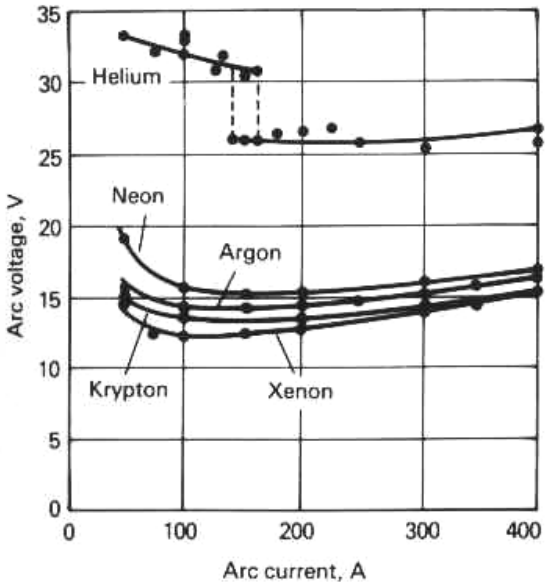

Figure 2.27. Effect of gas composition on arc voltage and current (Smart, 1986)

The curves would all be displaced downward for shorter arc lengths, but relative positions would be maintained. To understand these phenomena, arc temperature distribution for a variety of shielding gases and mixtures, electrode shapes, currents, arc voltage (electrode gap), and anode materials have been measured in order to clarify welding arc fundamentals (Lancaster, 1988).

Li and Wu (1997), introduced a three dimensional model for fluid flow and heat transfer in the interfacial region between the TIG arc plasma weld pool. The predicted current density and heat flux distributions in welding arcs were compared with experimental measurements taken from the literatures. The validity of the model was verified through TIG welding experiments.

Wu, Ushio and Tanaka (1997), developed a mathematical model to predict the velocity, temperature, and current density distributions in argon welding arcs. Also, comprehensive model of the TIG welding process, where a dynamic two-way coupling between the welding arc and the weld pool surface was represented.

Wu, Ushio and Tanaka (1999), analyzed the behavior of the TIG welding arc. They prepared the set of conservation equations for mass, momentum, energy, current and a mathematical model has been developed to predict the velocity, temperature, and current density distributions in argon welding arcs. They also obtained close agreement for the current and heat flux density with literature.

Wu and Gao (2002), developed the correlation of the heat flux distribution at the anode of a TIG welding arc. They analyzed the heat transfer contributions to the anode heat flux in TIG by using the models of TIG welding arc and the anode boundary layer. The results showed that, the energy carried by the electrons constituted most of the heat on the anode surface.

2.7. Energy and Heat in Arc Welding Processes

Welding and Joining processes are essential for the development of virtually every manufactured product. However, these processes often appear to consume greater fractions of the product cost and to create more of the production difficulties than might be expected. There are a number of reasons that explain this

situation:

- First, welding and joining are multifaceted both in terms of process variations (such as fastening, adhesive bonding, soldering, brazing, arc welding, diffusion bonding, and resistance welding) and in the disciplines needed for problem solving (such as mechanics, materials science, physics, chemistry, and electronics). An engineer with unusually broad and deep training is required to bring these disciplines together and to apply them effectively to a variety of processes.
- Second, welding or joining difficulties usually occur far into the manufacturing process, where the relative value of scrapped parts is high.
- Third, a very large percentage of product failures occur at joints because they are usually located at the highest stress points of an assembly and are therefore the weakest parts of that assembly. Careful attention to the joining processes can produce great rewards in manufacturing economy and product reliability (ASM, 2002).

One distinguishing feature of all fusion welding processes is the intensify of the heat source used to melt the liquid. Virtually every concentrated heat source has been applied to the welding process. However, many of the characteristics of each type of heat source are determined by its intensity, For example, when considering a planar heat source diffusing into a very thick slab, the surface temperature will be a function of both the surface power density and the time. Figure 2.28 shows how this temperature will vary on steel with power densities that range from 400 to 8000 W/cm^2. At the lower value, it takes 2 min to melt the surface. If that heat source were a point on the flat surface, then the heat flow would be divergent and might not melt the steel. Rather, the solid metal would be able to conduct away the heat as fast as it was being introduced. It is generally found that heat-source power densities of approximately 1000 W/cm^2 air necessary to melt most metals (Eagar, 1986a).

At the other end of the power density spectrum, heat intensities of 10^6 or 10^7 W/cm^2 will vaporize most metals within a few microseconds. At levels above these

values, all of the solid that interacts with the heat source will be vaporized, and no fusion welding can occur. Thus, the heat sources for all fusion welding processes should have power densities between approximately 0.001 and 1 MW/cm^2.

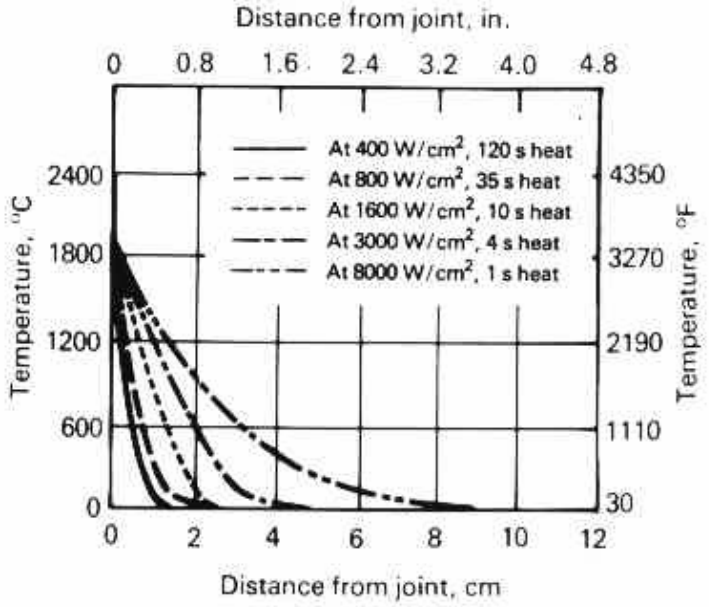

Figure 2.28. Temperature distribution after specific heating time in a thick steel plate (Eagar, 1986a)

The fact that power density is inversely related to the interaction time of the heat source on the material is evident in Figure 2.29. Because, this represents a transient heat conduction problem.

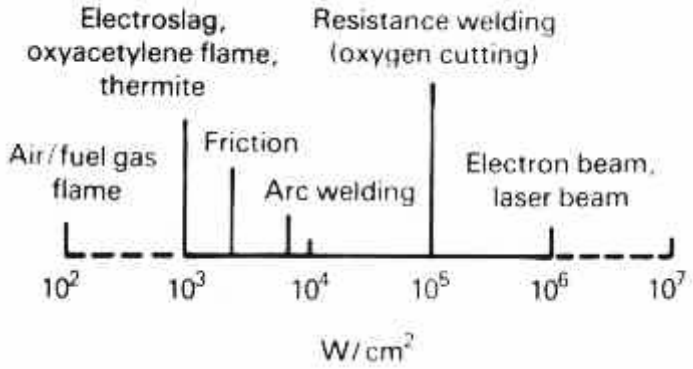

Figure 2.29. Spectrum of heat intensities used for fusion welding (Eagar, 1986a)

2.7.1. Heat Flow in Fusion Welding

During fusion welding, the thermal cycles produced by the moving heat source cause physical stale changes, metallurgical phase transformation, and transient thermal stress and metal movement. After welding is completed, the finished product may contain physical discontinuities that are due to excessively rapid solidification, or adverse micro-structures that are due to inappropriate cooling, or residual stress and distortion that are due to the existence of incompatible plastic strains. In order to analyze these problems, an analysis of welding heat flow must be presented focusing on the heat flow in the fusion welding process.

The welding heat source moves at a constant speed along a straight path. The end result, after either initiating or terminating the heat source, is the formation of a transient thermal state in the weldment. At some point after heat source initiation but before termination, the temperature distribution is stationary, or in thermal equilibrium, with respect to the moving coordinates. A physical model of the welding system is shown in Figure 2.30 (Chon and Tso, 1986).

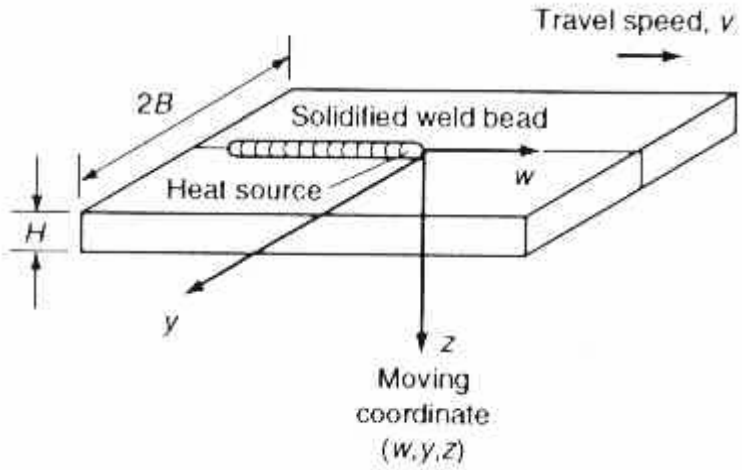

Figure 2.30. Schematic of the heat flow in fusion welding (Chon and Tso, 1986)

The origin of the moving coordinates coincides with the center of the heat source. The intense welding heat melts the metal and forms a molten pool. Some of the heat is conducted into the base metal and some is lost from either the arc column or the metal surface to the environment surrounding the plate. Three metallurgical

zones are formed in the plate upon completion of the thermal cycle: the weld metal (WM) zone, the heat affected zone (HAZ), and the base metal zone (BM). The peak temperature and the subsequent cooling rates determine the HAZ structures, whereas the thermal gradients, the solidification rates, and the cooling rates at the liquid-solid pool boundary determine the solidification structure of the WM zone. The size and flow direction of the pool determines the amount of dilution and weld penetration. The material response in the temperature range near melting temperatures is primarily responsible for the metallurgical changes.

Two thermal states, quasi-stationary and transient, are associated with the welding process. The transient thermal response occurs during the source initiation and termination stages of welding, the latter of which is of greater metallurgical interest. Hot cracking usually begins in the transient zone, because of the nonequilibrium solidification of the base material. A crack that forms in the source initiation stage may propagate along the weld if the solidification strains sufficiently multiply in the wake of the welding heat source. During source termination, the weld pool solidifies several times faster than the weld metal in the quasi-stationary state. Cracks usually appear in the in the weld crater and may propagate along the weld. Another dominant transient phenomenon occurs when a short repair weld is made to a weldment. Rapid cooling results in a brittle HAZ structure and either causes cracking problems or creates a site for fatigue crack initiation (Chon and Tso, 1986).

The quasi-stationary thermal state represents a steady thermal response of the weldment in respect to the moving heat source. The majority of the thermal expansion and shrinkage in the base material occurs during the quasi-stationary thermal cycles. Residual stress and weld distortion are the thermal stress and strain that remain in the weldment after completion of the thermal cycle.

Zhu and Chao (2002), investigated the effect of temperature dependent material property on the transient temperature, residual stress and distortion and distortion in computational simulation of welding process. Results showed that the thermal conductivity has certain effect on the distribution of transient temperature fields during the welding; the yield stress and Young's Modulus have significant and small effects, respectively, on the residual stress and distortion after welding.

2.7.2. Heat Input in TIG

The heat input rate is one of the most important variables in fusion welding, since it governs heating rate, cooling rate and weld pool size. The metallurgical feature that is directly affected by heat input rate is the grain size in the heat affected zone and in the weld metal. Grains in the solidifying weld metal grow coherently with grains in the solid metal at the fusion boundary. So that, the longer the time spent above the grain coarsening temperature of the alloy, the coarser is the structure in the heat affected zone and in the weld metal. In the case of steels various properties, particularly notch toughness, deteriorate as the grain size increases (Tsai, 1980).

Besides, heat input usually varies directly with increasing section thickness and inversely with increasing preheat temperature. As the thickness of the parts to be welded increases, the extra material adjacent to the weld bead acts as a heat sink making the weld cool more rapidly. The influence of plate thickness on thermal behavior of the plate can be summarized as:

- Cooling rate of HAZ increases with increasing plate thickness.
- Time at the elevated temperature and the width of the HAZ decreases as the plate thickness increases.

Generally speaking, the higher the heat input rate, the lower is the cooling rate and the larger is the weld pool. There is an inverse relationship between weld pool size and cooling rate. For example, as we increase the current, cooling rate decreases with the welding speed kept constant.

Welding process parameters (for example current and voltage) control the arc discharge at the cathode. Although the electron flow enters the anode spot and constitutes 85% of the energy going into the weld pool, thus making current density the single most important welding parameter that determines weld pool shape, events at the anode can only be controlled indirectly by controlling the cathode.

Current density and heat input measurements at the anode have been made to better understand how process parameter that are largely controlling events at the cathode will, in turn, influence the shape and melting rate of the weld pool. The

relative contributions of heat transfer to the workpiece in terms of the TIG welding process are shown in Figure 2.31.

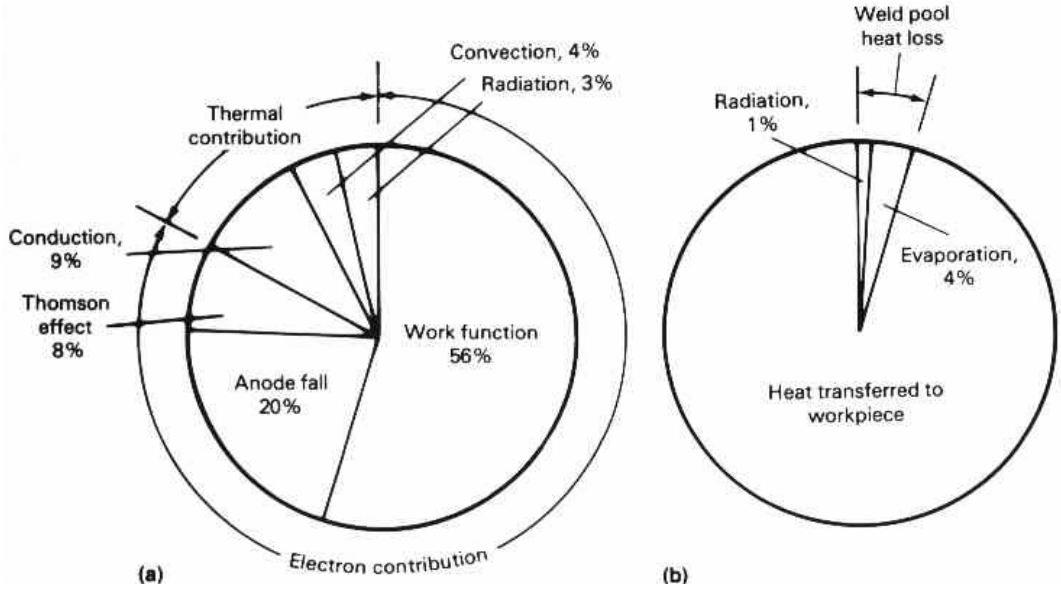

Figure 2.31. Relative heat transfer contributions with TIG welding. (a) Contribution of individual parameters to anode heat input. (b) Heat output at cathode (workpiece) relative to weld pool heat loss (AWS, 1976)

It is possible to make weld pool of any size, simply by increasing the heat input rate. However, this will make the weld pool difficult to control as it becomes larger, and the grain size may become undesirably large. In steel welding it is therefore necessary to seek a heat input rate for the optimum combination of grain size and cooling rate (Lancaster, 1993).

The size of heat input in arc welding depends mainly on the current, arc voltage and the welding speed (Henry and Claussen, 1998).

In general, heat input (kJ/mm) to the base material is calculated as (ASM, 1988):

$$H = \frac{EI}{1000V} \tag{2.4}$$

where E is the voltage, I is the current and V is the welding speed. The heat input given as above is the nominal heat input as arc efficiency is not

considered in the calculation. As shown in Figure 2.32, only part of the total arc energy available is transferred to the weldment. So that, only part of the energy which enters the weldment is used to melt the weld bead; whereas the remainder heats up the base metal and forms the heat affected zone. In general, the heat actually transferred to the workpiece, in units of kJ/mm, is defined as the net heat input, H_n:

$$H_n = \frac{F_1 EI}{1000V} \tag{2.5}$$

where F_1 is the heat transfer efficiency. The value of F_1 is generally between 0.7 and 1.0 for most of the arc welding processes. TIG welding which is the least efficient process has an efficiency of 0.7 (ASM, 1988).

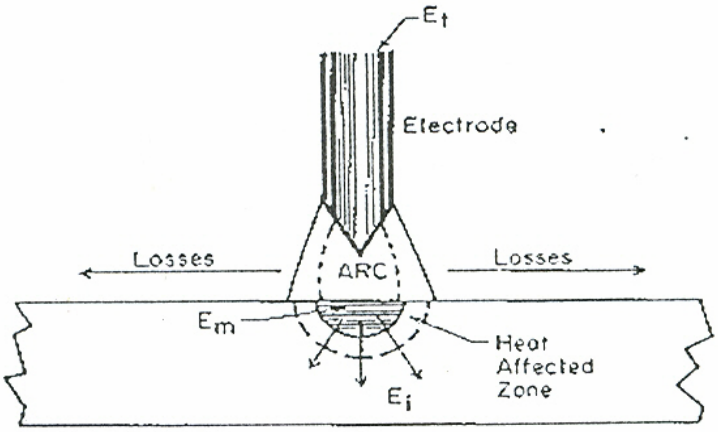

Figure 2.32. Energy Distribution at the Welding Arc Where E_t = Total Energy Input/Unit Length; E_i = Total Energy Entering Plate; E_m = Energy to Melt Weld Bead; $E_t = E_i$ + Losses (Niles, 1975)

Zhu and Chao (2002), investigated the effect of temperature-dependent material property on the transient temperature, residual stress and distortion in computational simulation of welding. They used thermocouples placed near the weld path center line and measured the transient temperature and residual stresses. They have determined that, the thermal conductivity has certain effect on the distribution of transient temperature fields, and the yield stress and Young's modulus have significant and small effects, respectively, on the residual stress and distortion after

welding.

Atkins and et al. (2002), compared the welding processes for the weldability testing of steels. They concluded that the minimum preheats for avoiding weld deposit hydrogen-induced cracking depends on the welding process used.

Arenas and Acoff (2002), analyzed postweld heat treated (PWHT) structures of gamma titanium aluminides by optical microscopy and X-ray diffraction techniques. They found that PWHT promotes the formation of the γ phase. This microstructural change resulted in the reduction of the fusion zone microhardness mainly due to the reduction of the hard, brittle α_2 phase.

Eroglu, Aksoy and Orhan (1999), investigated the effects of coarse grain size with varying heat inputs on microstructure and mechanical properties of weld metal heat affected zone. They observed that, the coarse initial grain size had a great influence on the microstructure, hardness and toughness of HAZ of a low carbon steel. Taking into consideration the plate thickness, a higher heat input should be used with respect to the maximum toughness of the HAZ in the welding of grain coarsened low carbon steels.

Zhang and Zhang (1999), developed a new TIG welding process that can increase the weld penetration by using two torches on the opposite sides of the workpiece and connecting them to the power supply in series. The welding current flowed from the power supply to a torch, then through the work more or less normally, tehn to another torch and finally returned to the power supply. Such a current flow concentrated the arcs and improved the weld penetration.

Graville (1973), studied on the properties of welded joints and possibility of cracking after welding. He found that possibility of cracking increased as the cooling rate increased. Also, according to him, the hardness in the HAZ of the weld metal would increase as the thickness increased (at least for those steels in which hardness varies with cooling rate. This includes, C, C-Mn and low alloy steels).

Flintham (1949), mentioned that excessively high preheat temperatures, in excess of 250 ^{o}C, would cause low values of yield strength and ultimate strength in low alloy steels.

Gayley and Willis (1944), commented on the beneficial value of

preheating and stated that the ductility and impact resistance of weld metal increased with increasing interpass temperature.

Cook and Rothchild (1954), also found an increase in ductility increase in ductility and a decrease in yield strength with increasing interpass temperature.

2.7.3. Effect of Cooling Rate on TIG Welded Joints

The cooling rate of the weld fusion zone should be known due to below facts (Lothongkum and et al., 2001):

- To avoid a martensitic transformation or possible cold cracking,
- To establish a relationship for cooling rates of wrought steel,
- To identify any rate sensitive metallurgical reaction occurring in the weld and HAZ,
- To prevent excessive grain coarsening in the HAZ.

Typically, weld metal cooling rate decreases rapidly as welds cool to room temperature. Therefore, weld cooling rate is usually measured experimentally as the slope of the cooling curve (temperature versus time) at a particular temperature of interest. Temperatures of interest that are used frequently for the estimation of cooling rate of steel are between 550°C and 700°C (Stout, 1987).

In his investigation, Adams (1958) has shown that the cooling rate, S, at the weld centerline of a thin plate workpiece, which requires less than four passes for full penetration, is given by the formula below;

$$S = 2\pi K\rho C(\frac{t}{H_n})^2 (T_i - T_0)^3 \qquad (2.6)$$

where T_i is the temperature of interest, K is the thermal conductivity of steel, ρ is density of steel, C is a generalized constant and t is the plate thickness. This equation applies to two dimensional heat flow situations.

It is known that rapid cooling of weld metal results in a loss of ductility. In

some instances, the tensile and yield strength are not appreciably affected by the cooling rate, but the elongation and reduction in area markedly decrease. The heat is absorbed by brine; water, oil, air, etc in heat treatment applications; whereas in welding the major portion of the heat is absorbed by the steel adjacent to the weld before it is radiated into the air. In welding, after the weld melt has passed by, the rate of cooling is governed by the contact with adjacent steel rather than by immersion in air. In the section on the solid weld, it was found by Henry et al. (1998) that as it was moved away from the weld melt, the base metal got cooler. That is to say, the temperature felt; heat was being absorbed from the hot regions near the weld by the cold regions farther away.

The weld metal and the heat affected base metal may receive, from the surrounding cold base metal, a quench that ranges from that of relatively slow air cooling to fast water quenching. Therefore, the weld metal and the heat affected base metal may contain soft and almost fully hardened structure or mixture of soft and hard structures (Stout, 1987).

Practices has shown that the cooling rates in the zones heated above the critical temperature during welding may be high enough to cause undercooling of austenite below 500°C and to form martensite. Martensite is favored by the large size of austenite grains in the zone adjacent to the weld melt, that has been heated about the melting point. All in all, the rate, at which the different regions of a weld, cool through the temperature range from the critical temperatures to below 500°C, varies with plate thickness, welding process and other variables.

As a result, it can be stated that the cooling rate depends mainly on three variables, the rate of heat input, the base metal temperature before welding and the section thickness and geometry. High heat inputs and preheating favor slow cooling, while heavy sections encourage fast cooling (Stout, 1987).

Wu (2000), examined the influence of vibration frequency on solidification of the weldments. It was found that gas inclusions, dross and slag were brought to the surface by process. This produced uniform, fine grained castings, and increased the toughness, ultimate tensile strength and yield strength of the cast material. This finer structure can provide better mechanical properties and eliminate hot cracking

sensitivity of the weld.

Poorhaydari, B.K. and et al. (2005) presented an innovative method for estimating the actual cooling rate in a TIG welded section. The method was based on applying a weighting factor to the Rosenthal analytical solutions for thick and thin plates. Their method can be used to obtain a weighted peak temperature profile and to calibrate the shape and size of the profile.

2.8. Multipass TIG Welding

TIG welding is one of the most important metal joining process widely used in industry, especially used in the fabrication of pressure vessels with stainless steels and other components. In most of the applications, the plates are welded using multipass welding methods. In a multipass welding operation, the residual stress pattern developed in the material changes with each weld pass. The temperature distribution that occurs during multipass welding affects the material microstructure, hardness, mechanical properties, weld pool geometry and the residual stresses that will be present in the material after cooling to room temperature (Murugan and Kumar, 1998). Because of this adverse effect of heat around the weld, the temperature must be as low as possible to narrow the HAZ when welding stainless steels.

Teng, Chang and Tseng (2003), analyzed the effect of welding sequences on residual stresses of multi pass but welded plates and circular path. They concluded that an extremely large tensile stresses occurs near the weld bead and a compressive stress appears away from the weld bead. Also, more free space should be available for expansion and shrinkage in the welding structure during the welding procedure to prevent the rigid restraint in the weld bead, and to decrease the residual stresses.

Murugan and et all (2001), have measured the temperature distribution and residual stresses during Manual Metal Arc welding. They determined that, the residual stresses are distributed in a larger region around the weld line of stainless steel weld pads as compared to the region over which the residual stress is distributed in low carbon steel weld pads, after the first pass. Also, the temperature range

between 275 and 700 ^{o}C (at the middle plane of the weld pad) is important with respect to formation of residual stresses in both stainless and low carbon steel weld pads.

2.8.1. HAZ in Multipass TIG Welding

In the HAZ of a single-pass weld, the grain coarsened zone (GC HAZ) is normally the region having the lowest toughness. Turning to a multipass weld, Figure 2.33 shows how grain coarsened heat affected zone can be modified by subsequent passes and can be categorized into four regions, depending on the reheating temperature (Haze and Aihara, 1988):

- Subcritically reheated grain-coarsened (SCGC) zone,
- Intercritically reheated grain-coarsened (ICGC) zone,
- Supercritically reheated grain-refined (SCGR) zone,
- Unaltered grain-coarsened (UAGC) zone,

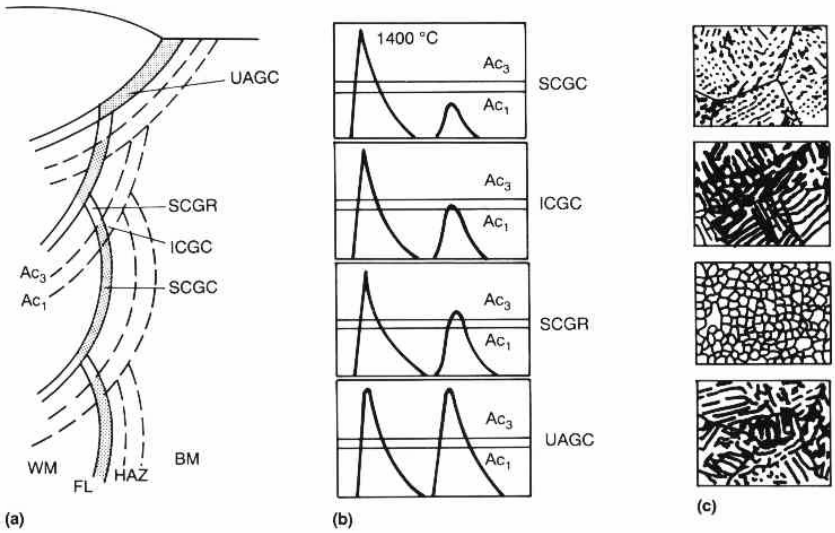

Figure 2.33. Schematic showing the different subzones that can form in the coarse-grained region of the HAZ in a multipass weld. (a) Position of subzones relative to base metal (BM) and weld metal (WM). (b) Plot of thermal cycles. (c) Microstructure at the different the different zones (Hazet and Aihara, 1988)

The multipass welding procedure can alternatively be controlled to limit the

size of the local brittle zones (LBZ) Figure 2.34 shows how this can be done with a high current gas tungsten arc welding procedure by adjusting the distance between the arcs (Onoe and Tanaka, 1979).

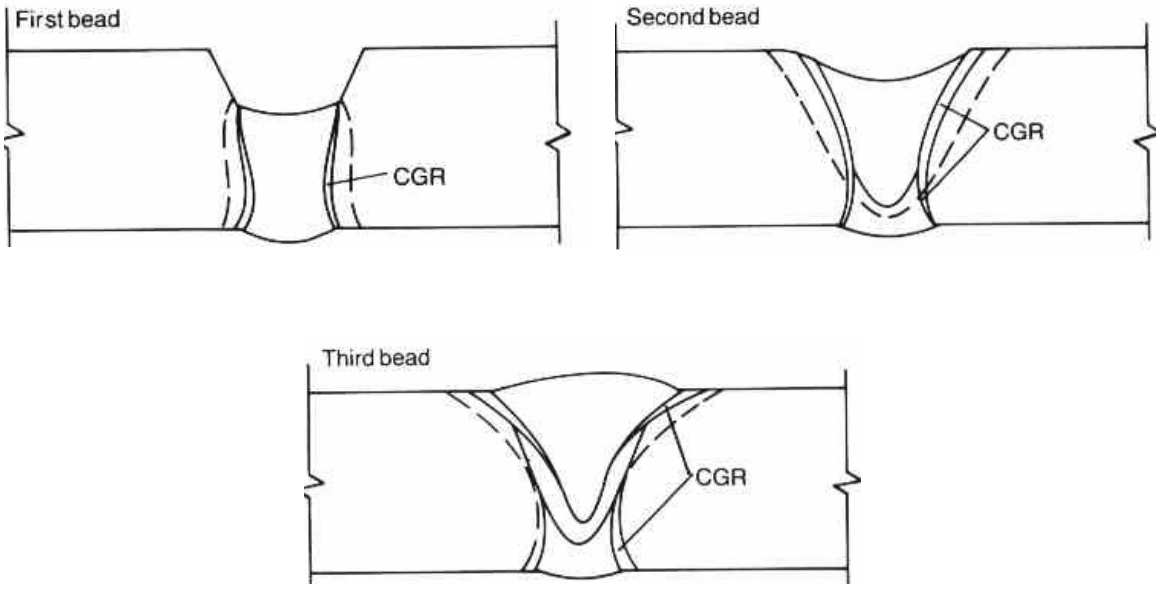

Figure 2.34. HAZ isotherms and the size and location of the coarse grained region (CGR) in a multipass weld (Onoe and Tanaka, 1979)

Special "temper-head" procedures have been developed for controlling the HAZ, and a need for these procedures arises in the following way. Low alloy steel weldments for critical applications require a postweld heat treatment (PWHT) in a furnace. This is done to temper the hard regions in the HAZ and to relieve residual stresses. If repairs become necessary on site after the component has been in service, PWHT is usually not feasible. The heat of the arc can then be used to achieve the tempering function of PWHT by suitable spatial positioning and sequencing of the individual passes. Grain refinement in the HAZ is also sought to increase the toughness and thereby offset the harmful effects of residual stresses that would remain in the absence of PWHT (Harrison and Hart, 1990).

An example of a two layer temper bead procedure is shown in Figure 2.35. The heat inputs of the first and second layer are carefully controlled, so that the heat from the second layer is used to refine the coarse grained region in the HAZ of the base metal due to the first layer (Alberry, 1989).

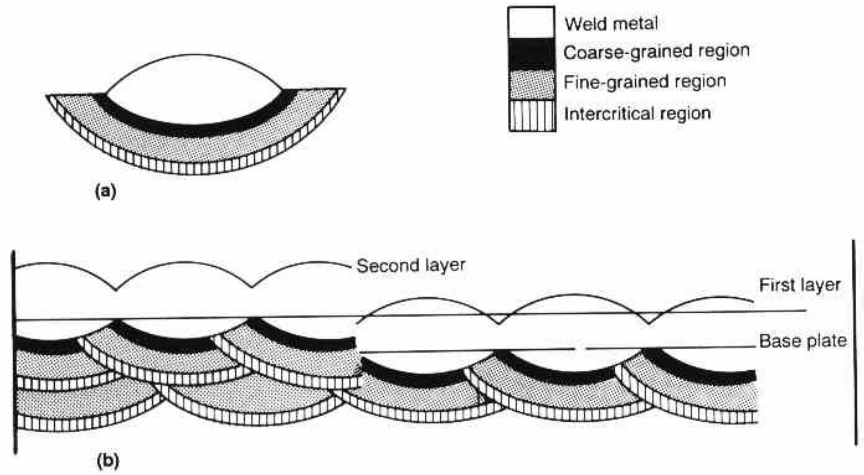

Figure 2.35. Two layer repair procedure (a) HAZ of a single weld bead, (b) First layer causes coarse grained regions to form in the HAZ of the base metal (right portion). Deposition of the second layer refines initial coarse grained regions (left portion) (International Institute of Welding, 1988)

This idea can be extended one step further by using a pulsed gas tungsten arc welding procedure whereby a given pulse in a pulsed weldment can be used to successively refine and temper preceding pulse pitch regions. The degree of microstructural refinement depends primarily on the welding speed and pulsing frequency, and these parameters can be controlled with great precision (Alberry, 1989).

Grossbeck and et al. (1998), developed techniques for welding V-Cr-Ti alloys. It was speculated that the resultant grain boundary precipitation resulting from heat treating a weld with higher levels of impurities than experienced in this study might limit its usefulness. Therefore, atmospheric purity remains an essential factor in GTA welding of vanadium alloys.

Grossbeck, King and Hoelzer (2000), studied the impurity effects on gas tungsten arc welds in V-Cr-Ti alloys. They observed that a major source of hydrogen was dissociation of water vapor by the electric arc of the welding torch.

Shankar and Wu (2001), investigated the experimental work on fatigue crack behavior of welded 5083-H321 aluminum alloy plates. They employed the three dimensional finite element analysis for cracks in the weld line. The results indicate that weld repair of cracks in welded joints provides little improvement in

residual life.

Arenas and Acoff (2001), analyzed postweld heat treated (PWHT) structures of gamma titanium aluminides by optical microscopy and X-ray diffraction techniques. It was found that PWHT promotes the formation of the γ phase. This microstructural change resulted in the reduction of the fusion zone microhardness mainly due to the reduction of the hard, brittle α_2 phase.

Singh and et al. (2003), carried out fatigue life evaluations on gas tungsten arc welded (TIG) load-carrying cruciform joints of AISI 304L stainless steel with lack of penetration (LOP) using conventional S-N and crack initiation-propagation (I-P) methods. The predicted lives were compared with the experimental values. They found that the fatigue lives of the joints with LOP=2 mm for 6 mm thickness plate were relatively higher than those for the joints with other LOP sizes. Also, they compared with BS 5400 design curve.

2.8.2. Fusion Zone in Multipass TIG Welding

In the weld metal of a multipass weld, reheating effects will lead to a gradient in microstructure similar to the case of the HAZ. However, instead of a detailed classification, as shown in Figure 2.36, the multipass weld metal is usually considered to consist of just two regions (International Institute of Welding, 1988):

- As deposited or primary region: where the microstructure develops as the weld cools from the liquid phase to ambient temperature.
- Reheated or secondary region: where regions with the original primary microstructure are reheated to temperatures above the A_c temperature. The tempered regions which are reheated to slightly lower temperatures are also generally considered to belong to this category.

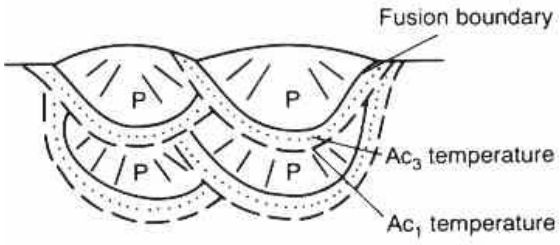

Figure 2.36. Primary and reaustenized regions in the weld metal region of a multipass weld (International Institute of Welding, 1988)

The properties of the weld metal depend on the relative area or volume fractions of the two regions, which in turn depend on the welding procedure, so the properties are procedure specific.

It has been known that solidification cracking can be avoided in austenitic stainless steel (especially 3XX series) welds by having a small concentration of ferrite in them. Recent work has shown, however, that residual ferrite content at room temperature is more than a symptom and that is really the solidification mode (whether the weld metal solidifies as primary austenite or ferrite) that is deciding criterion. Brooks and et al (1999), found that susceptibility to solidification cracking is least for a primary ferrite solidification mode, when the solidification mode corresponds to the types shown in Figure 2.37.

It is believed that low melting point liquid phases solidifying in the intercellular regions do not wet the $\delta - \gamma$ interphase boundaries as easily as they would $\delta - \delta$ or $\gamma - \gamma$ boundaries. In the ferritic austenitic solidification mode, the $\delta - \gamma$ interphase boundary area is greater at temperatures just below the nominal solidus temperature, and this is the reason for a greater resistance to solidification cracking (Siewert, 1988).

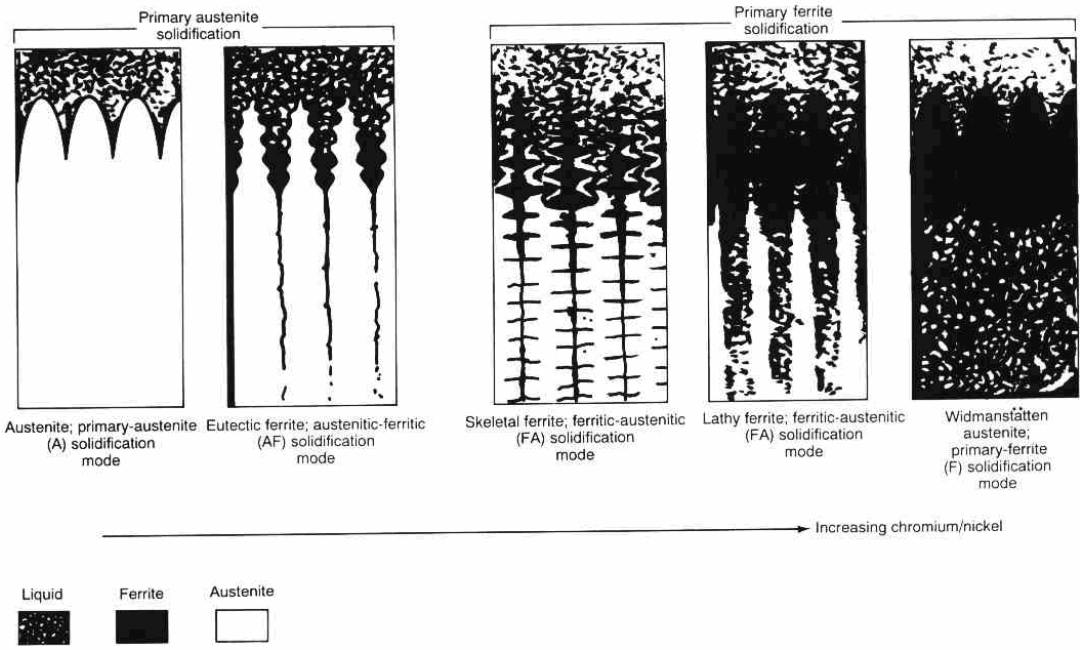

Figure 2.37. Solidification and transformation behavior of TIG welding of austenitic stainless steels (Siewert, 1988)

Timofeev and et al. (1999), studied on the fracture toughness of austenitic welded joints. It was shown that the generalized dependence for austenitic stainless steels cannot be based on the linear mechanics criteria. The fracture toughness temperature dependence was given for austenitic steels and their welds were constructed using the criteria of nonlinear fracture mechanics (J_{IC} and J_R curves).

Brooks and Garrison (1999), studied the weld microstructure development and properties of precipitation-strengthened martensitic stainless steels PH 13-8 Mo, Custom 450 and 15-5 PH. During further solidification and cooling almost complete homogenization occurred as a result of solid state diffusion. The welds in all three alloys exhibited good resistance to solidification cracking and generally exhibited tensile and impact properties similar to those of the base metal. Also, they examined the cracking behavior and mechanical properties in terms of microstructural evolution. However, in almost all cases, the weld charpy impact energies were somewhat less than those of the base metal.

Eroğlu and et al. (1999), investigated the effects of coarse initial grain size with varying heat inputs on microstructure and mechanical properties of weld metal

and heat-affected zone (HAZ). They observed that the coarse initial grain size had a great influence on the microstructure, hardness and toughness of HAZ of a low carbon steel. Thus, taking into consideration the plate thickness, a higher heat input should be used with respect to the maximum toughness of the HAZ in the welding of grain-coarsened low carbon steels.

Benedetti and et al. (2000), studied the effect of gas tungsten arc welding on the microstructure and electrochemical corrosion of Al-Zn-Mg-Fe alloys submitted to different heat treatments using optical microscopy and corrosion potential measurements in chloride solutions. The electrochemical techniques were very sensitive to the change in the phase composition produced by welding. Welding caused a decrease in the mean grain size, in the hardness and in the corrosion resistance of the age-hardened alloys.

Yuri and et al. (2000), studied on effect of welding structure and δ-ferrite on fatigue properties for TIG welded austenitic stainless steels at cryogenic temperatures. It was found in this study, fatigue crack initiation sites of SUS304L weld metals were usually at blowholes with a diameter of 200-700 μm, and those of SUS316L weld metals were at weld pass interface boundaries created during welding. Also, microvoids, which were undetectable by conventional inspection procedures, caused reduced fatigue resistance.

Dye, Hunziker and Reed (2001), carried out numerical analysis in order to predict the processing conditions necessary to cause the occurrence of interdendritic microporosity, constitutional liquation and solidification cracking. Although the models developed were of general applicability, their behavior was examined particularly with respect to the tungsten inert gas welding of the nickel-based superalloy IN718. They also presented weldability maps, on which the conditions for successful processing were identified.

Wahab and Sakano (2001), studied on the corrosion fatique behavior of welded steel structures. They observed that, fatigue crack propagation in the corrosive medium is strongly influenced by weld-geometry parameter (weld-toe undercut) which played a significant role in reducing the fatigue life and fatigue strength of butt-welded structures, and accelerated the time to propagate to failure. it

has been also found that the threshold stress intensity factor of butt-welded structures attains a much lower value in corrosive environment than in air environment and its effect needs to be included in fatigue assessment.

Munitz and et al. (2001), investigated the microstructure and defect formation by optical and scanning electron microscopy. It was found that, after resolidification, a continuous $Al_{12}Mg_{17}$ phase existed along the partially melted zone grain boundaries that markedly reduced the joint strength to below that of fully annealed Mg-AZ91D alloys. In contrast, specimens machined from welded metal exhibited improved strength and ductility that resulted from the microstructural refinement caused by the rapid cooling during resolidification of the fusion zone.

Saito and et al. (2002), investigated neutron irradiation effects on the mechanical properties of 316L SS welded joints. The results of post irradiation experiments indicated that sufficient ductility was still maintained for tungsten inert gas (TIG) and electron beam (EB) welded joints; whereas, the impact properties of metal inert gas (MAG) weld metal are extremely poor. Consequently, the soundness of the 316L SS base metal and its TIG and EB welded joints are retained after 0.2–0.5 dpa neutron irradiation.

Owen and et al. (2003), used synchrotron X-ray diffraction methods to provide non-destructive information about the residual stress field in TIG welded 2024 Al alloy. It was found in their study that the magnitudes of the tensile longitudinal stresses decrease along the plate due to progressive heating up of the plate ahead of the arc during welding, so that steady-state conditions are not achieved.

2.9. Molten Weld Pool Phenomena during Welding

Molten weld pools are dynamic. Liquid in the weld pool is acted on by several strong forces, which can result in high-velocity fluid motion. The four primary driving forces in GTA weld pools are:

- Marangoni forces
- Surface tension gradients

- Electromagnetic or Lorentz forces
- Buoyancy forces
- Aerodynamic drag forces

caused by passage of the arc over the weld pool surface. Marangoni forces are dominant at lower currents (under 200 A) where the weld pool presents recirculating flows. In this regime, electromagnetic forces increase with the welding current; they are not negligible at currents close to 200 A, and could possibly dominate the flows at higher currents. The arc pressure and gas shear act over the free surface affecting the properties of the weld pool. These forces increase with the welding current; therefore they could potentially be the dominant forces at high currents. Because of the difficulty of studying the weld pool in the high productivity regime, there has been no agreement in the past about which is actually the dominant force (Sacks and Bohnart 2005).

Fluid flow velocities exceeding 1 m/s have been observed in gas tungsten arc (GTA) welds under ordinary welding conditions, and higher velocities have been measured in submerged arc welds. Fluid flow is important because it affects weld pool shape and is related to the formation of a variety of weld defects. Moving liquid transports heat and often dominates heat transport in the weld pool. Because heat transport by mass flow depends on the direction and speed of fluid motion, weld pool shape can differ dramatically from that predicted by conductive heat flow. Temperature gradients are also altered by fluid flow, which can affect weld microstructure. A number of defects in TIG welds have been attributed to fluid flow or changes in fluid flow, including lack of penetration top bead roughness, humped beads, finger penetration, and undercutting (Kou, 1987).

Most experimental and theoretical work on weld pool fluid flow and its effects have been directed toward TIG welding. The motivation for much of this work was the observation of dramatically different weld pool shapes for TIG welds made using identical welding parameters on different heats of the same material with the same nominal composition. An extreme example of weld shape variability is shown in Figure 2.38. Early observations of variable weld shape (often referred to as variable penetration) were not only an intellectual puzzle but also growing practical

problem. Gas tungsten arc welding is commonly used for high-precision, high-quality automated welding applications, where reproducibility of weld shape or penetration is critical (Christensen, 1965).

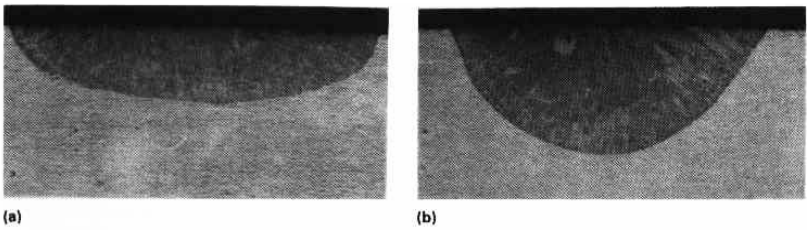

Figure 2.38. Partial penetration TIG welds made under the same welding condition on two heats of type 304L. (a) 3 ppm S,d/w= 0.2.(b) 160 ppm S, d/w= 0.40 (9X) (Christensen, 1965)

The possibility that fluid flow in the weld pool could alter weld shape has been recognized for many years. In 1965 Christensen et al proposed that convection is partially responsible for deviations in weld pool shapes from those predicted by conduction solutions.

Zhang, Kovacevic and Li (1995), proposed a polar coordinate model to characterize the weld pool geometrically. They proposed a neural network to identify the parameters in real time. Then, a real time system was developed to sense and process the image and identifies the polar coordinate model. They showed that, the weld penetration can be accurately determined using the model parameters.

Li and Wu (1997), introduced a three-dimensional model for fluid flow and heat transfer in the interfacial region between the TIG arc plasma and weld pool. They compared the predicted current density and heat flux with experimental measurements taken from literatures. The computed current densities, heat flux and arc pressure at the anode were taken as inputs to the calculation of weld pool behavior.

Jones and et al. (1996), studied the dynamic behavior of gas metal arc welding process. Also, they studied the detailed description of the droplet formation and fluid behavior in the weld pool. It was concluded that, fluid motion both within the drop and the weld pool had a significant effect on the quality of the

weld produced.

Hellinga, and et al. (1997), modeled arc TIG weld pool dynamics under static (steady state) conditions to provide a relationship between the controllable process parameter values and the characteristic weld geometry parameters. The non-linearity of the model was demonstrated, and the gain, damping and natural frequency were estimated.

Kim and Na (1998), investigated the heat transfer, fluid flow and phase change of the weld pool in pulsed current gas tungsten arc welding. The numerical model for pulsed current welding was applied to AISI 304 stainless ateel and compared with the results of the constant current.

Zhang and Kovacevic (1998), developed a closed loop system to control the weld fusion, which is specified by top-side and back-side bead widths of the weld pool. A neurofuzzy model was used to model nonlinear dynamic process. Based on the dynamic fuzzy model, a predictive control system was developed to control the welding process.

Hong, Weckman and Strong (1998), studied on the influence of thermofluids phenomena in gas tungsten arc welds in high and low thermal conductivity metals. They used comprehensive numerical model of stationary GTA welding which includes a $k-\varepsilon$ turbulence model successfully to predict the weld pool size and shape of GTA welds produced in AISI 304 stainless steel plates with three different sulphur contents as well as 6061 and 1100 aluminum plates. Comparisons between the predicted results from the laminar flow model and the turbulent flow model indicated that the level of turbulence in the AISI 304 stainless steel weld pools may not be intense; however, its influence on the final weld pool size and shape was significant.

Urena, Escelara and Gil (2000), described the influence of interface reactions on fracture mechanisms in TIG arc-welded aluminum matrix composites. They deduced that the proportion of interfacial failure increases in the weld material because of the formation of Al_4C_3, which reduces the strength of the matrix/reinforcement interface, limiting the number of cracked particles.

Mendez and Eagar (2000), estimated the characteristics properties of the

weld pool during high productivity arc welding. They described a new methodology for studying complex engineering problems. This method enables one to systematically solve problems that are very challenging with either dimensional analysis or analysis of differential equations alone.

Hong and et al. (2000), developed vision based GTA weld pool sensing and control system using neurofuzzy logic control. Relatively clear weld pool images captured using LaserStrobe technique.

Zhao and et al. (2001), investigated the technical characteristics of pulsed TIG welding with wire filler metal and developed intelligent control for the shape of the weld pool in pulsed TIG welding. Also, they designed a double-variable, self adaptive fuzzy controller for controlling the shape of the weld pool.

Fan, Tsai and Na (2001), analyzed the fluid flow driven by a combination of electromagnetic force, buoyancy force, arc drag force, and surface tension gradient for a partially or fully penetrated weld pool in stationary gas tungsten arc welding. Surface tension on the top and the bottom free surfaces of the weld pool is found to play a critical role in determining the flow pattern in the weld pool. They compared the calculated GTA weld bead geometry with the experimental results.

Saeed, Lou and Zhang (2002), presented a novel computation method of the 3D weld pool surface from specular reflection of laser beams in TIG welding process. A mathematical and simulation model were developed implementing the technique. The developed model was tested on objects with a priori knowledge of geometry having specular surface to test the effectiveness of the measurement technique. They monitored the free weld pool surface for studying and controlling the welding process. However, due to the strong arc and the mirror-like surface, limited achievement has been made by them.

2.10. Weld Modeling and Control

With the increasing demands for high quality welds, the need to eliminate the human operator from the feedback path for correction of the welding process has become evident. Of the several manufacturing technologies, welding alone has

defied true automation. Even with excellent controllers for the several controllable variables such as voltage, current, and travel speed, the human operator still provides the only commercially-viable feedback loop. Recent research in intelligent, closed-loop, automatic control of the welding process is making steps in eliminating the human operator from the feedback loop while providing high quality consistent welds. However, it is still necessary to have the human operator monitor the weld in progress and make corrections to compensate for minor variations in joint fit-up, plate thickness, variations in thermal conditions, or one or more of several of the uncontrollable variables. A review of some of the more noteworthy intelligent control techniques for automated welding follows. This is by no means an exhaustive review of artificial neural network applications for intelligent weld control. Furthermore, other equally capable intelligent control schemes using fuzzy logic, neurofuzzy models, and rule-based expert systems have been successfully applied to intelligent weld control (George and et al., 2001).

Maropoulos and et al. (2000), developed an integrated design and planning for welding. They discussed the definition and implementation of CAPABLE/Welding, a newly developed aggregate process planning system for supporting early design assessment of complex fabrications. The use of relevant design rules to generate weld features is discussed in this paper using as an example the design procedure for a complex fabrication. They have developed, two methods, i.e. manual input and information abstraction for the aggregate product modeling procedure. The manual input method was suitable for the gradual addition of design information to the product model during the design process.

Luo and et al. (2002), developed vision based neurofuzzy logic control of weld pool sensing system for weld pool sensing and control. They used laser strobe technique on top of the high shutter speed camera. Laser strobe technique provided clear image capturing of weld pool geometry.

Wu and et al. (2003), developed a camera system with a composite light filter to form a visions sensing system of low cost. They provided that, the measured results were useful for developing a welding process control system and verifying the mathematical models of weld pool behaviors.

Zhao and et al. (2004), developed a three dimensional numerical model to investigate the dynamic characteristics of the weld pool geometry when the welding current and welding speed undergo a step-change. They conducted the welding experiments in order to compare the three dimensional numerical model with the predicted numerical model.

2.10.1. Welding and Bonding

Most welding processes require the application of heat or pressure, or both, to produce a bond between the parts being joined. The welding control system must include means for controlling the applied heat, pressure, and filler material, if used, to achieve the desired weld microstructure and mechanical properties. Welding usually involves the application or development of localized heat near the intended joint. Welding processes that use an electric arc are the most widely used in the industry. Other externally applied heat sources of importance include electron beams, lasers, and exothermic reactions (oxyfuel gas and thermit). For fusion welding processes, a high energy density heat source is normally applied to the prepared edges or surfaces of the members to be joined and is moved along the path of the intended joint. The power and energy density of the heat source must be sufficient to accomplish local melting (George and et al., 2001).

2.10.2. Control System Requirements

Insight into the control system requirements of the different welding processes can be obtained by consideration of the power density of the heat source, interaction time of the heat source on the material, and effective spot size of the heat source.

A heat source power density of approximately 10^3 W/cm^2 is required to melt most metals (Eagar, 1986b). Below this power density the solid metal can be expected to conduct away the heat as fast as it is being introduced. On the other hand, a heat source power density of 10^6 or 10^7 or will cause vaporization of most

metals within a few microseconds, so for higher power densities no fusion welding can occur. Thus, it can be concluded that the heat sources for all fusion welding processes lie between approximately 10^3 and 10^6 W/cm^2 heat intensity. Examples of welding processes that are characteristic of the low end of this range include oxyacetylene welding, electroslag welding, and thermit welding. The high end of the power density range of welding is occupied by laser beam welding and electron beam welding. The midrange of heat source power densities is filled by the various arc welding processes. For pulsed welding, the interaction time of the heat source on the material is determined by the pulse duration, whereas for continuous welding the interaction time is proportional to the spot diameter divided by the travel speed. The minimum interaction time required to produce melting can be estimated from the relation for a planar heat source given by (Eagar, 1986b):

$$t_m = \left[K / P_d\right]^2 \tag{2.7}$$

where P_d is the heat source density (watts per square centimeter) and K is a function of thermal conductivity and thermal diffusivity of the material. For steel, Eagar (1986b) gives K equal to 5000 W/cm^2. Using this value for K, one sees that the minimum interaction time to produce melting for the low power density processes, such as oxyacetylene welding with a power density on the order of 10^3 W/cm^2, is 25 s, while for the high energy density beam processes, such as laser beam welding with a power density on the order of 10^6 W/cm^2, is 25 μs. Interaction times for arc welding processes lie somewhere between these extremes.

2.10.3. Arc Welding as a Multivariable Process

Any arc welding process can be controlled by a number of parameters, and the ultimate objectives of the process are specified in terms of numerous parameters as well as shown in Figure 2.39.

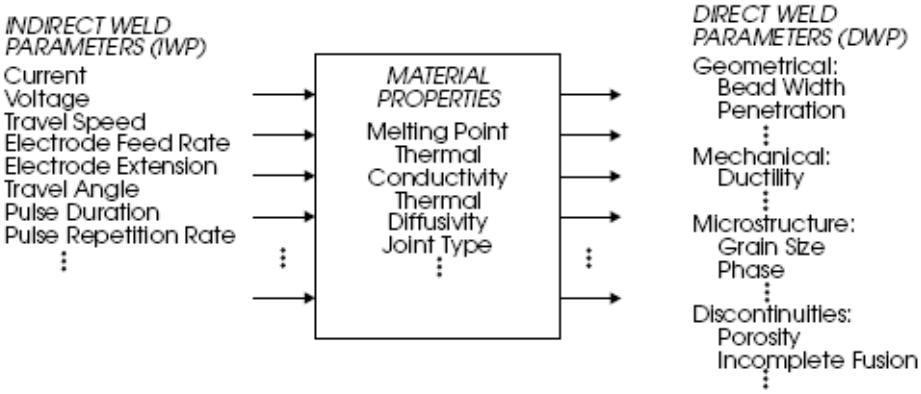

Figure 2.39. Input and output variables of the general arc welding process (George and et al., 2001)

As a result, any arc welding process can generally be viewed as a multiple-input/multiple-output system. The lack of reliable, general, and yet computationally fast, physical models of this multivariable system makes the design of a generalized real-time controller for arc welding nontrivial. Each process has its own characteristics which usually are related to a number of external parameters. Generally, these relationships are not well quantified.

One of the basic issues to be considered regarding the generalized control for arc welding is to determine what is to be controlled and which parameters are accessible to enact control actions on the process. In other words, the input parameters and the output parameters of the process, or the plant, have to be determined. The input parameters to any arc welding process typically include those controlled by the welding equipment, such as arc current, voltage, torch travel speed, and filler wire rate. Most of these equipment parameters may be adjusted on-line and thus they are available for real-time control of the welding process. Other input parameters may be selected by the welder, but they are usually static and not changeable during welding. These parameters include the electrode type and dimensions, filler wire composition and dimensions, workpiece dimensions and composition, etc.

Tarng and et al. (1999), developed a neural network model and simulated annealing (SA) algorithm to model and optimize the gas tungsten arc welding process. An SA algorithm applied to counter propagation network to optimize the

process. Experimental results showed that TIG performance can be enhanced by using SA technique with neural network.

2.10.4. Traditional Approaches to Arc Welding Modeling and Control

Applications of control for arc welding have thus far been largely focused on the control of one, or at most two, parameters of the process. The control techniques for these parameters have usually been limited to classical feedback control, based on the assumptions of linear and time invariant behavior of the controlled systems. Examples of such control schemes include voltage and current control of the welding power source, control of the arc voltage through adjustment of the arc length, and other isolated single variable control applications. The welding control applications mentioned above are usually adequate for their specific purposes, i.e., to maintain one or two system parameters at predefined values. These traditional schemes, however, are not easily applicable to the more complex task of directly controlling outputs of the entire process through the available equipment parameters, i.e., controlling the Direct weld parameter (DWP) in terms of the indirect weld parameter (IWP) (Cook, 1981 and 1990). Conceptually, the IWPs can be thought of as causes, with the DWPs as effects, both being related by the material properties of the weldment itself. One of the main obstacles to designing a general welding controller for any arc welding process, such as TIG welding, is that the process to be controlled is not thoroughly understood. The current approaches to welding rely extensively on human expertise and trial-and-error methods. For a given task, the human welder selects the process constants (electrode size, material and tip preparation, gas type and flow rate, etc.) and sets the variable equipment parameters (arc current, voltage, torch travel speed, filler wire rate, etc.). These selections are usually based on past experience. Through initial trials the variable equipment parameters are adjusted, and this process is repeated until the desired results (weld bead size, appearance, etc.) are obtained. Improvements on two aspects of this procedure can be proposed at this point. First, improvements in the initial selection of the indirect weld parameters would reduce the number of iterations necessary to

obtain the desired direct weld parameters. This initial selection is static and can be carried out off-line, prior to welding. Secondly, once the process has started, sensory feedback and other available process information can be monitored in real-time and used to update the IWP which control the welding equipment. These updates must be obtained on-line and the corresponding control actions must be executed at a high enough rate to effectively control short-term transients of the process.

Controlling a multivariable system is not a trivial task without an adequate quantitative model. In the case of arc welding, relationships between the various process inputs and outputs are not well defined. Furthermore, the process variables are coupled (i.e., any given input parameter affects more than one output parameter) and in general the welding processes are nonlinear (the output parameters are not adequately described in terms of a linear combination of the input parameters and their time derivatives). All of these facts add to the difficulty of designing a general controller for arc welding. Substantial research has been carried out to mathematically model and control the TIG welding process, as well as other arc welding processes. Each welding process is primarily governed by specific control variables (Dornfeld and et al., 1982). The available weld process models can be classified from either of two viewpoints. One classification arises from the methods by which the models are derived, while the other is concerned with the ability of the models to describe the dynamic behavior of the process as well as the static one. In broad terms, weld process models are either derived from the fundamental physics of heat transfer, or they are constructed from empirical data. The models derived from heat transfer physics frequently assume that the arc can be modeled as a heat source of a given form (a point source, a disk-shaped source of heat, etc.) and then the laws of heat conduction are applied to calculate the temperatures at various points in the workpiece (Rosenthal, 1941; Nunes, 1983; Tsai, 1983). Of specific interest is the boundary at which the temperature equals the melting temperature of the welded metal, i.e., the boundary of the molten weld pool. These results may either be derived analytically or computationally to a varying degree. The analytical derivations usually require significant simplifications, such as assuming that the welded workpiece is either infinitely thick or of a specific shape, the thermal properties of

the molten pool (e.g., heat conduction and density) are homogeneous and the same as those of the solid metal, etc. As a result the analytically derived models are usually fairly inaccurate when compared to the results of actual welding operations. On the other hand they frequently offer some insight into the mechanisms of the welding process and they may illustrate how the individual process inputs and outputs are related. Computer solutions based on the physics of heat conduction can be made more accurate by including some of the calculations omitted in the analytical simplifications. Finite-difference techniques and related methods carry the computational solution of the heat equation to its fullest accuracy (Eraslan and et al., 1986; Zacharia and et al., 1988a-1988b). The drawbacks of such approaches, however, are that they are computationally intensive (which usually renders them impractical for real-time use) and they do not offer the insight into the interactions of process variables that the analytical models may give. An alternative to the physics-based models, discussed above, are the empirically derived models (Jackson and Shrubsall, 1953; McGlone, 1982). These models may simply consist of one or more equations relating the process outputs to the process inputs, and derived by obtaining a best fit of experimental data to the given equations. In such cases the models are derived without any consideration of the underlying physics of the process. A number of weld process models can be placed between the two extremes of pure physics-derived and empirical models. Frequently, physics-based models are derived using the necessary approximations and then various “empirical constants” and other unspecified variables are tuned until the model adequately agrees with experimental welding data. By the same token, empirical models frequently use pieces of general knowledge of the process, derived from the underlying physics. Therefore, the physics-based and the empirical models define the opposite extremes in approaches to weld modeling.

For the purpose of system control it is important to distinguish between static models and dynamic ones. A static model describes the process in its steady-state, i.e., it does not consider short-term transients of the process. A dynamic model, however, yields both the dynamic and the static responses of the process, and thus it is more general. The lack of dynamic considerations is usually tolerable when the

initial set point values for the equipment parameters of the process are selected with the aid of a model. Once the process has started, however, its dynamics must be adequately incorporated into the control scheme. Some adaptive, dynamic control schemes for the TIG welding process are discussed in (Suzuki and et al., 1991).

There are at least two roles for models in a generic nonadaptive weld process controller. First, a model can be used in defining the initial equipment parameters of the process. The welder specifies the desired DWP, such as weld bead width, penetration, etc., and the model can be used to arrive at suitable IWP, such as welding current, travel speed, etc. Secondly, a model can be executed in parallel with the actual process and provide calculations for DWP that cannot be measured directly in real-time. Thus, a weld model can provide the controller at any time with an estimate of the weld bead penetration, although it may not be measurable in real-time. Adaptive controllers may require a process model to compare against the physical process for computation of errors used to intact parameter adaptation.

Bicknell, Smith and Lucas (1994), developed a novel sensor system for the control and measurement of bead size in TIG welding. They used a passive vision-based sensor combined infrared imaging of the weld pool and selective optical filtering to reduce excessive arc glare and improve contrast between weld pool and heat affected zone (HAZ). The arc interruption and external illumination techniques, used by the other researchers, were not required in their study. Their technique has been successfully applied to both pulsed and continuous TIG welding of stainless steel in order to maintain the bead size during a welding run.

Zhang and Kovacevic (1998), developed a closed-loop system to control the weld fusion which was specified by the top side and back side bead widths. A neurofuzzy model was used to model the nonlinear dynamic welding process. They developed the dynamic fuzzy model based on a predictive control system. Their experiment also confirmed the effectiveness of the developed control system for achieving the desired fusion state.

Gao and Wu (2001), established an experimental study for determination of weld pool geometry in gas tungsten arc welding. A composite light filter was designed for CCD camera system to eliminate the high intensity light coming from

the arc. They obtained image capturing using camera system. Also, image capturing algorithm was developed in order to measure the weld pool characteristics.

Luo and et al. (2002), developed vision based neurofuzzy logic control of weld pool geometry. They used LaserStrobe vision system to eliminate the interference from the welding arc. Also, it was concluded that image processing based on blob detection and connectivity analysis provides online information about the weld pool geometry.

2.10.4.1. Neural Networks

As the name indicates, a neural network resembles, to a certain degree, biological nervous systems as we currently understand them. While most traditional computers rely on a single or few computational units to perform their tasks, the neural network typically consists of a relatively large number of computational units, connected with an even larger number of communication links. The underlying principle aims to examine numerous hypotheses simultaneously and process data in a distributed fashion. In essence the neural network is a self-adaptive structure which incrementally alters its inner workings until it achieves the desired performance. The fundamental building block of an artificial neural network is the perceptron which was introduced by Rosenblatt (Rosenblatt, 1988). Originally designed for pattern recognition and as a research tool for modeling brainlike functions of a biological system, the perceptron pattern-mapping architecture can be generalized to the processing element present in the back-error propagation systems used today. These processing elements, as shown in Figure 2.40, are linked together with variable weights into a massively parallel environment. A neural net can achieve human-like performance due to its ability to form competing hypotheses simultaneously.

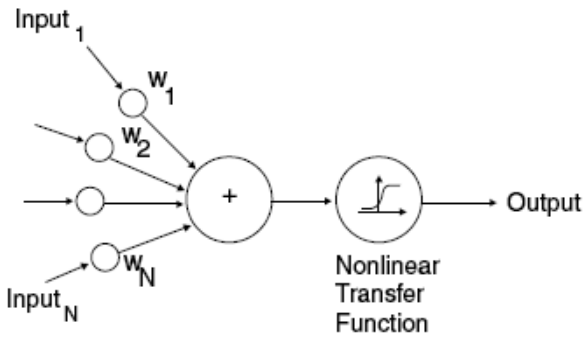

Figure 2.40. The processing element of a neural network (Rosenblatt, 1988)

A neural network and its adaptation procedure using back propagation is best illustrated by an example. Figure 2.41 shows a small neural network consisting of eight nodes, arranged in two hidden layers of three nodes each and one output layer of two nodes (Rosenblatt, 1988).

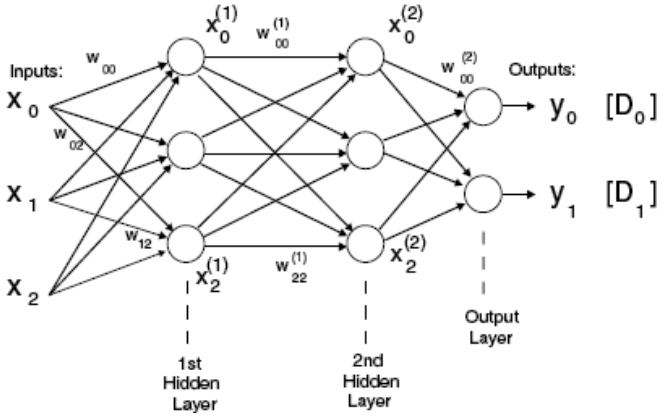

Figure 2.41. Three-input, two output network, using two hidden layers of three nodes each, fully interconnected (Rosenblatt, 1988)

Each node *i* in the first hidden layer produces a single numeric output which we denote as $x_i^{(1)}$. Similarly the nodes of the second hidden layer are labeled $x_0^{(2)}$, $x_1^{(2)}$ and $x_2^{(2)}$. The three inputs and two outputs of the network are x_0 through x_2 and y_0 through y_1 respectively. Each node accepts numeric data through a number of input links, each of which multiplies the input data with a weight factor. The weight factor associated with the link from $x_i^{(1)}$ to the node producing $x_j^{(2)}$ is annotated as $w_{ij}^{(1)}$ and a similar convention holds for the links between other layers. Each node

calculates its output by summing its weighted inputs and using the result *s* as the argument of a nonlinear function associated with the node.

$$f(s) = [1 + \exp[-(s - c)]]^{-1} \tag{2.8}$$

where *s* is the sum of the node inputs and *c* is an internal offset value. Clearly the node output will be confined to the range 0<f(s)<1. Because the limiting values, 0 and 1, will only be approached as *s* approaches +/- infinity, all input and output data are scaled so that they are confined to a subinterval of [0 … 1]. A practical region for the data is chosen to be [0.1 … 0.9]. In this case each input or output parameter *p* is normalized as p_n before being applied to the neural network according to:

$$p_n = \left[\frac{(0.9 - 0.1)}{(P_{\max} - P_{\min})} \right] (p - p_{\min}) + 0.1 \tag{2.9}$$

where $p_{\max}$ and $p_{\min}$ are the maximum and minimum values, respectively, of data parameter *p*. The network starts calculating its output values by passing the weighted inputs to the nodes in the first layer. The resulting node outputs of that layer are passed on, through a new set of weights, to the second layer, and so on until the nodes of the output layer compute the final outputs. Before practical application, the network has to be trained to perform the mapping of the three input parameters to the two output parameters. This is done by repeatedly applying training data to its inputs, calculating the corresponding outputs by the network, comparing them to the desired outputs, and altering the internal parameters of the network for the next round. The training starts by assigning small random values to all weights (w_{ij}) and node offsets (c_j) in the network. The first three input data values are presented to the network which in turn calculates the two output values. Because the initial weights and node offsets are random these values will generally be quite different from the desired output values, D_0 and D_1. Therefore, the differences between the desired and calculated outputs have to be utilized to dictate improved network values, tuning

each weight and offset parameter through back propagation. The weights preceding each output node are updated according to

$$w_{ij}(t+1) = w_{ij}(t) + nd_j x_i^{(2)} \tag{2.10}$$

where n is a correction gain and d_j is the correction factor;

$$d_j = y_j(1-y_j)(d_j - y_j) \tag{2.11}$$

Clearly, each weight will be increased if the calculated output from its node is less than the desired value, and vice versa. The correction factors used to update weights preceding the hidden layer nodes are updated according to;

$$d_j = x_j(1-x_j)\sum_k (d_k - w_{jk}) \tag{2.12}$$

where the k applies to the node layer succeeding the one currently being updated. The offset parameter c of each node is treated as an additional weight factor and updated in the same manner.

The weights and offsets of the neural network are recalculated during the back propagation as outlined above. Then the network repeats the calculation of the output values based on the same input data, compares them to the desired output values, and readjusts the network parameters through yet another back propagation phase. This cycle is repeated until the calculated outputs have converged sufficiently close to the desired outputs or an iteration limit has been reached. Once the neural network has been tuned to the first set of input/output data, additional data sets can be used for further training in the same way. To ensure concurrent network adaptation to all sets of data, the entire training process may be repeated until all transformations are adequately modeled by the network. This requires, of course, that all the data sets were obtained from the same process and therefore the underlying input/output transformation is consistent. As noted above, the training iteration

process may be terminated either by a convergence limit or simply by limiting the total number of iterations. In the former case we use an error measure e defined as the following:

$$e = \max_{k=1.....K} \left[\sum_{m=0}^{M-1} (d_{k,m} - y_{k,m})^2 \right] \quad (2.13)$$

where K is the number of input/output data sets used for training, M is the number of network output parameters in each data set, and ($d_{k,m}$-$y_{k,m}$) is the error in the network calculation of parameter m in data set k. The error measure, e, changes after each round of network weight adjustments. In the long run e decreases as the network is refined by training iterations. Using this indicator one can program the network to terminate the iterative tuning process as soon as e reaches some threshold value, e_0. Alternatively, a given network may not be able to reduce the error measure down to the specified e_0. In that case the iterations may be terminated by simply specifying a maximum number for them.

The training mode, as described above, is a precondition for actually applying the neural network in the application mode. In this mode entirely new input data is presented to the network which, in turn, predicts new outputs based on the transfer characteristics learned during the training. If this new data is obtained from the same local region of operation of the process as during the training phase, data from the input/output relations should be governed by the same underlying process and the neural network should perform adequately. The neural network is not updated in the application mode.

When compared to other modeling methodologies, neural networks have certain drawbacks as well as advantages. The most notable drawback is the lack of comprehension of the physics of the process. Relating the qualitative effects of the network structure or parameters to the process parameters is usually impossible. On the other hand, most physical models resort to substantial simplifications of the process and therefore trade accuracy for comprehensibility. The advantages of neural models include relative accuracy, as illustrated in the following sections, and generality. If the training data for a neural network is general enough, spanning the

entire ranges of process parameters, the resulting model will capture the complexion of the process, including nonlinearities and parameter cross couplings, over the same ranges. Model development is much simpler than for most other models. Instead of theoretical analysis and development for a new model the neural network tailors itself to the training data. Finally, the neural network can calculate its result relatively fast, as the input data is propagated once through the network in the application mode.

Yasuo and et al. (1999), developed an intelligent welding robot system with visual sensors in order to realize full automatic welding of thin mild steel plates including automatic seam tracking and automatic control of welding conditions. They also investigated CCD camera and a penetration control system using neural network in TIG welding of steels. The constructed camera system with neural network provided effective control of penetration in thin mild steel plates.

2.10.4.1.1. Neural Network Applications

Neural networks can be applied to a diversity of tasks. In general, the network associates a given input vector (x_1, x_2, … x_n) with a particular output vector (y_1, y_2, … y_m), although the function linking the two may be unknown and may be highly nonlinear (Lippmann, 1987). (A linear function is one that can be represented as $f(x) = mx + c$, where m and c are constants; a nonlinear one may include higher order terms for x, or trigonometric or logarithmic functions of x)

2.10.4.1.2. Nonlinear Estimation

Neural networks provide a useful technique for determining the values of variables that cannot be measured easily, but which are known to depend in some complex way on other more accessible variables. The measurable variables form the network input vector and the unknown variables constitute the output vector. We can call this use *nonlinear estimation*. The network is initially trained using a set of examples known as the training data. Supervised learning is used, so each example in

the training comprises two vectors: an input vector and its corresponding desired output vector (Willis, 1991). (This assumes that some values for the less accessible variable have been obtained to form the desired outputs.) During training, the network learns to associate the example input vectors with their desired output vectors. When it is subsequently presented with a previously unseen input vector, the network is able to interpolate between similar examples in the training data to generate an output vector.

2.10.4.1.3. Classification

Often the output vector from a neural network is used to represent one of a set of known possible outcomes, i.e., the network acts as a *classifier*. For example, a speech recognition system could be devised to recognize three different words: *yes*, *no*, and *maybe*. The digitized sound of the words would be preprocessed in some way to form the input vector. The desired output vector would then be either (0, 0, 1), (0, 1, 0), or (1, 0, 0), representing the three classes of word. Such a network would be trained using a set of examples known as the *training data*. Each example would comprise a digitized utterance of one of the words as the input vector, using a range of different voices, together with the corresponding desired output vector. During training, the network learns to associate similar input vectors with a particular output vector. When it is subsequently presented with a previously unseen input vector, the network selects the output vector that offers the closest match. This type of classification would not be straightforward using non-connectionist techniques, as the input data rarely correspond exactly to any one example in the training data (Rumelhart, 1986).

2.10.4.1.4. Clustering

Clustering is a form of unsupervised learning, i.e., the training data comprises a set of example input vectors without any corresponding desired output vectors. As successive input vectors are presented, they are clustered into *N* groups,

where the integer *N* may be prespecified or may be allowed to grow according to the diversity of the data. For instance, digitized preprocessed spoken words could be presented to the network. The network would learn to cluster together the examples that it considered to be in some sense similar to each other. In this example, the clusters might correspond to different words or different voices.

Once the clusters have formed, a second neural network can be trained to associate each cluster with a particular desired output. The overall system then becomes a classifier, where the first network is unsupervised and the second one is supervised. Clustering is useful for data compression and is an important aspect of *data mining*, i.e., finding patterns in complex data (Hallam, 1990).

2.10.4.1.5. Content-Addressable Memory

The use of a neural network as a content-addressable memory is another form of unsupervised learning, so again there are no desired output vectors associated with the training data. During training, each example input vector becomes stored in a dispersed form through the network. When a previously unseen vector is subsequently presented to the network, it is treated as though it were an incomplete or error-ridden version of one of the stored examples. So the network regenerates the stored example that most closely resembles the presented vector. This can be thought of as a type of classification, where each of the examples in the training data belongs to a separate class, and each represents the ideal vector for that class. It is useful when classes can be characterized by an ideal or perfect example. For example, printed text that is subsequently scanned to form a digitized image will contain noisy and imperfect examples of printed characters. For a given font, an ideal version of each character can be stored in a content-addressable memory and produced as its output whenever an imperfect version is presented as its input (Rumelhart, 1986).

2.10.4.1.6. Nodes and Interconnections

Each node, or neuron, in a neural network is a simple computing element having an input side and an output side. Each node may have directional connections to many other nodes at both its input and output sides. Each input x_i is multiplied by its associated weight w_i. Typically, the node's role is to sum each of its weighted inputs and add a bias term w_0 to form an intermediate quantity called the *activation*, *a*. It then passes the activation through a nonlinear function f_t known as the *transfer function* or *activation function*. Figure 2.42 shows the function of a single neuron. The behavior of a neural network depends on its topology, the weights, the bias terms, and the transfer function. The weights and biases can be learned, and the learning behavior of a network depends on the chosen training algorithm. Typically a sigmoid function is used as the transfer function, as shown in Figure 2.43(a). The *sigmoid* function is given by:

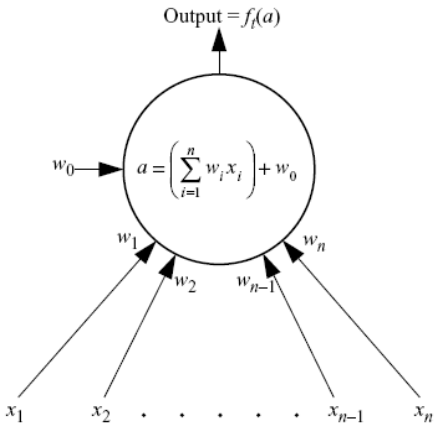

Figure 2.42. A single neuron (Hallam, 1990)

$$f_t(a) = \frac{1}{1+e^{-a}} \tag{2.14}$$

For a neuron, the activation *a* is given by:

$$a = \left(\sum_{i=1}^{n} (w_i x_i)\right) + w_o \tag{2.15}$$

where n is the number of inputs and the bias term w_0 is defined separately for each node. Figures 2.43 (b) and (c) show the ramp and step functions, which are alternative nonlinear functions sometimes used as transfer functions (Hallam, 1990).

Many network topologies are possible, but we will concentrate on a selection which illustrates some of the different applications for neural networks. We will start by looking at single and multilayer perceptrons, which can be used for categorization or, more generally, for nonlinear mapping.

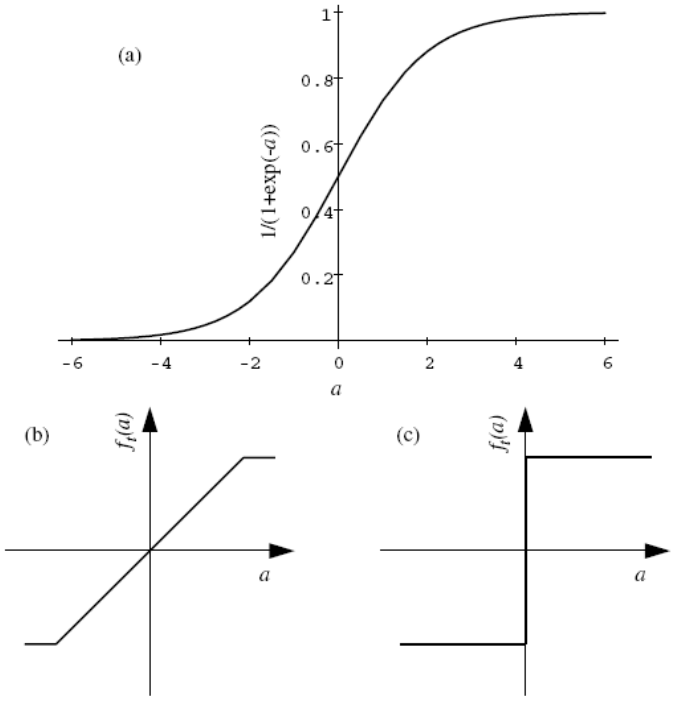

Figure 2.43. Nonlinear Transfer functions: (a) a sigmoid function, (b) a ramp function, (c) a step function (Hallam, 1990)

2.10.4.2. Applications of Neural Network Systems in Weld Modeling and Control

Selecting the appropriate indirect weld parameters for a given weld geometry is a nontrivial task. Generally, each parameter of the welding equipment affects a number of geometrical attributes of the weld pool. Current, for instance, affects both weld pool width and penetration. The human welder or weld designer usually selects the indirect weld parameters based on previous experience, handbook

recommendations, etc., and then fine tunes the selection with trial experiments. This approach can be complemented or replaced by the neural network scheme.

Zeng et al. (2003), demonstrated that a Artificial Neural Network (ANN) can provide equipment welding parameters necessary to produce high-integrity welds. In their research they utilized a commercial neural network package called Brainmaker (1993) to simulate a manual TIG welding parameter predictor. The IWP chosen for their neural predictor are welding current and voltage, the amount of filler rod consumed, weight of weld metal deposited, and arcing time per meter of weld. The inputs to the network are material type, joint type, welding position, shielding gas, sheet thickness, joint gap, and filler rod diameter. Material type and joint type are represented as symbolic variables such that several input neurons, allowing only a binary input value (i.e., 0 or 1), facilitate the representation of different materials (e.g., mild steel, stainless steel, etc.) and different welding positions (e.g., flat position, H/V position, vertical position, or overhead position).

Their network was trained using the back propagation learning algorithm. The raw data was provided by the Welding Institute in which 40 input/output training instances were used. Material types varying between mild steel and stainless steel, and each of the four possible welding positions were included in the training set. Extensive experiments highlighted that only one hidden layer did not provide the error tolerance desired by Zeng. Therefore, two hidden layers of 50 neurons in the first layer and 25 neurons in the second layer converged to an acceptable error tolerance of 4%. Tests indicated that good prediction was achieved.

The back propagation network has also been implemented by Andersen and et al. (1992 and 1993) to relate welding process variables to weld bead geometry. They employed two neural networks. One network was trained to derive DWP's from IWP's while another network was trained to yield IWP's from DWP's. This approach is illustrated in Figure 2.44. The user specifies the required weld geometry by the reference or setpoint DWP's (DWPREF). Assuming that the network has been properly trained off-line with previous sets of actual weld parameters, the network produces a set of IWP's that can be used as weld equipment settings.

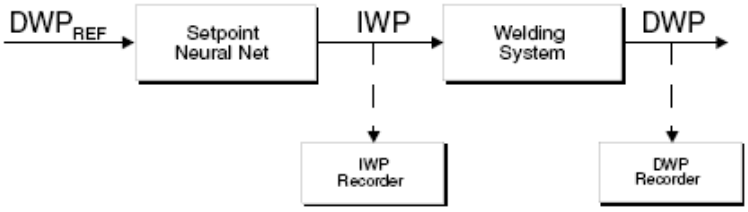

Figure 2.44. Indirect weld parameter selector using neural network (Andersen and et al., 1990)

If the network parameters include the ones having principal roles in controlling the weld pool, the welder can achieve the required DWP's with minimal experimentations or experience. While the weld is performed, the IWPs may be recorded in the IWP recorder, and similarly, the resulting DWPs can be determined and stored in the DWP recorder after welding. Once these data are available the neural network can be refined by additional off-line training with the new data, and thus its characteristics are continuously updated as future welds are produced.

Andersen and et al., (1990), used actual GTA weld data to evaluate the accuracy of the neural networks for weld modeling. The data consisted of values for voltage, current, travel speed, and wire feed speed, and the corresponding bead width, penetration, reinforcement height, and bead cross-sectional area. In all, 42 such data sets were used, of which 31 data sets were selected at random and used for training purposes while the remaining 11 data sets were presented to the trained networks as new application data for evaluation purposes. Thus the networks were evaluated using data that had not been used for training.

Networks consisting of 36, 48, 60, and 72 nodes using various numbers of hidden layers were built. The 31 sets of welding data were used for training each of the networks. Using a learning rate of $\eta = 0.1$, the number of training iterations required to reduce the conversion measurement, e_0, down to 0.09 is illustrated in Figure 2.45. Andersen and et al. (1990) defined a training iteration as one round of network adaptation to all sets of training data. Figure 2.44 clearly indicates that there is an optimum number of hidden layers that requires the least amount of training iterations for this particular problem. Although the training iterations take place off-line and are therefore irrelevant to on-line modeling, they can be fairly time

consuming. Thus, it is clear that training time optimization is advantageous for extensive experiments.

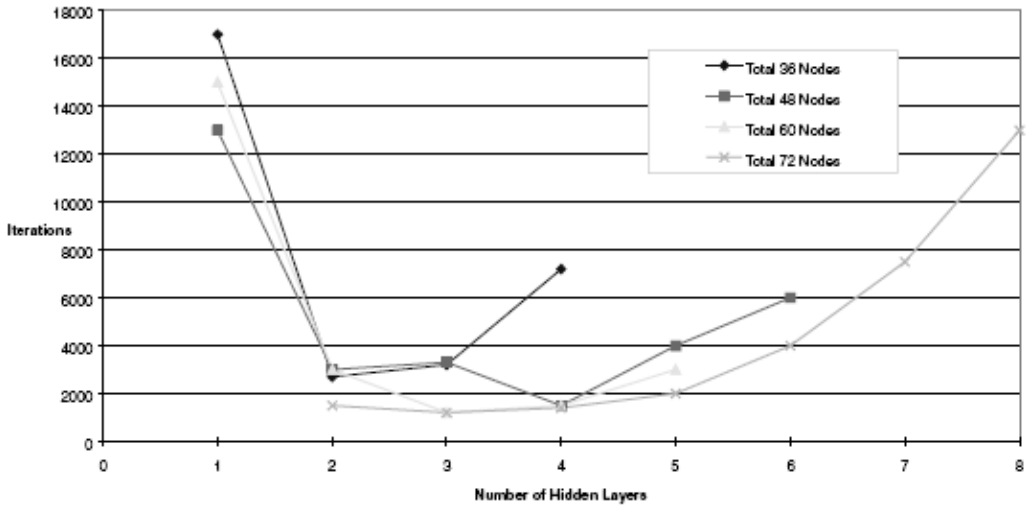

Figure 2.45. Number of iterations required for convergence of various network configurations. The error threshold e_0 is 0.09 and the correction gain η is 0.1 for all networks (Andersen and et al., 1990)

Each network configuration resulted in comparable performance. Figure 2.46 summarizes the performances of each of the networks for the four DWPs. The bars show standard deviations of the modeling errors for the various networks using the 11 tested data sets. Most of the errors are on the order of 5 to 10%, with penetration errors typically in the 20% range. These results agree with other similar experiments reported by Andersen, in that modeling accuracy is typically on the order of 10 to 20%.

An observation relating to the weld modeling experiments should be noted here. The precision of the bead measurements was 0.1 mm, which corresponds to 2 to 7% precision for the average bead width and penetration, respectively. Furthermore, inaccuracies in measurements of the data, which were used to train the neural network model, tend to degrade the general performance of the model. Width measurements are generally more reliable than penetration measurements, as they are made in several locations along the top of the bead. A penetration measurement is usually made on a single cross section, as it requires chemical etching, which results in a relatively blurred boundary between the bead and the surrounding base metal.

This difference is reflected in the consistently lower accuracy of the penetration modeling, compared with the width modeling.

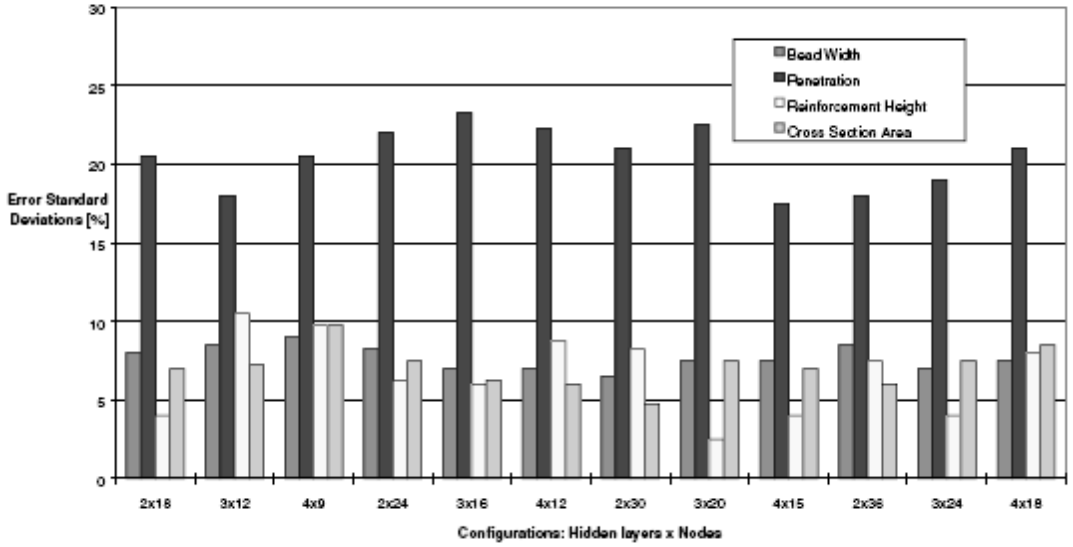

Figure 2.46. Standard deviations of mapping errors (%) for various network configurations, shown for all four DWPs (Andersen, 1992)

The two neural network schemes presented by Zeng and Andersen (1997) apply to static parameter settings only. Therefore, dynamic control of the welding process is left to the various controllers of the welding equipment, such as the automatic voltage controller (AVC), power source (usually constant current for TIG welding), etc. Thus, it is the responsibility of these controllers to maintain the parameters, selected by the neural network, constant in the presence of noise or process perturbations.

Tay and Butler (1997), described an application of an integrated method using experimental designs and neural network for modeling a metal inert gas welding process. They used an adaptive neural network to approximate the stochastically non linear dynamics of the welding process to optimize the basic welding parameters. The results showed that the proposed adaptive neural network is capable of mapping the complex relationships between the welding parameters and the corresponding output weld quality.

Wikle, Zee and Chin (1999), developed a sensing system for weld process control. The gas tungsten arc welding process was monitored with a point infrared

sensor. Welding process control was demonstrated on both constant thickness plates and plates with a step change in thickness.

Dae-Cheol and et al. (1999), described a new method of perform in multi-stage metal forming processes considering workability limited by ductile fracture. The finite element simulation combined with ductile fracture criterion performed in order to predict ductile fracture. They also implemented artificial neural network using Taguchi combinations for minimizing objective functions relevant to forming process. They also analyzed different welding technologies for cost savings.

Jarmai and Farkas (1999), developed cost calculation and optimization of the welded steel structures. They emphasized the role of fabrication costs, especiallythe role of welding costs using different welding technologies.

Vitek and et al. (2001), presented a neural network model for prediction of plasma augmented laser welded steel sheets. They analyzed the experimental weld pool shapes and used to train a neural network to predict weld pool shape as a function of process conditions. The predictions of neural network model showed excellent agreement with the experimental results, indicating that a neural network model is a viable means for predicting weld pool shape.

Nagesh and Datta (2002), explored use of artificial neural network to model the submerged arc welding process. Back propagation neural network was used to associate the welding process variables with the features of the bead geometry and penetration. They obtained good agreement with the predicted and measured results.

Gao and Wu (2002), proposed a model describing the relationship between the front side geometrical parameters of the weld pool and the back weld width with sufficient accuracy in conjunction with neural network. The model was used in the back weld width control test and a satisfactory result was obtained in their study.

2.10.4.2.1. Real-Time Monitoring of Weld Joint Penetration with Neural Network

A rather elaborate implementation of monitoring weld joint penetration using machine vision and a high-shutter-speed camera assisted with pulsed laser illumination is presented by Kovacevic, et al. (1995, 1996a, 1996b and 1996c). In their research, they employ an ANN to emulate the human operator's ability to extract weld penetration information from the geometrical appearance of the weld pool (Kovacevic and Zhang, 1996a). Conceptually, Kovacevic (1996b) believes that the human welder relies on the geometrical appearance parameters, which include size and shape information, of the weld pool to represent weld penetration. Kovacevic's model uses an empirically derived relationship between the sag of the weld near the rear of the pool and the root face bead width (Lin and Eagar, 1984; Rokhlin and Guu, 1993; Zhang and et al., 1993). Thus, their ANN weld penetration estimator is trained with the length and the included rear angles of the weld pool to represent the pool's size and shape, respectively. The objective of Kovacevic's (1996a) experiments was to monitor, in real-time, the full penetration state of the weld pool which is described by the root face bead (backside) width. Extensive neural network configurations were tested in order to examine the possibility of using different pool parameters as inputs to represent the weld penetration. Each of the networks, however, contained only one output node which was responsible for calculating the backside bead width.

They employed a commercial neural network software package to facilitate the training of the various neural network configurations. An extended delta-bar-delta (EDD) learning algorithm was used to overcome the slow convergence rate associated with the back propagation learning algorithm. Only one hidden layer was used in which the number of nodes, n_2, was calculated by the following equation:

$$\frac{N}{10(n_1+n_3)} < n_2 < \frac{N}{5(n_1+n_3)} \tag{2.10}$$

where N is the number of samples, and n_1 and n_3 are the number of elements in the input and output layer, respectively. Kovacevic (1996c) found that while none of the input parameters (width, length, length-to-width ratio, or rear angles) alone can accurately assess the penetration, a combination of the length and rear angles of the weld pool provided sufficient information to accurately model the relationship between the weld pool and weld penetration. Furthermore, monitoring was possible in real-time at a rate of 5 Hz.

2.10.4.2.2. Closed-Loop Control of GTA Weld Bead Geometry

An approach to closed-loop control, using neural networks, has been attempted by a number of researchers using various welding processes, such as TIG, GMAW, RSW, Variable Polarity Plasma Arc welding (VPPAW), etc., and a wide range of sensing devices, such as optical, arc, infrared, acoustical, ultrasonic, etc. (Rosenthal, 1941; Nunes, 1983; Tsai, 1983; Kovacevic and Zhang, 1996d).

Andersen (1993) developed a digital welding control system for the TIG welding process in which the objective was to maintain constant weld bead dimensions when a variation in the welding environment was encountered, such as a variation in the thickness of the plate upon which the weld was being performed (Nunes, 1983). This is a practical consideration when welding items of relatively complex shapes, where the varying thermal conditions can affect the geometry of the molten pool. Andersen's control system is most readily explained by reference to Figure 2.47, which illustrates the main components. The desired bead width and penetration are specified by the user as WREF and PREF, respectively. These parameters, as well as the workpiece thickness, H, are fed to a neural network set point selector, which yields the nominal travel speed, current, and arc length (V_0, I_0, and L_0, respectively). Arc initiation and stabilization is controlled in an open-loop fashion by the weld start sequencer. Given the desired equipment parameters the arc is typically initiated and established at a relatively low current, with the other equipments parameters set at some nominal values. Once the arc has been established the equipment parameters are ramped to the set point values specified by the neural

network. When the set point values have been reached, at time $t = T$, the closed-loop control is enacted. The bead width from the process can be monitored in real-time. A real-time penetration sensor is not readily available; therefore, a second neural network is run in parallel with the process to yield estimates of the penetration. The measured bead width and the estimated penetration are subtracted from the respective reference values, processed through proportional-plus-integral controllers, and added to the final values obtained from the set point sequencer. When a workpiece thickness variation is encountered in the process, the system adjusts the current and the travel speed accordingly to maintain constant bead geometry.

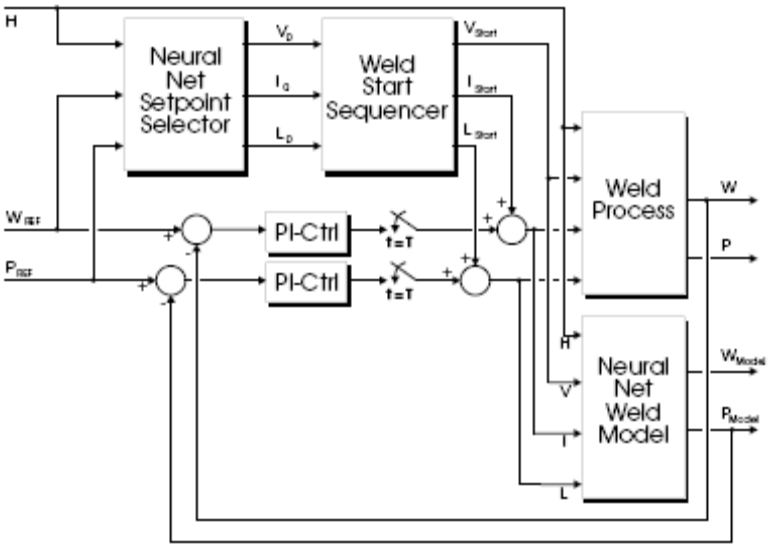

Figure 2.47. Closed-loop TIG welding control system (Andersen, 1993)

3. MATERIAL AND METHOD

3.1. Material

3.1.1. Workpiece Materials

The materials selected for the experiments were AISI type 304, 304L and 316L stainless steel plates with different thicknesses. Among the austenitic stainless steel, AISI type 304 and 316 stainless steel plates are the most versatile and the most widely used in the fabrication of pressure vessels plates. Their chemical composition, mechanical properties, weldability and corrosion/oxidation resistance provide the best all-round performance stainless steel at relatively low cost. They also have excellent low temperature properties and responds well to hardening by cold working. Typical chemical compositions and mechanical properties and size of the materials used in this study were given in Table 3.1 and Table 3.2, respectively.

Table 3.1. Chemical analysis of workpiece materials

	Percent Composition (%)								
Material	C	Mn	P	S	Si	Cr	Mo	Ni	Cu
AISI 304	0.08	2.00	0.04	0.030	1.00	19	0.20	10.5	0.02
AISI304L	0.02	1.52	0.02	0.017	0.53	18.09	0.25	8.49	0.11
AISI316L	0.03	2.00	0.04	0.030	1.00	16.0	0.15	10.5	0.02

Table 3.2. Dimensions and mechanical properties of workpiece materials

Material (AISI)	**Thickness (mm)**	**Width (mm)**	**Length (mm)**	**Tensile load (kg)**
304	1.2	16	240	1325
304L	5	12	240	4500

It is important to understand the microstructure and behavior of the stainless steels to be welded. The next section explains the general properties and weldability of the austenitic stainless steels for the particular applications.

3.1.2. Welding Stainless Steels

The stainless properties of stainless steels are primarily due to the presence of chromium in quantities greater than roughly 12 weight percent. This level of chromium is the minimum level of chromium to ensure a continuous stable layer of protective chromium-rich oxide forms on the surface. The ability to form chromium oxide in the weld region must be maintained to ensure stainless properties of the weld region after welding. In commercial practice, however, some stainless steels are sold containing as little as 9 weight percent chromium and will rust at ambient temperatures.

Stainless steels are generally classified by their microstructure and are identified as ferritic, martensitic, austenitic, or duplex (austenitic and ferritic). The microstructure significantly affects the weld properties and the choice of welding procedure used for these stainless steel alloys. In addition, a number of precipitation-hardenable (PH) stainless steels exist. Precipitation-hardenable stainless steels have martensitic or austenitic microstructures (Kou, 1987).

Iron, carbon, chromium and nickel are the primary elements found in stainless steels and significantly affect microstructure and welding. Other alloying elements are added to control microstructure or enhance material properties. These other alloys affect welding properties by changing the chromium or nickel equivalents and thereby changing the microstructure of the weld metal. Generally, 200 and 300 series alloys are mostly austenitic and 400 series alloys are ferritic or martensitic, but exceptions exist.

Stainless steels are subject to several forms of localized corrosive attack. The prevention of localized corrosive attack is one of the concerns when selecting base metal, filler metal and welding procedures when fabricating components from stainless steels.

Stainless steels are subject to weld metal and heat affected zone cracking, the formation of embrittling second phases and concerns about ductile to brittle fracture transition. The prevention of cracking or the formation of embrittling

microstructures is another major concern when welding or fabricating stainless steels.

3.1.3. Welding of Austenitic Stainless Steels

Austenitic stainless steels have high ductility, low yield stress and relatively high ultimate tensile load, when compare to a typical carbon steel. Ideally, austenitic stainless steels exhibit a single-phase, the face-centered cubic (FCC) structure, that is maintained over a wide range of temperatures. This structure results from a balance of alloying additions, primarily nickel, that stabilize the austenite phase from elevated to cryogenic temperatures. Because these alloys are predominantly single phase, they can only be strengthened by solid-solution alloying or by work hardening (Jeffus, 2004).

The austenitic stainless steels were developed for use in both mild and severe corrosive conditions. Austenitic stainless steels are used at temperatures that range from cryogenic temperatures, where they exhibit high toughness, to elevated temperatures, where they exhibit good oxidation resistance. Because the austenitic materials are nonmagnetic, they are sometimes used in applications where magnetic materials are not acceptable.

The most common types of austenitic stainless steels are the 200 and 300 series. Within these two grades, the alloying additions vary significantly. Furthermore, alloying additions and specific alloy composition can have a major effect on weldability and the as-welded microstructure. The 300 series of alloys typically contain from 8 to 20 weight percent Ni and from 16 to 25 weight percent Cr.

Stainless steel has a very thin and stable oxide film rich in chrome. This film reforms rapidly by reaction with the atmosphere if damaged. If stainless steel is not adequately protected from the atmosphere during welding or is subject to very heavy grinding operations, a very thick oxide layer will form. This thick oxide layer, distinguished by its blue tint, will have a chrome depleted layer under it, which will impair corrosion resistance. Both the oxide film and depleted layer must be removed,

either mechanically (grinding with a fine grit is recommended, wire brushing and shot blasting will have less effect), or chemically (acid pickle with a mixture of nitric and hydrofluoric acid). Once cleaned, the surface can be chemically passivated to enhance corrosion resistance, (passivation reduces the anodic reaction involved in the corrosion process).

Major concerns, when welding the stainless steels, are the susceptibility to solidification and liquation cracking and carbide form at grain boundaries. Cracks can occur in various regions of the weld with different orientations, such as centerline cracks, transverse cracks, and microcracks in the underlying weld metal or adjacent heat-affected zone (HAZ). These cracks are primarily due, to low-melting liquid phases, which allow boundaries to separate under the thermal and shrinkage stresses during weld solidification and cooling.

As illustrated in Figure 3.1, if any part of stainless steel is heated in the range of 500 to 800 ^{o}C for any reasonable time there is a risk that the chrome will form chrome carbides (a compound formed with carbon) with any carbon present in the steel. This reduces the chrome available to provide the passive film and leads to preferential corrosion, which can be severe. This is often referred to as sensitization. Therefore it is advisable when welding stainless steel to use low heat input and restrict the maximum interpass temperature to around 175 °C, although sensitization of modern low carbon grades is unlikely unless heated for prolonged periods. Small quantities of either titanium (321) or niobium (347) added to stabilize the material will inhibit the formation of chrome carbides.

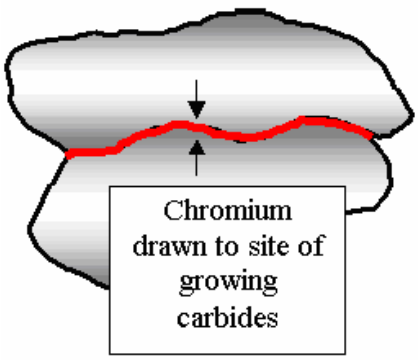

Figure 3.1. Chrome carbide precipitation in stainless steels

To resist oxidation and creep high carbon grades such as 304H or 316H are often used. Their improved creep resistance relates to the presence of carbides and the slightly coarser grain size associated with higher annealing temperatures. Because the higher carbon content inevitably leads to sensitization, there may be a risk of corrosion during plant shut downs, for this reason stabilized grades may be preferred such as 347H.

To ensure good corrosion resistance of the weld root it must be protected from the atmosphere by an inert gas shield during welding and subsequent cooling. The gas shield should be contained around the root of the weld by a suitable dam, which must permit a continuous gas flow through the area. Welding should not commence until sufficient time has elapsed to allow the volume of purging gas flowing through the dam to equal at least the 6 times the volume contained in the dam. Once purging is complete the purge flow rate should be reduced so that it only exerts a small positive pressure, sufficient to exclude air. If good corrosion resistance of the root is required the oxygen level in the dam should not exceed 0.1% (1000 ppm); for extreme corrosion resistance this should be reduced to 0.015% (150 ppm). Backing gasses are typically argon or helium; Nitrogen Is often used as an economic alternative where corrosion resistance is not critical, N_2+10%He is better. A wide variety of proprietary pastes and backing materials are available than can be use to protect the root instead of a gas shield. In some applications where corrosion and oxide cooking of the weld root is not important, such as large stainless steel ducting, no gas backing is used (Kou, 1987).

Even with the serious cracking concerns, and sensitization problems the austenitic stainless steels are generally considered the most weldable of the stainless steels. Because of their physical properties, the welding behavior of austenitic stainless steels is different than the ferritic, martensitic, and duplex stainless steels. For example, the thermal conductivity of austenitic alloys is roughly half that of ferritic alloys. Therefore, the weld heat input that is required to achieve the same penetration is reduced. In contrast, the coefficient of thermal expansion of austenite is 30 to 40 percent greater than that of ferrite, which can result in increases in both distortion and residual stresses, due to welding. Since the high coefficient of

expansion associated with this material welding distortion can be quite savage. The molten weld pool of the austenitic stainless steels is commonly more viscous, or sluggish, than ferritic and martensitic alloys. This slows down the metal flow and wettability of welds in austenitic alloys, which may promote lack of fusion defects.

Main characteristics of Austenitic stainless steels are as follows (ASM, 2002):

- Not magnetic or only slightly magnetic
- Not attacked by a 10% solution of Nitric Acid (HNO_3) in alcohol
- Quite ductile and easily deformable by mechanical working which increases both hardness and strength: this characteristic is called strain hardening
- Easily welded, with the needed precautions
- Thermal conductivity only between one third and one half that of other steels
- Coefficient of thermal expansion by 30-40%, even 50% greater

3.1.4. Electrodes

In this study, AWS A 5.12-80 EW Th-2 Thoriated (red color code) Tungsten was used as an electrode material. The shape and corresponding dimensions of the electrodes used in the experiments are shown in Figure 3.2.

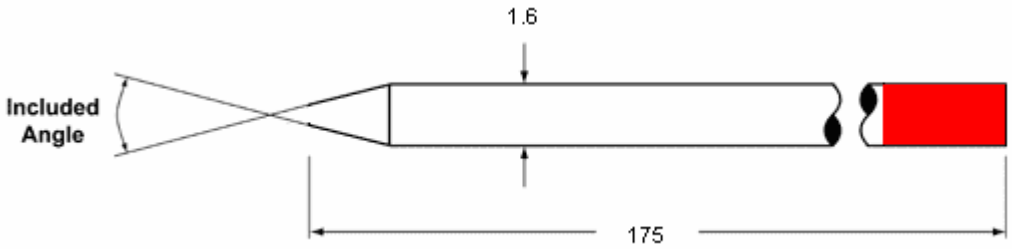

Figure 3.2. Electrode shape used in the experiments

The thermionic emission of tungsten can be improved by alloying it with metal oxides that have very low work functions. The electrodes are able to handle higher welding currents without failing. Thorium oxide is one such additive.

Thoriated tungsten electrodes are superior to pure tungsten electrodes in several respects. The thoria provides about 20% higher current-carrying capacity, generally longer life, and greater resistance to contamination of the weld. With these electrodes, arc starting is easier, and the arc is more stable than with pure tungsten or zirconiated tungsten electrodes.

The EWTh-1 and EWTh-2 electrodes are designed for direct current electrode negative (DCEN) applications. They maintain a sharpened tip configuration during welding, which is desirable for welding of stainless steel. They are not often used with AC, because it is difficult to maintain the balled end, which is necessary for AC welding without splitting the electrode.

3.1.5. Filler Metals

The thickness of the part to be welded will determine the need for filler metal. Material thinner than the 4.2 mm can be successfully welded without filler metal additions. Filler metal when needed, can be added manually in straight length or automatically. AWS A5.9 ER308L and ER316L filler metals were used in the temperature measurement during multipass welding of stainless steels. The chemical composition of these filler metals used in welding of 5 mm, 8 mm and 10 mm thickness specimens are shown in Table 3.3.

Table 3.3. The composition of filler metal used in multipass welding

Workpiece	Filler Type	C	Si	Mn	Ni	Cr	Mo	S	P
AISI 304L	ER308L	0.030	0.40	1.80	10.5	20.0	0.30	0.25	0.030
AISI 316L	ER316L	0.030	0.45	1.80	12.5	18.5	3.00	0.025	0.030

3.1.6. Mechanical Welding Robot

The mechanical welding robot, shown in Figure 3.3, was arranged for the linear movement on the weld pad center line. Some modifications were made on the system to adapt according to the TIG welding process.

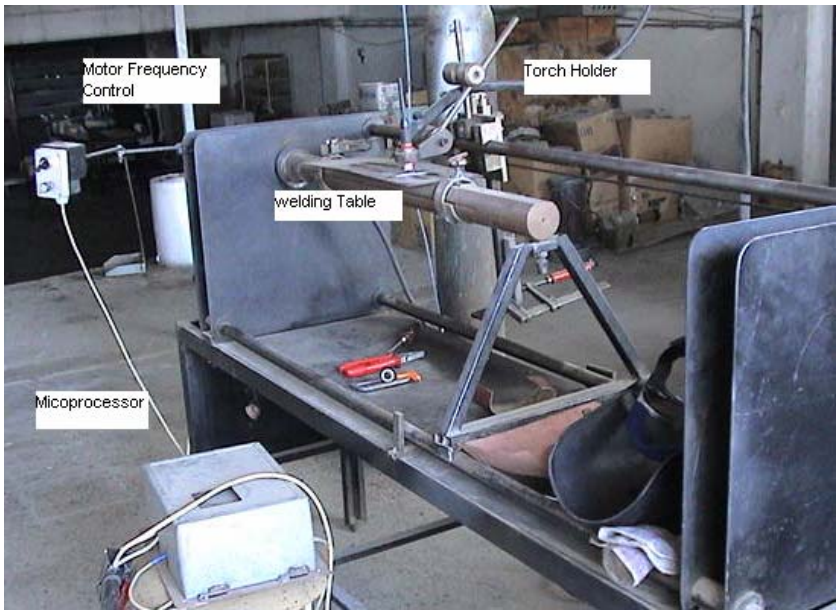

Figure 3.3. Welding robot used in the experiments

The basic features of the system include:

- 22 mm welding torch holder with adjustable torch angle,
- Chain-gear drive system for torch movement,
- Graded belt-pulley system for the required torch speeds,
- Adjustable microprocessor speed control system,
- Adjustable frequency control,
- Adjustable welding table for different workpieces,

In order to determine the velocity of the welding torch over the weld path centerline, the frequency calibrations were adjusted from 10 Hz to 70 Hz. The calibration of the velocity and frequency control of the welding robot was made and the related velocity-time graph of robot is shown in Figure 3.4 and Figure 3.5 respectively.

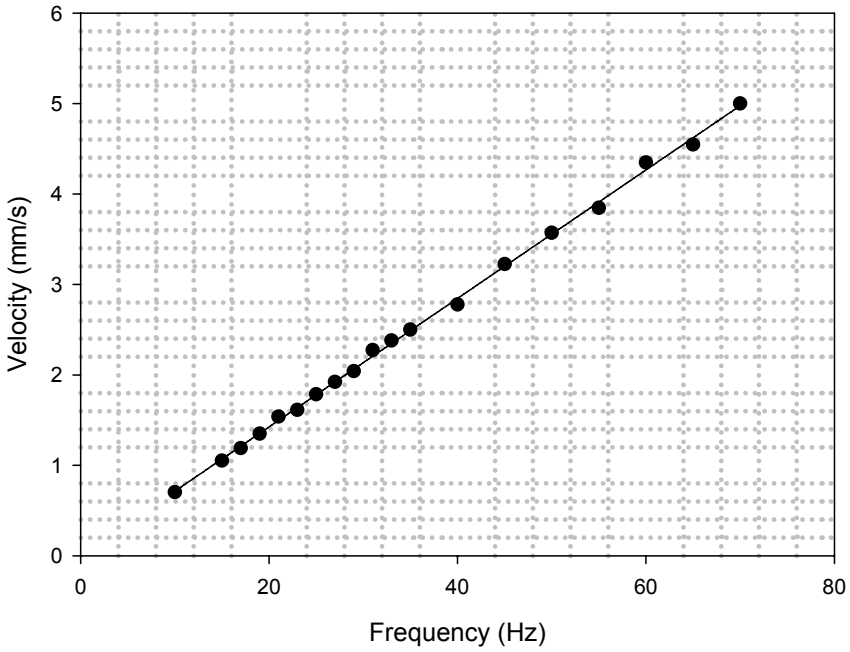

Figure 3.4. Calibrated torch velocity-frequency control

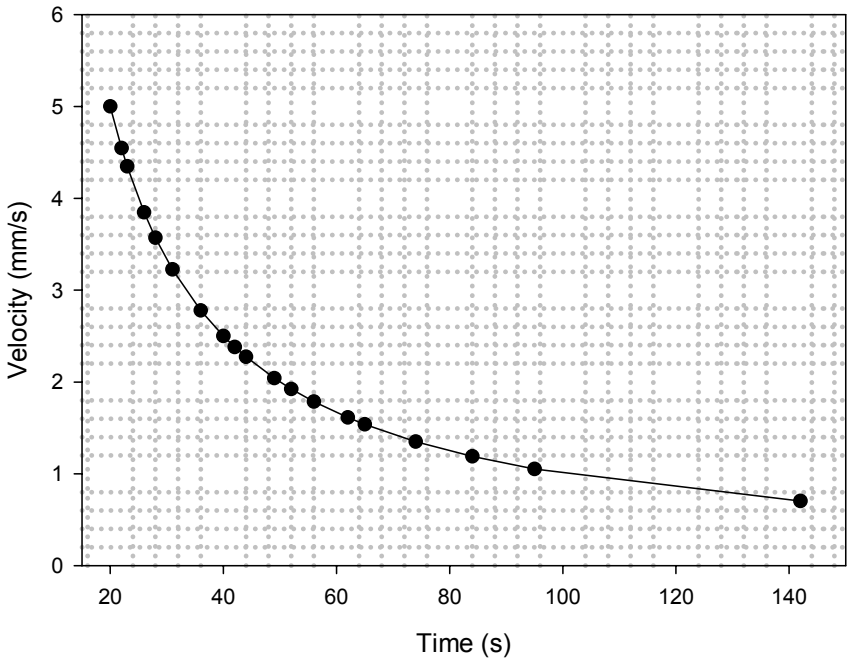

Figure 3.5. Calibrated torch velocity-time graph

3.1.7. TIG Welding Machine

Welding machines consist of power sources. Power sources are apparatuses that are used to supply current and voltage that are suitable for particular welding processes.

Arc welding requires that an electric arc be established between an electrode and the work-piece to produce the heat needed for melting the base plate. Because utility energy is not delivered at the proper voltage and current, it must be converted to the required levels by the welding power source.

Arc power sources convert the customary 240 or 480 V alternating current (ac) utility power to a range from 20 to 80 V and simultaneously increase the current proportionately. Galvanic isolation is also provided from the utility line voltage to ensure operator safety. Motor or engine-driven welding generators are wound to deliver the correct voltage and current directly; therefore, no transformer is necessary. Actual arc voltage is established by factors other than the power source (for example, electrode type, base metal type, shielding gas and standoff distance)

The National Electrical Manufacturers Association (NEMA) categorizes arc welding machines into three classes on the basis of duty cycle (ASM, 1998):

- *Class I:* rated output at 60, 80, or 100% duty cycle,
- *Class II:* rated output at 30, 40, or 50% duty cycle,
- *Class III:* rated output at 20% duty cycle

Duty cycle is the ratio of arc time to total lime based on a 10 min averaging period. A 60% machine will deliver 6 min of arc time and 4 min off time without overheating. NEMA requires most welding machines to produce a maximum of 125% of rated output current. No minimum current is specified, but 10% (of rating) is typical.

The experiments were performed on a Fronius Variostar WTU 305 type TIG welding machine with a maximum 300 A current. Some of the technical data of Fronius Variostar WTU 305 type machine are;

- Class I type welding machine,
- 50 Hz, 12.5 kVA,
- Maximum 300 A capacity,
- Adjustable arc jump frequency,
- Electronic control of current,
- Cooler fan,
- Adjustable gas flow,
- Rod electrode,
- Overvoltage and temperature indicator,
- Continuously adjustable welding current,
- Adjustable downslope control,
- Frequency range selector,
- AC/DC selector,
- Changeable Anode and Cathode connections.

3.1.8. Measurement of Temperature Distribution

K type thermocouples (T/C) were used to measure the temperature distribution during multipass welding of AISI 304L and AISI 316L stainless steels. These thermocouples withstand high temperatures about more than 1600 ^{o}C. Arrangement employed in the measurement is shown in Figure 3.6.

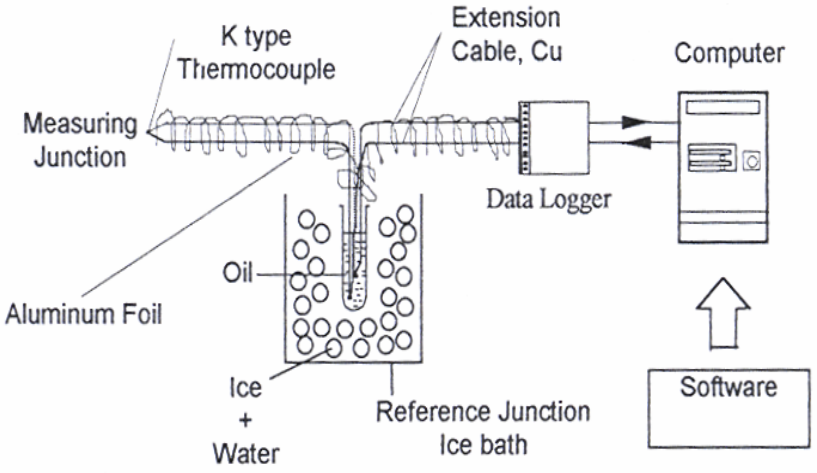

Figure 3.6. Schematic view of temperature measurement arrangement used in the experiments

Measuring junction (MJ) was placed into a measuring point to sense the temperature at that point. There are some desired properties from a measuring junction such as good electrical contact, low electrical resistance, and high mechanical strength. Welding, soldering, brazing, or twisting is some manufacturing processes for MJ. In this study, twisting method was used.

The other end of the thermocouple is replaced into a small oil-filled tube, which is placed into ice-water mixture to supply 0 ^{o}C reference junction (RJ). Copper wires were used to connect to measurement instrument.

The electromotor-force (emf) produced by the thermocouples is in the level of mV and measured by a data logger. The data stored in the computer in the form of mV was later converted to degree Celsius using the calibration curve shown in Figure 3.7, and a FORTRAN program was written and given in Appendix A.

Various reading on the system was performed using a data logger (P.A. Hilton Ltd). The measured parameters are outputs of the thermocouples and voltage and current transducers. The data logger's interface is a multi channel analog and digital unit with both input and output capability. Command and data are transfer via 8 wires RS 232 serial link using ASCII character string sent and receive by a controlling computer as shown in Figure 3.8.

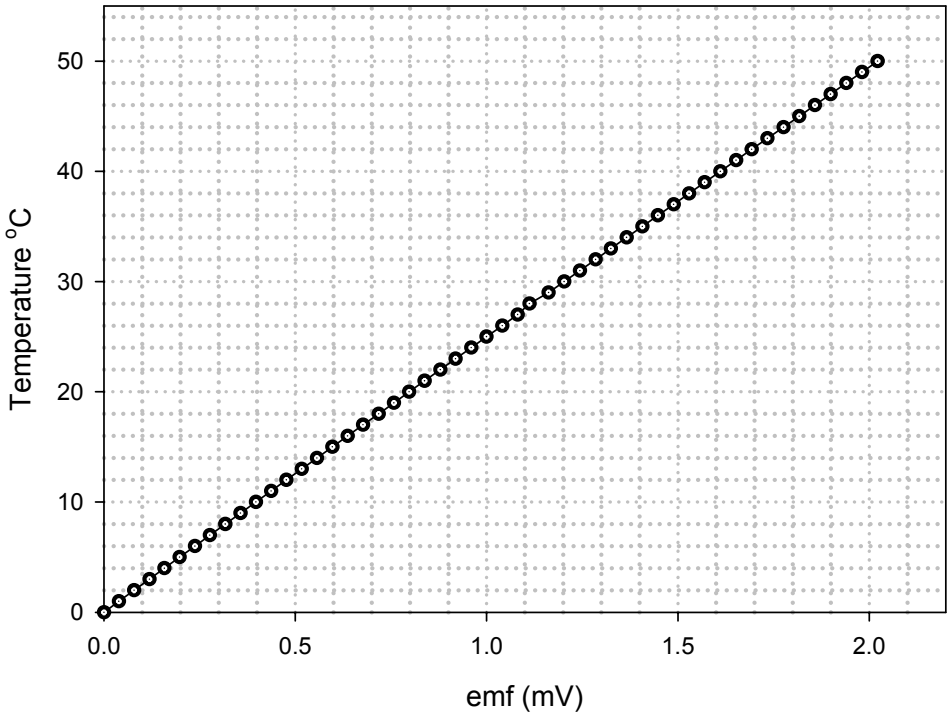

Figure 3.7. Calibration curve for K type T/C used in the experiments

Figure 3.8. Data logger system used in the experiments

The thermocouples were fixed to the workpiece by using eight special screws which was arranged not to damage thermocouple during the measurement. Mounting condition of the thermocouples to the workpieces is shown in Figure 3.9.

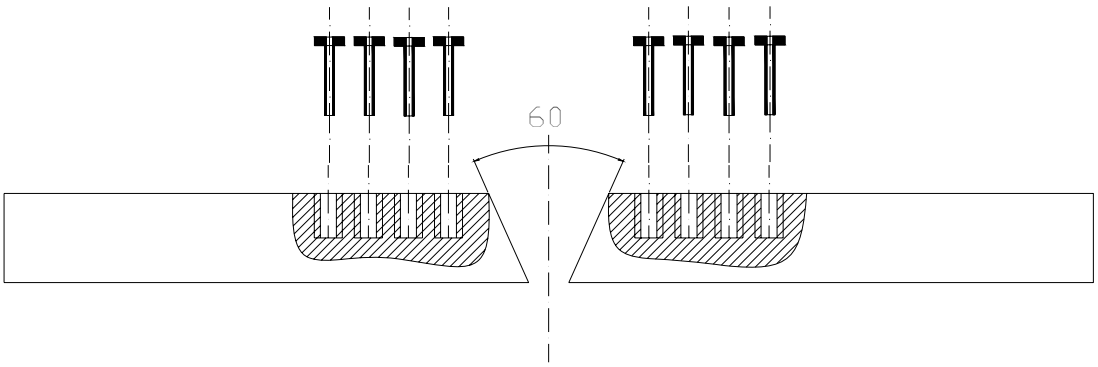

Figure 3.9. Thermocouple mounting position for temperature distribution

3.1.9. Optical Microscopy

Optical microscopy was used to examine the upper width (UW), upper height (UH), penetration (P) and area of penetration (AP) structures of the welded specimens. The workpieces were sectioned to produce specimens for optical microscopy. These specimens were cleaned and polished using different grades of abrasive paper and diamond paste. The specimens were etched using the Marble's etchant media given in Table 3.4. On completion of etching process, the specimens were rinsed in clean water to remove chemicals and stop any reactions from proceeding further. After specimens were water rinsed, they were cleaned in ethanol (C_2H_5OH) solution and then dried.

Table 3.4. Etching reagents for austenitic stainless steels

Etching Composition (Marble's region)	**$CuSO_4$ (g)**	**HCl (ml)**	**H_2SO_4 (ml)**	**Etching time (sec)**
$CuSO_4 + HCl + H_2SO_4$	8	20	5	65

In macro examinations of the specimens MOTIC stereo microscope with image capture device mounted on top of the lens section of the microscope. The special apparatus was used in order to place the etched specimen under the

microscope. The specimens were placed in the middle part of the apparatus and placed under the microscope. Then, the related measurements were established.

3.1.10. Microhardness Tests

The specimens prepared for optical microscopy were reused for the microhardness measurements. These were performed on SHIMADZU HV2000 type microhardness tester. A hardness Vickers (HV_{30}) microhardness tester with an objective lens of 50X was used. The indenter was pyramid with an angle of 136^{o} between the opposite faces. The measurements were taken under a 30g load. Readings were taken at various points along the cross section of welding zone. In order to eliminate the effect of indentations, the readings were taken by allowing at least two widths of Vickers indentations apart. Microhardness measurements were then used to study the variation in the hardness throughout the thermally influenced layers.

3.1.11. Weld Pool Shape Analysis

The specimens prepared for optical microscopy were also used to examine weld pool shape. Macrographs were taken of each cross section using stereo microscope with 50X lens. The weld pool profile was outlined by using Image-pro Plus 4.5 and NIH ImageJ softwares from the micrographs. The spatial calibrations were made on the macrographs before the measurement. Heat affected zone on the top section of the etched samples was measured with a sensitivity of 0.01. The line drawing of the pool profiles upper width (UW), upper height (UH), penetration (P) and area of penetration (AP) were then measured on the outlined profile.

3.2. Method

3.2.1. Design, Analysis and Optimization of the Experiments

The purpose of product or process development is to improve the performance characteristics of the product or process relative to customer needs and expectations. The purpose of experimentation should be to understand how to reduce and control variation of a product or process; subsequently, decisions must be made concerning which parameters affect the performance of a product or process (Ross, 1995).

A designed experiment is the simultaneous evaluation of two or more factors (parameters) for their ability to affect the resultant average or variability of particular product or process characteristics. To accomplish this in an effective and statistically proper fashion, the levels of the factors are varied in a strategic manner, the results of the particular test combinations are observed, and the complete set of results is analyzed to determine the influential factors and preferred levels, and whether increases or decreases of those levels will potentially lead to further improvement. It is important to note that this is an iterative process; the first round through the design of experiments (DOE) process will many times lead to subsequent rounds of experimentation. The beginning round, often referred to as a screening experiment, is used to find the few important, influential factors out of the many possible factors involved with a product or process design. This experiment is typically a small experiment with many factors at two levels. Later rounds of experiments typically involve few factors at more than two levels to determine conditions of further improvement.

The DOE process is divided into three main phases which encompass all experimentation approaches. The three phases are; the planning phase, the conducting phase, and the analysis phase (Ross, 1995).

The planning phase is by far the most important phase for the experiment to provide the expected information. An experimenter will learn something from

any experiment; sometimes the information is in a positive sense and sometimes in a negative sense. Positive information is an indication of which factors and which levels lead to improved product or process performance. Negative information is an indication of which factors don't lead to improvement, but no indication of which factors do. If the experiment includes the real, yet unknown, influential factors and appropriate levels, the experiment will tend to yield positive information. If the experiment does not include the real influential factors, the experiment will yield negative information. The planning phase is when factors and levels are selected and, therefore, is the most important stage of experimentation. Also, the correct selection of factors and levels is nonstatistical in nature and is more dependent upon product and process expertise.

The second most important phase is the conducting phase, when test results are actually collected. If experiments are well planned and conducted, the analysis is actually much easier and more likely to yield positive information about factors and levels.

The analysis phase is when the positive or negative information concerning the selected factors and levels is generated based on the previous two phases. The analysis phase is least important in terms of whether the experiment will successfully yield positive results. This phase, however, is the most statistical in nature of the three phases of the DOE by a wide margin. Because of the heavier involvement of statistics, the analysis phase is typically the least understood by the product or process expert (Ross, 1995).

3.2.1.2. Response Surface Methodology (RSM)

In the early stages of experimental work, experimenters typically use screening experiment designs that normally consist of trials run at the extreme lower- and upper-bound level setting combinations of the variable study ranges. They provide information on the direct additive effects of the study variables and on pairwise (two-variable) interaction effects. Screening designs enable experimenters

to select the best materials and equipment from available alternatives and to focus on the correct variables and ranges for further study.

In the later stages of the experimental work, the goal shifts from screening to product and process optimization. The statistical experiment designs most widely used in optimization experiments are termed "response surface designs." In addition to trials at the extreme level settings of the variables, response surface designs contain trials in which one or more of the variables are set at the midpoint of the study range (other levels in the interior of the range may also be represented). Thus, these designs provide information on direct effects, pairwise interaction effects and curvilinear variable effects. Response surface methodology (RSM) is the combination of mathematical and statistical techniques used in empirical study of relationships and optimization, where several independent variables influence a dependent variable or response, the goal being to secure the optimal response. In applying the RSM, the response or dependent variables influence on an independent variable is viewed as a surface to which a mathematical model is fitted. The eventual objective of the RSM is to determine the optimum operating conditions for the system or to determine a region of the factor space in which the operating conditions for the system or to determine a region of the factor space in which operating requirements are satisfied (Design Expert, 2003).

3.2.1.3. Central Composite Design (CCD)

Most practitioners of RSM generate experiment designs and analyze their data using a statistical software program running on a computer. Many of these programs can generate many classes of RSM designs and, in some cases, offer several varieties of each class. However, the central composite design is the most popular of the many classes of RSM designs due to the following three properties (Design Expert, 2003):

- A central composite design (CCD) can be run sequentially. It can be naturally partitioned into two subsets of points; the first subset estimates linear and two-factor interaction effects while the second subset estimates

curvature effects. The second subset need not be run when analysis of the data from the first subset points indicates the absence of significant curvature effects.

- CCDs are very efficient, providing much information on experiment variable effects and overall experimental error in a minimum number of required runs.
- CCDs are very flexible. The availability of several varieties of CCDs enables their use under different experimental regions of interest and operability.

A second-order model can be constructed efficiently with central composite designs (CCD). CCDs are first-order (2^n) designs augmented by additional centre and axial points to allow estimation of the tuning parameters of a second-order model. Figure 3.10 shows a CCD for 3 design variables.

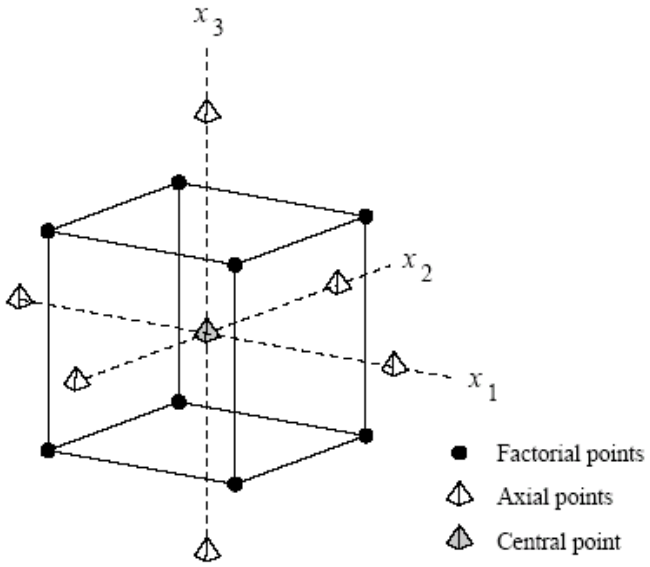

Figure 3.10. Central composite designs for 3 design variables at 2 levels (Design Expert, 2003)

As shown, in Figure 3.10, the design involves 2^n factorial points, 2^n axial points and 1 central point. CCD presents an alternative to 3^n designs in the construction of second-order models because the number of experiments is reduced as compared to a full factorial design (15 in the case of CCD compared to 27 for a

full-factorial design). Hence, in the case of problems with a large number of designs variables, use of central composite design may be time-consuming.

In most statistical software programs, there are three main varieties of CCD. These are face-centered, rotatable (circumscribed) and inscribed CCD. Many experimenters are uncertain about the best variety to use in a given study. To make the right selection, the differences between these varieties should be understood in terms of the experimental region of interest and region of operability, according to the following definitions.

i. Region of interest: A geometric region defined by lower and upper limits on study-variable level setting combinations that are of interest to the experimenter.

ii. Region of operability: A geometric region defined by lower and upper limits on study-variable level setting combinations that can be operationally achieved with acceptable safety and that will output a testable product.

Figure 3.25 presents a face-centered CCD for two study variables: time and temperature. Both coded and natural variable level settings for time and temperature are shown in the figure. The design consists of a center point, four factorial points (the intersection points of the ±1 coded variable bounds) and four axial points (points parallel to each variable axis on a circle of radius equal to 1.0 and origin at the center point). The dots in Figure 3.11 identify the variable level setting combinations that constitute the nine design points (experiment runs).

The radius, designated α, determines the geometry of the design region. An α of 1.0 defines a square design geometry (a cube for three variables, a hypercube for four or more variables, etc.). As the value of α increases, the axial points extend beyond the faces of the square and the design region becomes more spherical.

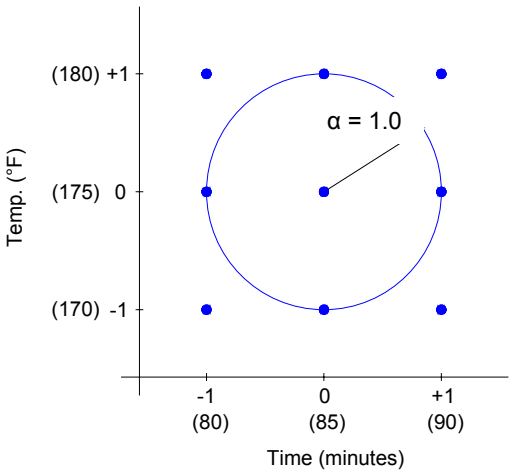

Figure 3.11. Two-variable face-centered CCD (Design Expert, 2003)

To successfully carry out any designed experiment, the region of operability must encompass the region of interest. In this example, this means that the process must be able to be operated at all time and temperature level setting combinations in the region of interest described by the variable ranges. Therefore, the first step in selecting the right variety of CCD is to compare the region of interest to the region of operability. If the process cannot be operated at one or more of the extremes of the region (in this case the corners of the square), then a face-centered CCD is inappropriate.

Rotatable (circumscribed) designs are the original form of the central composite design. Figure 3.12 presents a rotatable CCD for time and temperature using the previously defined lower and upper variable bounds. As the Figure 3.12 shows, the rotatable CCD uses an α value of 1.4 to describe a circular design geometry (a sphere for three variables, a hypersphere for four or more variables, etc.).

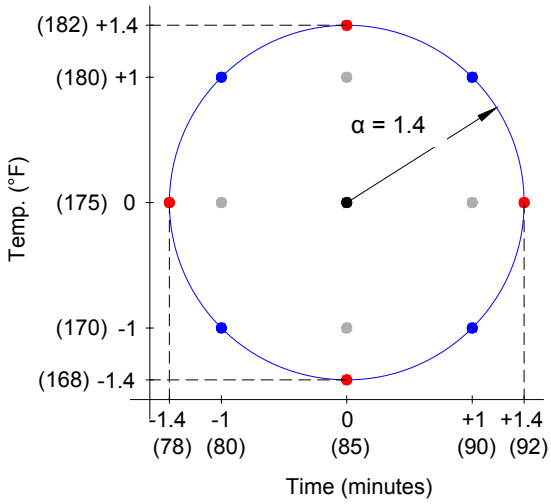

Figure 3.12. Two-variable rotatable (circumscribed) CCD (Design Expert, 2003)

For a given number of variables, α value required to achieve rotatability is computed as $\alpha = \left[2^n\right]^{1/4}$ where n is the number of study variables or factors. Rotatability refers to the uniformity of prediction error. In rotatable designs, all points at the same radial distance (r) from the center point have the same magnitude of prediction error. In most rotatable designs the factorial points and axial points lie on different concentric geometric spheres and thus have different magnitudes of prediction error. For example, in the 2^3 rotatable CCD, the factorial points are located on a sphere of radius 1.73, while the axial points are located on a sphere of radius 1.68. Setting α to 2^n changes the design from a rotatable CCD to a spherical CCD. In spherical CCDs, all design points occur on the same geometric sphere. These designs are not exactly rotatable, but they are near-rotatable.

The value of making rotatability (or near-rotatability) a design goal becomes clear when you consider that the location of the optimum point within the region of interest is not known before the experiment is conducted, so it's desirable that all points a given distance (r) from the center point in any direction have the same magnitude of prediction error.

Relative to the α value of 1.0 in the face-centered design, the rotatable design α value of 1.4 has extended the design region beyond the defined variable bounds. Thus, predicted responses at or near the axial points, which would have been

extrapolations in a face-centered design, are within the design region in rotatable design. This is an important consequence, because the magnitude of prediction error increases geometrically with distance outside the design region.

However, extending the axial points beyond the defined variable bounds when using rotatable CCDs requires operating the process at five level settings of each variable. The face-centered CCD, in contrast, requires operating the process at only three level settings of each variable. This makes the face-centered CCD a simpler design to carry out.

Figure 3.13 presents an inscribed CCD for time and temperature, again using the previously defined lower and upper variable bounds. The inscribed CCD also uses an α value of 1.4 to describe a circular geometric region (a sphere for three variables, a hypersphere for four or more variables, etc.). However, inscribing restricts the actual design region to the defined variable ranges by locating the axial points at the lower and upper bounds of the variable ranges. The factorial points are brought into the interior of the design space (inscribed) and set at a distance from the center point that preserves the proportional distance of the factorial points to the axial points. For example, given a rotatable CCD for two variables ($\alpha = 1.4$) with coded variable bounds of ±1, the factorial points would range between -1 and +1 and the axial points would range between -1.4 and +1.4. In the corresponding inscribed design, the factorial points would range between -0.7 and +0.7 and the axial points would range between -1 and +1 (Garcia, 1995).

As a summary, the inscribed option is a convenient way to generate a rotatable CCD that enables to study the full ranges of the experiment variables while excluding nonallowable operating conditions at one or more of the extremes of the design region. Face-centered CCD, should be used whenever the region of operability encompasses the full region of interest as described by the variable ranges or when nonallowable operating conditions exist at only one of the extremes of the design region.

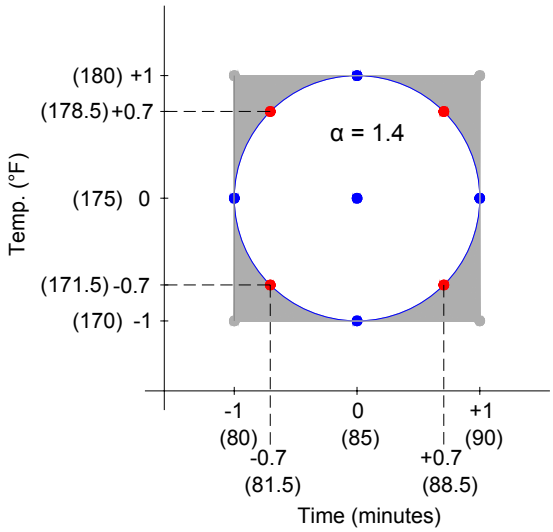

Figure 3.13. Two-variable inscribed CCD (Design Expert, 2003)

In rotatable and near-rotatable CCDs, each experiment variable is represented at five levels. The face-centered CCD requires only three levels of each experiment variable, making it the simplest variety of CCD to carry out as well as the least prone to corruption due to sources of experimental error associated with setup and operation. Compared to face-centered CCDs, rotatable or near-rotatable CCDs offer reduced prediction error for, and improved estimation of, quadratic (curvature) effects. However, given a reasonable magnitude of overall experimental error, say a 5-percent RSD, these benefits do not outweigh the added complexity of requiring each variable to be run at five levels (Design Expert, 2003).

3.2.2. Design Expert 6.0 Software Package

In this study, for the design of experiments (DOE), analysis and optimization of the process, version 6.0 of Design Expert software was used. Design-Expert software features and analyzes two-level factorial, general (multilevel) factorial, fractional factorial, Taguchi orthogonal arrays, Plackett-Burman, and combined mixture/process designs, as well as response surface methods (RSM) analysis for up to 10 process factors or 24 mixture components. Software offers powerful evaluation capability for generations of various statistical measures on the design matrix. The

analysis includes standard ANOVA as well as various diagnostic plots on the residuals. The regression engine handles up to a full cubic polynomial model with forward, backward or stepwise algorithms. The program generates 2D contour plots and rotatable 3D graphs. The program's numerical optimization function finds the most desirable factor settings for up to 12 responses simultaneously. Unique tools for generating and graphing propagation of error (POE) make it possible to reach goals for reducing variation (Design Expert, 2003).

Design of experiments (DOE) methods use probability and statistics to define the minimum number of experiments needed to identify significant cause-and-effect relationships between a given number of factors and one or more responses. Mathematically, DOE methods are well developed to identify efficient experimental designs. The three major components of DOE are design, analysis, and optimization. The strength of Design Expert 6.0 is the ease with which these tasks can be carried out and the usefulness of information provided in the displays. Principally, program provides many powerful statistical tools (Design Expert, 2003).

- Standard two-level full and fractional factorials (up to 256 runs) for testing up to 15 factors simultaneously, now also with minimum aberration blocking choices.
- General (multilevel) factorial designs (up to 32,000 runs) using factors with mixed levels.
- Taguchi orthogonal arrays.
- High-resolution irregular fractions, such as 4 factors in 12 runs.
- Placket-Burman designs for 11, 19, 23, 27 or 31 factors in 12, 20, 24, 28 or 32 runs respectively.
- Response Surface Method (RSM) designs, including central composite (small, face-centered, etc.), Box-Behnken (3-level), hybrid and D-optimal.
- Mixture designs, such as simplex-lattice, simplex-centroid screening (for up to 24 components) and D-optimal.
- Combined mixture and process designs.
- Ability to graph any two columns of data on the XY graph (this is a great way to view a blocked effect)

- Easy-to-use automatic or manual model reduction.
- Ability to easily analyze designs with botched or missing data.

3.2.2.1. Design of Experiments (DOE)

The underlying goal of this study is to determine the effect of TIG weld parameters on the weld bead geometry and quality of the welded joints. In this study, rotatable (circumscribed) central composite design of Response Surface Methodology was chosen for the design of experiments. For this purpose, initially upper and lower values of the experiment factors (process parameters), given in Table 3.5, were determined for the temperature and weld pool measurements in TIG welded AISI 304 1.6 mm stainless steel sheets.

Table 3.5. Lower and upper values of experiment factors

Factors	Units	Minimum value	Maximum value	Low level (-1)	High level (+1)
Welding speed	mm/s	1.0696	3.5546	1.69	2.93
Current	A	20	150	52	117
Gas flow rate	l/min	8	12	9	11
Gap	mm	1	4	1.75	3.25

Number of factors and their low level (-1) and high level (+1) values were then entered as seen in Figure 3.14.

Name	Units	Low	High
V	(mm/s)	1.69	2.93
I	(A)	52	117
F	(l/min)	9	11
G	(mm)	1.75	3.25

Figure 3.14. Design expert response surface design tab

As shown in Figure 3.15 at the bottom of the central composite design form type of the design were set to “Full” and value of blocks were entered 1 since all test

specimens were manufactured from the same block of brass and the number of experiments were given by software. The default selection of "Alpha" set at 2 in coded units is the axial distance from the center point and makes the design rotatable.

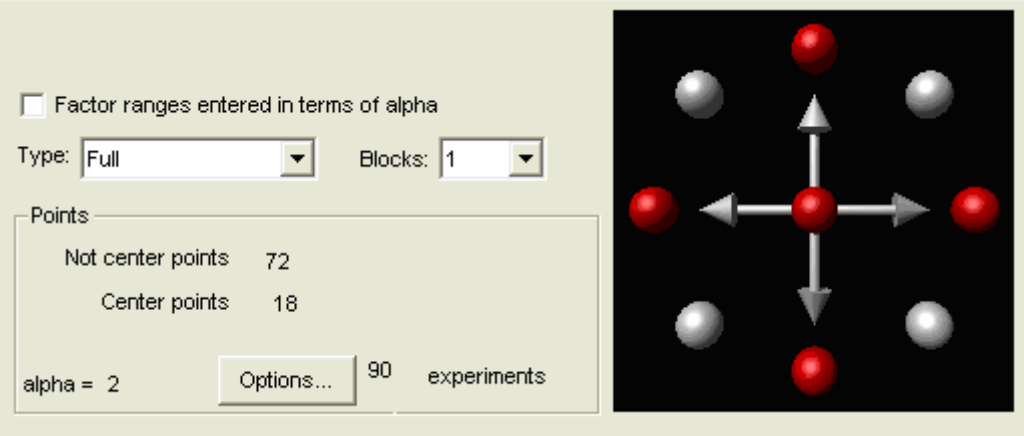

Figure 3.15. Central composite design dialog box

Then the program asks for the number of the responses and their definitions together with units as shown in Figure 3.16.

After identifying the names and units of the responses, to get the design layout of experiments, the continue button was pressed and then completed design layout was given by program as seen in Figure 3.17. The four columns on the left of the design layout identify the experimental runs. Experimental runs were randomized by Design Expert. Three columns at the right side of these columns identify the values of the process parameters at each experiment.

Responses: 6

Name	Units
TL	(kgf)
HAZ	(mm)
UW	(mm)
UH	(mm)
P	(mm)
AP	mm2

Figure 3.16. Completed response form

After completing experiments according to the design layout given by Design Expert, the values of responses were entered to the columns and then analysis and optimization of the results were carried out. Analysis and optimization of each response were made separately.

Std	Run	Block	Factor 1 A:V	Factor 2 B:I	Factor 3 C:F	Factor 4 D:G	Response 1 TL kgf	Response 2 HAZ mm	Response 3 UW mm	Response 4 UH mm	Response 5 P mm	Response 6 AP mm2
24	1	Block 1	2.31	85.00	10.00	2.50	1100	4.12	5.78	0.18	1.06	6.58
26	2	Block 1	1.53	10.00	10.00	2.50	750	2.55	4.22	0.09	0.75	4.6
10	3	Block 1	2.31	85.00	10.00	2.50	1100	4.14	5.82	0.19	1.06	6.55
38	4	Block 1	1.07	20.00	8.00	1.00	950	3.4	5.14	0.1	0.98	6.08
11	5	Block 1	1.07	20.00	8.00	4.00	1000	3.8	5.33	0.09	0.94	6.11
40	6	Block 1	0.61	30.00	10.00	2.50	1150	5.96	8.56	0.12	1.06	8.38
22	7	Block 1	2.31	85.00	10.00	2.50	1100	4.12	5.82	0.17	1.03	6.09
17	8	Block 1	1.53	30.00	10.00	0.50	1175	4.03	5.52	0.2	1.08	6.38
34	9	Block 1	1.53	30.00	6.00	2.50	1200	4.32	6.2	0.09	0.91	6.38
14	10	Block 1	1.07	40.00	8.00	4.00	1100	5.56	7.72	0.18	1.16	7.77
16	11	Block 1	2.45	30.00	10.00	2.50	900	3.1	5.63	0.08	0.97	5.43
1	12	Block 1	1.99	20.00	8.00	4.00	975	2.68	5.53	0.03	0.86	5.76
12	13	Block 1	1.53	30.00	14.00	2.50	1025	4	5.62	0.22	1.02	6.22
39	14	Block 1	1.07	40.00	12.00	1.00	1150	5.23	7.42	0.22	1.08	7.52
6	15	Block 1	1.07	40.00	8.00	1.00	1125	5.44	7.69	0.18	1.08	7.48
21	16	Block 1	2.31	85.00	10.00	2.50	1150	4.13	5.96	0.18	0.96	7
8	17	Block 1	1.99	20.00	12.00	1.00	1050	2.54	5.45	0.09	0.9	5.81
30	18	Block 1	1.53	30.00	10.00	5.50	875	4.43	6.5	0.18	0.78	6.78
31	19	Block 1	1.99	40.00	8.00	1.00	1150	4.66	7.01	0.12	1.02	7.09
13	20	Block 1	2.31	85.00	10.00	2.50	1050	4.14	5.78	0.16	1.06	6.23
37	21	Block 1	1.07	40.00	12.00	4.00	1125	5.53	7.89	0.2	1.12	7.82
29	22	Block 1	1.53	50.00	10.00	2.50	1250	5.32	7.23	0.28	1.1	7.11
27	23	Block 1	1.99	40.00	12.00	1.00	1025	4.73	7.02	0.16	1.05	7.12
7	24	Block 1	1.99	40.00	12.00	4.00	1050	4.89	7.22	0.13	0.98	7.23
23	25	Block 1	1.07	20.00	12.00	1.00	1000	3.26	5.03	0.15	0.95	6.01
19	26	Block 1	1.99	40.00	8.00	4.00	1000	4.94	7.28	0.13	1.03	7.26

Figure 3.17. Some part of design layout (Partially shown)

3.2.2.2. Optimization of TIG Welding Process Parameters

3.2.2.2.1. Selection of Function and Constraints

The objective functions selected for optimization were the TL, HAZ, UW, UH, P, AP. The area in which the solution for the function lies decreases as the number of constraints increases. Therefore, the mentioned parameters were given

as constraints in their equation form. In optimization, generally the constraints with their upper limits should be given in such a way that their value will be less than or equal to the related value. Also, the function, as well as the constraint functions, will usually be minimized or maximized.

To obtain a strong weld in any application, it is always desirable to have maximum tensile load, depth of penetration and area of penetration with minimum heat affected zone, upper width and upper height without sacrificing other bead qualities.

3.2.2.2.2. Optimization of the Objective Function

The main purpose of this study is to minimize and maximize the total weld quality characteristics mentioned above with their limits as constraints. The model is a nonlinear equation with constraints. The constrained optimization of a scalar function of several variables at an initial estimate, which is referred as "constrained nonlinear optimization," is mathematically stated as the following:

Maximize		Minimize
$TL(V,I,F,G)>X_1$		$HAZ(V,I,F,G)<X_2$
$P(V,I,F,G)>X_5$		$UW(V,I,F,G)<X_3$
$AP(V,I,F,G)>X_6$		$UH(V,I,F,G)<X_4$
subject to	and	subject to
$HAZ(V,I,F,G)<X_2$		$TL(V,I,F,G)>X_1$
$UW(V,I,F,G)<X_3$		$P(V,I,F,G)>X_5$
$UH(V,I,F,G)<X_4$		$AP(V,I,F,G)>X_6$

Where, X_n is the upper limit of each constraint.

The limits of the constraints were established by data obtained from the unconstrained optimization with a view that they should provide a feasible solution to the objective function. Also, the constraints were given in the form of equations. Several numerical methods are available for optimization of nonlinear equations with constraints.

3.2.2.2.3. Optimization with Design Expert 6.0

The optimization module in Design-Expert searches for a combination of factor levels that simultaneously satisfy the requirements placed on each of the responses and factors. Optimization of one response or the simultaneous optimization of multiple responses can be performed graphically or numerically.

Numerical Optimization optimizes any combination of one or more goals. The goals may apply to either factors or responses. The possible goals are: maximize, minimize, target, within range, none (for responses only) and set to an exact value (factors only). A minimum and a maximum level must be provided for each parameter included in the optimization. A weight can be assigned to a goal to adjust the shape of its particular desirability function. Desirability is an objective function that ranges from zero outside of the limits to one at the goal. A value of "1" represents the ideal case; a value of "0" indicates that one or more responses fall outside desirable limits. The numerical optimization finds a point that maximizes the desirability function. The characteristics of a goal may be altered by adjusting the weight or importance. For several responses and factors, all goals get combined into one desirability function. The default value of one creates a linear ramp function between the low value and the goal or the high value and the goal. Increased weight (up to 10) moves the result towards the goal. Reduced weight (down to 0.1) creates the opposite effect. The "importance" of a goal can be changed in relation to the other goals. The default is for all goals to be equally important at a setting of 3 pluses (+++). If it is necessary one goal to be most important, importance value can be changed to 5 pluses (+++++) (Design Expert, 2003).

For this study, the goals of the factors were obtained between their lower (-1) and upper (+1) values. Before the optimization module, the goals for the responses were selected according to the Table 3.6.

Table 3.6. Goal criteria appointment for the responses

Condition	Response	Goal
1	TL	maximize
	HAZ	in range
	UW	in range
	UH	in range
	P	maximize
	AP	in range
2	TL	maximize
	HAZ	minimize
	UW	minimize
	UH	in range
	P	maximize
	AP	in range
3	TL	maximize
	HAZ	minimize
	UW	minimize
	UH	minimize
	P	maximize
	AP	minimize

3.2.2.2.4. Optimization with Language for Interactive General Optimization (LINGO)

Language for Interactive General Optimization (LINGO) is a simple tool for utilizing the power of linear and nonlinear optimization to formulate large problems concisely, solve them, and analyze the solution. Optimization helps us to find the answer that yields the best result; attains the highest profit, output, or happiness; or the one that achieves the lowest cost, waste, or discomfort. Often these problems involve making the most efficient use of our resources including money, time, machinery, staff, inventory, and more. Optimization problems are often classified as linear or nonlinear, depending on whether the relationships in the problem are linear with respect to the variables.

In this study, since all of the response equations are nonlinear, programs were written using LINGO nonlinear programming technique (NLP) with Global (GO) optimization method to optimize the welding parameters and responses and to solve the nonlinear equations with constrained and unconstrained.

3.2.2.3. Weld Pool Shape Model and Prediction

3.2.2.3.1. Development of Mathematical Model and Prediction

Weld pool geometry which includes penetration, bead height and bead width are important physical properties of a weldment. It is said that the cooling rate of a weld can be predicted from the weld cross-sectional area and the arc-travel rate. The weld pool cross-sectional area together with its height and width affects the total shrinkage, which determines largely the residual stresses and thus the distortion. When welding brittle materials like cast iron, the shrinkage may give rise to crack formation.

Several welding parameters seem to affect the bead geometry. Since the weld bead results from the solidification of liquid metal, the interfacial tensions play a significant role in determining the ultimate bead geometry. Summarizing, it can be stated that the weld pool geometry and penetration affect the weldment characteristics and are dependent on a number of welding variables.

In the present investigation an attempt was made to study and predict some of the weldment characteristics such as upper height, upper width, heat affected zone, penetration and area of penetration, as it was affected by welding parameters like arc length, welding speed rate, welding current, gas flow rate and gap distance.

For a fairly limited number of weld trials it can be concluded that high correlations can be achieved by using prediction program when predicting bead width, bead height, penetration and area of penetration for single butt welds, 1.2 mm, in AISI 304 stainless steel.

Knowing the values of these shape parameters may be sufficient for certain applications, but they do not provide an actual predicted weld pool profile. Such a

predicted cross-sectional profile would allow for a visual means of assessing the accuracy in the profile predictions and also allow for a visual means of evaluating the effect of process parameters on the weld pool shape. To address this need for predicting the actual weld profiles, a program was written in MATLAB programming language to convert the predicted shape parameters into a weld profile.

3.2.2.3.2. Neural Network Analysis (NN) and Prediction

Neural networks are a highly flexible modeling tool with an ability to learn the relationships between input variables and output feature spaces. Neural Networks are superior to traditional approaches in modeling manufacturing processes with highly non-linear, strongly coupled characteristics. A network structure consists of layers of three types of nodes: input nodes, hidden nodes, and output nodes (George, 2001). Schematic diagram of neural network used in this thesis is shown in Figure 3.18.

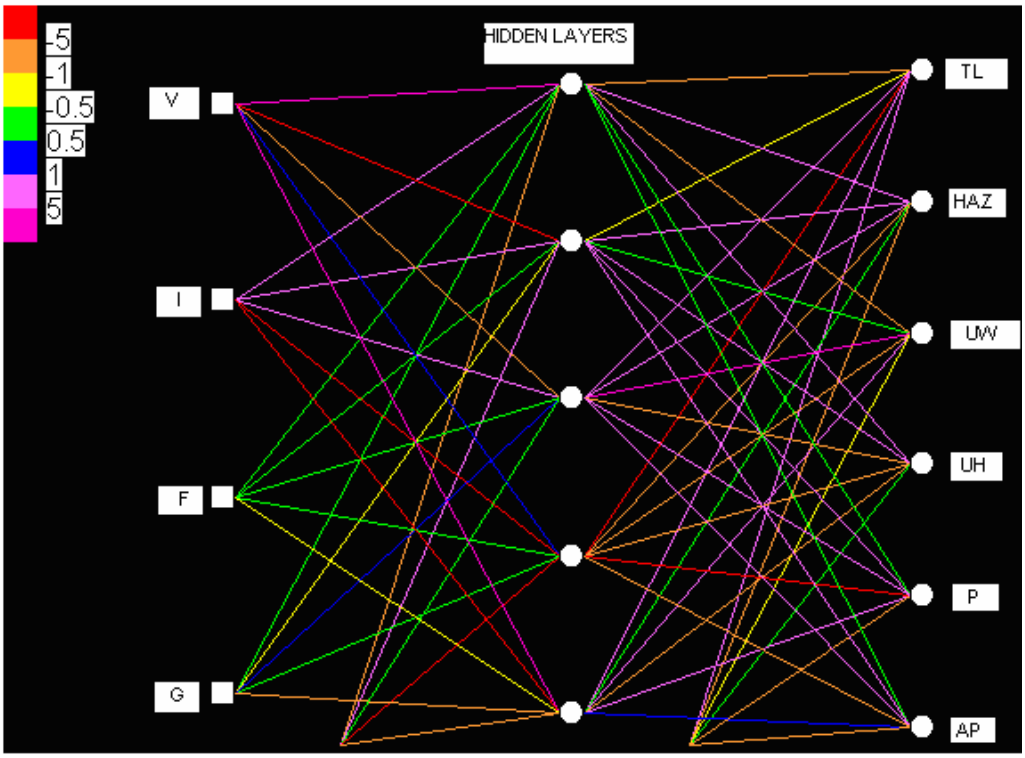

Figure 3.18. Configuration neural network used in the experiments

In principle, the hidden layer can consist of multiple sublayers. In this study five layers of hidden nodes were considered. The number of input and output nodes (four and six respectively in the schematic diagram of Figure 3.18) represent the input and output variables. When applied to the problem of weld pool shape prediction as a function of weld process variables, the four input nodes correspond to the four process variables (welding speed, arc current, gas flow rate, arc gap).

The number of hidden nodes is adjustable and is optimized for maximum predictive accuracy, as described below. The nodes are connected to each other so that the value of one node in one layer will affect the value of another node in the next higher layer. The relative influence that a given node has is specified by the "weight" that is assigned to each connection. The different weights for the node connections are shown schematically in Figure 3.18 by different line colors. The network is based on the following sequence of steps:

- convert input values V_i to normalized inputs I_i,
- sum all (weighted) input contributions to each hidden node S_j,
- convert each sum to a hidden node value H_j using a transfer function,
- sum all (weighted) hidden node contributions to each output node S_k,
- convert each sum to a normalized output value O_k using a transfer function,
- convert normalized outputs to real output values V_k.

The nomenclature for the above variables uses the following conventions. Real variables are denoted by V while neural network variables are given by I, H, or O, for the input, hidden, and output layers respectively; S denotes the summed input to a node. The subscripts i, j, and k refer to the individual nodes in the input, hidden, and output layers respectively. The summed input to a node is converted by a transfer function to an output value at the same node. In the present investigation, a sigmoidal function was used as the transfer function. The sigmoidal function at the hidden nodes would be:

$$H_i = [1 + \exp(-S_i)]^{-1} \tag{3.1}$$

This function has the property that for summed input values in the vicinity of zero, the transfer function behaves linearly with respect to the input, whereas at the extreme values of the summed input ($-\infty$ and $+\infty$) the transfer function approaches limiting values (0 and 1 respectively). As a result, unlike linear regression analyses, the neural network develops a non-linear relationship between the inputs and the outputs.

The neural network analysis involves training of the network using a training data set to learn the relationships between the inputs and the outputs and thereby achieve optimal accuracy. Training takes the form of adjusting the weights (connections) between the nodes in the different layers. Once the optimal neural network weights are determined, the process of calculating the outputs from a set of inputs is a rapid and trivial task and can be accomplished in a simple spreadsheet format, for example. Neural network training is carried out with the use of a training data set that contains sets of inputs and corresponding, experimentally determined outputs.

The neural network is developed by comparing the predicted output values with the actual outputs and, using an optimization scheme, adjusting the weights to minimize the prediction error. Through the learning process, which involves thousands of iterations, a complex relationship between the inputs and output can evolve, but it is based on the experimental data that were provided. Eventually, with minimal influence from the user, the network learns a scheme in which outputs are associated with the inputs.

In the present analysis of the thesis, a feed-forward network with a back-propagation network scheme was utilized. In this study to obtain an accurate model ninety train data and forty-seven test data were used to construct and optimize the model.

3.2.3. Temperature Distribution during Multipass TIG Welding

Due to the intense concentration of the heat in the heat source of TIG welding, the regions near the weld line undergo severe thermal cycles. The thermal

cycles cause non-uniform heating and cooling in the material, thus generating inhomogeneous plastic deformation, residual stresses, heterogen microstructure (especially when welding austenitic stainless steels), warped weld pool geometry. The presence of residual stresses can be detrimental to the performance of the welded products. Tensile residual stresses are generally detrimental, increasing the susceptibility of a weld to fatigue damage, stress corrosion cracking and fracture.

Stainless steel plates of different thicknesses are used in the industry and thicker plates are normally joined by multipass welding. In a multipass welding operation, the number of thermal cycles that the material undergoes during welding is same as the number of passes, and with each pass, the residual stress in the regions adjoining the weld, after each pass of welding.

Very limited experimental data is available regarding temperature distribution during multipass welding of plates in the literature. Experimental work was carried out to find out the temperature distribution during multipass welding of stainless steel plates.

Two plates of size 150x120 (thickness of 8 and 10 mm) which would form a single V-groove (60^o) joint between them were used during the experiment to make a finished weld pad. The two plates to be welded were tightened on the welding table with a clamping device to prevent any lack of rigidity under the welding torch which is connected to the welding robot.

Thermocouples were fixed in the middle region of the plate, at mid plane level. Temperatures were measured at different distances from the weld pad centre line on both the left and right side plates of the weld pad. The dimensional details of plates used in the experiments and the positions where thermocouples were fixed are shown in Figure 3.19.

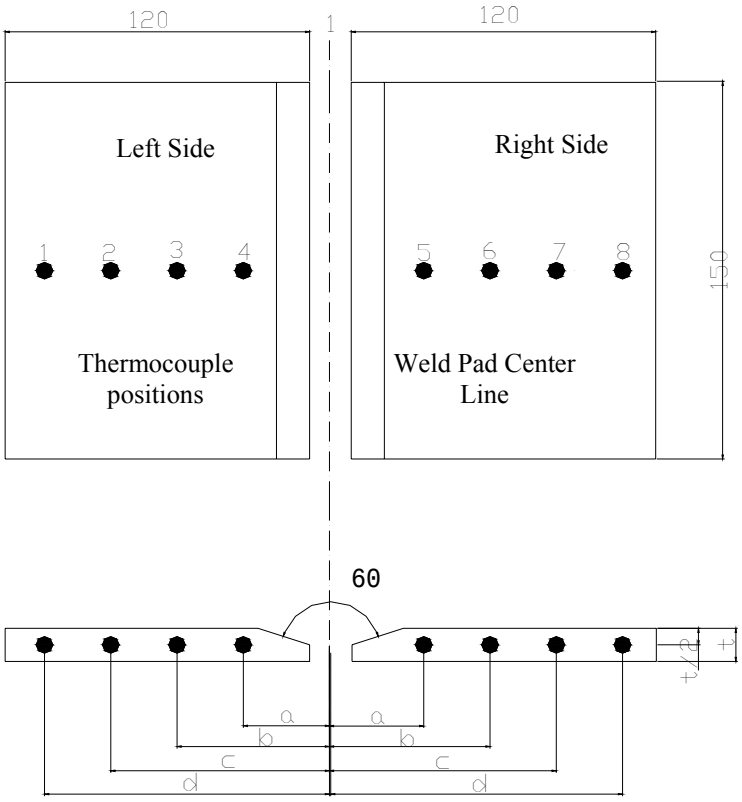

Thickness (mm)	a (mm)	b (mm)	c (mm)	d (mm)
8	12.5	22.5	32.5	42.5
10	12.5	22.5	32.5	42.5

Figure 3.19. Schematic representation of workpieces used for the temperature distribution experiments

The TIG welding parameters used in this study are listed in Table 3.7. The selection of welding parameters were made on the basis of the workpiece material to be welded and thickness.

99.99% pure argon gas was used as a shielding gas in the experiments with the given flow rate in Table below. A time gap of 2 min was waited between the each passes. This duration was utilized to ensure that the thermocouple connections to the workpieces were not disturbed during the welding.

Table 3.7. Welding parameters during multipass welding

Material (AISI)	Thickness (mm)	Current (A)	Electrode diameter (mm)	Gas flow (l/min)	Pass number	Welding speed (mm/s)
304L	8	160	2.4	12	1	1.785
					2	1.612
					3	1.538
					4	1.351
	10	180		15	1	1.923
					2	1.785
					3	1.612
					4	1.538
					5	1.351
					6	1.190
316L	8	160	2.4	12	1	1.785
					2	1.612
					3	1.538
					4	1.351
	10	180		15	1	1.923
					2	1.785
					3	1.612
					4	1.538
					5	1.351
					6	1.190

3.2.4. Effect of Electrode Tip Angle on Penetration and Weld Structure

The shape of the tungsten electrode tip is an important process variable in TIG welding. Tungsten electrode may be used with variety of tip preparations. For DC welding, thoriated, ceriated, or lanthanated tungsten electrodes are usually used. Regardless of the electrode tip geometry selected, it is important that a consistent electrode geometry should be used once a welding procedure is established. Changes in electrode geometry can significantly influence the weld bead shape and size; therefore, electrode tip configuration is a welding variable that should be studied during the welding procedure development.

In this study DCEN type polarity and EWTh-2 thoriated tungsten electrode with various tip angles, θ, (0^o or 180^o, 15^o, 30^o, 45^o, 60^o, 75^o, 90^o) and butt joint were used to study the effect of tip geometry on the penetration and weld structure of the

TIG welded 4 mm AISI 304 joints. The electrode geometry used in the experiments with varying tip shape is shown in the Figure 3.20.

Figure 3.20. Electrode geometry and tip angles (θ) used in the experiments

The welding parameters used to examine the effect of electrode tip geometry on the microhardness of welded joints are shown in the Table 3.8.

Table 3.8. Welding parameters used to investigate the effect of electrode tip angle on microhardness

Material (AISI)	Thickness (mm)	Electrode diameter (mm)	Welding speed (mm/s)	Current (A)	Gap Distance (mm)	Gas flow (l/min)
304	4	2.4	1.923	80	2	8

3.2.5. Effect of TIG Welding Process Parameters on Microstructure Microhardness and Weld Pool Shape

The primary variables in TIG welding as explained in previous sections are; arc gap, welding current, travel speed, and shielding gas flow rate. The amount of energy produced by the arc is proportional to the current and arc gap (voltage). The amount transferred per unit length of weld is inversely proportional to the travel speed. However, because all of these variables interact strongly, it is impossible to treat them as truly independent variables when establishing welding procedures for fabricating specific joints.

Series of experiments under the different welding conditions were established in order to investigate the effect of welding parameters on the weld bead geometry, microstructure, and microhardness. The electrode material, tip geometry and

thickness were kept constant as EWTh-2 thoriated, 45°, and 2.4 mm respectively, whereas the others were altered in accordance with the Table 3.9 given below.

Table 3.9. Process parameters and their levels

Material (AISI)	Thickness (mm)	Symbol	Process Parameter	Unit	Level 1	Level 2	Level 3	Level 4
304	4 mm	A	Welding Speed	mm/s	1.612	1.785	1.923	2.040
		B	Welding Current	A	60	70	80	90
		C	Flow Rate	l/min	8	10	12	14
		D	Arc Gap	mm	1	2	3	4

Sixteen experiments are conducted to study the entire welding parameter space. The experimental layout for the welding process parameters using the L_{16} array is shown in Table 3.10.

Table 3.10. Experimental layout

Experiment number	Process Parameter Level			
	A Welding Speed	B Welding Current	C Flow Rate	D Arc Gap
1	1	3	1	2
2	2	3	1	2
3	3	3	1	2
4	4	3	1	2
5	3	1	1	2
6	3	2	1	2
7	3	3	1	2
8	3	4	1	2
9	3	3	1	2
10	3	3	2	2
11	3	3	3	2
12	3	3	4	2
13	3	3	1	1
14	3	3	1	2
15	3	3	1	3
16	3	3	1	4

3.2.6. Tension Test

A number of mechanical properties are used to characterize welds, including strength, ductility, hardness and toughness. In general, the same samples and procedures are used in other areas of metallurgy. However, a prominent concern

regarding the mechanical performance of welds is the direct comparison with base material. The goal is to ensure that the weld is not the weakest component of a structure, or if it is, to compensate for this in the design.

The tension testing of welds is somewhat more involved than testing base metal because a weld test section is heterogeneous; containing weld metal, heat affected zone, and unaffected base metal. To obtain an accurate assessment of the strength and ductility of welds, several different specimens and orientations may be used. These are; All-Weld-Metal Test, Transverse Weld Test, Longitudinal Weld Test.

In this section of the study, tensile test specimens were taken from the weld bead according to the transverse tensile test method. Moreover, tensile test specimens were prepared in such a way that the weld zones were centered in the gage length. At the same time, heat affected zone and was placed in the gage length perpendicular to the weld. The tensile test specimens were prepared in accordance with the TS 287 EN 895 Standard as shown in Figure 3.21.

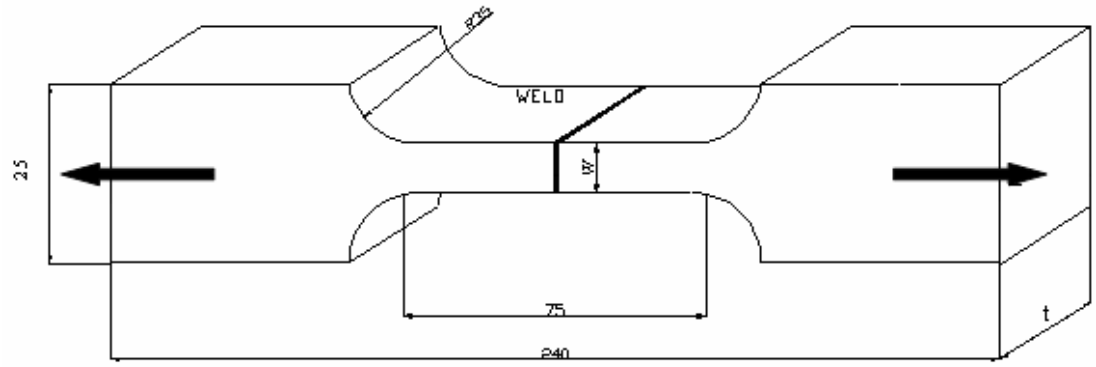

Material (AISI)	Thickness t, (mm)	Width w, (mm)
304	1.2	16
304L	5	12

Figure 3.21. Tensile test loading condition of the welded samples

The welding parameters used in tensile test study are tabulated as shown in Table 3.11. To examine the each welding parameter on the Tensile load of the joints, workpiece and electrode material, and joint type (60^o V-groove joint) kept constant

whereas the others (welding current, welding speed, gap distance or arc length, gas flow rate, electrode tip angle) were changed. For each level of process parameters were matched with each other and then the samples were welded under two passes.

Table 3.11. Welding parameters for tensile test measurements

Material (AISI)	Thickness (mm)	Process Parameter	Unit	Level 1	Level 2	Level 3	Level 4	Level 5	Level 6	Level 7
304L	5 mm	Welding Speed	mm/s	1.53	1.785	2.040	2.380	2.63	--	--
		Welding Current	A	50	60	70	80	90	--	--
		Flow Rate	l/min	4	6	8	10	12	--	--
		Arc Gap	mm	1	2	3	4	5	--	--
		Tip Angle	Degree	0^o	15^o	30^o	45^o	60^o	75^o	90^o

4. RESULTS AND DISCUSSION

As a part of the study mathematical models were developed to relate the process parameters and then the weld quality responses have been analyzed using the developed models for TIG welding of 1.2 mm AISI 304 stainless steel.

The optimizations of the quality responses were carried out using the optimization module of Design Expert 6.0 software and Language for Interactive General Optimization (LINGO). The mathematical models thus developed for optimization are also helpful in predicting the weld bead quality parameters and in setting process parameters at optimum values to achieve the desirable weld quality at a relatively low cost with a high degree of repeatability and increased production rate.

The research works of this thesis were carried out in the following steps:

- ✓ Identifying the important process control variables,
- ✓ Developing the design matrix,
- ✓ Conducting the experiments as per the design matrix,
- ✓ Recording the responses,
- ✓ Developing the mathematical models,
- ✓ Calculating the coefficients of the polynomials,
- ✓ Arriving at the final mathematical models,
- ✓ Checking the adequacy of the models developed and analysis of the results,
- ✓ Conducting the conformity test,
- ✓ Presenting the direct and interaction effects of different process parameters on bead geometry graphically,
- ✓ Analyzing the results.

The independently controllable process parameters affecting weld pool geometry and the quality of the weld pool were welding speed (V), welding current (I), shielding gas flow rate (F), gap distance or arc length (G). Also, quality

responses or outputs were defined as tensile load (TL), heat affected zone (HAZ), upper width (UW), upper height (UH), penetration (P) and area of penetration (AP).

Process parameters values (V, I, F, G) are defined by Design Expert 6.0 software which was used for the design of experiments. Rotatable (circumscribed) central composite design (CCD) of Response Surface Methodology (RSM) was chosen for the design of experiments.

Different experimental conditions for the ranges of welding speed, welding current, gas flow rate and arc gap were defined by software. Each set of experiment which was carried out by two replications was randomized. The experimental conditions were collected in the program to develop design matrix as given in Table 4.1.

After completing the development of design matrix, the experiments were conducted according to the design matrix and the welding responses were recorded as given in Table 4.1.

Table 4.1. Design matrix and measured values for welding responses

Run	Process Parameters				Welding Responses					
	V (mm/s)	I A	F (I/min)	G (mm)	TL (kgf)	HAZ (mm)	UW (mm)	UH (mm)	P (mm)	AP (mm^2)
1	2.3101	85	10	2.5	1100	4.12	5.78	0.18	1.06	6.58
2	1.5311	10	10	2.5	750	2.55	4.22	0.09	0.75	4.6
3	2.3101	85	10	2.5	1100	4.14	5.82	0.19	1.06	6.55
4	1.0696	20	8	1	950	3.40	5.14	0.1	0.98	6.08
5	1.0696	20	8	4	1000	3.80	5.33	0.09	0.94	6.11
6	0.6081	30	10	2.5	1150	5.96	8.56	0.12	1.06	8.38
7	2.3101	85	10	2.5	1100	4.12	5.82	0.17	1.03	6.09
8	1.5311	30	10	0.5	1175	4.03	5.52	0.2	1.08	6.38
9	1.5311	30	6	2.5	1200	4.32	6.2	0.09	0.91	6.38
10	1.0696	40	8	4	1100	5.56	7.72	0.18	1.16	7.77
11	2.4541	30	10	2.5	900	3.10	5.63	0.08	0.97	5.43
12	1.9926	20	8	4	975	2.68	5.53	0.03	0.86	5.76
13	1.5311	30	14	2.5	1025	4.00	5.62	0.22	1.02	6.22
14	1.0696	40	12	1	1150	5.23	7.42	0.22	1.08	7.52
15	1.0696	40	8	1	1125	5.44	7.69	0.18	1.08	7.48
16	2.3101	85	10	2.5	1150	4.13	5.96	0.18	0.96	7.00
17	1.9926	20	12	1	1050	2.54	5.45	0.09	0.90	5.81
18	1.5311	30	10	5.5	875	4.43	6.50	0.18	0.78	6.78
19	1.9926	40	8	1	1150	4.66	7.01	0.12	1.02	7.09
20	2.3101	85	10	2.5	1050	4.14	5.78	0.16	1.06	6.23
21	1.0696	40	12	4	1125	5.53	7.89	0.20	1.12	7.82
22	1.5311	50	10	2.5	1250	5.32	7.23	0.28	1.10	7.11
23	1.9926	40	12	1	1025	4.73	7.02	0.16	1.05	7.12
24	1.9926	40	12	4	1050	4.89	7.22	0.13	0.98	7.23

Continue of Table 4.1

Run	Process Parameters				Welding Responses					
	V (mm/s)	I A	F (I/min)	G (mm)	TL (kgf)	HAZ (mm)	UW (mm)	UH (mm)	P (mm)	AP (mm^2)
25	1.0696	20	12	1	1000	3.26	5.03	0.15	0.95	6.01
26	1.9926	40	8	4	1000	4.94	7.28	0.13	1.03	7.26
27	2.3101	85	10	2.5	1100	4.13	5.79	0.18	0.96	5.18
28	1.0696	20	12	4	1025	3.53	5.22	0.19	0.90	5.98
29	1.9926	20	8	1	1100	2.55	5.48	0.09	0.92	5.53
30	1.9926	20	12	4	1000	2.78	5.64	0.10	0.89	5.63
31	1.9926	40	8	4	1230	3.79	9.08	0.09	0.94	7.87
32	2.5606	70	8	1	1227	4.63	9.02	0.18	1.17	8.80
33	1.9926	70	12	1	1265	5.10	8.12	0.11	1.24	8.60
34	2.2766	55	14	2.5	1287	4.45	7.12	0.08	1.23	7.10
35	2.2766	55	6	2.5	1237	4.43	7.88	0.06	1.18	7.03
36	2.3101	85	10	2.5	1375	4.45	7.98	0.07	1.25	7.97
37	2.2766	55	10	5.5	1245	4.52	8.53	0.15	0.98	4.88
38	2.5606	70	12	1	1265	4.60	8.26	0.16	1.20	7.20
39	2.8446	55	10	2.5	1230	3.20	7.86	0.09	1.06	5.54
40	2.5606	70	12	4	1212	4.78	8.39	0.17	1.00	8.00
41	2.2766	55	10	0.5	1320	4.39	6.36	0.14	1.11	5.80
42	1.9926	40	8	1	1275	3.35	8.36	0.10	1.13	8.30
43	2.2766	25	10	2.5	1050	2.54	5.90	0.02	0.80	5.30
44	2.3101	85	10	2.5	1380	4.45	7.99	0.08	1.25	7.98
45	2.3101	85	10	2.5	1375	4.44	7.98	0.08	1.23	7.95
46	2.3101	85	10	2.5	1375	4.45	8.00	0.07	1.25	7.98
47	2.5606	40	12	1	1300	2.98	5.98	0.04	0.95	5.02
48	2.5606	40	12	4	1235	3.06	6.54	0.08	0.87	5.63
49	2.5606	40	8	1	1300	2.99	5.90	0.03	0.93	5.42
50	1.9926	40	12	4	1275	3.6	7.72	0.10	0.95	6.56
51	2.3101	85	10	2.5	1375	4.44	7.98	0.08	1.25	7.98
52	2.5606	40	8	4	1225	3.08	6.42	0.04	0.89	5.48
53	2.3101	85	10	2.5	1380	4.46	7.98	0.08	1.22	7.99
54	2.5606	70	8	4	1325	4.79	8.45	0.15	1.14	7.20
55	2.2766	85	10	2.5	1300	5.61	9.51	0.25	1.14	9.19
56	1.9926	70	8	4	1250	5.35	8.96	0.14	1.19	9.06
57	1.7086	55	10	2.5	1325	5.00	8.84	0.08	1.15	8.98
58	1.9926	40	12	1	1280	3.40	7.17	0.09	1.10	7.90
59	1.9926	70	8	1	1300	5.10	8.57	0.17	1.27	7.34
60	1.9926	70	12	4	1260	5.30	8.63	0.12	1.17	8.55
61	2.3101	85	10	2.5	1000	6.5	7.66	0.11	1.18	7.56
62	4.0516	110	10	2.5	1150	4.82	7.21	0.15	1.10	7.63
63	2.3101	85	10	2.5	1020	6.44	7.66	0.11	1.18	7.56
64	3.0576	110	10	0.5	1030	5.2	6.86	0.19	1.21	7.62
65	2.5606	150	12	4	1050	7.8	10.56	0.18	1.21	9.69
66	2.3101	85	10	2.5	1100	6.43	7.66	0.11	1.18	7.56
67	3.5546	150	8	4	1000	6.8	8.87	0.08	1.18	6.98
68	3.0576	190	10	2.5	980	8.2	11.12	0.22	1.22	10.48
69	2.5606	70	8	4	1385	4.79	7.22	0.15	1.14	7.20
70	2.5606	150	12	1	1100	7.5	9.73	0.18	1.18	9.78
71	2.5606	70	8	1	1375	4.63	6.98	0.18	1.22	8.80
72	3.0576	30	10	2.5	900	3.8	4.35	0.09	0.89	5.23
73	3.5546	70	8	4	980	4.6	5.78	0.15	0.98	5.89
74	3.5546	70	12	4	950	4.4	5.75	0.18	0.99	5.78
75	2.3101	85	10	2.5	1000	6.52	7.66	0.11	1.18	7.56

Continue of Table 4.1

Run	Process Parameters				Welding Responses					
	V (mm/s)	I A	F (I/min)	G (mm)	TL (kgf)	HAZ (mm)	UW (mm)	UH (mm)	P (mm)	AP (mm^2)
76	2.5606	70	12	1	1385	4.6	6.86	0.16	1.20	7.20
77	3.5546	150	12	4	975	6.5	8.78	0.09	1.19	6.86
78	2.5606	150	8	4	950	7.9	10.48	0.20	1.16	9.79
79	3.5546	150	8	1	1050	6.35	8.56	0.10	1.20	6.73
80	2.5606	150	8	1	1000	7.4	9.86	0.19	1.19	9.72
81	3.0576	110	6	2.5	1020	6.7	7.72	0.10	1.16	7.39
82	3.5546	70	12	1	1000	4.1	5.63	0.10	1.10	5.56
83	3.0576	110	10	5.5	975	7.2	8.23	0.09	0.98	6.98
84	3.5546	150	12	1	1050	6.3	8.5	0.09	1.21	6.79
85	3.0576	110	14	2.5	1020	6.2	7.21	0.14	1.19	7.67
86	2.3101	85	10	2.5	1050	6.5	7.66	0.11	1.18	7.56
87	2.5606	70	12	4	1385	4.78	7.23	0.17	1.00	7.98
88	2.0636	110	10	2.5	1250	6.8	9.93	0.18	1.21	7.88
89	3.5546	70	8	1	950	4.3	5.68	0.08	1.18	5.63
90	2.3101	85	10	2.5	1050	6.45	7.66	0.11	1.18	7.56

4.1. Direct Effects of Welding Parameters

4.1.1. Welding Speed

Welding speed is the linear rate at which the arc is moved along the weld joint. The velocity of the welding torch affects not only the rate of solidification, but also the shape of the weld pool and the propensity to develop centerline hot cracks. The shape of the weld pool is dictated by the velocity at which the welding torch moves and by the rate at which heat can be removed at the solid-liquid interface. To keep a constant shape, the rate of new melting must be exactly balanced by the solidification rate.

High welding speed has a negative effect on all the pool responses. This is because, when V increases, the welding torch travels at a greater speed over the base metal, resulting in a lower metal deposition rate on the joint. However, further increase in welding speed imparts less heat input to the base metal. Thus, melting of the base metal first increases and then decreases with increasing speed. As the speed is increased further, there is tendency toward undercutting along the edges of the weld pool, because there is insufficient melted metal to fill the path.

4.1.1.1. Effect of Welding Speed on Tensile Load

Both welding speed and current influence the heat transfer to the parent metal and hence size and shape of the melt region. The size and, especially, the shape of the melt region in the TIG welding affect the tensile load and therefore, the structure, penetration depth and quality of the resultant weld.

Arc penetration is usually inversely proportional to welding speed. At high welding speeds due to the insufficient penetration, low tensile load was observed. However, excessive slow welding speeds caused excessive penetration and flat weld bead. As given in Figure 4.1, the maximum transverse tensile load of 1265 kgf was obtained at 2.31 mm/s welding speed. Further increase in welding speed caused sudden decrease in TL due to the insufficient heat input caused low deposition and penetration.

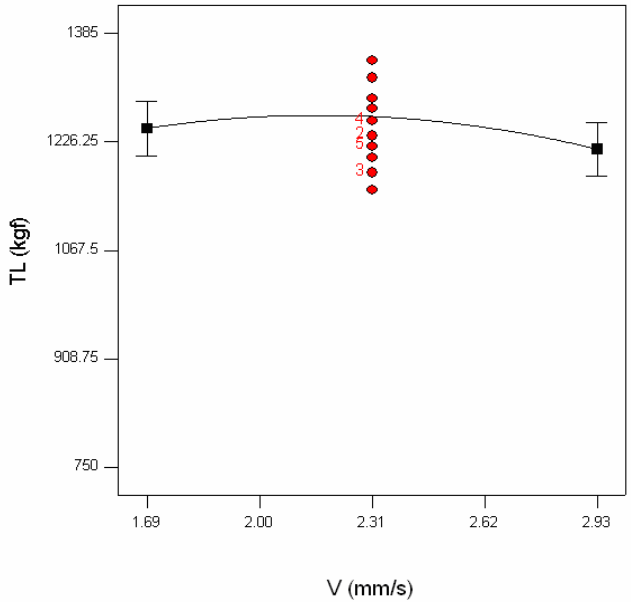

Figure 4.1. Effect of welding speed on tensile load required to cause fracture for 19.2 mm^2 area

4.1.1.2. Effect of Welding Speed on Heat Affected Zone

Welding velocity and hence heat flow during welding strongly affects the width of the heat affected zone by raising the temperature of the parent metal adjacent to the fusion boundary and, therefore, the microstructure and properties of the resultant weld is changed. They all affect the mechanical properties of the resultant joint either by causing a loss of tensile and impact strength, an increase in hardness, or the formation of cracks.

As shown in Figure 4.2, when the welding speed was increased the width of the heat affected zone decreased. At low welding speed of 1.07 mm/s, high heat affected zone of 6.51 mm was obtained due to the high heat input rate. Also, at high welding speed of 3.55 mm/s low heat affected zone of 4.83 mm was observed due to the low heat input rate.

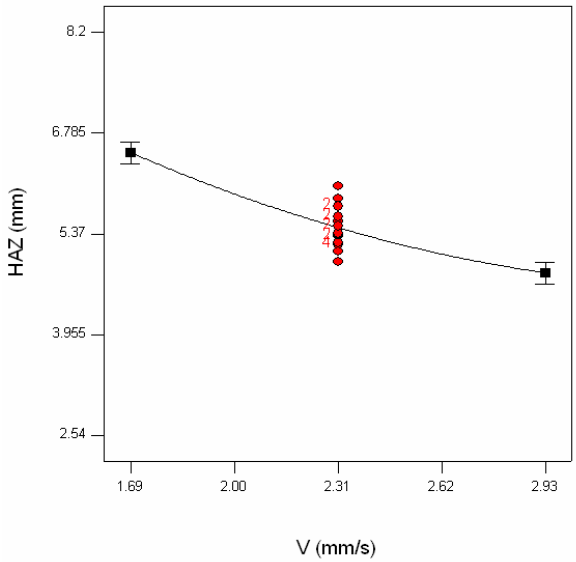

Figure 4.2. Effect of welding speed on heat affected zone

4.1.1.3. Effect of Welding Speed on Upper Width

Both welding speed and current are directly responsible for any change in the upper width. Their effects are the same as the heat affected zone. When heat affected zone increases the upper width also increases. As shown in Figure 4.3,

increasing welding speed decreased the upper height due to the low deposition effect of insufficient heat input. The minimum 7.85 mm and maximum 9.51 mm upper width values were obtained at 3.55 and 1.07 mm/s welding speeds respectively.

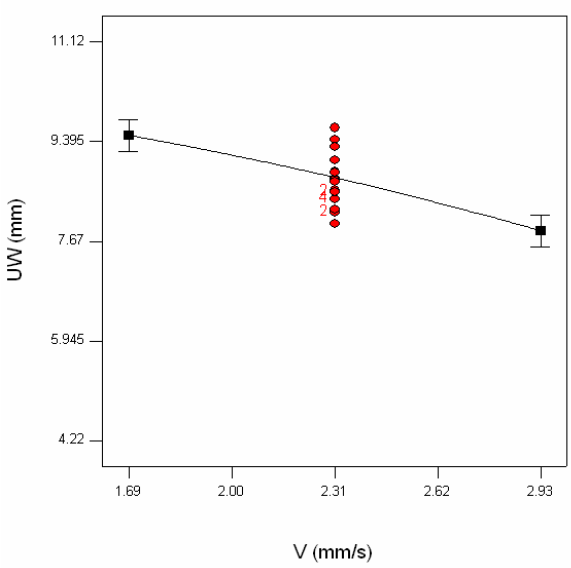

Figure 4.3. Effect of welding speed on upper width

4.1.1.4. Effect of Welding Speed on Upper Height

Also, another negative effect of high welding speed is lowering the upper height. Increasing welding speed decreased the upper height due to insufficient melting rate of the base metal. As indicated in Figure 4.4, the minimum 0.10 mm and maximum 0.21 mm upper height values were obtained at 3.55 mm/s and 1.07 mm/s welding speeds respectively.

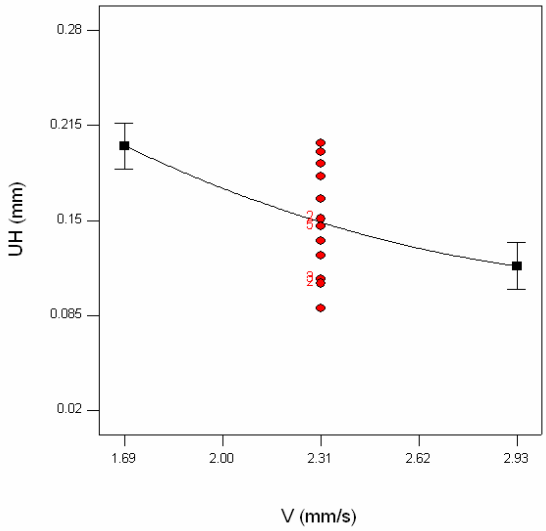

Figure 4.4. Effect of welding speed on upper height

4.1.1.5. Effect of Welding Speed on Penetration

From the view point of penetration, melting rate becomes significant. Increasing welding speed decreased the penetration. Maximum penetration was obtained at minimum welding speed. As shown in Figure 4.5, minimum 1.14 mm and maximum 1.22 mm P values were obtained at 3.55 mm/s and 1.07 mm/s welding speeds respectively.

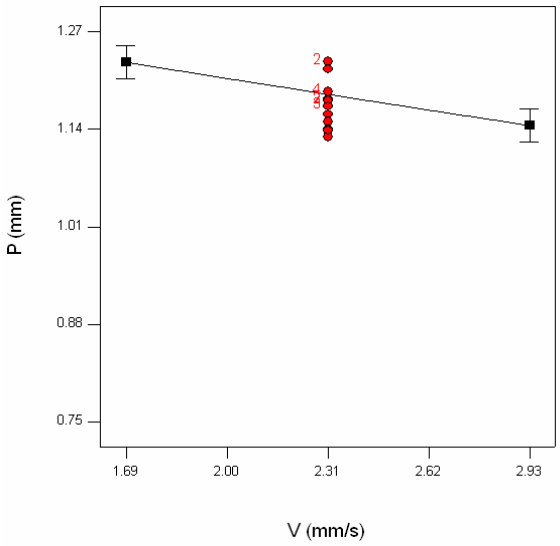

Figure 4.5. Effect of welding speed on penetration

4.1.1.6. Effect of Welding Speed on Area of Penetration

Area of penetration is directly related to the depth and width of the penetration. As the welding speed increased the area of penetration decreased gradually because of the decreased penetration and width of the penetration. As illustrated in Figure 4.6, the maximum value of 10.73 mm^2 and minimum value of 6.45 mm^2 were obtained for AP at 1.07 mm/s and 3.55 mm/s welding speeds.

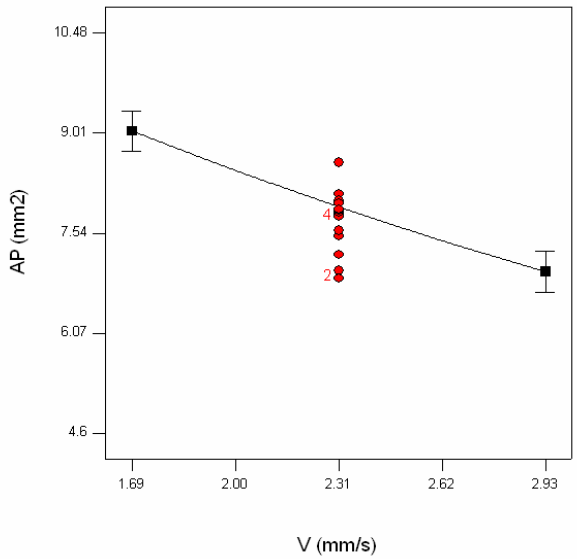

Figure 4.6. Effect of welding speed on area of penetration

4.1.2. Welding Current

Current is one of the most important operating conditions to control in any welding operations since a change in current affects the quality of welding. The magnitude of the current has a great influence on the tensile load and quality of the TIG welded joints. According to the heat input formula ($H = \frac{EI}{1000V}$), any change in current strongly affects the heat input rate and deposition rate. Increasing current increases the heat input which in turn increases the melting rate of the base metal, as a consequence of which weld bead width and heat affected zone is increased, a fact which is also true for the behavior of weld width with increasing welding current.

Because of the intense heat of the arc some erosion of the electrode will occur. This eroded metal is transferred across the arc. Slow erosion of the electrode results in limited tungsten inclusions in the weld which sometimes may not be acceptable. Because, the tungsten inclusions are hard spots that cause stresses to concentrate, possibly resulting in weld failure. Therefore, the selection of the optimum current depends on the material type, thickness and welding speed.

4.1.2.1. Effect of Welding Current on Tensile Load

As shown in Figure 4.7, increasing current up to 85 A, caused an increase in tensile load up to 1300 kgf. However, further increase in current (over 85A) reduced the tensile load due to the unsuitable welding speed and current combination caused undercutting along the edges of the weld bead. 1199 kgf and 1225 kgf tensile load values were obtained at minimum 20 A and maximum 150 A respectively.

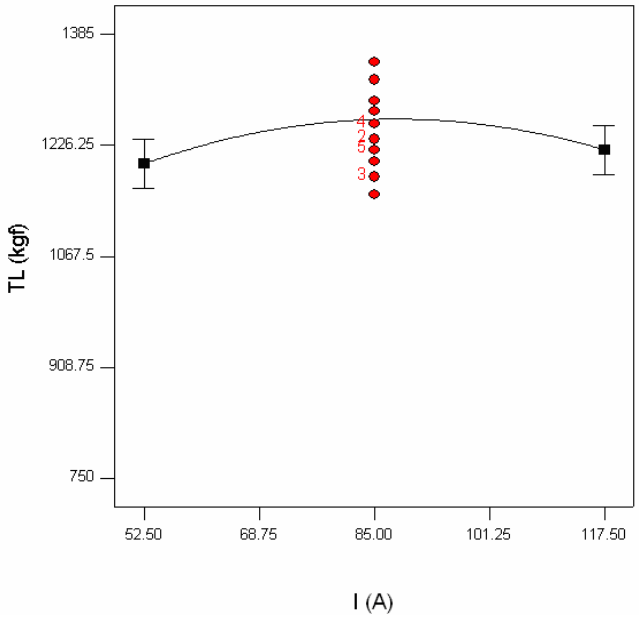

Figure 4.7. Effect of welding current on tensile load required to cause fracture for 19.2 mm^2 area

4.1.2.2. Effect of Welding Current on Heat Affected Zone

As the term heat affected zone indicates that, a region where the peak temperatures are low (according to the fusion zone) to cause melting but high enough to cause the microstructure and properties of the materials to change significantly. In welding of stainless steels, it is required using a low welding current setting with faster welding speed combination in order to obtain a heat affected zone as small as possible. Because, some stainless steels are subject to carbide precipitation. Carbide precipitation, the combining of carbon with chromium, occurs in some stainless steels when they are kept at a temperature between 625 ^{o}C and 815 ^{o}C for a long time.

Heat formula given above emphasizes that increasing welding current causes high heat input to the base metal. High welding current creates higher heat affected zone. This is unacceptable negative condition for welding of stainless steels. Therefore, the current and welding speed should be in a combination which produces narrow heat affected zone. In optimization section of the study, an attempt was made to determine the best welding parameter combination to optimize the welding responses (TL, HAZ, UW, UH, P, AP).

Figure 4.8 shows the effect of welding current on heat affected zone. Increasing current from minimum 20 A to maximum 150 A caused 3.98 mm and 6.86 mm heat affected zones respectively.

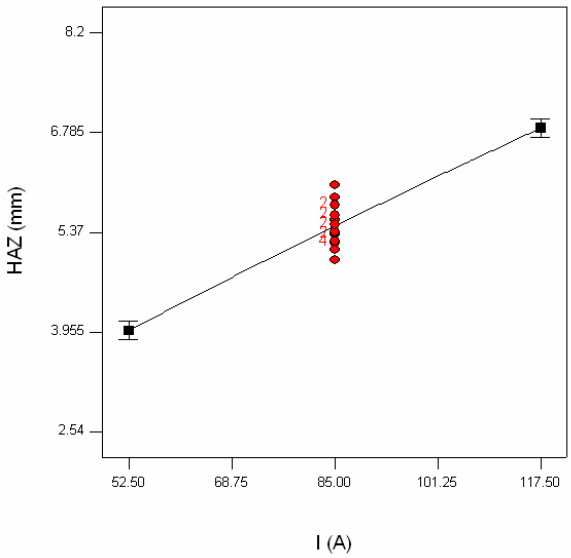

Figure 4.8. Effect of welding current on heat affected zone

4.1.2.3. Effect of Welding Current on Upper Width

Here, the same effect of current was observed for the upper width. Any change in current greatly influenced the upper width. High heat input with unsuitable welding speed increased the upper width. As shown in Figure 4.9, increasing current from minimum to maximum value increased the upper width from 7.20 mm to 10.02 mm.

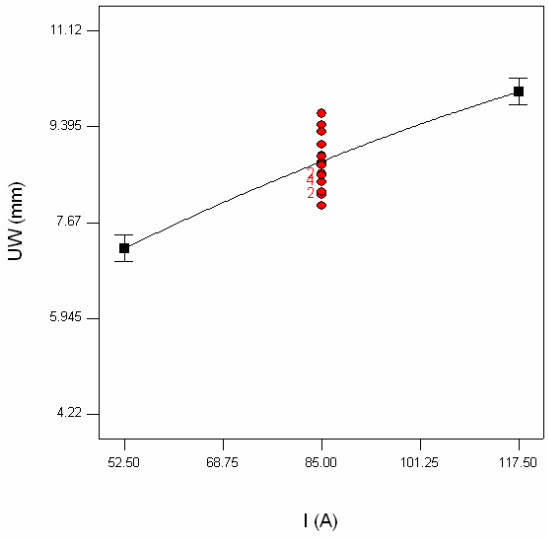

Figure 4.9. Effect of welding current on upper width

4.1.2.4. Effect of Welding Current on Upper Height

Figure 4.10 shows the effect of current on upper height. Upper height value greatly influenced with increasing current. Increasing current from minimum to maximum value increased upper height from 0.11 mm to 0.18 mm.

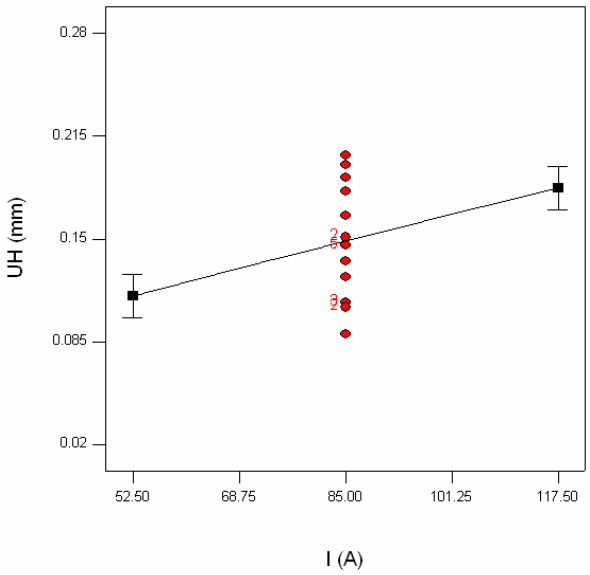

Figure 4.10. Effect of welding current on upper height

4.1.2.5. Effect of Welding Current on Penetration

Weld penetration is the distance that the fusion line extends below the surface of the material being welded. As explained earlier according to the heat input formula, welding current is of primary importance to generate sufficient heat to melt the base metal and hence control of penetration. An increase or decrease in the current will increase or decrease the weld penetration respectively.

As Figure 4.11 illustrates, weld penetration is directly related to welding current. Increasing welding current to from 20 to 85 A increased the penetration from 1.02 mm to 1.22 mm respectively. Further increase caused a reduction in penetration due to the high heat input under constant speed formed undercutting along the weld pad.

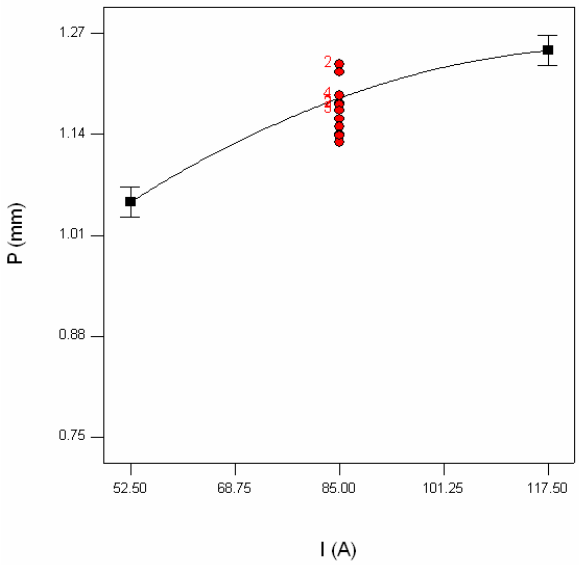

Figure 4.11. Effect of welding current on penetration

4.1.2.6. Effect of Welding Current on Area of Penetration

Welding parameters (especially welding speed and current) which affect the penetration and upper width also directly affect the area of penetration. As shown in Figure 4.12, increasing the welding current from minimum to maximum increased the area of penetration from 6.65 mm^2 to 9.13 mm^2 respectively.

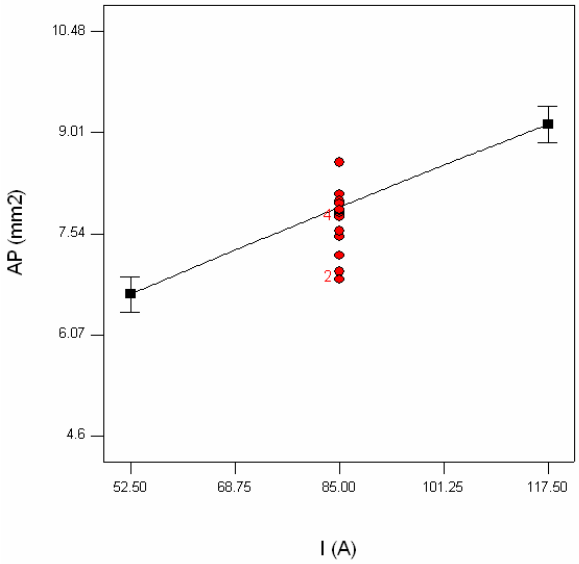

Figure 4.12. Effect of welding current on area of penetration

4.1.3. Gas Flow Rate

In TIG welding, shielding gas plays an important role. During TIG welding, the weld pool, the arc, the tungsten electrode and the heated section of the workpieces should be protected from the atmospheric contamination by a shielding gas argon or helium or mixture of them.

Composition of a shielding mixture in arc welding depends mostly on the kind of material to be welded. The selection of the shielding gas should, by all means, take into account chemical–metallurgical processes between the gases and the molten pool that occur during welding. Density of the shielding gas has an important influence on the efficiency of shielding the arc and the weld pool against the ambient atmosphere. The values indicating relative density of the shielding gas with regard to air are of primary importance. Argon and carbon dioxide are gases having by far the highest density and therefore, form an efficient gas shielding around the arc.

Mainly, the shielding gas is delivered around the tungsten electrode through a concentric nozzle. Shielding gas flow requirements are based on cup or nozzle size, weld pool size, and air movement. In general, the flow rate increases in proportion to the cross-sectional area at the nozzle. So nozzle size must be adequate to cover the welding area. The nozzle diameter is selected to suit the size of the weld pool and the reactivity of metal to be welded. A small nozzle assist to maintain a more stable and a positive arc, to permit welding in more restricted areas and to have a better vision of the weld. Whereas, larger nozzles provide better shielding gas blankets at slower gas discharge rates than smaller nozzles.

The weld quality can be adversely affected by improper gas flow settings. The lowest possible gas flow rates and the shortest preflow or postflow time can help reduce the cost of welding by saving the expensive shielding gas. The minimum flow rate is determined by the need for a stiff stream to overcome the heating effects of the arc and cross drafts. Excessive flow rates cause turbulence in the gas stream which may aspirate atmospheric contamination into the weld pool. The flow rate of shielding gas required depends mainly on:

- ✓Wind or draft speed,

- ✓Type of shielding gas,
- ✓Size of nozzle,
- ✓Type of base metal and size of weld pool,
- ✓Amount of current, welding speed and arc length,
- ✓Distance of gas nozzle orifice from the work surface.

The results showed that the effect of shielding gas on the responses is not significant. Its effect is more pronounced on the penetration and hence microstructure. But, its value must be compatible with welding speed, current and arc length. Because insufficient flow causes extreme heat on the surface, hard arc initiation and unacceptable welding quality. On the contrary, excessive flow of gas results with unnecessary cost and increase in turbulence. The exact gas flow rate is determined by trial and error.

4.1.3.1. Effect of Gas Flow Rate on Tensile Load

The experimental results showed that the effect of gas flow rate on tensile load is not so much significant. As illustrated in Figure 4.13, slight change in tensile load of 1260 kgf and 1276 kgf was observed when flow rate is increased from 9 I/min to 11 I/min.

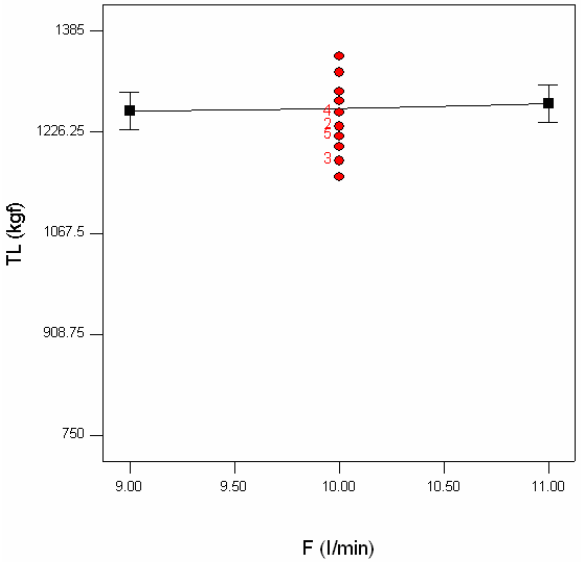

Figure 4.13. Effect of gas flow rate on tensile load required to cause fracture for 19.2 mm^2 area

4.1.3.2. Effect of Gas Flow Rate on Heat Affected Zone

As shown in Figure 4.14, increasing gas flow rate from minimum to maximum value slightly reduced the width of the heat affected zone from 5.51 mm to 5.43 mm due to the cooling effect of the shielding gas.

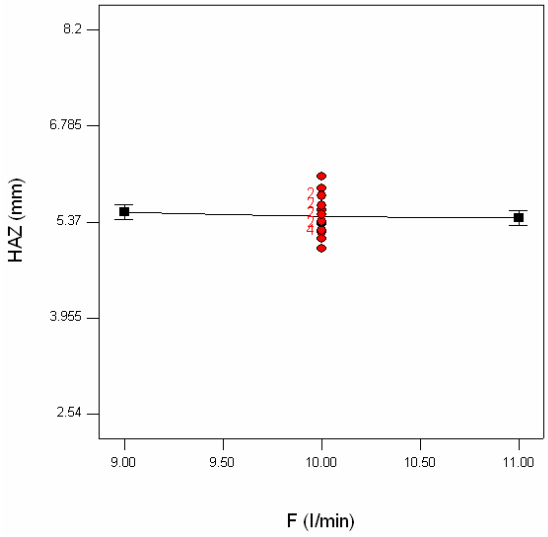

Figure 4.14. Effect of gas flow rate on heat affected zone

4.1.3.3. Effect of Gas Flow Rate on Upper Width

Experimental results showed that, the same trend with the heat affected zone was observed for the upper width. Figure 4.15 shows the effect of gas flow rate on upper width. Increasing flow rate slightly decreased the upper width from 8.81 mm to 8.72 mm.

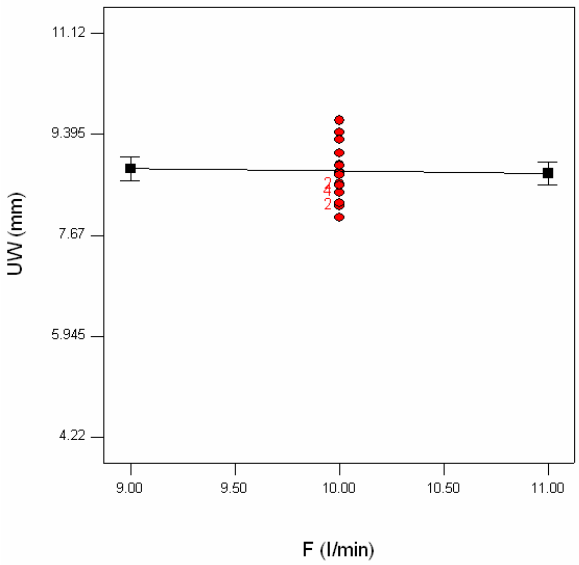

Figure 4.15. Effect of gas flow rate on upper width

4.1.3.4. Effect of Gas Flow Rate on Upper Height

In practice, it is desired to have the upper height as small as possible for the strength and visual inspection of the joints. The effect of gas flow rate on upper height is again least pronounced. As illustrated in Figure 4.16, increasing gas flow rate slightly increased the upper height from 0.14 mm to 0.15 mm.

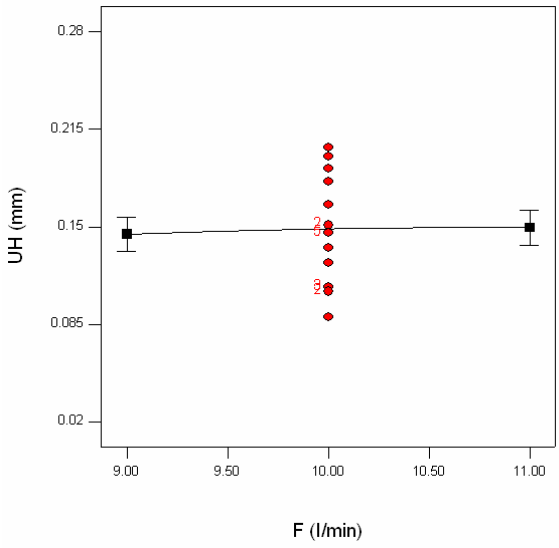

Figure 4.16. Effect of gas flow rate on upper height

4.1.3.5. Effect of Gas Flow Rate on Penetration

Penetration directly related to the welding current (heat input) and welding speed. The effect of gas flow rate is not much affect the penetration depth. Its effect can be seen by adding another inert gas. The effect of gas and gas flow rate on penetration can be increased by changing the gas type and mixture (Ar-He, Ar-H_2). Especially H_2 addition increases the strength of the joint. Durgutlu (2004) who reported that penetration depth and weld bead width increased with increasing hydrogen content in the shielding gas mixture.

Figure 4.17 shows the effect of gas flow rate on the penetration profile. Changing gas flow rate from minimum to maximum value was not changed the penetration so much. 1.18 mm and 1.19 mm penetration was obtained for minimum and maximum flow rates respectively.

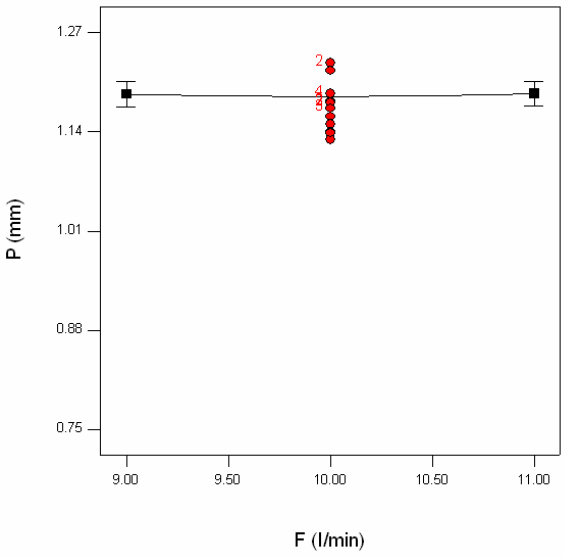

Figure 4.17. Effect of gas flow rate on penetration

4.1.3.6. Effect of Gas Flow Rate on Area of Penetration

Figure 4.18 shows the effect of gas flow rate on area of penetration. Here, is also slight change in area of penetration from 8.58 mm^2 to 8.55 mm^2 was observed under minimum and maximum flow rates respectively.

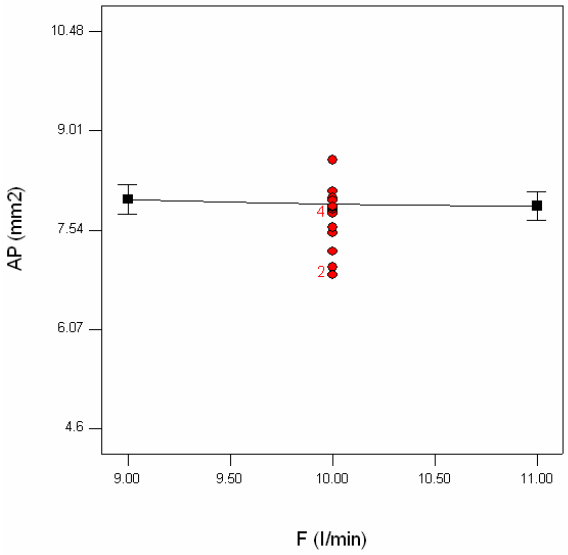

Figure 4.18. Effect of gas flow rate on area of penetration

4.1.4. Gap Distance (Arc Length)

Arc voltage and arc length are related terms that are often used interchangeably. However, they are different. Arc voltage is an approximate means of stating the physical arc length in electrical terms. The same physical arc length, however, could yield different arc voltage readings, depending on the factors gap distance, current and electrode extension. When all variables are held constant, a reliable relationship exists between the two: an increase in arc voltage will result in longer arc. Although, in many practices it is stated that arc length should be equal to about 1.5 times the electrode diameter, it can vary depending on the specific applications and particularly on the operator's preference. In accordance with the arc efficiency formula of $Q = \eta EI$ (where η: arc efficiency, E: voltage, I: current, Q: heat flow) higher arc lengths cause higher arc voltage and will decrease the arc

efficiency. In general, it can be stated that the greater the arc length, the higher is the heat leakage to the surrounding atmosphere which results with inefficient welding. Whereas the opposite is also true.

4.1.4.1. Effect of Gap Distance on Tensile Load

Effect of gap distance on tensile load, Figure 4.19, showed that tensile load started to increase to a gap distance of 2 mm (1273 kgf) than followed by decreasing toward the 4 mm (1248 kgf). This is due to the not concentrated heat, and increasing heat leakage to the base metal with increasing arc gap.

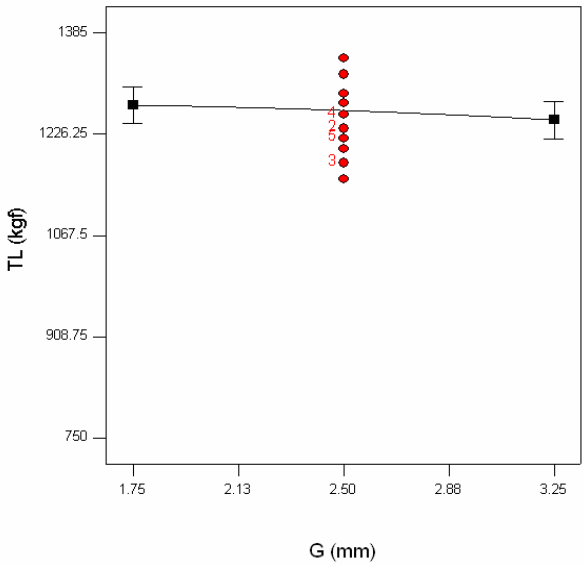

Figure 4.19. Effect of gap distance on tensile load required to cause fracture for 19.2 mm^2 area

4.1.4.2. Effect of Gap Distance on Heat Affected Zone

Figure 4.20 shows the effect of gap distance on heat affected zone. As the arc gap increased from 1 mm to 4 mm, the heat affected zone also increased from 5.40 mm to 5.57 mm respectively. The increase in the width of the heat affected zone is due to the cone shape of the arc. When the stand-off distance of the welding torch from the base metal increases the base of the cone shape increases to a certain value. So, this will widen the heat affected zone. Further increase in arc gap decreases the

heat affected zone due to the low heat input and high heat leakage. This study supported the theory of increasing gap distance causes the heat leakage to the base metal and the environment.

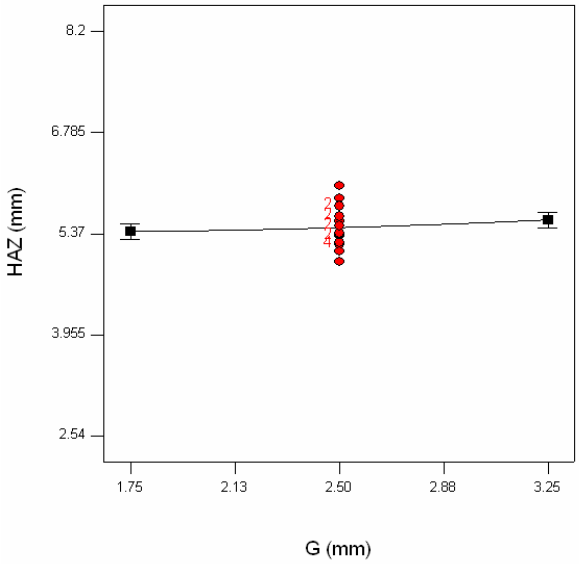

Figure 4.20. Effect of gap distance on heat affected zone

4.1.4.3. Effect of Gap Distance on Upper Width

As mentioned above, increasing arc length increases the base of the arc cone shape. This will increase upper width and also heat affected zone. As shown in Figure 4.21, the percentage increase in upper width is much more than the heat affected zone. Because, the heat flow in welding process is from the fusion zone to the heat affected zone. So, it is expected that the increase in upper width is higher than that of the heat affected zone. Minimum 8.65 mm and maximum 8.87 mm upper width was obtained with increasing gap distance from 1 mm to 4 mm respectively.

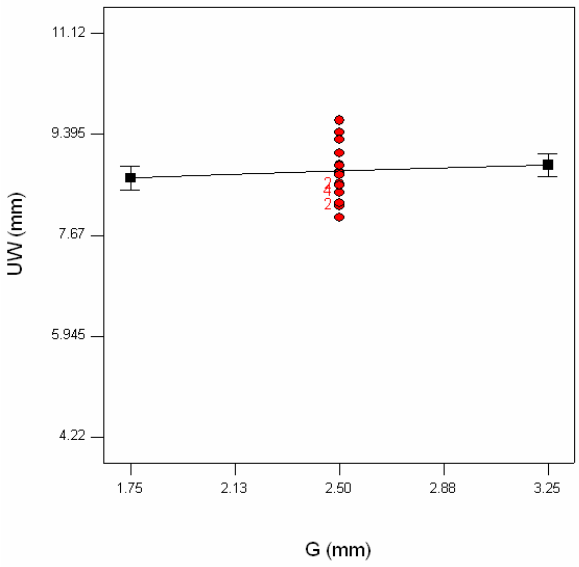

Figure 4.21. Effect of gap distance on upper width

4.1.4.4. Effect of Gap Distance on Upper Height

In accordance with the welding efficiency formula given above, when the gap distance increases the arc voltage increases and hence the overall efficiency of the welding process decreases. As shown in Figure 4.22, increase in arc gap decreased the upper height from 0.15 mm to 0.14 mm.

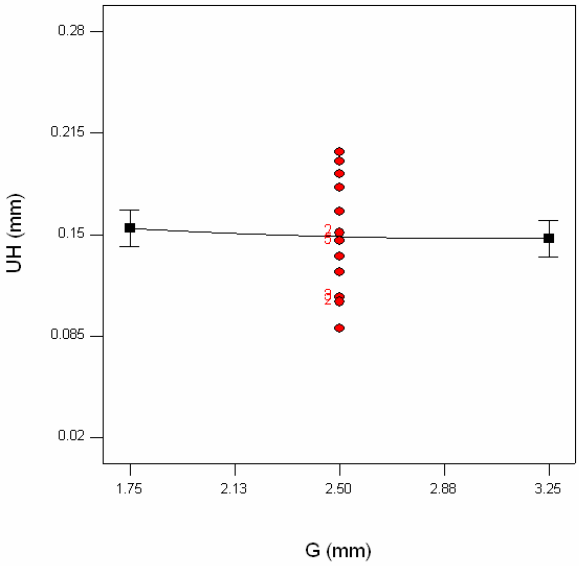

Figure 4.22. Effect of gap distance on upper width

4.1.4.5. Effect of Gap Distance on Penetration

Penetration is proportional to the heat input to the workpiece. As the heat input increases then the penetration increases. Therefore, smaller depth to width ratio is obtained under large gap distance. Experimental results, plotted in Figure 4.23, showed that, increasing arc gap decreased the penetration remarkably. When the arc gap increased from minimum to maximum value it decreased from 1.19 to 1.16 mm respectively.

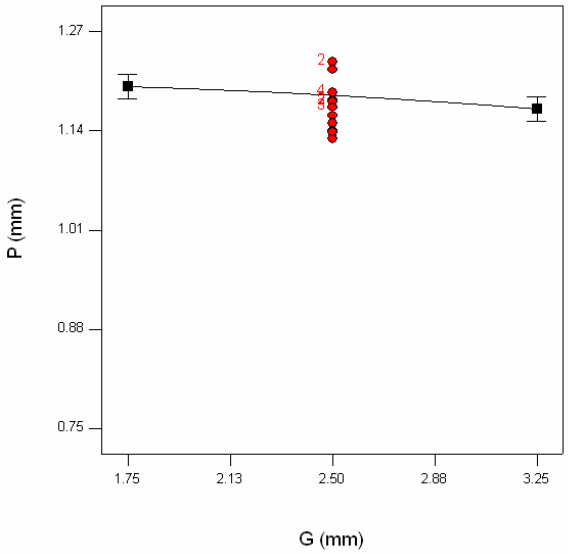

Figure 4.23. Effect of gap distance on penetration

4.1.4.6. Effect of Gap Distance on Area of Penetration

Hence the area of penetration is dependent on the penetration and upper width, the same trend with the penetration was observed for area of penetration. As indicated in Figure 4.24, it increased to 8.42 mm^2 with the arc gap of 2.5 mm. The minimum and maximum values were obtained as 7.92 mm^2 and 7.90 mm^2 for 1mm and 4 mm arc lengths respectively.

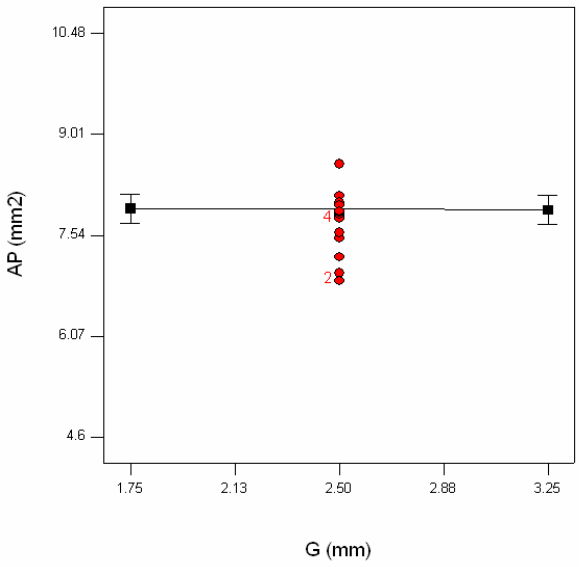

Figure 4.24. Effect of gap distance on area of penetration

4.2. Interaction Effects of Weld Parameters on Welding Responses

An interaction occurs when the response is different depending on the settings of two factors. Plots make to interpret two factor interactions. Actually, interaction is not a desirable feature since it creates difficulties to predict the effect of each factor on the process. As a part of the study, the interaction effects of the welding parameters on the welding responses were analyzed.

4.2.1. Transverse Tensile Load

Figures 4.25-4.30 show the interaction effects of the TIG welding process parameters on the transverse tensile load of 1.2 mm AISI 304 stainless steel sheet. Figure 4.25 indicates that, when welding current was 117 A, increasing the welding speed caused an increase in tensile load from 1174 kgf to 1199 kgf, however when the current decreased to 52 A, increasing welding speed decreased the tensile load from 1210 kgf to 1123 kgf. The intersection of the two curves can be reached when welding speed is approximately 2.15 mm/s. Therefore, for higher tensile load, lower

current should be selected up to 2.15 mm/s and beyond this point higher current should be selected.

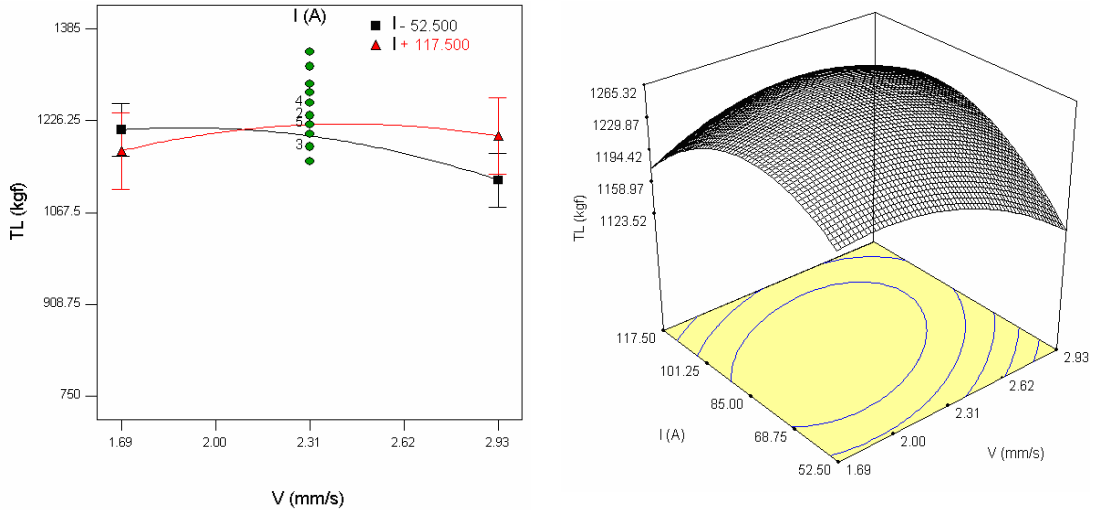

(a) (b)

Figure 4.25. Interaction effects of V and I on TL at F=10 I/min and G= 2.5 mm, (a. 2D interaction plot, b. 3D response surface plot)

Figure 4.26 indicates that, when gas flow rate was 11 I/min, increasing welding speed increased tensile load slightly from 1226 kgf to 1245 kgf. However, when the gas flow rate decreased to 9 I/min, increasing welding speed decreased the tensile load slightly to 1215 kgf. So, it was concluded that, there is negligible effect of gas flow rate on the tensile load.

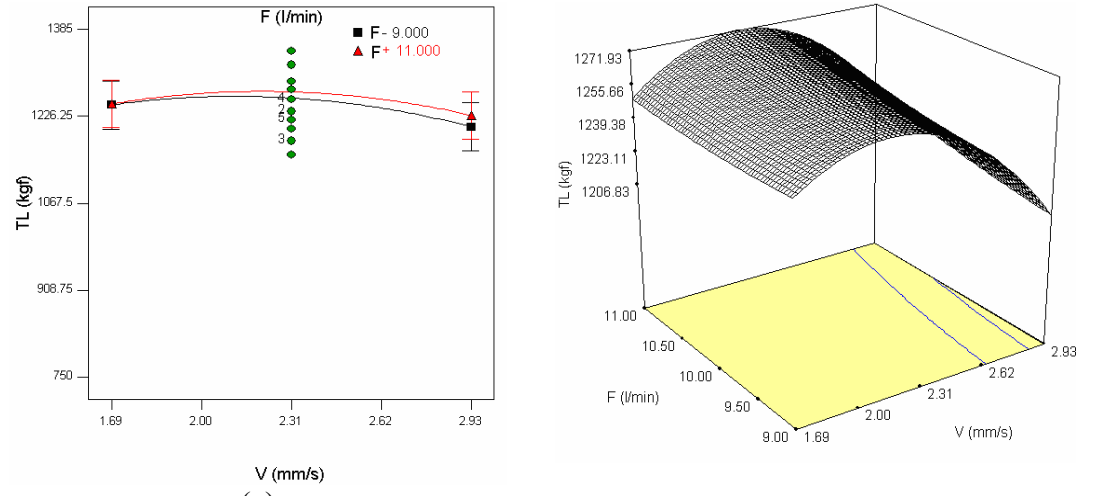

(a) (b)

Figure 4.26. Interaction effects of V and F on TL at I=85 A and G= 2.5 mm, (a. 2D interaction plot, b. 3D response surface plot)

Figure 4.27 indicates that, when welding speed was 1.69 mm/s, increasing gap distance caused a slight decrease in tensile load from 1260 kgf to 1226 kgf. However, when the welding speed increased to 2.93 mm/s, increasing gap distance slightly increased the tensile load from 1205 kgf to 1219 kgf. The intersection of the two curves can be reached when gap distance is approximately 3.62 mm. Therefore, for higher tensile load, lower welding speed should be selected up to 3.62 mm and beyond this point higher welding speed should be selected.

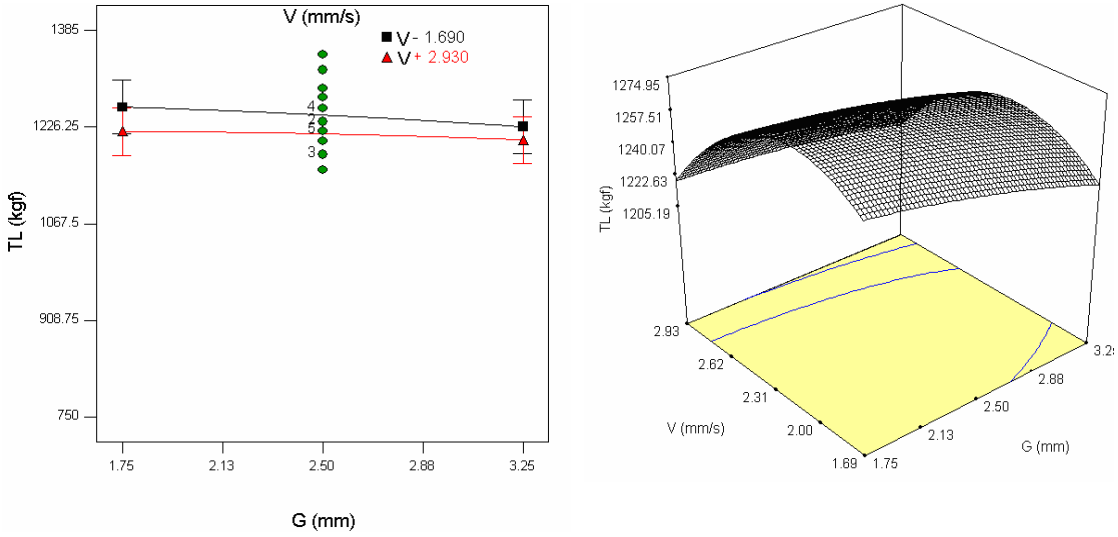

(a) (b)

Figure 4.27. Interaction effects of G and V on TL at F=10 I/min and I=85 A, (a. 2D interaction plot, b. 3D response surface plot)

Figure 4.28 indicates that, when gas flow was 11 I/min, increasing the welding current up to 85 A increased the tensile load from 1199 kgf to 1275 kgf, however when the gas flow rate decreased to 9 I/min, increasing welding current up to 85 A increased the tensile load to 1257 kgf further increase in welding current decreased the tensile load. The intersection point of the two curves can be reached when the welding current is 52 A. Therefore for higher tensile load lower gas flow rate should be selected up to 85 A and beyond this point higher gas flow rate should be selected.

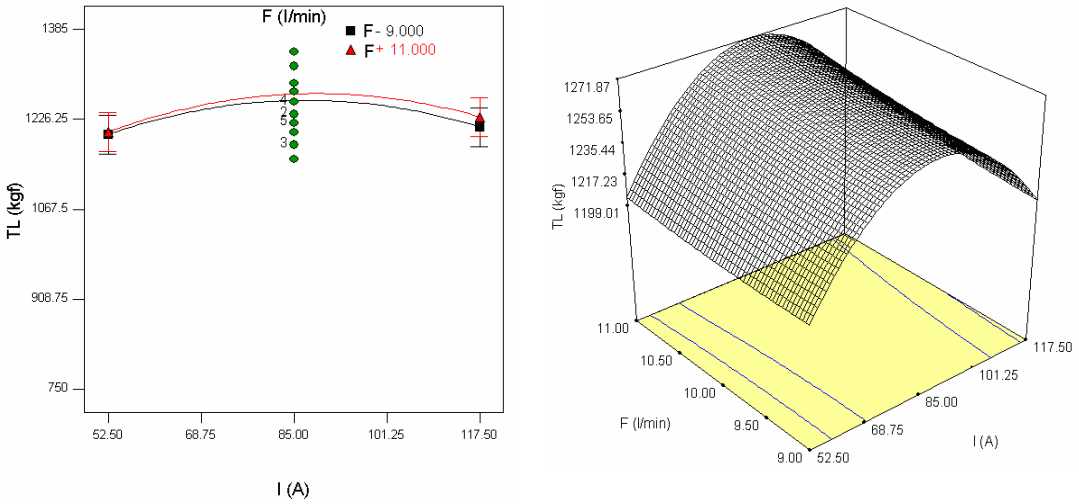

(a) (b)

Figure 4.28. Interaction effects of F and I on TL at V=2.31 mm/s and G= 2.5 mm, (a. 2D interaction plot, b. 3D response surface plot)

Figure 4.29 indicates that, when gap distance was 1.75 mm, increasing welding current up to 85 A caused an increase in tensile load from 1205 kgf to 1275 kgf. However, when the gap distance increased to 3.25 mm, increasing the welding current up to 85 A increased the tensile load from 1187 kgf to 1240 kgf. Further increase in welding current decreased the tensile load for the two gap distances.

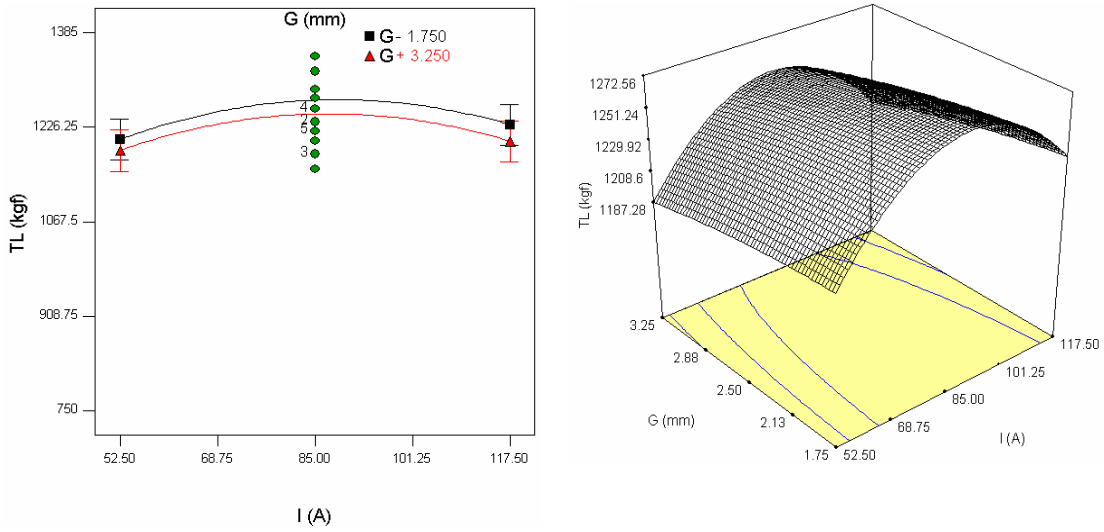

(a) (b)

Figure 4.29. Interaction effects of I and G on TL at F=10 I/min and V=2.31 mm/s, (a. 2D interaction plot, b. 3D response surface plot)

Parallel lines in Figure 4.30 indicates that, no interaction was observed between gas flow rate and gap distance. When gap distance was 1.75 mm, increasing gas flow rate caused a slight increase in tensile load from 1268 kgf to 1279 kgf. When the gap distance increased to 3.25 mm, increasing the gas flow rate slightly increased the tensile load from 1244 kgf 1250 kgf.

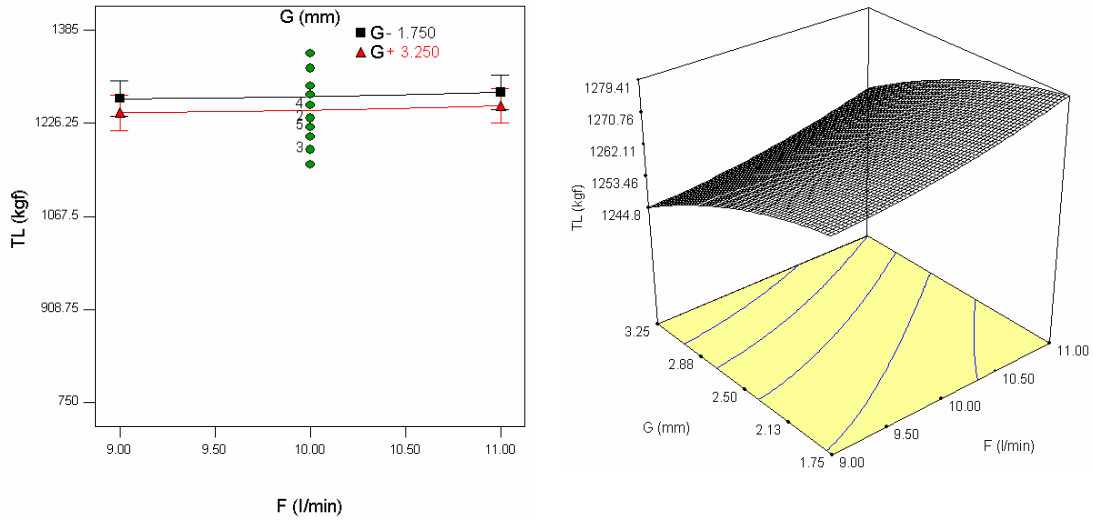

(a) (b)

Figure 4.30. Interaction effects of G and F on TL at I=85 A and V=2.31 mm/s, (a. 2D interaction plot, b. 3D response surface plot)

4.2.2. Heat Affected Zone

Figures 4.31-4.36 shows the interaction effects of the TIG welding process parameters on the heat affected zone. As shown in Figure 4.30, at the welding current of 117 A, increasing welding speed decreased the heat affected zone from 8.16 mm to 5.95 mm. However, when the current decreased to 52.5 mm, increasing the welding speed also decreased the heat affected zone from 4.76 mm 3.60 mm. The intersection of the two curves can be reached approximately at 4.5 mm/s. therefore to obtain minimum heat affected zone lower current should be used up to 4.5 mm/s, beyond this point higher current (up to 117 A) may be used.

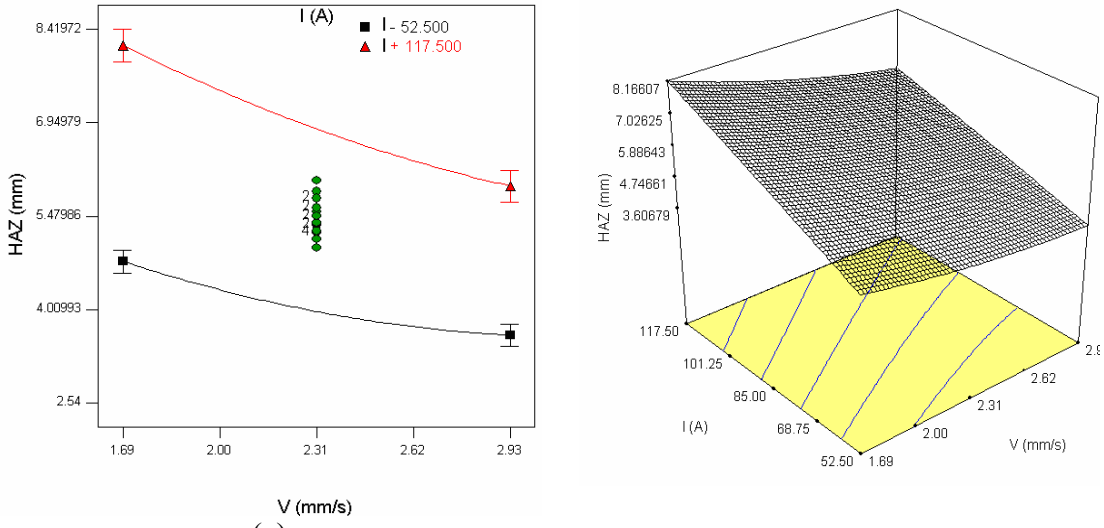

(a) (b)

Figure 4.31. Interaction effects of V and I on HAZ at F=10 I/min and G= 2.5 mm, (a. 2D interaction plot, b. 3D response surface plot)

Paralel lines in Figure 4.32 indicate that there are not any interactions between gas flow rate and welding speed. When gas flow rate was 9 I/min, increasing welding speed decreased the heat affected zone from 6.56 mm to 4.88 mm. However, increasing gas flow rate to 11 I/min caused a decrease in heat affected zone from 6.48 mm to 4.79 mm. Therefore, in order to obtain narrow heat affected zone higher flow rate may be selected.

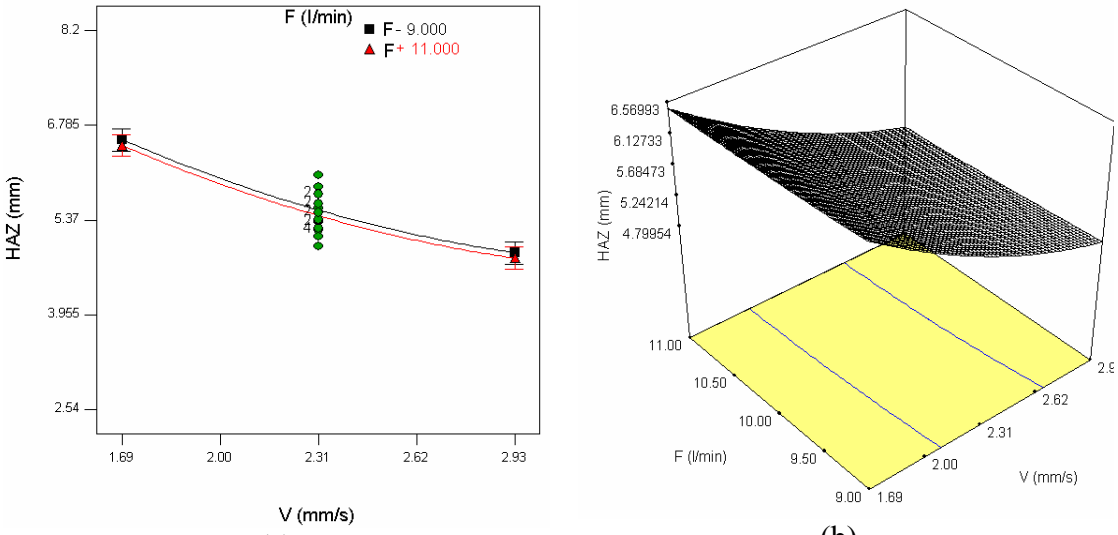

(a) (b)

Figure 4.32. Interaction effects of V and F on HAZ at I=85 A and G= 2.5 mm, (a. 2D interaction plot, b. 3D response surface plot)

Figure 4.33 indicates that, when gap distance was 3.25 mm, increasing the welding speed decreased the heat affected zone from 6.60 mm to 4.94 mm, however, when the gap distance decreased to 1.75 mm, increasing welding speed caused a decrease in heat affected zone from 6.46 mm to 4.75 mm. The intersection point of two curves can be reached at approximately welding speed of 1.38 mm/s. Therefore, in order to obtain narrow heat affected zone lower gap distance should be used before and after this point.

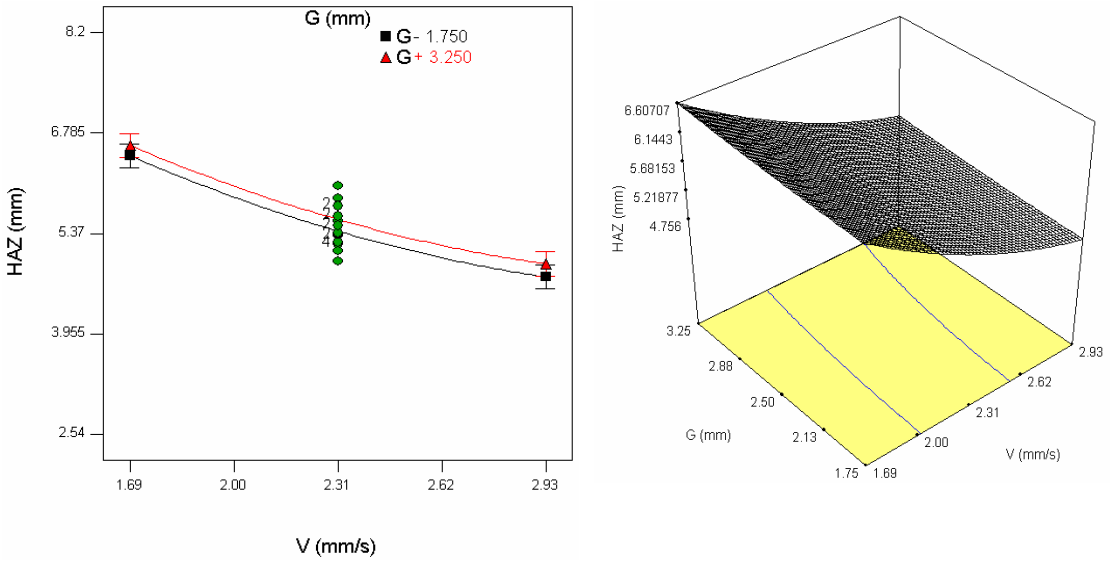

(a) (b)

Figure 4.33. Interaction effects of G and V on HAZ at F=10 I/min and I=85 A, (a. 2D interaction plot, b. 3D response surface plot)

Two parallel lines in Figure 4.34 indicate that, there is not interaction between current and gas flow rate. Slight reduction in heat affected zone was observed under high and low gas flow rates. When gas flow rate was 9 I/min, increasing current increased the heat affected zone from 4.03 mm to 6.92 mm. When the gas flow rate increased to 11 I/min, increasing current increased the heat affected zone from 3.96 mm to 6.82 mm. therefore for narrower heat affected zone higher gas flow rates may be selected.

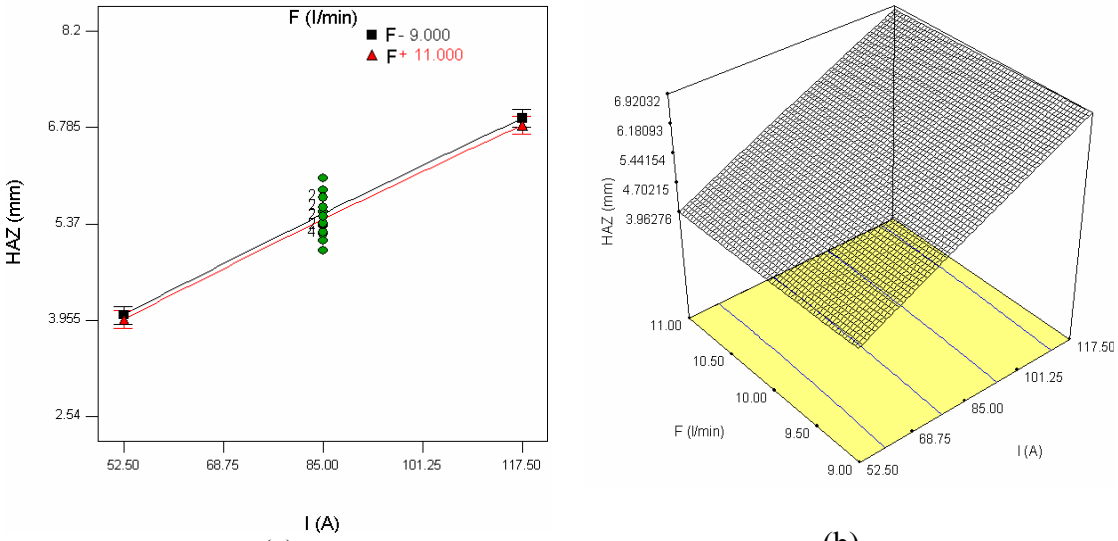

(a) (b)

Figure 4.34. Interaction effects of F and I on HAZ at V=2.31 mm/s and G= 2.5 mm, (a. 2D interaction plot, b. 3D response surface plot)

Figure 4.35 indicates that, when the gap distance was 3.25 mm, increasing welding current increased the heat affected zone from 4.06 mm to 6.98 mm. However, when the gap distance is decreased to 1.75 mm, increasing current caused an increase in heat affected zone from 3.94 mm to 6.77 mm. The intersection of the two curves may be reached approximately at 50 A. Therefore, for narrow heat affected zone, higher gap distance should be selected up to 50 A and beyond this point lower gap distance should be selected.

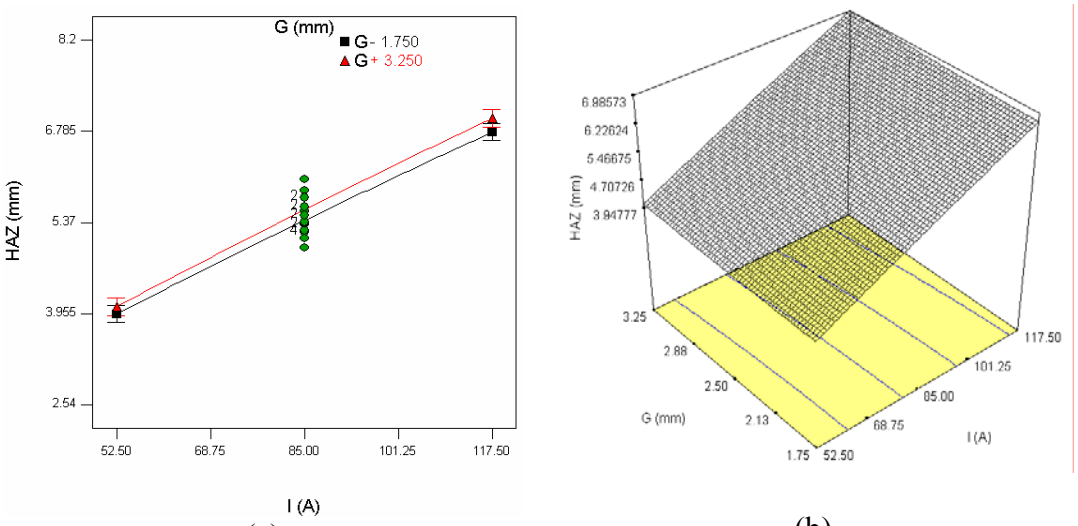

(a) (b)

Figure 4.35. Interaction effects of I and G on HAZ at F=10 I/min and V=2.31 mm/s, (a. 2D interaction plot, b. 3D response surface plot)

Parallel lines in Figure 4.36 indicates that, there is not interaction between gap distance and gas flow rate. When gap distance was 3.25 mm, increasing gas flow rate slightly decreased heat affected zone from 5.62 mm to 5.54 mm. However, when gap distance decreased to 1.75 mm, increasing gas flow rate caused a decrease in heat affected zone from 5.46 mm to 5.37 mm. Therefore, in order to obtain narrower heat affected zone, lower gap distance should be selected under constant welding speed and welding current.

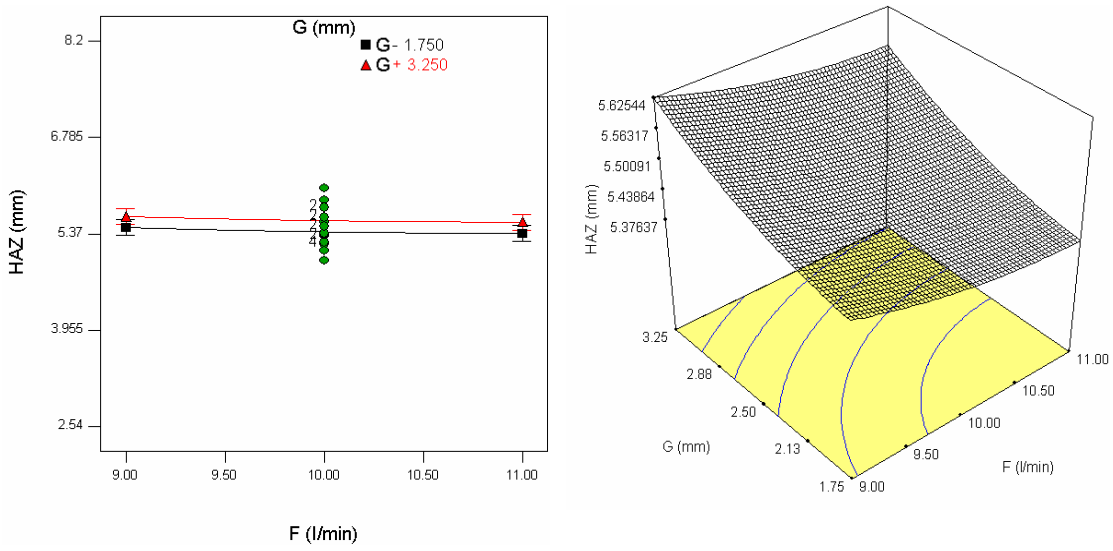

(a) (b)

Figure 4.36. Interaction effects of G and F on HAZ at I=85 A and V=2.31 mm/s, (a. 2D interaction plot, b. 3D response surface plot)

4.2.3. Upper Width

Figures 4.37-4.42 shows the interaction effects of the TIG welding process parameters on the upper width. Parallel lines in Figure 4.37 indicate that, there is not any interaction effect between welding current and welding speed. When the welding current was 117 A, increasing welding speed decreased the upper width from 10.85 mm to 9.00 mm. However, when the welding current decreased to 52 A, increasing welding speed resulted a decrease in upper width from 7.83 mm to 6.37. Therefore, in order to obtain low upper width, lower welding current should be used under constant gas flow rate and gap distance.

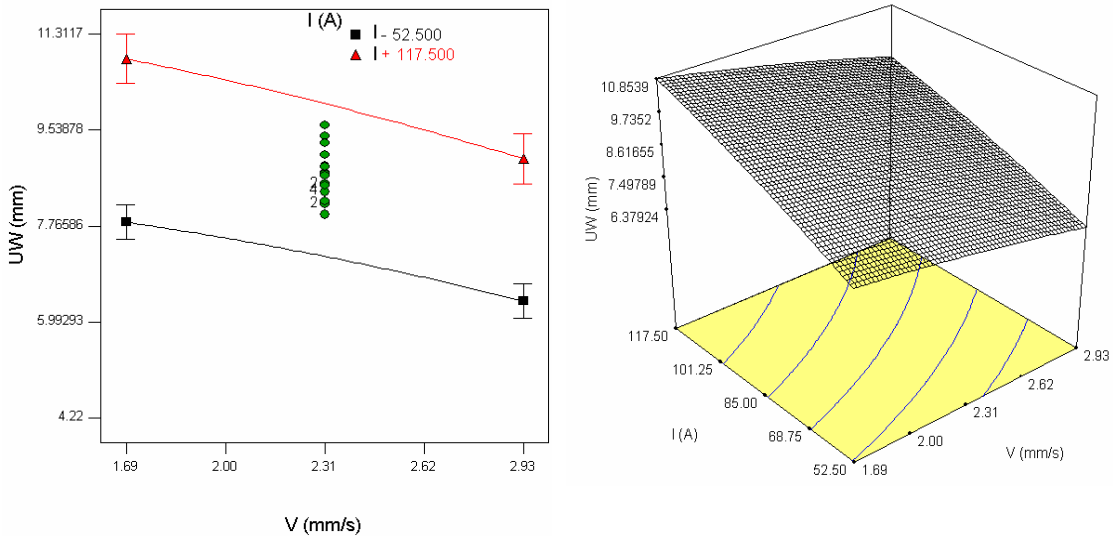

(a) (b)

Figure 4.37. Interaction effects of V and I on UW at F=10 I/min and G= 2.5 mm, (a. 2D interaction plot, b. 3D response surface plot)

Figure 4.38 indicates that, when gas flow rate was 9 I/min, increasing welding speed caused a significant decrease in upper width from 9.58 mm to 7.84 mm. At the gas flow rate of 11 I/min, increasing welding speed decreased upper width from 9.40 to 7.84 mm. The intersection point of the two curves can be reached at the welding speed of 2.93 mm/s. Therefore, in order to obtain low upper width high gas flow rate should be used up to this point under constant welding current and gap distances.

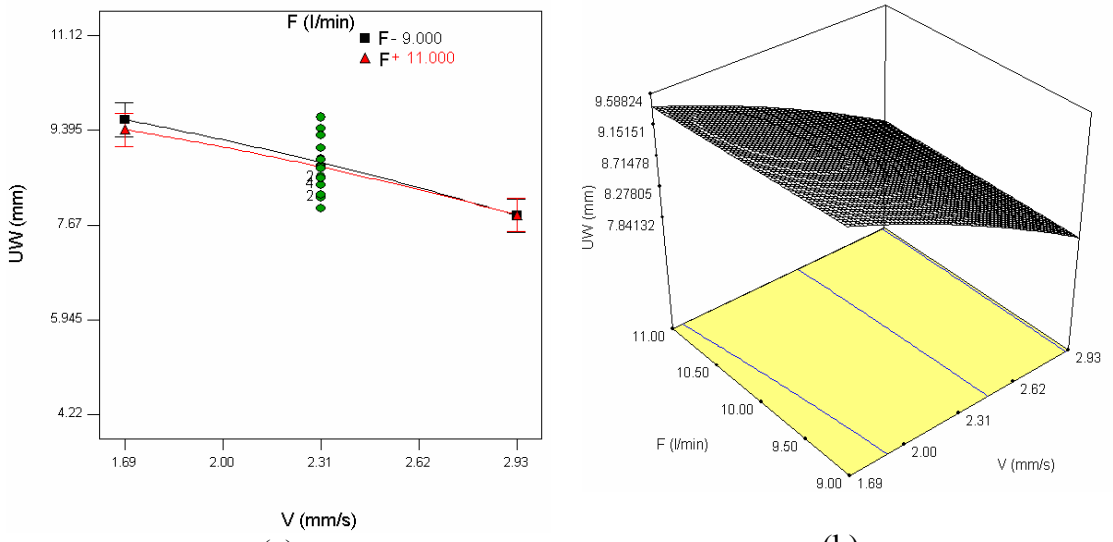

(a) (b)

Figure 4.38. Interaction effects of V and F on UW at I=85 A and G= 2.5 mm,
(a. 2D interaction plot, b. 3D response surface plot)

Parallel lines in Figure 4.39 indicates that, there is not interaction between gap distance and welding speed. When gap distance was 3.25 mm, increasing welding speed significantly decreased upper width from 9.60 mm to 7.94 mm. However, when gap distance decreased to 1.75 mm, increasing welding speed caused a decrease in upper width from 9.38 mm to 7.73 mm. Therefore, in order to obtain lower upper width, lower gap distance should be selected under constant gas flow rate and welding current.

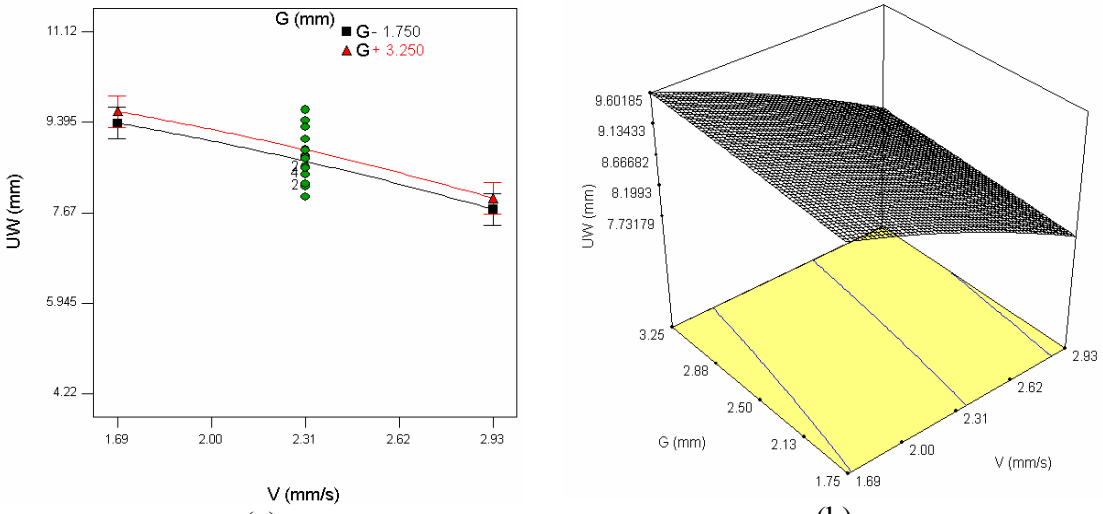

(a) (b)

Figure 4.39. Interaction effects of G and V on UW at F=10 I/min and I=85 A,
(a. 2D interaction plot, b. 3D response surface plot)

Parallel lines in Figure 4.40 indicates that, there is not interaction between gap flow rate and welding current. When gas flow rate was 9 I/min, increasing welding current significantly increased upper width from 7.24 mm to 10.26 mm. However, when gas flow rate increased to 11 I/min, increasing welding current caused an increase in upper width from 7.15 mm to 9.98 mm. Therefore, in order to obtain lower upper width, higher gas flow rate should be selected under constant welding speed and gap distance.

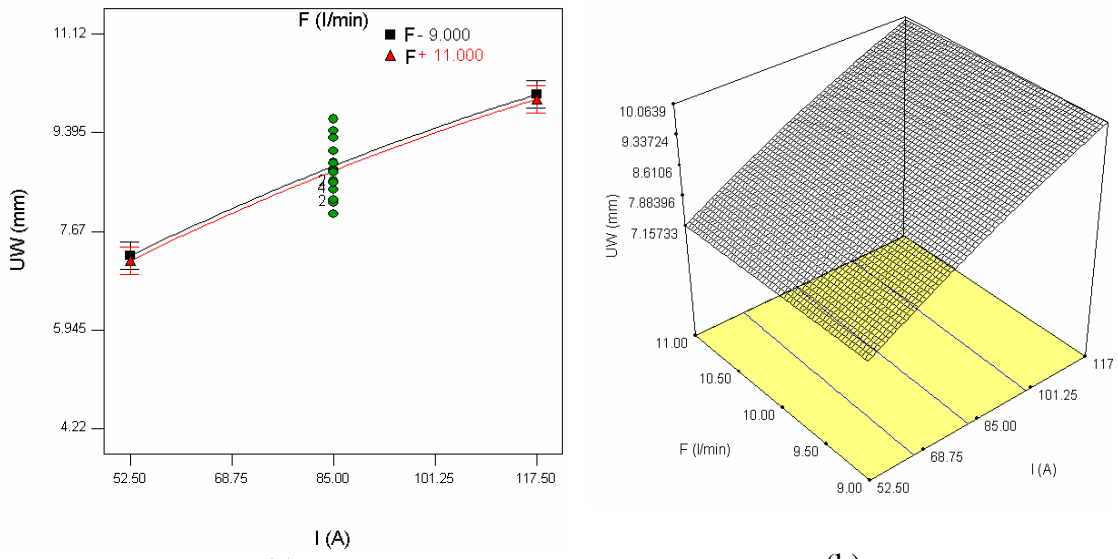

(a) (b)

Figure 4.40. Interaction effects of F and I on UW at V=2.31 mm/s and G= 2.5 mm, (a. 2D interaction plot, b. 3D response surface plot)

Figure 4.41 indicates that, when the gap distance was 3.25 mm, increasing welding current increased the upper width from 7.28 mm to 10.14 mm. However, when the gap distance was decreased to 1.75 mm, increasing welding current caused an increase in upper width from 7.10 mm to 9.88 mm. The intersection of the two curves can be reached approximately at 45 A. Therefore, for low upper width, higher gap distance should be selected up to 45 A, and beyond this point lower gap distance should be selected.

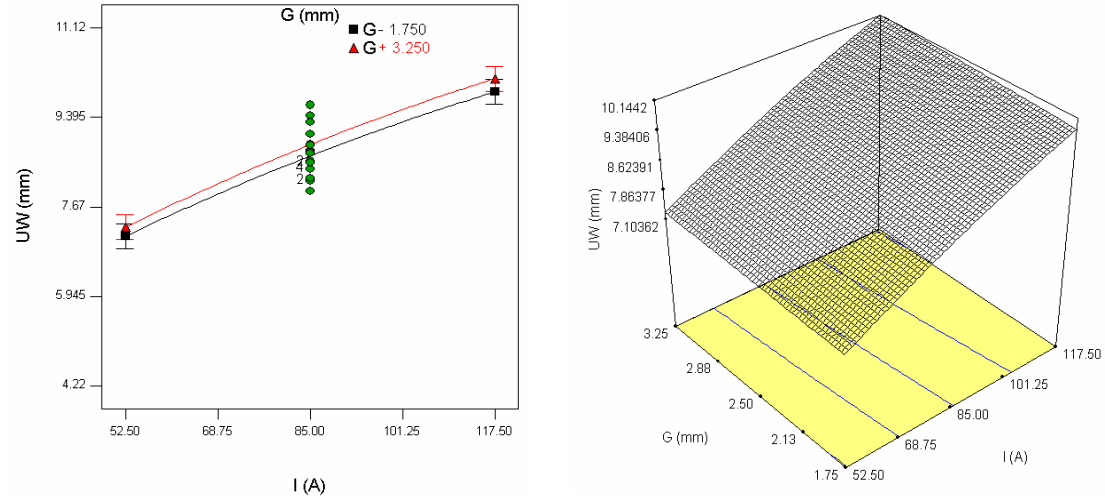

(a) (b)

Figure 4.41. Interaction effects of I and G on UW at F=10 I/min and V=2.31 mm/s, (a. 2D interaction plot, b. 3D response surface plot)

Parallel lines in Figure 4.42 indicates that, there is not interaction between gap distance and gas flow rate. When gap distance was 3.25 mm, increasing gas flow rate slightly decreased upper width from 8.89 mm to 8.83 mm. However, when gap distance decreased to 1.75 mm, increasing gas flow rate caused a decrease in upper width from 8.70 mm to 8.59 mm. Therefore, in order to obtain low upper width, lower gap distance should be selected under constant welding speed and welding current.

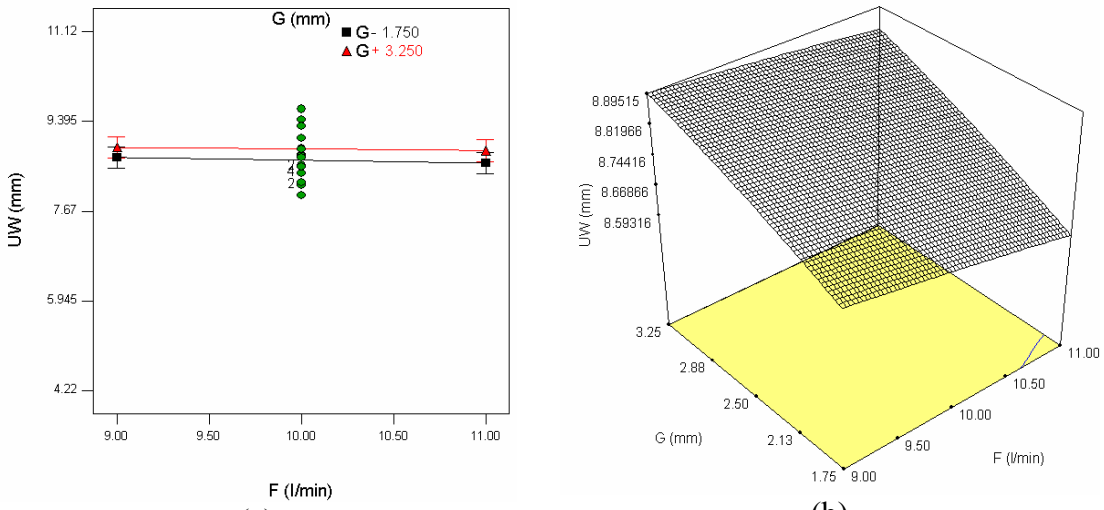

(a) (b)

Figure 4.42. Interaction effects of G and F on UW at I=85 A and V=2.31 mm/s, (a. 2D interaction plot, b. 3D response surface plot)

4.2.4. Upper Height

Figures 4.43-4.48 shows the interaction effects of the TIG welding process parameters on the upper height. Figure 4.43 indicates that, when welding current was 117 A, increasing the welding speed caused a decrease in upper height from 0.25 mm to 0.13 mm, however when the current decreased to 52 A, increasing welding speed decreased the upper height from 0.15 mm to 0.09 mm. The intersection of the two curves can be reached when welding speed is approximately 3.86 mm/s. Therefore, for lower upper height, lower current should be selected up to 3.86 mm/s and beyond this point higher current may be selected.

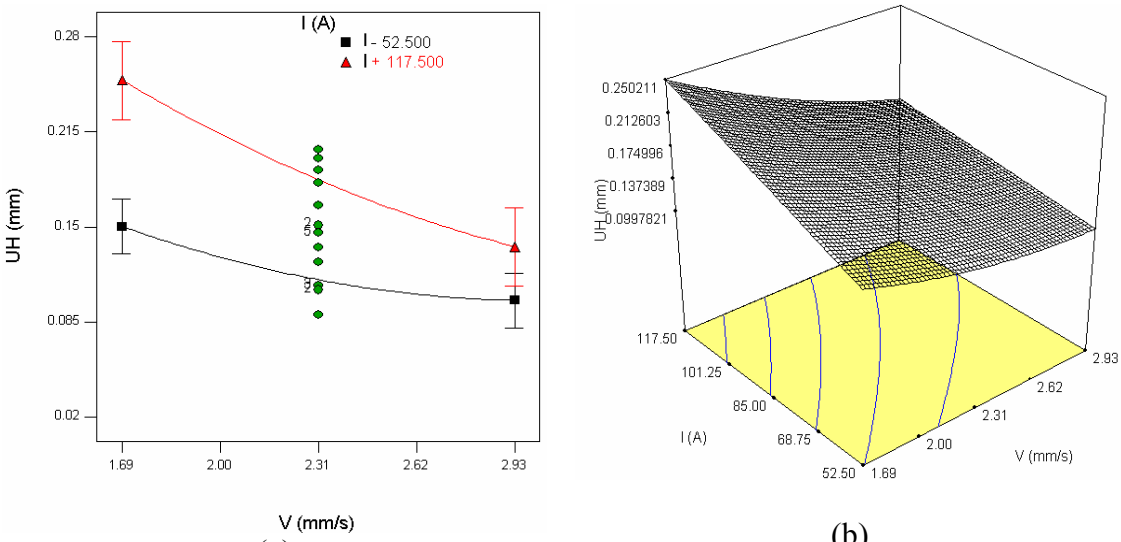

Figure 4.43. Interaction effects of V and I on UH at F=10 I/min and G= 2.5 mm, (a. 2D interaction plot, b. 3D response surface plot)

Parallel lines in Figure 4.44 indicates that, there is not interaction between gas flow rate and welding speed. When gas flow rate was 9 I/min, increasing welding speed significantly decreased upper height from 0.20 mm to 0.11 mm. However, when gas flow rate increased to 11 I/min mm, increasing welding speed caused a decrease in upper height from 0.19 mm to 0.11 mm. Therefore, in order to obtain lower upper height, lower gas flow rate should be selected under constant gap distance and welding current.

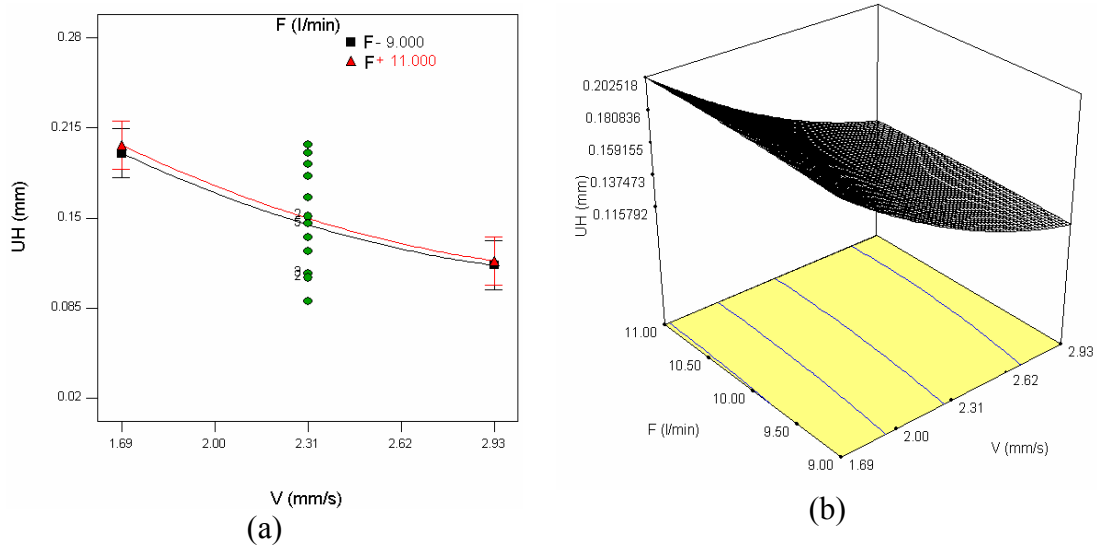

Figure 4.44. Interaction effects of V and F on UH at I=85 A and G= 2.5 mm, (a. 2D interaction plot, b. 3D response surface plot)

Figure 4.45 indicates that, when gap distance was 3.25 mm, increasing the welding speed decreased the upper height from 0.19 mm to 0.12 mm, however, when the gap distance decreased to 1.75 mm, increasing welding speed caused a decrease in upper height from 0.20 mm to 0.12 mm. The intersection point of two curves can be reached at the welding speed of 2.93 mm/s. Therefore, in order to obtain lower upper height higher gap distance should be used up to this point under constant gas flow rate and welding current.

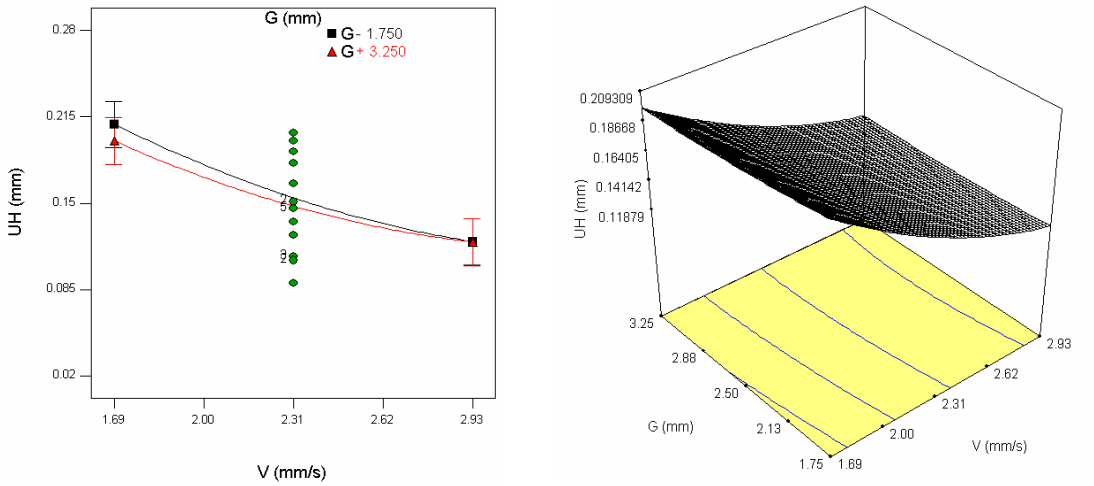

(a) (b)

Figure 4.45. Interaction effects of G and V on UH at F=10 I/min and I=85 A, (a. 2D interaction plot, b. 3D response surface plot)

Figure 4.46 indicates that, when gas flow rate was 9 I/min, increasing welding current significantly increased upper height from 0.10 mm to 0.18 mm. However, when gas flow rate increased to 11 I/min, increasing welding current caused an increase in upper height from 0.11 mm to 0.17 mm. The intersection point of the two lines can be reached at the welding current of 117 A. Therefore, in order to obtain lower upper height, lower gas flow rate should be selected up to this point under constant welding speed and gap distance.

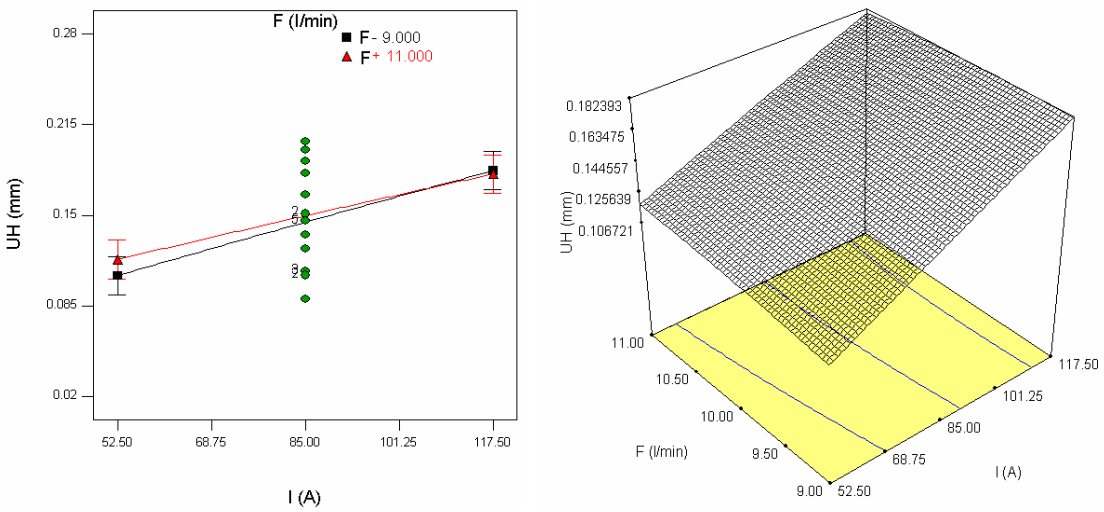

(a) (b)

Figure 4.46. Interaction effects of F and I on UH at V=2.31 mm/s and G= 2.5 mm, (a. 2D interaction plot, b. 3D response surface plot)

Figure 4.47 indicates that, when the gap distance was 3.25 mm, increasing welding current increased the upper height from 0.11 mm to 0.17 mm. However, when the gap distance was decreased to 1.75 mm, increasing welding current caused an increase in upper width from 0.11 mm to 0.19 mm. The intersection of the two curves can be reached at the welding current of 52 A. Therefore, for low upper height, higher gap distance should be selected under constant gas flow rate and welding speed.

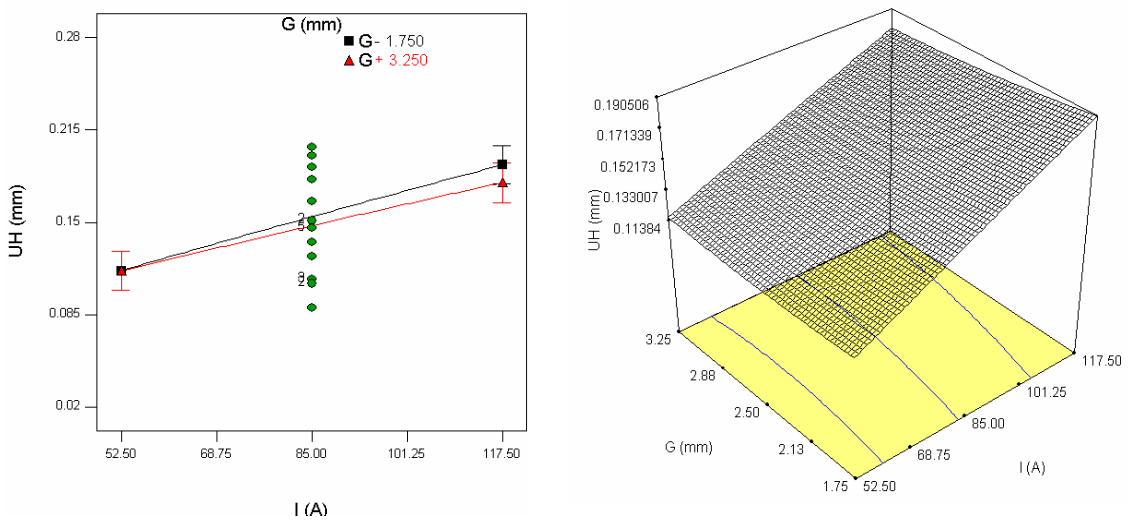

(a) (b)

Figure 4.47. Interaction effects of I and G on UH F=10 I/min and V=2.31 mm/s, (a. 2D interaction plot, b. 3D response surface plot)

Figure 4.48 indicates that, when gap distance was 3.25 mm, increasing gas flow rate slightly increased upper height from 0.142 mm to 0.149 mm. However, when gap distance decreased to 1.75 mm, increasing gas flow rate caused a decrease in upper height from 0.151 mm to 0.153 mm. The intersection point of two lines may be reached at the gas flow rate of 11 I/min. Therefore, in order to obtain low upper height, higher gap distance should be selected under constant welding speed and welding current.

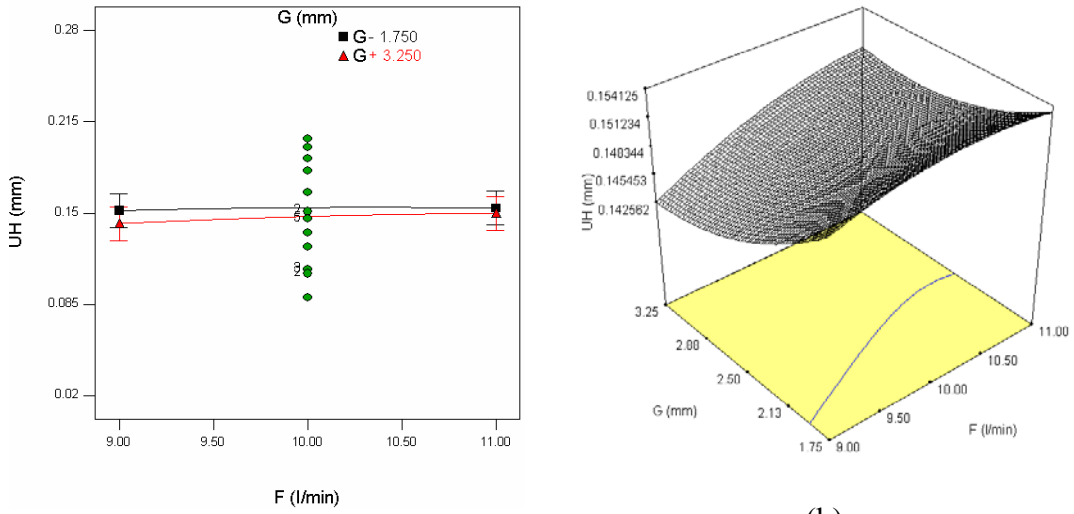

(a) (b)

Figure 4.48. Interaction effects of G and F on UH at I=85 A and V=2.31 mm/s, (a. 2D interaction plot, b. 3D response surface plot)

4.2.5. Penetration

Figures 4.49-4.54 shows the interaction effects of the TIG welding process parameters on the penetration. Figure 4.49 indicates that, when the welding current was 117 A, increasing welding speed decreased the penetration from 1.28 mm to 1.21 mm. However, when the welding current decreased to 52 A, increasing welding speed resulted a decrease in upper width from 1.10 mm to1.00. The intersection point of the two lines can be reached at the welding speed of 0.76 mm/s Therefore, in order to obtain high penetration, lower welding current should be used up to this point and beyond this point higher welding current with constant gas flow rate and gap distance should be used.

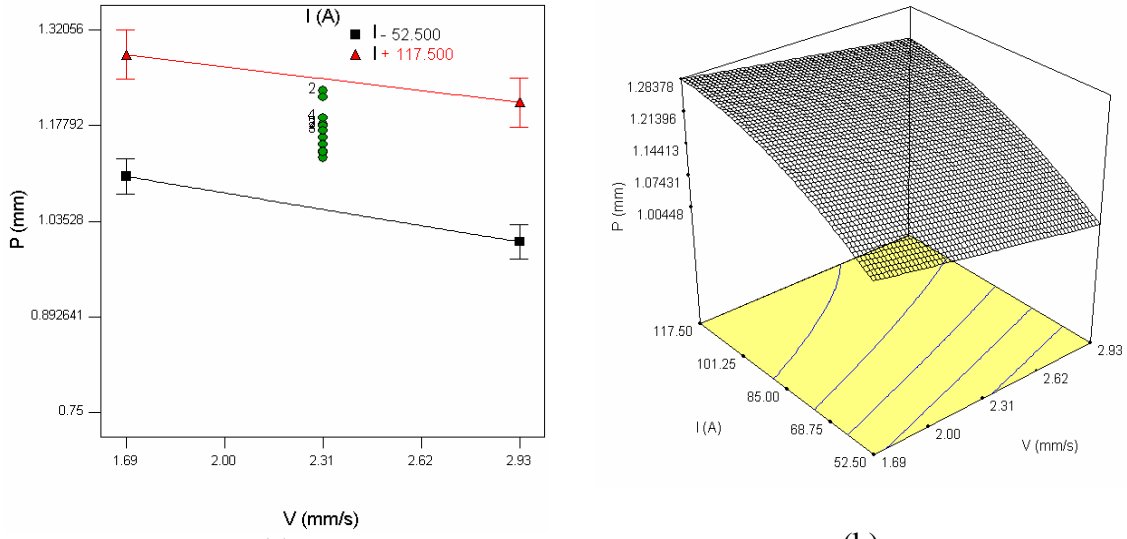

(a) (b)

Figure 4.49. Interaction effects of V and I on P at F=10 I/min and G= 2.5 mm, (a. 2D interaction plot, b. 3D response surface plot)

Figure 4.50 indicates that, when gas flow rate was 9 I/min, increasing welding speed significantly decreased penetration from 1.19 mm to 1.16 mm. However, when gas flow rate increased to 11 I/min mm, increasing welding speed caused a decrease in penetration from 1.23 mm to 1.14 mm. The intersection point of the two curves can be reached approximately at the welding speed of 3.55 mm/s. Therefore, in order to obtain high penetration, lower gas flow rate should be selected up to 3.55 mm/s welding speed under constant gap distance and welding current.

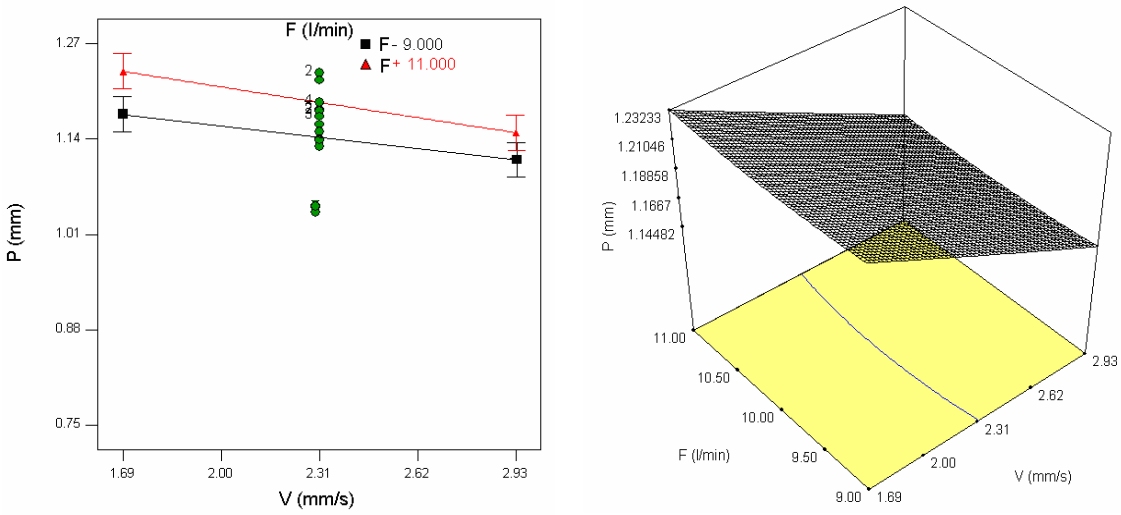

(a) (b)

Figure 4.50. Interaction effects of V and F on P at I=85 A and G= 2.5 mm, (a. 2D interaction plot, b. 3D response surface plot)

Figure 4.51 indicates that, when gap distance was 3.25 mm, increasing the welding speed significantly decreased the penetration from 1.22 mm to 1.11 mm, however, when the gap distance decreased to 1.75 mm, increasing welding speed caused a decrease in penetration from 1.23 mm to 1.16 mm. The intersection point of two curves can be reached at the welding speed of 1.38 mm/s. Therefore, in order to obtain high penetration low gap distance should be used beyond this point.

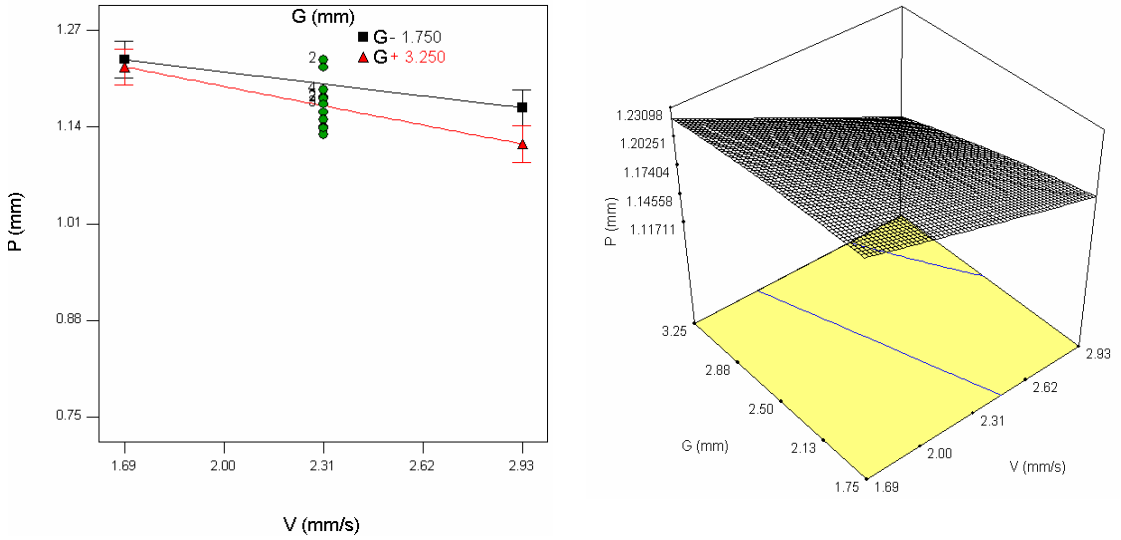

(a) (b)

Figure 4.51. Interaction effects of G and V on P at F=10 I/min and I=85 A, (a. 2D interaction plot, b. 3D response surface plot)

Figure 4.52 indicates that, when gas flow rate was 9 l/min, increasing welding current significantly increased penetration from 0.98 mm to 1.15 mm. However, when gas flow rate increased to 11 l/min, increasing welding current caused an increase in penetration from 1.05 mm to 1.23 mm. The intersection point of the two lines can be reached approximately at the welding current of 134 A. Therefore, in order to obtain high penetration, high gas flow rate should be selected up to this point under constant welding speed and gap distance.

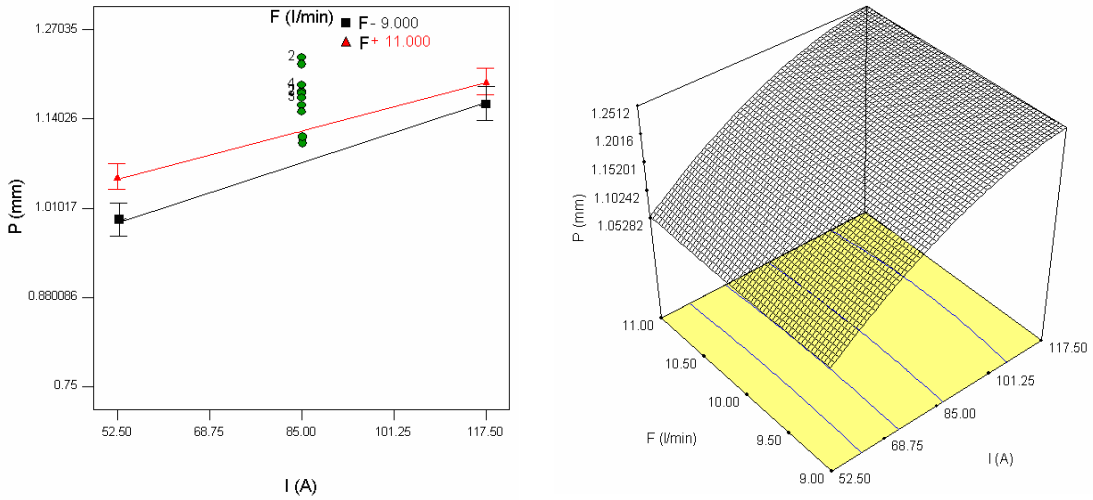

(a) (b)

Figure 4.52. Interaction effects of F and I on P at V=2.31 mm/s and G= 2.5 mm, (a. 2D interaction plot, b. 3D response surface plot)

Figure 4.53 indicates that, when the gap distance was 3.25 mm, increasing welding current increased the penetration from 1.02 mm to 1.23 mm. However, when the gap distance was decreased to 1.75 mm, increasing welding current caused an increase in penetration from 1.07 mm to 1.25 mm. The intersection of the two curves can be reached approximately at the welding current of 134 A. Therefore, for high penetration, low gap distance should be selected up to this point under constant gas flow rate and welding speed.

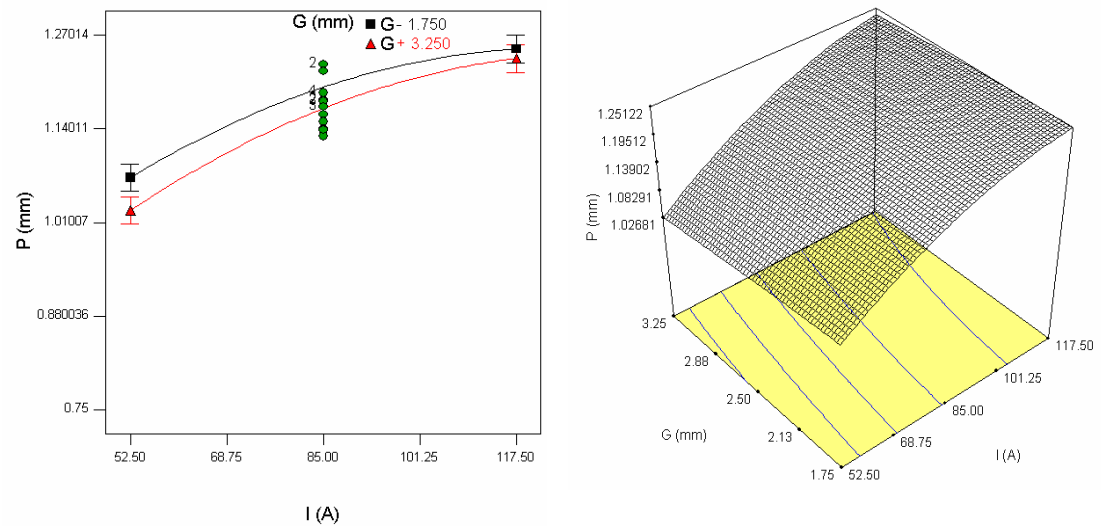

(a) (b)

Figure 4.53. Interaction effects of I and G on P at F=10 I/min and V=2.31 mm/s, (a. 2D interaction plot, b. 3D response surface plot)

Parallel lines in Figure 4.54 indicates that, when gap distance was 3.25 mm, increasing gas flow rate slightly increased penetration from 1.172 mm to 1.170 mm. However, when gap distance decreased to 1.75 mm, increasing gas flow rate caused an increase in penetration from 1.19 mm to 1.20 mm. Therefore, in order to obtain high penetration, low gap distance should be selected under constant welding speed and welding current.

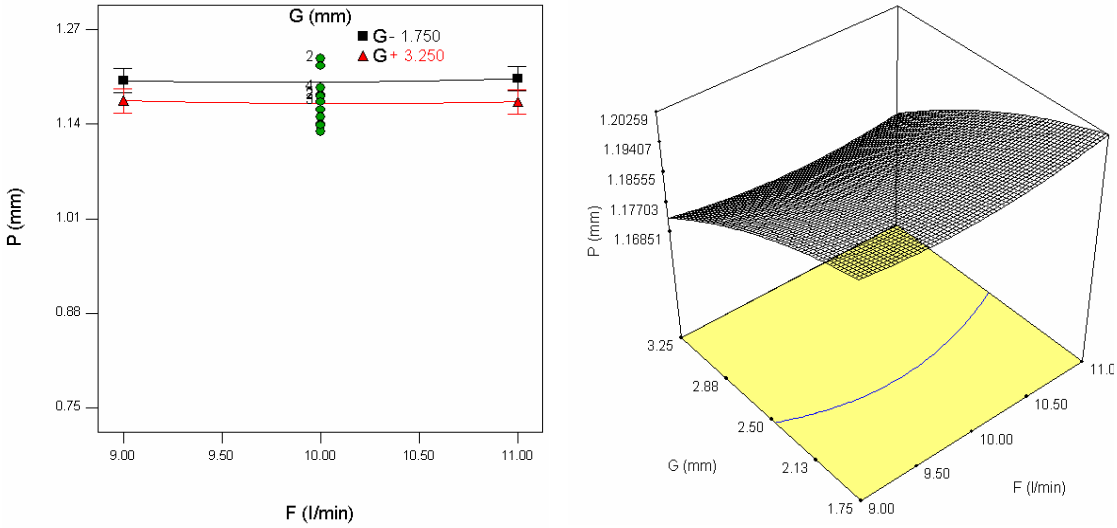

(a) (b)

Figure 4.54. Interaction effects of G and F on P at I=85 A and V=2.31 mm/s, (a. 2D interaction plot, b. 3D response surface plot)

4.2.6. Area of Penetration

Figures 4.55-4.60 shows the interaction effects of the TIG welding process parameters on the area of penetration. Figure 4.54 indicates that, when welding current was 117 A, increasing the welding speed caused a decrease in area of penetration from 10.5 mm^2 to 7.87 mm^2, however when the current decreased to 52 A, increasing welding speed decreased the area of penetration from 7.46 mm^2 to 6.01 mm^2. The intersection of the two curves can be reached when welding speed is approximately 4.55 mm/s. Therefore, for higher area of penetration, high current should be selected up to 4.55 mm/s.

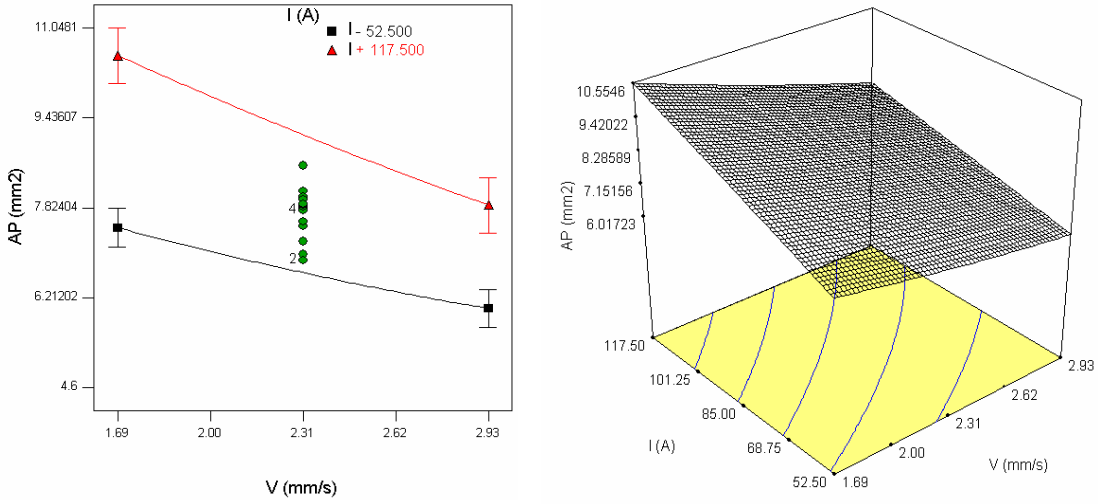

(a) (b)

Figure 4.55. Interaction effects of V and I on AP at F=10 I/min and G= 2.5 mm, (a. 2D interaction plot, b. 3D response surface plot)

Figure 4.56 indicates that, when gas flow rate was 9 I/min, increasing welding speed significantly decreased area of penetration from 9.13 mm^2 to 7.01 mm^2. However, when gas flow rate increased to 11 I/min mm, increasing welding speed caused a decrease in area of penetration from 8.98 mm^2 to 7.01 mm^2. The intersection point of the two curves can be reached approximately at the welding speed of 2.93 mm/s. Therefore, in order to obtain high area of penetration, lower gas flow rate should be selected up to 2.93 mm/s welding speed under constant gap distance and welding current.

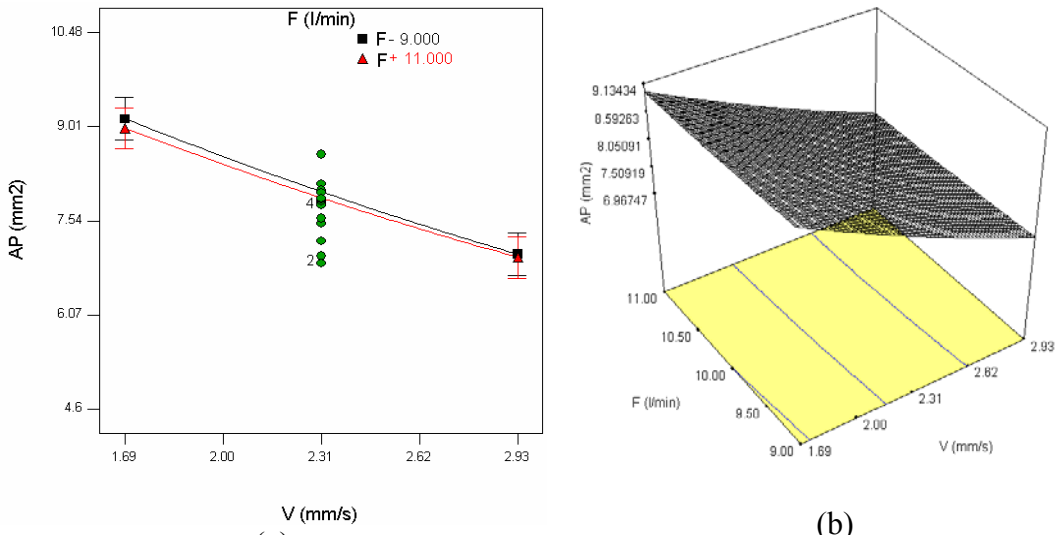

(a) (b)

Figure 4.56. Interaction effects of V and F on AP at I=85 A and G= 2.5 mm, (a. 2D interaction plot, b. 3D response surface plot)

Figure 4.57 indicates that, when gap distance was 3.25 mm, increasing the welding speed significantly decreased the area of penetration from 9.03 mm^2 to 6.98 mm^2, however, when the gap distance decreased to 1.75 mm, increasing welding speed caused a decrease in area of penetration from 9.03 mm^2 to 6.33 mm^2. The intersection point of two curves can be reached at the welding speed of 1.69 mm/s. Therefore, in order to obtain high area of penetration high gap distance should be used beyond this point under constant gas flow rate and welding current.

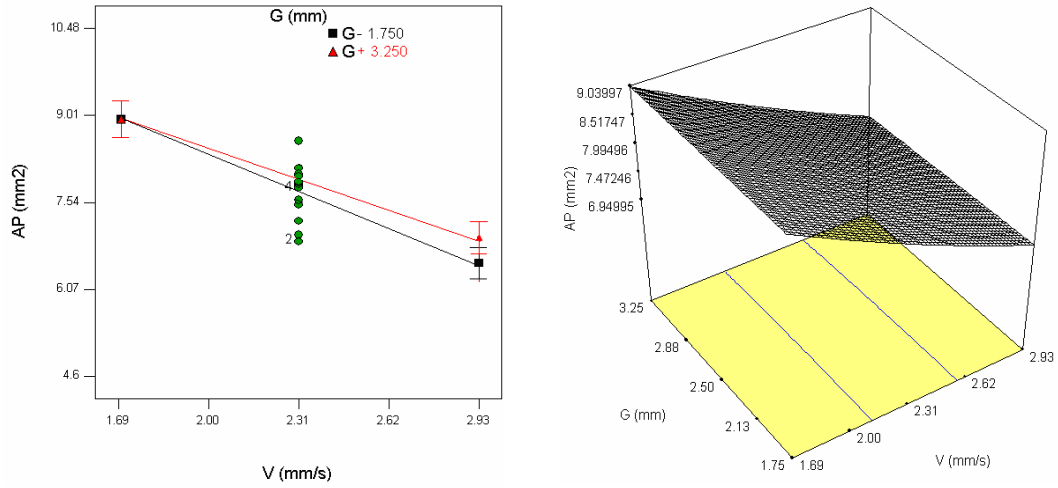

(a) (b)

Figure 4.57. Interaction effects of G and V on AP at F=10 I/min and I=85 A, (a. 2D interaction plot, b. 3D response surface plot)

Figure 4.58 indicates that, when gas flow rate was 9 I/min, increasing welding current significantly increased area of penetration from 6.71 mm^2 to 9.21 mm^2. However, when gas flow rate increased to 11 I/min, increasing welding current caused an increase in area of penetration from 6.64 mm^2 to 9.08 mm^2. The intersection point of the two lines can be reached approximately at the welding current of 48 A. Therefore, in order to obtain high area of penetration, low gas flow rate should be selected beyond this point under constant welding speed and gap distance.

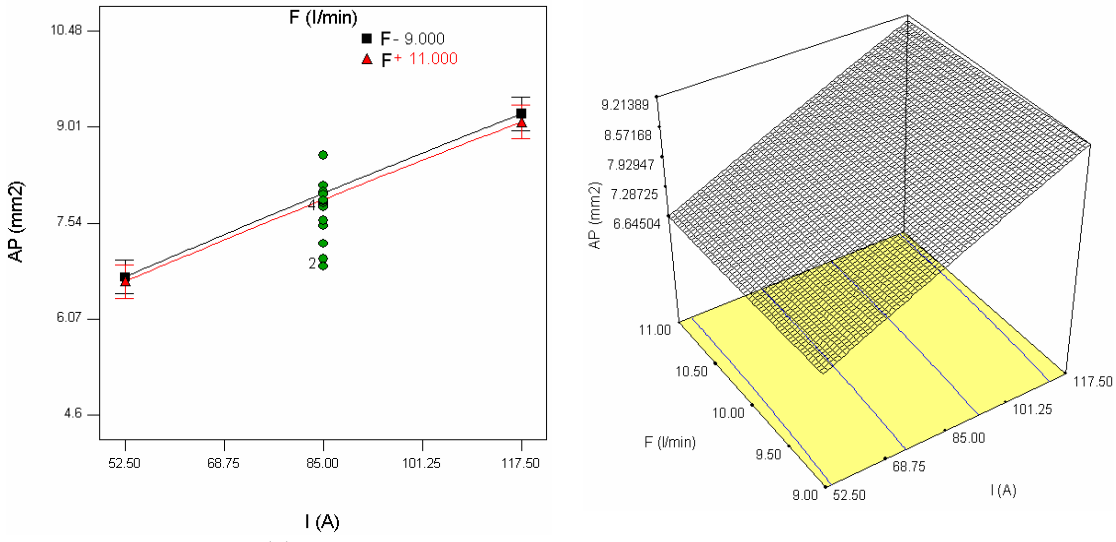

(a) (b)

Figure 4.58. Interaction effects of F and I on AP at V=2.31 mm/s and G= 2.5 mm, (a. 2D interaction plot, b. 3D response surface plot)

Figure 4.59 indicates that, when the gap distance was 3.25 mm, increasing welding current increased area of penetration from 6.66 mm^2 to 9.12 mm^2. However, when the gap distance was decreased to 1.75 mm, increasing welding current caused an increase in area of penetration from 6.60 mm^2 to 8.98 mm^2. The intersection of the two curves can be reached approximately at the welding current of 60 A. Therefore, for high area of penetration, low gap distance should be selected up to this point beyond this point high welding current should be selected under constant gas flow rate and welding speed.

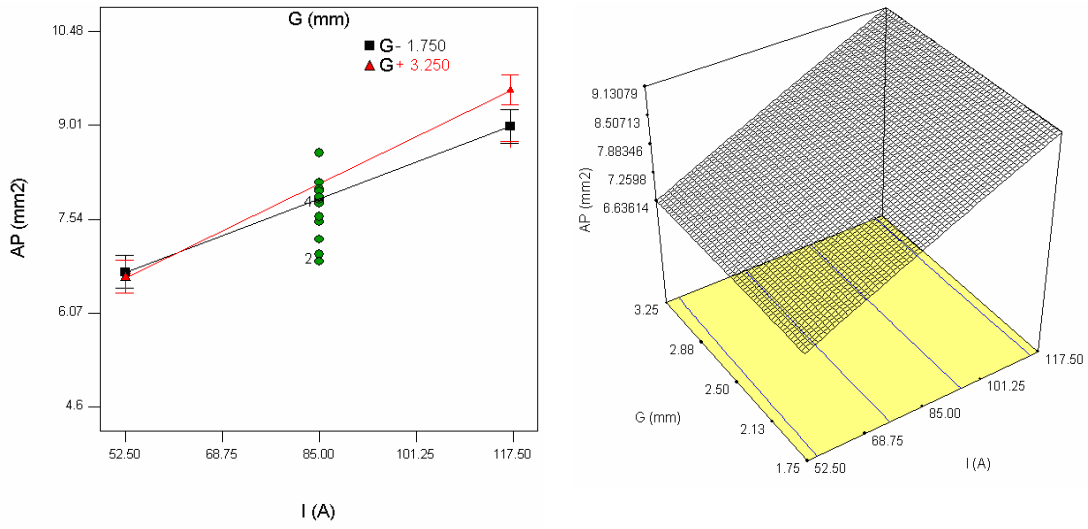

(a) (b)

Figure 4.59. Interaction effects of I and G on AP at F=10 I/min and V=2.31 mm/s, (a. 2D interaction plot, b. 3D response surface plot)

Figure 4.60 indicates that, when gap distance was 3.25 mm, increasing gas flow rate slightly increased penetration from 8.01 mm^2 to 7.88 mm^2. However, when gap distance decreased to 1.75 mm, increasing gas flow rate caused an increase in penetration from 7.65 mm^2 to 7.88 mm^2. The intersection of the two lines can be reached at the gas flow rate of 11 I/min. Therefore, in order to obtain high penetration, higher gap distance should be selected up to this point under constant welding speed and welding current.

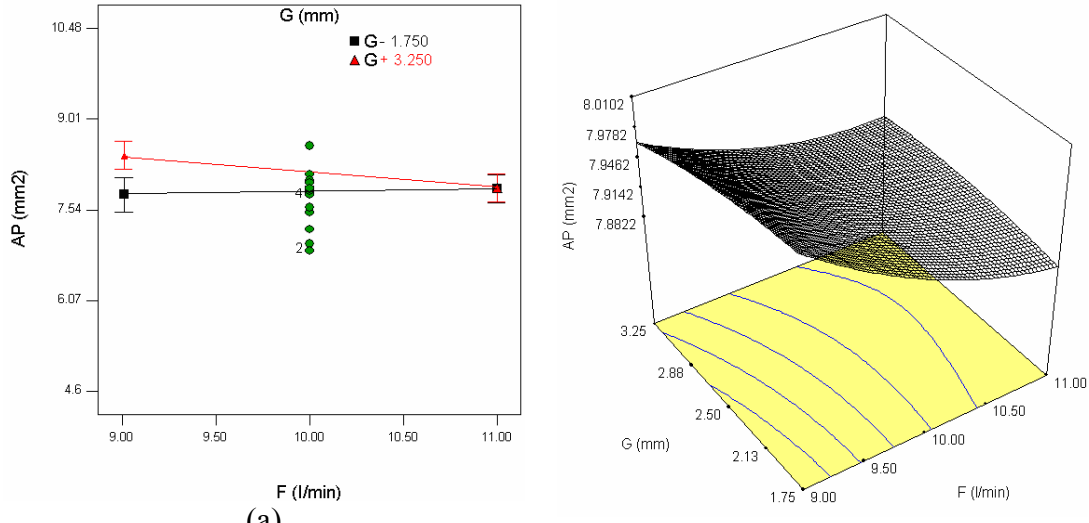

(a) (b)

Figure 4.60. Interaction effects of G and F on AP at I=85 A and V=2.31 mm/s, (a. 2D interaction plot, b. 3D response surface plot)

4.3. Mathematical Modeling and Statistical Analysis of the Results

4.3.1. Sequential Model Sum of Squares

Then regression calculations were carried out to fit the best model to the selected responses. The program calculates the effects for all model terms and produces statistics such as F-values, lack of fit and R-squared values for comparing the models. If a statistically significant model is detected, the program will underline and note the "Suggested" model and becomes the default model.

There are three choices for selecting the statistical significance. These are 0.1, 0.05 and 0.1. In this study the statistical significance threshold was selected as 0.05. The suggested models for each response are shown in Tables 4.2-4.8.

The Sequential Model Sum of Squares summary table shows how terms of increasing complexity contribute to the total model and accumulating improvement in the model fit as terms are added.

The model hierarchy is described below:

- **Linear:** the significance of adding the linear terms to the mean and blocks.
- **2FI:** the significance of adding the two factor interaction terms (2FI) to the mean, block and linear terms already in the model.
- **Quadratic:** the significance of adding the quadratic terms to the mean, block, linear and two factor interaction terms already in the model.
- **Cubic:** the significance of the cubic terms beyond all other terms.

For each source of terms (Linear, 2FI, Quadratic, etc.), the probability (PROB>F) value was examined to see if it falls down 0.05.

F test is used for comparing model variance with residual (error) variance. If the variances are close to the same, the ratio will be close to one and it is less likely that any of the factors have a significant effect on the response (Calculated by Model Mean Square divided by Residual Mean Square).

The F value was used in this thesis to test the significance of adding new model terms to those terms already in the model. For instance, the significance of the linear terms was tested after removing the effect of average and the blocks. Then, the significance of the quadratic terms was tested after removing the average, block and linear effects.

From the view point of sequential model sum of squares the Prob>F value under 0.05 is acceptable and suitable for the related response model. As indicated Table 4.2, for TL response analysis, since Prob>F value 0.0001<0.05, the quadratic model was found as the best choice for modeling Tensile load response. So, quadratic model terms are significant, but adding the cubic order terms will not significantly improve the fit. (Even if they were significant, the cubic terms would be aliased, so they wouldn't be useful for modeling purposes).

Table 4.2. Summary of sequential model sum of squares for tensile load

Response: TL

Sequential Model Sum of Squares

Source	Sum of Squares	DF	Mean Square	F Value	Prob > F	
Mean	1.197E+008	1	1.197E+008			
Linear	62704.60	4	15676.15	0.81	0.5201	
2FI	4.750E+005	6	79172.91	5.38	0.0001	
Quadratic	3.886E+005	4	97150.64	9.41	< 0.0001	Suggested
Cubic	3.729E+005	20	18647.22	2.55	0.0032	Suggested
Residual	4.017E+005	55	7303.63			
Total	1.214E+008	90	1.349E+006			

Sequential model sum of square analysis of HAZ (Figure 4.3) showed that, the Prob>F value (0.0001<0.05) of quadratic model of the quadratic terms were lower than the significance threshold value. So, the quadratic model was the best choice and adequate for HAZ modeling.

Since, Prob>F (0.0001<0.05) value, Table 4.4, was lower than the target value, the quadratic model for Sequential model sum of square analysis of UW was chosen as quadratic type.

Table 4.3. Summary of sequential model sum of squares for heat affected zone

Response: HAZ

Sequential Model Sum of Squares

Source	Sum of Squares	DF	Mean Square	F Value	Prob > F	
Mean	2138.22	1	2138.22			
Linear	127.05	4	31.76	145.45	< 0.0001	
2FI	0.95	6	0.16	0.71	0.6445	
Quadratic	6.42	4	1.60	10.74	< 0.0001	Suggested
Cubic	2.93	20	0.15	0.98	0.5024	
Residual	8.26	55	0.15			
Total	2283.84	90	25.38			

Table 4.4. Summary of sequential model sum of squares for upper width

Response: UW

Sequential Model Sum of Squares

Source	Sum of Squares	DF	Mean Square	F Value	Prob > F	
Mean	5216.96	1	5216.96			
Linear	136.93	4	34.23	49.87	< 0.0001	
2FI	18.52	6	3.09	6.12	0.1559	
Quadratic	3.33	4	0.83	1.71	< 0.0001	Suggested
Cubic	17.52	20	0.88	2.54	0.0033	Aliased
Residual	18.97	55	0.34			
Total	5412.24	90	60.14			

For UH analysis, Table 4.5, for the factor interactions as suggested in Table 4.5, we must choose suitable highest order model. Because higher order model already includes the lower order model terms. So, here for UH, P and AP, Table 4.5-4.7, the quadratic model was adequate and the best choice since their Prob>F value lower than 0.05.

Table 4.5. Summary of sequential model sum of squares for upper height

Response: UH

Sequential Model Sum of Squares

Source	Sum of Squares	DF	Mean Square	F Value	Prob > F	
Mean	1.61	1	1.61			
Linear	0.066	4	0.016	9.01	< 0.0001	
2FI	0.011	6	1.860E-003	1.02	0.4190	
Quadratic	0.021	4	5.297E-003	3.23	0.0168	Suggested
Cubic	0.045	20	2.271E-003	1.61	0.0833	Aliased
Residual	0.078	55	1.410E-003			
Total	1.83	90	0.020			

Table 4.6. Summary of sequential model sum of squares for penetration

Response: P

Sequential Model Sum of Squares

Source	Sum of Squares	DF	Mean Square	F Value	Prob > F	
Mean	106.46	1	106.46			
Linear	0.79	4	0.20	29.29	< 0.0001	
2FI	0.11	6	0.018	3.07	0.0094	
Quadratic	0.23	4	0.057	18.04	< 0.0001	Suggested
Cubic	0.12	20	5.789E-003	2.66	0.0022	
Residual	0.12	55	2.177E-003			
Total	107.81	90	1.20			

Table 4.7. Summary of sequential model sum of squares for area of penetration

Response: AP

Sequential Model Sum of Squares

Source	Sum of Squares	DF	Mean Square	F Value	Prob > F	
Mean	4647.92	1	4647.92			
Linear	81.89	4	20.47	32.93	< 0.0001	
2FI	8.83	6	1.47	2.64	0.0219	Suggested
Quadratic	1.62	4	0.40	0.72	0.5840	Suggested
Cubic	17.85	20	0.89	2.00	0.0223	
Residual	24.55	55	0.45			
Total	4782.65	90	53.14			

4.3.2. Lack of Fit Test

In this section of the study, a comparison of residual error to the Pure Error from replicated design points was made by using the Lack of Fit Tests. Models with lowest Prob>F values were discarded from the selecting model as a response predictor. In the lack of fit tests, the model, which has not so small F value and probability value greater than 0.05 was desirable.

The lacks of fit tables were then examined as shown in Tables 4.8-4.13. The test on TL and HAZ responses are given in, Tables 4.8-4.9. As suggested in Table 4.8, although cubic model seemed as an alternative choice, it was ignored due to the high Prob>F value. Model analysis performed on the HAZ response (Table 4.9) showed that, since the highest order model terms are significant in our design, the quadratic model was the best choice.

As shown in Tables 4.10-4.13, also the quadratic model showed the best logical choice for UW, UH, P and AP response prediction model.

As a result the selected quadratic models for tensile load (TL), heat affected zone (HAZ), upper width (UW), upper height (UH), penetration (P) and

area of penetration (AP) analysis would be the logical choices since their probability values smaller than 0.05 and cubic order terms will not significantly improve the fit.

Table 4.8. Lack of fit test for TL

Lack of Fit Tests

Source	Sum of Squares	DF	Mean Square	F Value	Prob > F	
Linear	1.468E+006	58	25315.53	4.02	< 0.0001	
2FI	9.933E+005	52	19101.22	3.03	0.0013	
Quadratic	6.047E+005	48	12597.10	2.00	0.0278	Suggested
Cubic	2.317E+005	28	8275.59	1.31	0.2400	Suggested
Pure Error	1.700E+005	27	6295.67			

Table 4.9. Lack of fit test for HAZ

Lack of Fit Tests

Source	Sum of Squares	DF	Mean Square	F Value	Prob > F	
Linear	13.93	58	0.24	1.40	0.1705	
2FI	12.98	52	0.25	1.46	0.1466	
Quadratic	6.57	48	0.14	0.80	0.7578	Suggested
Cubic	3.63	28	0.13	0.76	0.7668	
Pure Error	4.63	27	0.17			

Table 4.10. Lack of fit test for UW

Lack of Fit Tests

Source	Sum of Squares	DF	Mean Square	F Value	Prob > F	
Linear	47.51	58	0.82	2.04	0.0224	
2FI	28.99	52	0.56	1.39	0.1788	Suggested
Quadratic	25.66	48	0.53	1.33	0.2139	Suggested
Cubic	8.13	28	0.29	0.72	0.7996	
Pure Error	10.83	27	0.40			

Table 4.11. Lack of fit test for UH

Lack of Fit Tests

Source	Sum of Squares	DF	Mean Square	F Value	Prob > F	
Linear	0.13	58	2.272E-003	2.60	0.0040	
2FI	0.12	52	2.319E-003	2.66	0.0037	
Quadratic	0.099	48	2.071E-003	2.37	0.0091	Suggested
Cubic	0.054	28	1.928E-003	2.21	0.0214	
Pure Error	0.024	27	8.727E-004			

Table 4.12. Lack of fit test for P

Lack of Fit Tests

Source	Sum of Squares	DF	Mean Square	F Value	Prob > F	
Linear	0.54	58	9.327E-003	8.72	< 0.0001	
2FI	0.43	52	8.331E-003	7.79	< 0.0001	
Quadratic	0.21	48	4.305E-003	4.03	0.0001	Suggested
Cubic	0.091	28	3.245E-003	3.03	0.0025	
Pure Error	0.029	27	1.069E-003			

Table 4.13. Lack of fit test for AP

Lack of Fit Tests

Source	Sum of Squares	DF	Mean Square	F Value	Prob > F	
Linear	47.96	58	0.83	4.58	< 0.0001	
2FI	39.14	52	0.75	4.17	< 0.0001	Suggested
Quadratic	37.52	48	0.78	4.33	< 0.0001	Suggested
Cubic	19.67	28	0.70	3.89	0.0003	
Pure Error	4.88	27	0.18			

4.3.3. Model Summary Statistics

The Model Summary Statistics Tables, Table 4.14-4.19, constituted to list other statistics such as Standard Deviation (Root MSE), R-Squared, Adjusted R-Squared, Predicted R-Squared and the predicted residual sum of squares (PRESS) statistic useful in comparing models. Since, the predicted residual sum of squares

(PRESS) is a measure of how well the model fits each point in the design, in this analysis, as a rule, the model which has low standard deviation, R-Squared near 1 and relatively low PRESS was chosen as a model.

Also, Tables 4.14-4.15 show that, there are two suggested model (linear-quadratic, 2FI-quadratic). The quadratic type model was chosen due to significant additional terms for UW, UH, P and AP responses. Hence, the Linear, 2FI model sources were discarded from the design.

Table 4.14. Model summary statistics for TL

Model Summary Statistics

Source	Std. Dev.	R-Squared	Adjusted R-Squared	Predicted R-Squared	PRESS	
Linear	138.83	0.0369	-0.0085	-0.0925	1.858E+006	
2FI	121.35	0.3161	0.2296	-0.0110	1.720E+006	
Quadratic	85.46	0.7638	0.6179	-0.1066	1.882E+006	Suggested
Cubic	101.63	0.5446	0.4596	0.2656	1.249E+006	Suggested

Table 4.15. Model summary statistics for HAZ

Model Summary Statistics

Source	Std. Dev.	R-Squared	Adjusted R-Squared	Predicted R-Squared	PRESS	
Linear	0.47	0.8725	0.8665	0.8531	21.38	
2FI	0.47	0.8790	0.8637	0.8335	24.24	
Quadratic	0.39	0.9231	0.9087	0.8856	16.66	Suggested
Cubic	0.39	0.9432	0.9082	0.7695	33.57	

Also, Tables 4.16-4.19 show that, there are two suggested model (linear-quadratic, 2FI-quadratic). The quadratic type model was chosen due to significant additional terms for UW, UH, P and AP responses. Hence, the linear, 2FI model sources were discarded from the design.

Table 4.16. Model summary statistics for UW

Model Summary Statistics

Source	Std. Dev.	R-Squared	Adjusted R-Squared	Predicted R-Squared	PRESS	
Linear	0.83	0.7012	0.6872	0.6640	65.62	
2FI	0.71	0.8131	0.7703	0.7249	53.72	Suggested
Quadratic	0.70	0.7961	0.7783	0.7224	54.21	Suggested
Cubic	0.59	0.9029	0.8428	0.7147	55.70	

Table 4.17. Model summary statistics for UH

Model Summary Statistics

Source	Std. Dev.	R-Squared	Adjusted R-Squared	Predicted R-Squared	PRESS	
Linear	0.043	0.2978	0.2647	0.2047	0.18	
2FI	0.043	0.3482	0.2657	0.1300	0.19	
Quadratic	0.040	0.4440	0.3402	0.1451	0.19	Suggested
Cubic	0.038	0.6494	0.4327	-0.0517	0.23	

Table 4.18. Model summary statistics for P

Model Summary Statistics

Source	Std. Dev.	R-Squared	Adjusted R-Squared	Predicted R-Squared	PRESS	
Linear	0.082	0.5796	0.5598	0.5183	0.65	
2FI	0.076	0.6591	0.6159	0.4910	0.69	
Quadratic	0.056	0.8262	0.7938	0.7043	0.40	Suggested
Cubic	0.047	0.9117	0.8571	0.4680	0.72	

Table 4.19. Model summary statistics for AP

Model Summary Statistics

Source	Std. Dev.	R-Squared	Adjusted R-Squared	Predicted R-Squared	PRESS	
Linear	0.79	0.6078	0.5893	0.5573	59.65	
2FI	0.75	0.6733	0.6320	0.5900	55.24	Suggested
Quadratic	0.75	0.6853	0.6266	0.5368	62.40	Suggested
Cubic	0.67	0.8178	0.7051	-0.1868	159.90	

4.3.4. Analysis of Variances (ANOVA)

The purpose of the ANOVA is to define welding process parameters which significantly affect the quality characteristic or the response of the welding process. This is accomplished by separating the total variability of the responses, which is measured by the sum of the squared deviations from the total mean of the responses, into contributions by each welding process parameter and the error. The percentage contribution by each of the process parameter in the total sum of the squared deviations can be used to evaluate the importance of the process parameter change on each response. In addition, the F test was used to determine which welding process parameters have a significant effect on the responses. Usually, the change of the welding process parameter had a significant effect on the related response when the F value is large.

Results of ANOVA, Table 4.20-4.25, indicated that welding speed, welding current, arc gap and flow rate are the significant welding process parameters affecting the welding quality characteristics.

Table 4.20. ANOVA for quadratic model of TL

Source	Sum of Squares	DF	Mean Square	F Value	Prob > F
Model	7.981E+005	14	57006.82	4.59	< 0.0001
A	*73279.01*	*1*	*73279.01*	*5.90*	*0.0176*
B	*37401.48*	*1*	*37401.48*	*3.01*	*0.0869*
C	*2245.15*	*1*	*2245.15*	*0.18*	*0.6721*
D	*19120.01*	*1*	*19120.01*	*1.54*	*0.2188*
A^2	*82139.56*	*1*	*82139.56*	*6.61*	*0.0121*
B^2	*2.248E+005*	*1*	*2.248E+005*	*18.08*	*< 0.0001*
C^2	*4332.49*	*1*	*4332.49*	*0.35*	*0.5567*
D^2	*13771.03*	*1*	*13771.03*	*1.11*	*0.2959*
AB	*49.44*	*1*	*49.44*	*3.977E-003*	*0.9499*
AC	*767.40*	*1*	*767.40*	*0.062*	*0.8044*
AD	*20.30*	*1*	*20.30*	*1.633E-003*	*0.9679*
BC	*356.91*	*1*	*356.91*	*0.029*	*0.8659*
BD	*242.05*	*1*	*242.05*	*0.019*	*0.8894*
CD	*595.02*	*1*	*595.02*	*0.048*	*0.8274*

As shown in Table 4.21-4.22, according to the larger F value, the most effective welding parameters on HAZ and UW were found as welding current, welding speed, arc gap and gas flow rate. The nature of the heat source is an important factor governing heat flow during welding. The efficiency and energy-density distribution of the heat source can directly affect heat flow during welding ($Q = \frac{EI}{1000V}$, where E: welding voltage, I: welding current, V: welding speed).

The welding heat source moves at a constant speed along a straight path. The origin of the moving coordinates coincides with the center of the heat source. The intense welding heat melts the metal and forms a molten weld pool. Some of the heat conducted into the base metal is used to melt the weld bead; whereas some is lost from either the arc column or the metal surface to the environment surrounding the plate and forms heat affected zone. Three metallurgical zones are formed in the plate upon completion of the thermal cycle: the weld metal (WM) zone, the heat-affected zone (HAZ), and the base metal (BM) zone. The peak temperature (formed by welding arc) and the subsequent cooling rates determine the HAZ structures, whereas the thermal gradients, the solidification rates, and the cooling rates at the liquid-solid pool boundary determine the solidification structure of WM zone.

Generally speaking, the higher the heat input rate, the lower is the cooling rate and the larger is the weld pool and heat affected zone. There is an inverse relationship between weld pool size and cooling rate. So, we can understand from here that it is possible to make the weld pool of any size, simply by increasing the heat input rate. However, this will make the weld pool difficult to control as it becomes larger, and the HAZ and weld width may become undesirably large.

Table 4.21. ANOVA for quadratic model of HAZ

Source	Sum of Squares	DF	Mean Square	F Value	Prob > F
Model	148.21	14	10.59	62.66	< 0.0001
A	*17.17*	*1*	*17.17*	*101.64*	*< 0.0001*
B	*93.61*	*1*	*93.61*	*554.06*	*< 0.0001*
C	*0.12*	*1*	*0.12*	*0.69*	*0.4077*
D	*1.76*	*1*	*1.76*	*10.40*	*0.0019*
A^2	*1.80*	*1*	*1.80*	*10.68*	*0.0016*
B^2	*1.96*	*1*	*1.96*	*11.59*	*0.0011*
C^2	*2.615E-003*	*1*	*2.615E-003*	*0.015*	*0.9013*
D^2	*0.12*	*1*	*0.12*	*0.74*	*0.3932*
AB	*0.63*	*1*	*0.63*	*3.74*	*0.0570*
AC	*7.363E-005*	*1*	*7.363E-005*	*4.358E-004*	*0.9834*
AD	*4.416E-007*	*1*	*4.416E-007*	*2.614E-006*	*0.9987*
BC	*3.360E-003*	*1*	*3.360E-003*	*0.020*	*0.8882*
BD	*0.13*	*1*	*0.13*	*0.78*	*0.3799*
CD	*9.352E-003*	*1*	*9.352E-003*	*0.055*	*0.8146*

Table 4.22. ANOVA for quadratic model of UW

Source	Sum of Squares	DF	Mean Square	F Value	Prob > F
Model	144.31	14	10.31	17.82	< 0.0001
A	*26.30*	*1*	*26.30*	*45.45*	*< 0.0001*
B	*98.81*	*1*	*98.81*	*170.78*	*< 0.0001*
C	*0.58*	*1*	*0.58*	*1.00*	*0.3195*
D	*2.41*	*1*	*2.41*	*4.16*	*0.0450*
A^2	*0.69*	*1*	*0.69*	*1.19*	*0.2793*
B^2	*2.32*	*1*	*2.32*	*4.02*	*0.0486*
C^2	*0.33*	*1*	*0.33*	*0.57*	*0.4511*
D^2	*5.937E-003*	*1*	*5.937E-003*	*0.010*	*0.9196*
AB	*1.73*	*1*	*1.73*	*3.00*	*0.0875*
AC	*4.480E-003*	*1*	*4.480E-003*	*7.743E-003*	*0.9301*
AD	*0.029*	*1*	*0.029*	*0.050*	*0.8235*
BC	*3.558E-003*	*1*	*3.558E-003*	*6.149E-003*	*0.9377*
BD	*0.067*	*1*	*0.067*	*0.12*	*0.7338*
CD	*0.049*	*1*	*0.049*	*0.084*	*0.7724*

Table 4.23 shows the ANOVA analysis for Upper Height response. UH is greatly influenced from the welding speed. The most effective welding parameters on this response may be arranged in order as welding speed, welding current, gas flow rate and welding gap.

It is known that rapid cooling of weld metal results in a loss of ductility and penetration. In some instances the tensile load are appreciably affected by the cooling rate due to the low penetration and the elongation and reduction in area markedly decrease. High welding currents and low travel speeds in gas tungsten arc welding provide a large amount of heat input per mm of weld and resulted with higher penetration into the base metal, higher heat affected zone and area of penetration. As a result, it can be stated that the penetration and area of penetration depend mainly on the rate of heat input (especially current and travel speed).

The obtained results on P and AP response analysis, (Table 4.24 and 4.25) have showed that welding current, welding speed, arc gap and gas flow rate respectively have a markedly effect on penetration profile.

Table 4.23. ANOVA for quadratic model of UH

Source		Sum of Squares	DF	Mean Square	F Value	Prob > F
Model		0.10	14	7.319E-003	3.75	< 0.0001
	A	*0.062*	*1*	*0.062*	*32.02*	*< 0.0001*
	B	*0.061*	*1*	*0.061*	*31.20*	*< 0.0001*
	C	*1.791E-003*	*1*	*1.791E-003*	*0.92*	*0.3410*
	D	*1.525E-003*	*1*	*1.525E-003*	*0.78*	*0.3793*
	A^2	*0.012*	*1*	*0.012*	*6.38*	*0.0136*
	B^2	*2.157E-004*	*1*	*2.157E-004*	*0.11*	*0.7404*
	C^2	*1.113E-003*	*1*	*1.113E-003*	*0.57*	*0.4524*
	D^2	*2.435E-003*	*1*	*2.435E-003*	*1.25*	*0.2674*
	AB	*8.110E-003*	*1*	*8.110E-003*	*4.16*	*0.0449*
	AC	*8.334E-005*	*1*	*8.334E-005*	*0.043*	*0.8368*
	AD	*1.382E-003*	*1*	*1.382E-003*	*0.71*	*0.4025*
	BC	*1.527E-003*	*1*	*1.527E-003*	*0.78*	*0.3791*
	BD	*1.823E-003*	*1*	*1.823E-003*	*0.93*	*0.3368*
	CD	*1.302E-003*	*1*	*1.302E-003*	*0.67*	*0.4164*

Table 4.24. ANOVA for quadratic model of P

Source		Sum of Squares	DF	Mean Square	F Value	Prob > F
Model		1.09	14	0.078	16.96	< 0.0001
	A	*0.053*	*1*	*0.053*	*11.61*	*0.0011*
	B	*0.40*	*1*	*0.40*	*87.44*	*< 0.0001*
	C	*2.232E-005*	*1*	*2.232E-005*	*4.858E-003*	*0.9446*
	D	*0.030*	*1*	*0.030*	*6.58*	*0.0123*
	A^2	*5.589E-003*	*1*	*5.589E-003*	*1.22*	*0.2736*
	B^2	*0.21*	*1*	*0.21*	*46.42*	*< 0.0001*
	C^2	*4.152E-004*	*1*	*4.152E-004*	*0.090*	*0.7645*
	D^2	*0.055*	*1*	*0.055*	*11.98*	*0.0009*
	AB	*3.476E-003*	*1*	*3.476E-003*	*0.76*	*0.3871*
	AC	*7.594E-004*	*1*	*7.594E-004*	*0.17*	*0.6855*
	AD	*0.017*	*1*	*0.017*	*3.64*	*0.0602*
	BC	*5.699E-004*	*1*	*5.699E-004*	*0.12*	*0.7257*
	BD	*0.013*	*1*	*0.013*	*2.80*	*0.0982*
	CD	*9.188E-004*	*1*	*9.188E-004*	*0.20*	*0.6560*

Table 4.25. ANOVA for quadratic model of AP

Source		Sum of Squares	DF	Mean Square	F Value	Prob > F
Model		98.17	14	7.01	12.94	< 0.0001
	A	*34.62*	*1*	*34.62*	*63.87*	*< 0.0001*
	B	*76.53*	*1*	*76.53*	*141.19*	*< 0.0001*
	C	*0.010*	*1*	*0.010*	*0.019*	*0.8902*
	D	*0.018*	*1*	*0.018*	*0.033*	*0.8562*
	A^2	*5.658E-003*	*1*	*5.658E-003*	*0.010*	*0.9189*
	B^2	*2.24*	*1*	*2.24*	*4.14*	*0.0455*
	C^2	*0.22*	*1*	*0.22*	*0.40*	*0.5270*
	D^2	*2.78*	*1*	*2.78*	*5.13*	*0.0264*
	AB	*2.33*	*1*	*2.33*	*4.30*	*0.0415*
	AC	*0.029*	*1*	*0.029*	*0.054*	*0.8168*
	AD	*0.089*	*1*	*0.089*	*0.16*	*0.6869*
	BC	*0.072*	*1*	*0.072*	*0.13*	*0.7158*
	BD	*0.024*	*1*	*0.024*	*0.044*	*0.8346*
	CD	*0.063*	*1*	*0.063*	*0.12*	*0.7334*

Also, the ANOVA in this case confirmed the adequacy of the quadratic model for all the responses (The model PROB>F is less than 0.05). In addition to these as indicated in following Tables, software provides residuals and diagnostics of models shown in Tables from 4.26 to 4.30.

4.3.5. Mathematical Modeling

The predictive models for TL, HAZ, UW, UH, P and AP are listed in both actual and coded terms in Tables 4.26-4.31. The coded (or pseudo) equation is useful for identifying the relative significance of the factors by comparing the factor coefficients. This comparison cannot be made with the actual equation because the coefficients are scaled to accommodate the units of each factor. The equations give identical predictions. These equations, used for prediction of welding parameters and responses, they have no block effects. Also, to contribute these Tables the degree of freedom was taken as 1 for testing coefficients of welding parameters.

95% confidence interval (CI) High and Low columns represent the range that the true coefficient should be found in 95% of the time. If this range spans 0 (one limit is positive and the other negative) then the coefficient of 0 could be true, indicating the factor has no effect. In addition, Variance Inflation Factor (VIF) measures how much the variance of the model is inflated by the lack of orthogonality in the design. If the center point is orthogonal to all other factors in the model, the VIF is 1. VIF values greater than 10 indicate that the factors are too correlated together (they are not independent).

Table 4.26. Model summary for TL

Factor	Coefficient Estimate	DF	Standard Error	95% CI Low	95% CI High	VIF
Intercept	1263.45	1	20.30	1223.01	1303.88	
A-V	-15.42	1	19.35	-53.98	23.13	3.72
B-I	9.89	1	15.33	-20.64	40.42	2.80
C-F	5.69	1	7.50	-9.24	20.62	1.57
D-G	-11.62	1	7.84	-27.24	4.01	1.57
A^2	-32.67	1	10.54	-53.66	-11.67	2.96
B^2	-53.80	1	8.96	-71.64	-35.96	2.23
C^2	1.93	1	3.09	-4.22	8.09	1.10
D^2	-3.19	1	3.62	-10.41	4.03	1.17
AB	28.14	1	18.68	-9.08	65.35	6.25
AC	4.77	1	7.37	-9.91	19.44	1.83
AD	4.64	1	7.69	-10.69	19.97	1.94
BC	3.30	1	6.88	-10.40	17.00	2.47
BD	-2.33	1	7.14	-16.57	11.90	2.42
CD	0.080	1	3.66	-7.22	7.38	1.01

Table 4.27. Model summary for HAZ

Factor	Coefficient Estimate	DF	Standard Error	95% CI Low	95% CI High	VIF
Intercept	5.46	1	0.077	5.30	5.61	
A-V	-0.84	1	0.074	-0.99	-0.70	3.72
B-I	1.44	1	0.058	1.32	1.55	2.80
C-F	-0.042	1	0.029	-0.099	0.015	1.57
D-G	0.082	1	0.030	0.023	0.14	1.57
A^2	0.21	1	0.040	0.13	0.29	2.96
B^2	-0.041	1	0.034	-0.11	0.026	2.23
C^2	0.019	1	0.012	-4.013E-003	0.043	1.10
D^2	0.027	1	0.014	-1.963E-004	0.055	1.17
AB	-0.26	1	0.071	-0.40	-0.12	6.25
AC	7.677E-004	1	0.028	-0.055	0.057	1.83
AD	0.010	1	0.029	-0.048	0.069	1.94
BC	-7.967E-003	1	0.026	-0.060	0.044	2.47
BD	0.025	1	0.027	-0.029	0.079	2.42
CD	1.397E-003	1	0.014	-0.026	0.029	1.01

Table 4.28. Model summary for UW

Factor	Coefficient Estimate	DF	Standard Error	95% CI Low	95% CI High	VIF
Intercept	8.77	1	0.14	8.49	9.05	
A-V	-0.83	1	0.13	-1.09	-0.56	3.72
B-I	1.41	1	0.11	1.20	1.62	2.80
C-F	-0.042	1	0.051	-0.14	0.060	1.57
D-G	0.11	1	0.054	1.791E-003	0.22	1.57
A^2	-0.095	1	0.072	-0.24	0.049	2.96
B^2	-0.16	1	0.061	-0.28	-0.035	2.23
C^2	-3.217E-003	1	0.021	-0.045	0.039	1.10
D^2	-0.011	1	0.025	-0.061	0.039	1.17
AB	-0.097	1	0.13	-0.35	0.16	6.25
AC	0.047	1	0.051	-0.053	0.15	1.83
AD	-1.811E-003	1	0.053	-0.11	0.10	1.94
BC	7.114E-004	1	0.047	-0.093	0.095	2.47
BD	0.020	1	0.049	-0.077	0.12	2.42
CD	0.013	1	0.025	-0.037	0.063	1.01

Table 4.29. Model summary for UH

Factor	Coefficient Estimate	DF	Standard Error	95% CI Low	95% CI High	VIF
Intercept	0.15	1	8.088E-003	0.13	0.16	
A-V	-0.041	1	7.711E-003	-0.056	-0.026	3.72
B-I	0.034	1	6.106E-003	0.022	0.046	2.80
C-F	2.296E-003	1	2.987E-003	-3.653E-003	8.246E-003	1.57
D-G	-3.186E-003	1	3.124E-003	-9.410E-003	3.038E-003	1.57
A^2	0.011	1	4.199E-003	2.825E-003	0.020	2.96
B^2	-6.801E-004	1	3.568E-003	-7.789E-003	6.428E-003	2.23
C^2	-1.351E-003	1	1.231E-003	-3.803E-003	1.101E-003	1.10
D^2	2.119E-003	1	1.444E-003	-7.573E-004	4.996E-003	1.17
AB	-0.016	1	7.444E-003	-0.031	-9.896E-004	6.25
AC	-6.474E-004	1	2.935E-003	-6.494E-003	5.199E-003	1.83
AD	3.079E-003	1	3.066E-003	-3.028E-003	9.186E-003	1.94
BC	-3.474E-003	1	2.740E-003	-8.933E-003	1.984E-003	2.47
BD	-3.064E-003	1	2.846E-003	-8.734E-003	2.607E-003	2.42
CD	1.394E-003	1	1.460E-003	-1.514E-003	4.302E-003	1.01

Table 4.30. Model summary for P

Factor	Coefficient Estimate	DF	Standard Error	95% CI Low	95% CI High	VIF
Intercept	1.19	1	0.011	1.16	1.21	
A-V	-0.042	1	0.011	-0.063	-0.021	3.72
B-I	0.098	1	8.450E-003	0.081	0.11	2.80
C-F	3.058E-004	1	4.133E-003	-7.928E-003	8.539E-003	1.57
D-G	-0.015	1	4.324E-003	-0.023	-6.083E-003	1.57
A^2	4.620E-004	1	5.811E-003	-0.011	0.012	2.96
B^2	-0.036	1	4.938E-003	-0.046	-0.026	2.23
C^2	3.203E-003	1	1.704E-003	-1.903E-004	6.597E-003	1.10
D^2	-3.265E-003	1	1.998E-003	-7.246E-003	7.165E-004	1.17
AB	6.681E-003	1	0.010	-0.014	0.027	6.25
AC	3.103E-004	1	4.062E-003	-7.781E-003	8.401E-003	1.83
AD	-9.778E-003	1	4.243E-003	-0.018	-1.326E-003	1.94
BC	-1.711E-004	1	3.792E-003	-7.725E-003	7.383E-003	2.47
BD	8.069E-003	1	3.939E-003	2.219E-004	0.016	2.42
CD	-1.120E-003	1	2.020E-003	-5.144E-003	2.905E-003	1.01

Table 4.31. Model summary for AP

Factor	Coefficient Estimate	DF	Standard Error	95% CI Low	95% CI High	VIF
Intercept	7.93	1	0.15	7.63	8.22	
A-V	-1.03	1	0.14	-1.32	-0.75	3.72
B-I	1.24	1	0.11	1.01	1.46	2.80
C-F	-0.048	1	0.055	-0.16	0.062	1.57
D-G	-8.017E-003	1	0.058	-0.12	0.11	1.57
A^2	0.082	1	0.078	-0.074	0.24	2.96
B^2	-0.030	1	0.066	-0.16	0.10	2.23
C^2	0.020	1	0.023	-0.025	0.066	1.10
D^2	-7.511E-003	1	0.027	-0.061	0.046	1.17
AB	-0.31	1	0.14	-0.58	-0.034	6.25
AC	0.025	1	0.054	-0.083	0.13	1.83
AD	-8.492E-003	1	0.057	-0.12	0.10	1.94
BC	-0.014	1	0.051	-0.12	0.087	2.47
BD	7.788E-003	1	0.053	-0.098	0.11	2.42
CD	0.016	1	0.027	-0.038	0.070	1.01

The response function representing any of the weld pool dimensions can be expressed as y = f (V, I, F, G). The relationship selected, being a second-degree response surface quadratic modeling, is expressed as follows;

$$Y = b_0 + b_1V + b_2I + b_3F + b_4G + b_{11}V^2 + b_{22}I^2 + b_{33}F^2 + b_{44}G^2 + b_{12}VI + b_{13}VF + b_{14}VG + b_{23}IF + b_{24}IG + b_{34}FG \quad (4.1)$$

Where "b" values are the coefficients of the models. The values of the coefficients were calculated by regression analysis with the help of ANOVA module of Design Expert 6.0 software.

The final mathematical models developed are given below. The process control variables are expressed in their coded form.

Transverse tensile load:

$$TL=630.03049 + 238.03487 * V + 8.10260 * I + 25.05345 * F + 4.03510 * G - 75.10057 * V^2 - 0.039932 * I^2 -1.78092 * F^2 - 7.09131 * G^2 - 0.059916 * V * I + 3.34043 * V * F + 0.73102 * V * G - 0.041339 * I * F + 0.045711 * I * G + 1.17361 * F * G \quad (4.2)$$

Heat affected zone:

$$HAZ=4.25726-2.25321 * V + 0.078141 * I + 0.027766 * F + 0.19755 * G + 0.35202 * V^2 - 1.17845E-004 * I^2 - 1.38373E-003 * F^2 - 0.021331 * G^2 - 6.77070E-003 * V * I - 1.03468E-003 * V * F + 1.07815E-004 * V * G - 1.26837E-004 * I * F + 1.06672E-003 * I * G - 4.65278E-003 * F * G \quad (4.3)$$

Upper width:

$$UW=3.30265 + 0.44806 * V + 0.089617 * I + 0.20048 * F + 0.074331 * G - 0.21720 * V^2 - 1.28410E-004 * I^2 - 0.015592 * F^2 - 4.65626E-003 * G^2 - 0.011222 * V * I +8.07090E-003 * V * F - 0.027623 * V * G +1.30514E-004 * I * F + 7.62815E-004 * I * G + 0.010625 * F * G \quad (4.4)$$

Upper height:

$$UH=0.083160 - 0.14708 * V + 4.27108E\text{-}003 * I + 0.026577 * F - 0.039542 * G + 0.029239 * V^2 - 1.23691E\text{-}006 * I^2 - 9.02466E\text{-}004 * F^2 + 2.98197E\text{-}003 * G^2 - 7.67366E\text{-}004 * V * I - 1.10081E\text{-}003 * V * F + 6.03239E\text{-}003 * V * G - 8.54959E\text{-}005 * I * F - 1.25432E\text{-}004 * I * G + 1.73611E\text{-}003 * F * G \quad (4.5)$$

Penetration:

$$P=0.64397 + 0.066087 * V + 6.96690E\text{-}003 * I + 0.018256 * F + 0.087894 * G - 0.019590 * V^2 - 3.88930E\text{-}005 * I^2 - 5.51306E\text{-}004 * F^2 - 0.014174 * G^2 + 5.02410E\text{-}004 * V * I - 3.32300E\text{-}003 * V * F - 0.020984 * V * G + 5.22375E\text{-}005 * I * F + 3.33420E\text{-}004 * I * G - 1.45833E\text{-}003 * F * G \quad (4.6)$$

Area of penetration:

$$AP=3.94256 - 0.19505 * V + 0.084155 * I + 0.21323 * F + 0.46969 * G - 0.019710 * V^2 - 1.26140E\text{-}004 * I^2 - 0.012660 * F^2 - 0.10079 * G^2 - 0.013011 * V * I - 0.020638 * V * F - 0.048323 * V * G + 5.88725E\text{-}004 * I * F + 4.53258E\text{-}004 * I * G + 0.012111 * F * G \quad (4.7)$$

4.3.5.1. Diagnostic Tests

The diagnostic details could best be analyzed by inspection of various plots. The most important diagnostic is the normal probability plot of the studentized residuals (the residual divided by the estimated standard deviation of that residual). The normal probability plot indicates whether the residuals follow a normal distribution, in which case the points will follow a straight line. The data points should be approximately linear. A non-linear pattern (such as an S-shaped curve)

indicates non-normality in the error term, which may be corrected by a transformation.

The obtained results from the diagnostic tests for TL, HAZ, UW, UH, P and AP showed that, the diagnosis of residuals revealed no statistical problems as shown in Figures 4.61-4.66, so the response surface plots of the factors can be generated.

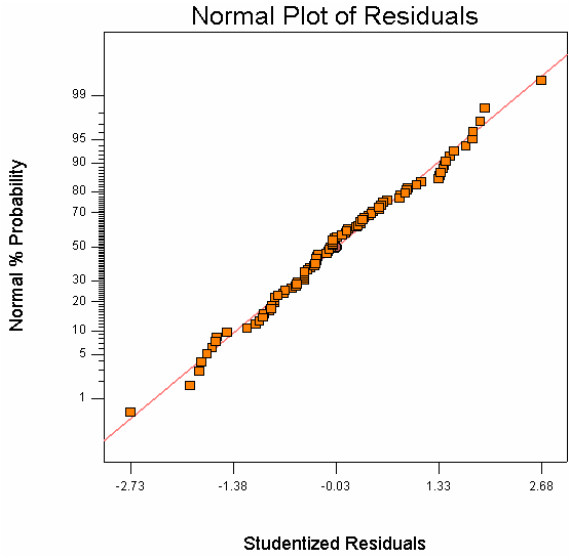

Figure 4.61. Normal probability plot of the residuals for the model of TL

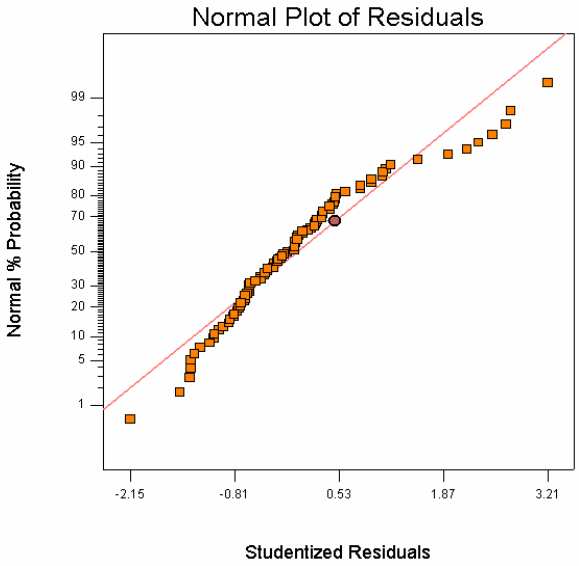

Figure 4.62. Normal probability plot of the residuals for the model of HAZ

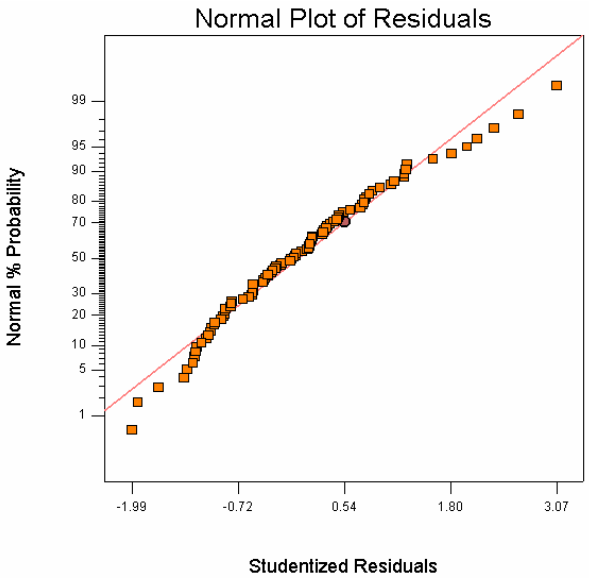

Figure 4.63. Normal probability plot of the residuals for the model of UW

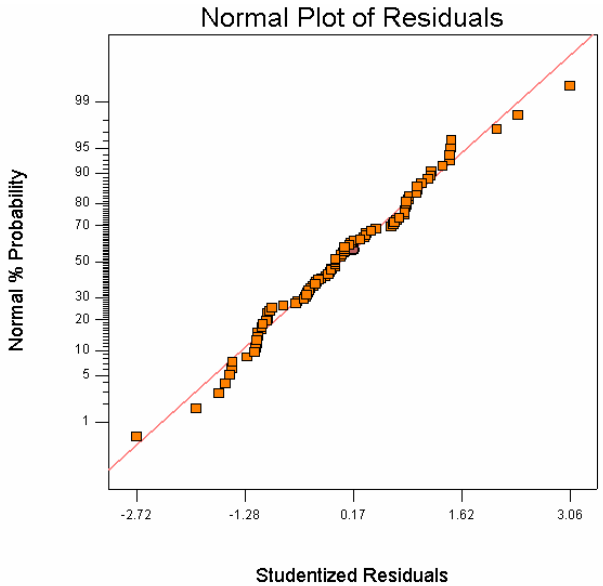

Figure 4.64. Normal probability plot of the residuals for the model of UH

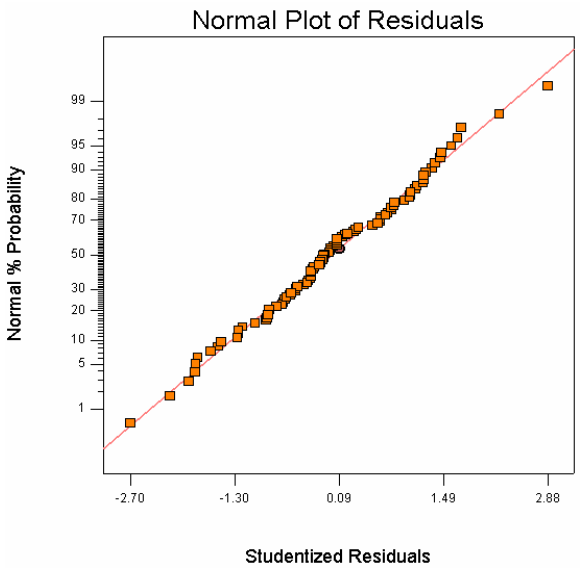

Figure 4.65. Normal probability plot of the residuals for the model of P

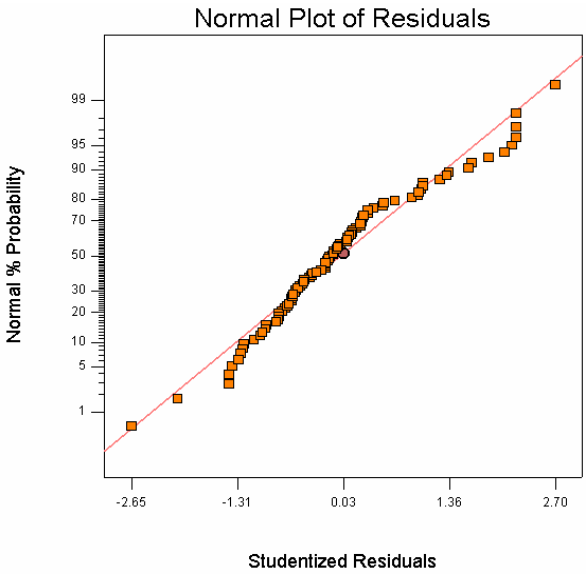

Figure 4.66. Normal probability plot of the residuals for the model of AP

Tables 4.32-4.37 show the diagnostic case studies for validation, approximation and comparison of the found response surface equations. Table 4.32 shows the actual values were obtained from the tensile test and predicted values from the derived response surface equations of 4.2, 4.3, 4.4, 4.5, 4.6 and 4.7. The maximum and minimum residuals for TL response are 229.56 and -263.05

respectively. Average error was obtained as 7.42%. Predicted results showed the good agreement with the measured actual results.

Table 4.32. Diagnostic case statistics for TL

Standard Order	Measured Value	Predicted Value	Residual	%Error	Leverage	Run order
1	1250	1225.68	24.32	1.98	0.055	22
2	1000	1032.48	-32.48	-3.15	0.162	30
3	750	1013.05	-263.05	-25.97	0.114	2
4	1150	1137.22	12.78	1.12	0.253	14
5	1100	1135.34	-35.34	-3.11	0.047	3
6	1100	1135.34	-35.34	-3.11	0.047	7
7	1050	1135.34	-85.34	-7.52	0.047	20
8	1025	986.45	38.55	3.91	0.21	28
9	950	1059.96	-109.96	-10.37	0.22	4
10	1100	1091.63	8.37	0.77	0.169	29
11	1150	1135.34	14.66	1.29	0.047	16
12	1025	1180.12	-155.12	-13.14	0.089	23
13	1200	1121.87	78.13	6.96	0.273	9
14	1100	1135.34	-35.34	-3.11	0.047	27
15	1000	1033.38	-33.38	-3.23	0.22	25
16	1175	1141.36	33.64	2.95	0.13	8
17	875	1019.93	-144.93	-14.21	0.305	18
18	975	1032.65	-57.65	-5.58	0.162	12
19	1100	1135.34	-35.34	-3.11	0.047	1
20	1025	1091.82	-66.82	-6.12	0.273	13
21	1050	1077.39	-27.39	-2.54	0.169	17
22	1000	998.95	1.05	0.11	0.21	5
23	1000	1141.44	-141.44	-12.39	0.082	26
24	900	1109.66	-209.66	-18.89	0.077	11
25	1150	1197.68	-47.68	-3.98	0.089	19
26	1125	1167.11	-42.11	-3.61	0.253	15
27	1125	1093.04	31.96	2.92	0.245	21
28	1050	1137.97	-87.97	-7.73	0.082	24
29	1100	1108.84	-8.84	-0.80	0.245	10
30	1230	1141.44	88.56	7.76	0.082	31
31	1260	1236.29	23.71	1.92	0.106	60
32	1300	1296.85	3.15	0.24	0.112	59
33	1280	1180.12	99.88	8.46	0.089	58
34	1325	1248.01	76.99	6.17	0.051	57
35	1250	1244.72	5.28	0.42	0.106	56
36	1300	1293.65	6.35	0.49	0.065	55
37	1325	1200.16	124.84	10.40	0.082	54
38	1380	1231.36	148.64	12.07	0.042	53
39	1225	1097.89	127.11	11.58	0.145	52
40	1375	1231.36	143.64	11.67	0.042	51
41	1275	1137.97	137.03	12.04	0.082	50
42	1300	1152.89	147.11	12.76	0.151	49
43	1235	1102.01	132.99	12.07	0.145	48

Continue of Table 4.32

Standard Order	Measured Value	Predicted Value	Residual	%Error	Leverage	Run order
44	1300	1142.92	157.08	13.74	0.151	47
45	1375	1231.36	143.64	11.67	0.042	46
46	1375	1231.36	143.64	11.67	0.042	45
47	1380	1231.36	148.64	12.07	0.042	44
48	1050	1097.18	-47.18	-4.30	0.08	43
49	1275	1197.68	77.32	6.46	0.089	42
50	1320	1234	86	6.97	0.094	41
51	1212	1199.31	12.69	1.06	0.082	40
52	1230	1166.24	63.76	5.47	0.053	39
53	1265	1236.11	28.89	2.34	0.088	38
54	1245	1121.01	123.99	11.06	0.235	37
55	1375	1231.36	143.64	11.67	0.042	36
56	1237	1212.06	24.94	2.06	0.206	35
57	1287	1193.66	93.34	7.82	0.206	34
58	1265	1274.33	-9.33	-0.73	0.112	33
59	1227	1251.04	-24.04	-1.92	0.088	32
60	1050	1186.07	-136.07	-11.47	0.063	90
61	950	1054.27	-104.27	-9.89	0.375	89
62	1250	1303.29	-53.29	-4.09	0.142	88
63	1200	1199.31	0.69	0.06	0.082	87
64	1050	1186.07	-136.07	-11.47	0.063	86
65	1020	1149.71	-129.71	-11.28	0.296	85
66	1050	944.96	105.04	11.12	0.346	84
67	975	1084.98	-109.98	-10.14	0.331	83
68	1000	1052.62	-52.62	-5.00	0.375	82
69	1020	1165.43	-145.43	-12.48	0.296	81
70	1150	1161.37	-11.37	-0.98	0.425	80
71	1050	959.84	90.16	9.39	0.346	79
72	1100	1121.46	-21.46	-1.91	0.418	78
73	1020	921.31	98.69	10.71	0.335	77
74	1265	1236.11	28.89	2.34	0.088	76
75	1000	1186.07	-186.07	-15.69	0.063	75
76	950	1018	-68	-6.68	0.368	74
77	980	1005.57	-25.57	-2.54	0.368	73
78	900	1023.68	-123.68	-12.08	0.234	72
79	1325	1251.04	73.96	5.91	0.088	71
80	1100	1133.22	-33.22	-2.93	0.425	70
81	1200	1200.16	-0.16	-0.01	0.082	69
82	980	837.32	142.68	17.04	0.436	68
83	1000	922.1	77.9	8.45	0.335	67
84	1100	1186.07	-86.07	-7.26	0.063	66
85	1050	1107.39	-57.39	-5.18	0.418	65
86	1030	1182.55	-152.55	-12.90	0.151	64
87	1020	1186.07	-166.07	-14.00	0.063	63
88	1150	920.44	229.56	24.94	0.27	62

Continue of Table 4.32

Standard Order	Measured Value	Predicted Value	Residual	%Error	Leverage	Run order
89	1000	1186.07	-186.07	-15.69	0.063	61
90	1150	1033.06	116.94	11.32	0.269	6
			%Average Error	7.42		

$$\%Error = \frac{Measured\ value - predicted\ value}{\text{Predicted value}} * 100$$

Table 4.33 shows the comparison of measured and predicted results for the HAZ response. The maximum and minimum residual values are 1.13 and -0.81 respectively. Average error was 6.58 %. Results showed a good agreement and not much deviations from the measured values.

Table 4.33. Diagnostic case statistics for HAZ

Standard Order	Measured Value	Predicted Value	Residual	%Error	Leverage	Run order
1	5.32	5.16	0.16	3.10	0.055	22
2	2.78	2.80	-0.022	-0.71	0.162	30
3	2.55	2.68	-0.13	-4.85	0.114	2
4	5.23	5.12	0.11	2.15	0.253	14
5	4.14	3.97	0.17	4.28	0.047	3
6	4.12	3.97	0.15	3.78	0.047	7
7	4.14	3.97	0.17	4.28	0.047	20
8	3.53	4.02	-0.49	-12.19	0.21	28
9	3.40	3.89	-0.49	-12.60	0.22	4
10	2.55	2.67	-0.12	-4.49	0.169	29
11	4.13	3.97	0.16	4.03	0.047	16
12	4.73	3.77	0.96	25.46	0.089	23
13	4.32	4.02	0.3	7.46	0.273	9
14	4.13	3.97	0.16	4.03	0.047	27
15	3.26	3.85	-0.59	-15.32	0.22	25
16	4.03	3.73	0.3	8.04	0.13	8
17	4.43	4.01	0.42	10.47	0.305	18
18	2.68	2.89	-0.21	-7.27	0.162	12
19	4.12	3.97	0.15	3.78	0.047	1
20	4.00	3.88	0.12	3.09	0.273	13
21	2.54	2.63	-0.092	-3.42	0.169	17
22	3.80	4.11	-0.31	-7.54	0.21	5
23	4.94	4.11	0.83	20.19	0.082	26
24	3.10	2.99	0.11	3.68	0.077	11
25	4.66	3.82	0.84	21.99	0.089	19
26	5.44	5.16	0.28	5.43	0.253	15
27	5.53	5.35	0.18	3.36	0.245	21
28	4.89	4.01	0.88	21.95	0.082	24

Continue of Table 4.33

Standard order	Measured Value	Predicted Value	Residual	%Error	Leverage	Run order
29	5.56	5.45	0.11	2.02	0.245	10
30	3.79	4.11	-0.32	-7.79	0.082	31
31	5.30	5.64	-0.34	-6.03	0.106	60
32	5.10	5.37	-0.27	-5.03	0.112	59
33	3.40	3.77	-0.37	-9.81	0.089	58
34	5.00	5.18	-0.18	-3.47	0.051	57
35	5.35	5.76	-0.41	-7.12	0.106	56
36	5.61	5.91	-0.3	-5.08	0.065	55
37	4.79	5.12	-0.33	-6.45	0.082	54
38	4.46	4.48	-0.023	-0.45	0.042	53
39	3.08	3.58	-0.5	-13.97	0.145	52
40	4.44	4.48	-0.043	-0.89	0.042	51
41	3.60	4.01	-0.41	-10.22	0.082	50
42	2.99	3.29	-0.3	-9.12	0.151	49
43	3.06	3.48	-0.42	-12.07	0.145	48
44	2.98	3.24	-0.26	-8.02	0.151	47
45	4.45	4.48	-0.033	-0.67	0.042	46
46	4.44	4.48	-0.043	-0.89	0.042	45
47	4.45	4.48	-0.033	-0.67	0.042	44
48	2.54	2.84	-0.3	-10.56	0.08	43
49	3.35	3.82	-0.47	-12.30	0.089	42
50	4.39	4.19	0.2	4.77	0.094	41
51	4.78	5.00	-0.22	-4.40	0.082	40
52	3.20	4.01	-0.81	-20.20	0.053	39
53	4.60	4.67	-0.066	-1.50	0.088	38
54	4.52	4.60	-0.081	-1.74	0.235	37
55	4.45	4.48	-0.033	-0.67	0.042	36
56	4.43	4.54	-0.11	-2.42	0.206	35
57	4.45	4.38	0.073	1.60	0.206	34
58	5.10	5.31	-0.21	-3.95	0.112	33
59	4.63	4.73	-0.1	-2.11	0.088	32
60	6.45	6.06	0.39	6.44	0.063	90
61	4.30	4.15	0.15	3.61	0.375	89
62	6.80	7.26	-0.46	-6.34	0.142	88
63	4.78	5.00	-0.22	-4.40	0.082	87
64	6.50	6.06	0.44	7.26	0.063	86
65	6.20	5.92	0.28	4.73	0.296	85
66	6.30	6.30	2.31	0.00	0.346	84
67	7.20	6.35	0.85	13.39	0.331	83
68	4.10	4.08	0.018	0.49	0.375	82
69	6.70	6.15	0.55	8.94	0.296	81
70	7.40	7.52	-0.12	-1.60	0.425	80
71	6.35	6.41	-0.057	-0.94	0.346	79
72	7.9	8.17	-0.27	-3.30	0.418	78
73	6.5	6.88	-0.38	-5.52	0.335	77
74	4.6	4.67	-0.066	-1.50	0.088	76

Continue of Table 4.33

Standard order	Measured Value	Predicted Value	Residual	%Error	Leverage	Run order
75	6.52	6.06	0.46	7.59	0.063	75
76	4.40	4.41	-0.013	-0.23	0.368	74
77	4.60	4.54	0.063	1.32	0.368	73
78	3.80	2.67	1.13	42.32	0.234	72
79	4.63	4.73	-0.1	-2.11	0.088	71
80	7.50	7.42	0.081	1.08	0.425	70
81	4.79	5.12	-0.33	-6.45	0.082	69
82	8.22	7.94	0.26	3.27	0.436	68
83	6.8	7.05	-0.25	-3.55	0.335	67
84	6.43	6.06	0.37	6.11	0.063	66
85	7.8	8.01	-0.21	-2.62	0.418	65
86	5.2	5.65	-0.45	-7.96	0.151	64
87	6.44	6.06	0.38	6.27	0.063	63
88	4.82	5.56	-0.74	-13.31	0.27	62
89	6.50	6.06	0.44	7.26	0.063	61
90	5.96	5.55	0.41	7.39	0.269	6
			%Average Error	6.58		

$$\%Error = \frac{Measured\ value - predicted\ value}{\Pr edicted\ value} * 100$$

Calculated UW values (Table 4.34) did not show high deviations from the predicted values. Its maximum and minimum residuals for this response are 0.120 and -0.120 respectively. Also, average error was found as 8.28%.

Table 4.34. Diagnostic case statistics for UW

Standard order	Measured Value	Predicted Value	Residual	%Error	Leverage	Run order
1	7.23	7.83	-0.600	-7.66	0.055	22
2	5.64	5.59	0.055	0.89	0.162	30
3	4.22	5.11	-0.890	-17.42	0.114	2
4	7.42	6.96	0.460	6.61	0.253	14
5	5.82	6.52	-0.700	-10.74	0.047	3
6	5.82	6.52	-0.700	-10.74	0.047	7
7	5.78	6.52	-0.740	-11.35	0.047	20
8	5.22	6.01	-0.790	-13.14	0.21	28
9	5.14	5.87	-0.730	-12.44	0.22	4
10	5.48	5.50	-0.017	-0.36	0.169	29
11	5.96	6.52	-0.560	-8.59	0.047	16
12	7.02	6.41	0.610	9.52	0.089	23
13	6.20	6.54	-0.340	-5.20	0.273	9
14	5.79	6.52	-0.730	-11.20	0.047	27
15	5.03	5.51	-0.480	-8.71	0.22	25

Continue of Table 4.34

Standard order	Measured Value	Predicted Value	Residual	%Error	Leverage	Run order
16	5.52	6.22	-0.700	-11.25	0.13	8
17	6.50	6.89	-0.390	-5.66	0.305	18
18	5.53	5.79	-0.260	-4.49	0.162	12
19	5.78	6.52	-0.740	-11.35	0.047	1
20	5.62	6.00	-0.380	-6.33	0.273	13
21	5.45	5.17	0.280	5.42	0.169	17
22	5.33	6.24	-0.910	-14.58	0.21	5
23	7.28	7.06	0.220	3.12	0.082	26
24	5.63	5.83	-0.200	-3.43	0.077	11
25	7.01	6.72	0.290	4.32	0.089	19
26	7.69	7.30	0.390	5.34	0.253	15
27	7.89	7.50	0.390	5.20	0.245	21
28	7.22	6.87	0.350	5.09	0.082	24
29	7.72	7.72	4.019	0.00	0.245	10
30	9.08	7.06	2.020	28.61	0.082	31
31	8.63	8.6	0.029	0.35	0.106	60
32	8.57	8.37	0.200	2.39	0.112	59
33	7.17	6.41	0.760	11.86	0.089	58
34	8.84	7.98	0.860	10.78	0.051	57
35	8.96	8.78	0.180	2.05	0.106	56
36	9.51	8.88	0.630	7.09	0.065	55
37	8.45	8.00	0.450	5.62	0.082	54
38	7.98	7.4	0.580	7.84	0.042	53
39	6.42	6.47	-0.051	-0.77	0.145	52
40	7.98	7.4	0.580	7.84	0.042	51
41	7.72	6.87	0.850	12.37	0.082	50
42	5.90	6.18	-0.280	-4.53	0.151	49
43	6.54	6.3	0.240	3.81	0.145	48
44	5.98	5.88	0.096	1.70	0.151	47
45	8.00	7.4	0.600	8.11	0.042	46
46	7.98	7.4	0.580	7.84	0.042	45
47	7.99	7.4	0.590	7.97	0.042	44
48	5.90	5.69	0.210	3.69	0.08	43
49	8.36	6.72	1.640	24.40	0.089	42
50	6.36	7.11	-0.750	-10.55	0.094	41
51	8.39	7.84	0.550	7.02	0.082	40
52	7.86	6.68	1.180	17.66	0.053	39
53	8.26	7.36	0.900	12.23	0.088	38
54	8.53	7.77	0.760	9.78	0.235	37
55	7.98	7.4	0.580	7.84	0.042	36
56	7.88	7.39	0.490	6.63	0.206	35
57	7.12	6.92	0.200	2.89	0.206	34
58	8.12	8.07	0.050	0.62	0.112	33
59	9.02	7.64	1.380	18.06	0.088	32
60	7.66	8.43	-0.770	-9.13	0.063	90
61	5.68	6.02	-0.340	-5.65	0.375	89

Continue of Table 4.34

Standard Order	Measured Value	Predicted Value	Residual	%Error	Leverage	Run
62	9.93	10.3	-0.370	-3.59	0.142	88
63	7.23	7.84	-0.610	-7.78	0.082	87
64	7.66	8.43	-0.770	-9.13	0.063	86
65	7.21	8.00	-0.790	-9.88	0.296	85
66	8.50	7.67	0.830	10.82	0.346	84
67	8.23	8.86	-0.630	-7.11	0.331	83
68	5.63	5.77	-0.140	-2.43	0.375	82
69	7.72	8.36	-0.640	-7.66	0.296	81
70	9.86	10.4	-0.540	-5.19	0.425	80
71	8.56	7.88	0.680	8.63	0.346	79
72	10.48	10.93	-0.450	-4.12	0.418	78
73	8.78	8.26	0.520	6.30	0.335	77
74	6.86	7.36	-0.500	-6.79	0.088	76
75	7.66	8.43	-0.770	-9.13	0.063	75
76	5.75	6.17	-0.420	-6.81	0.368	74
77	5.78	6.29	-0.510	-8.11	0.368	73
78	4.35	5.19	-0.840	-16.18	0.234	72
79	6.98	7.64	-0.660	-8.64	0.088	71
80	9.73	10.15	-0.420	-4.14	0.425	70
81	7.22	8.00	-0.780	-9.75	0.082	69
82	11.12	10.03	1.090	10.87	0.436	68
83	8.87	8.34	0.530	6.35	0.335	67
84	7.66	8.43	-0.770	-9.13	0.063	66
85	10.56	10.82	-0.260	-2.40	0.418	65
86	6.86	8.1	-1.240	-15.31	0.151	64
87	7.66	8.43	-0.770	-9.13	0.063	63
88	7.21	6.12	1.090	17.81	0.27	62
89	7.66	8.43	-0.770	-9.13	0.063	61
90	8.56	6.83	1.730	25.33	0.269	6
			%Average Error	8.28		

$$\%Error = \frac{Measured\ value - predicted\ value}{\Pr edicted\ value} * 100$$

Table 4.35 shows the comparison of predicted and measured UH values. Here is also good agreement was obtained. The maximum and minimum residuals are 0.12 and -0.10 respectively. Average error of 26.41% was obtained.

Table 4.35. Diagnostic case statistics for UH

Standard order	Measured Value	Predicted Value	Residual	%Error	Leverage	Run Order
1	0.28	0.16	0.120	75.00	0.055	22
2	0.10	0.11	-0.014	-9.09	0.162	30
3	0.09	0.09	-0.614	-1.10	0.114	2
4	0.22	0.21	5.158	4.76	0.253	14
5	0.19	0.13	0.062	46.15	0.047	3
6	0.17	0.13	0.042	30.77	0.047	7
7	0.16	0.13	0.032	23.08	0.047	20
8	0.19	0.17	0.019	11.76	0.21	28
9	0.10	0.14	-0.041	-28.57	0.22	4
10	0.09	0.07	0.019	26.76	0.169	29
11	0.18	0.13	0.052	38.46	0.047	16
12	0.16	0.13	0.033	23.08	0.089	23
13	0.09	0.08	0.011	13.92	0.273	9
14	0.18	0.13	0.052	38.46	0.047	27
15	0.15	0.17	-0.020	-11.76	0.22	25
16	0.20	0.14	0.056	42.86	0.13	8
17	0.18	0.15	0.030	20.00	0.305	18
18	0.03	0.07	-0.037	-55.22	0.162	12
19	0.18	0.13	0.052	38.46	0.047	1
20	0.22	0.15	0.072	46.67	0.273	13
21	0.09	0.09	-6.448	-6.25	0.169	17
22	0.09	0.12	-0.030	-25.00	0.21	5
23	0.13	0.09	0.033	34.02	0.082	26
24	0.08	0.08	-2.488	-2.44	0.077	11
25	0.12	0.11	0.012	9.09	0.089	19
26	0.18	0.19	-0.012	-5.26	0.253	15
27	0.20	0.21	-7.751	-4.76	0.245	21
28	0.13	0.14	-6.389	-7.14	0.082	24
29	0.18	0.16	0.016	12.50	0.245	10
30	0.09	0.097	-6.954	-7.22	0.082	31
31	0.12	0.17	-0.049	-29.41	0.106	60
32	0.17	0.16	7.929	6.25	0.112	59
33	0.09	0.13	-0.037	-30.77	0.089	58
34	0.08	0.16	-0.078	-50.00	0.051	57
35	0.14	0.14	0.438	0.00	0.106	56
36	0.26	0.15	0.100	73.33	0.065	55
37	0.15	0.11	0.040	36.36	0.082	54
38	0.08	0.12	-0.039	-33.33	0.042	53
39	0.04	0.08	-0.040	-50.00	0.145	52
40	0.08	0.12	-0.039	-33.33	0.042	51
41	0.10	0.14	-0.036	-28.57	0.082	50
42	0.03	0.081	-0.051	-62.96	0.151	49
43	0.08	0.12	-0.037	-33.33	0.145	48
44	0.04	0.097	-0.057	-58.76	0.151	47
45	0.07	0.12	-0.049	-41.67	0.042	46
46	0.08	0.12	-0.039	-33.33	0.042	45
47	0.08	0.12	-0.039	-33.33	0.042	44

Continue of Table 4.35

Standard order	Measured Value	Predicted Value	Residual	%Error	Leverage	Run Order
48	0.02	0.081	-0.061	-75.31	0.08	43
49	0.10	0.11	-8.174	-9.09	0.089	42
50	0.14	0.13	8.534	7.69	0.094	41
51	0.17	0.14	0.033	21.43	0.082	40
52	0.09	0.099	-8.519	-9.09	0.053	39
53	0.16	0.13	0.032	23.08	0.088	38
54	0.15	0.14	5.805	7.14	0.235	37
55	0.07	0.12	-0.049	-41.67	0.042	36
56	0.06	0.082	-0.022	-26.83	0.206	35
57	0.08	0.13	-0.047	-38.46	0.206	34
58	0.11	0.17	-0.060	-35.29	0.112	33
59	0.18	0.12	0.058	50.00	0.088	32
60	0.11	0.13	-0.016	-15.38	0.063	90
61	0.08	0.097	-0.017	-17.53	0.375	89
62	0.18	0.20	-0.023	-10.00	0.142	88
63	0.17	0.14	0.033	21.43	0.082	87
64	0.11	0.13	-0.016	-15.38	0.063	86
65	0.14	0.11	0.028	27.27	0.296	85
66	0.09	0.11	-0.019	-18.18	0.346	84
67	0.09	0.15	-0.055	-40.00	0.331	83
68	0.10	0.099	1.084	1.01	0.375	82
69	0.10	0.11	-0.011	-9.09	0.296	81
70	0.19	0.22	-0.030	-13.64	0.425	80
71	0.1	0.13	-0.034	-23.08	0.346	79
72	0.2	0.18	0.022	11.11	0.418	78
73	0.09	0.1	-0.015	-10.00	0.335	77
74	0.16	0.13	0.032	23.08	0.088	76
75	0.11	0.13	-0.016	-15.38	0.063	75
76	0.18	0.13	0.054	38.46	0.368	74
77	0.15	0.1	0.047	50.00	0.368	73
78	0.09	0.08	0.010	12.50	0.234	72
79	0.18	0.12	0.058	50.00	0.088	71
80	0.18	0.20	-0.019	-10.00	0.425	70
81	0.15	0.11	0.040	36.36	0.082	69
82	0.22	0.16	0.063	37.50	0.436	68
83	0.08	0.11	-0.030	-27.27	0.335	67
84	0.11	0.13	-0.016	-15.38	0.063	66
85	0.18	0.18	2.982	0.00	0.418	65
86	0.19	0.14	0.047	35.71	0.151	64
87	0.11	0.13	-0.016	-15.38	0.063	63
88	0.15	0.11	0.043	36.36	0.27	62
89	0.11	0.13	-0.016	-15.38	0.063	61
90	0.12	0.22	-0.100	-45.45	0.269	6
			%Average Error	26.41		

$$\%Error = \frac{Measured\ value - predicted\ value}{\text{Pr}edicted\ value} * 100$$

Penetration prediction did not show high deviation. Here is also close agreement was obtained. Thus, maximum and minimum residuals are 0.13 and -0.13 respectively. Also, average error was 4.68%.

Table 4.36. Diagnostic Case Statistics for P

Standard Order	Measured Value	Predicted Value	Residual	%Error	Leverage	Run Order
1	1.10	1.15	-0.05	-4.35	0.055	22
2	0.89	0.83	0.06	7.23	0.162	30
3	0.75	0.88	-0.13	-14.77	0.114	2
4	1.08	1.10	-0.02	-1.82	0.253	14
5	1.06	1.03	0.03	2.91	0.047	3
6	1.03	1.03	2.09	0.00	0.047	7
7	1.06	1.03	0.03	2.91	0.047	20
8	0.90	0.93	-0.03	-3.23	0.210	28
9	0.98	0.96	0.02	2.08	0.220	4
10	0.92	0.93	-0.02	-1.08	0.169	29
11	0.96	1.03	-0.07	-6.80	0.047	16
12	1.05	1.07	-0.02	-1.87	0.089	23
13	0.91	1.02	-0.11	-10.78	0.273	9
14	0.96	1.03	-0.07	-6.80	0.047	27
15	0.95	0.98	-0.03	-3.06	0.220	25
16	1.08	1.01	0.07	6.93	0.130	8
17	0.78	0.84	-0.06	-7.14	0.305	18
18	0.86	0.85	0.02	1.18	0.162	12
19	1.06	1.03	0.03	2.91	0.047	1
20	1.02	1.02	0.66	0.00	0.273	13
21	0.90	0.94	-0.04	-4.26	0.169	17
22	0.94	0.93	7.52	1.08	0.210	5
23	1.03	0.99	0.04	4.04	0.082	26
24	0.97	0.95	0.02	2.11	0.077	11
25	1.02	1.06	-0.04	-3.77	0.089	19
26	1.08	1.08	-2.18	0.00	0.253	15
27	1.12	1.07	0.05	4.67	0.245	21
28	0.98	0.98	-0.55	0.00	0.082	24
29	1.16	1.07	0.09	8.41	0.245	10
30	0.94	0.99	-0.05	-5.05	0.082	31
31	1.17	1.15	0.02	1.74	0.106	60
32	1.27	1.20	0.07	5.83	0.112	59
33	1.10	1.07	0.03	2.80	0.089	58
34	1.15	1.16	-0.01	-0.86	0.051	57
35	1.19	1.16	0.03	2.59	0.106	56
36	1.14	1.24	-0.10	-8.06	0.065	55
37	1.14	1.10	0.04	3.64	0.082	54
38	1.22	1.12	0.10	8.93	0.042	53
39	0.89	0.93	-0.04	-4.30	0.145	52
40	1.25	1.12	0.13	11.61	0.042	51
41	0.95	0.98	-0.03	-3.06	0.082	50

Continue of Table 4.36

Standard Order	Measured Value	Predicted Value	Residual	%Error	Leverage	Run Order
42	0.93	1.03	-0.10	-9.71	0.151	49
43	0.87	0.91	-0.04	-4.40	0.145	48
44	0.95	1.03	-0.08	-7.77	0.151	47
45	1.25	1.12	0.13	11.61	0.042	46
46	1.23	1.12	0.11	9.82	0.042	45
47	1.25	1.12	0.13	11.61	0.042	44
48	0.80	0.93	-0.13	-13.98	0.080	43
49	1.13	1.06	0.07	6.60	0.089	42
50	1.11	1.12	-0.01	-0.89	0.094	41
51	1.00	1.09	-0.09	-8.26	0.082	40
52	1.06	1.07	-0.01	-0.93	0.053	39
53	1.20	1.18	0.02	1.69	0.088	38
54	0.98	0.91	0.07	7.69	0.235	37
55	1.25	1.12	0.13	11.61	0.042	36
56	1.18	1.12	0.06	5.36	0.206	35
57	1.23	1.11	0.12	10.81	0.206	34
58	1.24	1.21	0.03	2.48	0.112	33
59	1.17	1.18	-5.52	-0.85	0.088	32
60	1.18	1.24	-0.06	-4.84	0.063	90
61	1.18	1.11	0.07	6.31	0.375	89
62	1.21	1.30	-0.09	-6.92	0.142	88
63	1.00	1.09	-0.09	-8.26	0.082	87
64	1.18	1.24	-0.06	-4.84	0.063	86
65	1.19	1.22	-0.04	-2.46	0.296	85
66	1.21	1.19	0.02	1.68	0.346	84
67	0.98	1.03	-0.05	-4.85	0.331	83
68	1.10	1.10	-0.27	0.00	0.375	82
69	1.16	1.23	-0.07	-5.69	0.296	81
70	1.19	1.21	-0.02	-1.65	0.425	80
71	1.20	1.19	0.01	0.84	0.346	79
72	1.16	1.22	-0.06	-4.92	0.418	78
73	1.19	1.12	0.07	6.25	0.335	77
74	1.20	1.18	0.02	1.69	0.088	76
75	1.18	1.24	-0.06	-4.84	0.063	75
76	0.99	0.95	0.05	4.21	0.368	74
77	0.98	0.97	7.88	1.03	0.368	73
78	0.89	0.88	6.23	1.14	0.234	72
79	1.22	1.18	0.04	3.39	0.088	71
80	1.18	1.23	-0.05	-4.07	0.425	70
81	1.14	1.10	0.04	3.64	0.082	69
82	1.22	1.09	0.13	11.93	0.436	68
83	1.18	1.13	0.05	4.42	0.335	67
84	1.18	1.24	-0.06	-4.84	0.063	66
85	1.21	1.22	-9.18	-0.82	0.418	65
86	1.21	1.23	-0.02	-1.63	0.151	64
87	1.18	1.24	-0.06	-4.84	0.063	63

Continue of Table 4.36

Standard Order	Measured Value	Predicted Value	Residual	%Error	Leverage	Run Order
88	1.10	1.13	-0.03	-2.65	0.270	62
89	1.18	1.24	-0.06	-4.84	0.063	61
90	1.06	1.07	-0.01	-0.93	0.269	6
			%Average Error	4.68		

$$\%Error = \frac{Measured\ value - predicted\ value}{\Pr edicted\ value} * 100$$

Area of penetration is the measure of the penetrated area. When both upper width and penetration increase it also increases. Here is also good agreement was obtained (Table 4.37). The maximum and minimum residuals are 1.71 and -2.16 respectively. And average error was 7.24%.

Table 4.37. Diagnostic case statistics for AP

Standard Order	Measured Value	Predicted Value	Residual	%Error	Leverage	Run Order
1	7.11	8.06	-0.95	-11.79	0.055	22
2	5.63	5.47	0.16	2.93	0.162	30
3	4.6	5.51	-0.91	-16.52	0.114	2
4	7.52	7.55	-0.03	-0.40	0.253	14
5	6.55	6.83	-0.28	-4.10	0.047	3
6	6.09	6.83	-0.74	-10.83	0.047	7
7	6.23	6.83	-0.60	-8.78	0.047	20
8	5.98	6.35	-0.37	-5.83	0.21	28
9	6.08	6.3	-0.22	-3.49	0.22	4
10	5.53	5.63	-0.10	-1.78	0.169	29
11	7.25	6.83	0.42	6.15	0.047	16
12	7.12	6.56	0.56	8.54	0.089	23
13	6.38	6.73	-0.35	-5.20	0.273	9
14	6.18	6.83	-0.65	-9.52	0.047	27
15	6.01	6.15	-0.14	-2.28	0.22	25
16	6.38	6.38	1.87	0.00	0.13	8
17	6.78	6.01	0.77	12.81	0.305	18
18	5.76	5.56	0.20	3.60	0.162	12
19	6.58	6.83	-0.25	-3.66	0.047	1
20	6.22	6.54	-0.32	-4.89	0.273	13
21	5.81	5.4	0.41	7.59	0.169	17
22	6.11	6.36	-0.25	-3.93	0.21	5
23	7.26	6.7	0.56	8.36	0.082	26
24	5.43	5.92	-0.49	-8.28	0.077	11
25	7.09	6.75	0.34	5.04	0.089	19
26	7.48	7.66	-0.18	-2.35	0.253	15
27	7.82	7.79	0.03	0.39	0.245	21

Continue of Table 4.37

Standard Order	Measured Value	Predicted Value	Residual	%Error	Leverage	Run Order
28	7.23	6.66	0.57	8.56	0.082	24
29	7.77	7.75	0.02	0.26	0.245	10
30	7.87	6.7	1.17	17.46	0.082	31
31	8.55	8.26	0.29	3.51	0.106	60
32	7.34	8.23	-0.89	-10.81	0.112	59
33	7.9	6.56	1.34	20.43	0.089	58
34	8.98	8.12	0.87	10.59	0.051	57
35	9.06	8.23	0.84	10.09	0.106	56
36	9.2	8.69	0.51	5.87	0.065	55
37	7.2	7.34	-0.14	-1.91	0.082	54
38	7.99	7.37	0.62	8.41	0.042	53
39	5.48	6.04	-0.56	-9.27	0.145	52
40	7.98	7.37	0.61	8.28	0.042	51
41	6.56	6.66	-0.10	-1.50	0.082	50
42	5.42	6.17	-0.75	-12.16	0.151	49
43	5.63	5.95	-0.32	-5.38	0.145	48
44	5.02	5.94	-0.92	-15.49	0.151	47
45	7.98	7.37	0.61	8.28	0.042	46
46	7.95	7.37	0.58	7.87	0.042	45
47	7.98	7.37	0.61	8.28	0.042	44
48	5.3	5.82	-0.52	-8.93	0.08	43
49	8.3	6.75	1.55	22.96	0.089	42
50	5.8	6.96	-1.16	-16.67	0.094	41
51	8	7.33	0.67	9.14	0.082	40
52	5.54	6.61	-1.07	-16.19	0.053	39
53	7.2	7.27	-0.07	-0.96	0.088	38
54	4.89	6.47	-1.58	-24.42	0.235	37
55	7.97	7.37	0.60	8.14	0.042	36
56	7.03	7.26	-0.23	-3.17	0.206	35
57	7.1	7.07	0.03	0.42	0.206	34
58	8.61	8.12	0.49	6.03	0.112	33
59	8.8	7.43	1.37	18.44	0.088	32
60	7.56	8	-0.44	-5.50	0.063	90
61	5.63	6	-0.37	-6.17	0.375	89
62	7.88	10.04	-2.16	-21.51	0.142	88
63	7.98	7.33	0.65	8.87	0.082	87
64	7.56	8	-0.44	-5.50	0.063	86
65	7.67	7.77	-0.10	-1.29	0.296	85
66	6.79	7.17	-0.38	-5.30	0.346	84
67	6.98	7.06	-0.08	-1.13	0.331	83
68	5.56	5.76	-0.20	-3.47	0.375	82
69	7.39	7.83	-0.44	-5.62	0.296	81
70	9.72	9.69	0.03	0.31	0.425	80
71	6.73	7.22	-0.49	-6.79	0.346	79
72	9.79	9.71	0.08	0.82	0.418	78
73	6.86	7.2	-0.34	-4.72	0.335	77

Continue of Table 4.37

Standard Order	Measured Value	Predicted Value	Residual	%Error	Leverage	Run Order
74	7.2	7.27	-0.07	-0.96	0.088	76
75	7.56	8	-0.44	-5.50	0.063	75
76	5.78	5.67	0.11	1.94	0.368	74
77	5.89	5.77	0.12	2.08	0.368	73
78	5.23	5.3	-0.07	-1.32	0.234	72
79	8.8	7.43	1.37	18.44	0.088	71
80	9.78	9.72	0.06	0.62	0.425	70
81	7.2	7.34	-0.14	-1.91	0.082	69
82	10.48	9.09	1.39	15.29	0.436	68
83	6.98	7.1	-0.12	-1.69	0.335	67
84	7.56	8	-0.44	-5.50	0.063	66
85	9.69	9.89	-0.20	-2.02	0.418	65
86	7.62	7.62	-0.62	0.00	0.151	64
87	7.56	8	-0.44	-5.50	0.063	63
88	7.63	5.92	1.71	28.89	0.27	62
89	7.56	8	-0.44	-5.50	0.063	61
90	8.38	7.72	0.66	8.55	0.269	6
			%Average Error	7.24		

$$\%Error = \frac{Measured\ value - predicted\ value}{\Pr edicted\ value} * 100$$

4.4. Optimization of TIG Welding Process Parameters

4.4.1. Optimization with Design Expert 6.0

The mathematical models developed are useful for selecting correct process parameters to achieve the desired weld pool quality or to predict weld pool quality for the given process parameters. These models facilitate optimization of the process and sensitivity analysis. They also help to improve the understanding of the effect of process parameters on pool quality, to evaluate the interaction effects of pool parameters and to optimize the bead quality to obtain a high-quality welded joint at a relatively low cost with high productivity.

Optimization problems are often classified as linear or nonlinear, depending on whether the relationships in the problem are linear with respect to the variables. In this part of the study, since all of the developed mathematical formulas were

quadratic, global nonlinear optimization was used to optimize the process parameters.

The goals of the factors were obtained between their lower (-1) and upper (+1) values. Before the optimization module, the goals for the responses were selected according to the Table 4.38.

Table 4.38. Optimization case for the responses

		Goal		
Case	**Responses**	**maximize**	**minimize**	**in range**
1	TL	√	X	X
	HAZ	X	X	√
	UW	X	X	√
	UH	X	X	√
	P	√	X	X
	AP	X	X	√
2	TL	√	X	X
	HAZ	X	√	X
	UW	X	√	X
	UH	X	X	√
	P	√	X	X
	AP	X	X	√
3	TL	√	X	X
	HAZ	X	√	X
	UW	X	√	X
	UH	X	√	X
	P	√	X	X
	AP	X	√	X

Table 4.39 shows the optimization results obtained according to the case 1. TL and P maximization (others kept constant) yielded two solutions of 1330.73 kgf and 1.27 mm respectively. The maximum tensile load obtained in this condition with the welding parameters of 1.73 mm/s velocity, 96.84 A current, 8 l/min shielding gas flow rate and 1.34 mm arc gap.

Table 4.39. Optimization results for the case 1

Name	Goal	Lower Limit	Upper Limit	Lower Weight	Upper Weight	Importance
V	is in range	1.0696	3.5546	1	1	3
I	is in range	20	150	1	1	3
F	is in range	8	12	1	1	3
G	is in range	1	4	1	1	3
TS	maximize	750	1380	1	1	3
HAZ	is in range	2.54	8.2	1	1	3
UW	is in range	4.22	11.12	1	1	3
UH	is in range	0.02	0.28	1	1	3
P	maximize	0.75	1.27	1	1	3
AP	is in range	4.6	10.48	1	1	3

Solution Number	V	I	F	G	TL	HAZ	UW	UH	P	AP
1	1.73	96.84	8.00	1.34	1330.73	7.078	10.08	0.231	1.270	9.926
2	1.73	96.77	8.00	1.36	1330.73	7.076	10.07	0.231	1.270	9.924

The optimization results of condition 2 are shown in Table 4.40. Here, UH and AP were kept constant whereas the others were set as indicated below. This optimization condition yielded six solutions. The maximum Tensile load of 1201.96 kgf was obtained for the welding parameters of V= 2.58 mm/s, I=52.69 A, F=8.19 l/min and G=1 mm.

Table 4.40. Optimization results for the case 2

Name	Goal	Lower Limit	Upper Limit	Lower Weight	Upper Weight	Importance
V	is in range	1.0696	3.5546	1	1	3
I	is in range	20	150	1	1	3
F	is in range	8	12	1	1	3
G	is in range	1	4	1	1	3
TS	maximize	750	1380	1	1	3
HAZ	minimize	2.54	8.2	1	1	3
UW	minimize	4.22	11.12	1	1	3
UH	is in range	0.02	0.28	1	1	3
P	maximize	0.75	1.27	1	1	3
AP	is in range	4.6	10.48	1	1	3

Continue of Table 4.40

Solution Number	V	I	F	G	TL	HAZ	UW	UH	P	AP
1	2.58	53.14	12.00	1.00	1190.53	3.877	6.534	0.110	1.103	6.526
2	2.59	53.51	12.00	1.00	1190.12	3.883	6.535	0.109	1.104	6.525
3	2.60	52.85	11.10	1.00	1195.15	3.865	6.608	0.109	1.102	6.571
4	2.64	53.49	10.11	1.00	1197.11	3.879	6.678	0.106	1.103	6.612
5	2.59	52.21	10.04	1.00	1198.56	3.853	6.676	0.106	1.099	6.616
6	2.58	52.69	8.19	1.00	1201.96	3.912	6.805	0.099	1.101	6.710

Case 3, shown in Table 4.41, is the more desirable and encountered situation in technique and literature. TL, P, and AP were maximized whereas the others were minimized. There were not any stationary welding parameters. In this situation two solutions which gave the maximum TL were obtained. The maximum TL (1235.88 kgf), P (1.142 mm), and AP (7.28 mm^2), and minimum HAZ (4.45 mm), UW (7.37 mm), UH (0.10 mm) were obtained with the welding parameters of 2.45 mm/s torch travel speed, 59.09 A current, 8 l/min gas flow rate, 1.71 mm gap distance or arc length.

Table 4.41. Optimization Results for the case 3

Name	Goal	Lower Limit	Upper Limit	Lower Weight	Upper Weight	Importance
V	is in range	1.0696	3.5546	1	1	3
I	is in range	20	150	1	1	3
F	is in range	8	12	1	1	3
G	is in range	1	4	1	1	3
TS	maximize	750	1380	1	1	3
HAZ	minimize	2.54	8.2	1	1	3
UW	minimize	4.22	11.12	1	1	3
UH	minimize	0.02	0.28	1	1	3
P	maximize	0.75	1.27	1	1	3
AP	maximize	4.6	10.48	1	1	3

Solution Number	V	I	F	G	TL	HAZ	UW	UH	P	AP
1	2.45	59.09	8.00	1.71	1235.88	4.453	7.370	0.105	1.142	7.287
2	2.45	59.19	8.00	1.73	1235.22	4.454	7.369	0.105	1.142	7.285

4.4.2. Optimization with LINGO

Language for Interactive General Optimization (LINGO) is a simple tool for utilizing the power of linear and nonlinear optimization to formulate large problems concisely, solve them, and analyze the solution. Optimization helps us to find the answer that yields the best result; attains the highest profit, output, or happiness; or the one that achieves the lowest cost, waste, or discomfort. Often these problems involve making the most efficient use of our resources including money, time, machinery, staff, inventory, and more. Optimization problems are often classified as linear or nonlinear, depending on whether the relationships in the problem are linear with respect to the variables. In this thesis, since all of the response equations are nonlinear, programs were written using LINGO nonlinear programming technique (NLP) with Global optimization method to optimize the welding parameters and responses and to solve the nonlinear equations. The optimization by LINGO was carried out as unconstrained and constrained optimization.

In technique, from the quality point of view, it is most desired to have maximum tensile load, penetration, area of penetration and minimum heat affected zone, upper width and upper height. This required constrained optimization. In constrained optimization the responses were carried out together not separately. To optimize (maximum or minimum) one response the other responses formed constraints. Therefore, the response which was optimized limited with the constraints in a given data range and nonlinear equations. However, in unconstrained optimization, each response was optimized separately in a given data range without applying any constraints.

At the end of the constrained and unconstrained optimization programs software provides the solution report which consists of optimized welding parameters, responses, dual price, reduced cost and slack or surplus. The slack or surplus column in the solution report tells us how close we are to satisfying a constraint as equality. This quantity, on less-than-or-equal-to (≤) constraints, is generally referred to as slack. On greater-than-or-equal-to (≥) constraints, this quantity is called a surplus. If a constraint is exactly satisfied as equality, the slack

or surplus value will be zero. If a constraint is violated, as in an infeasible solution, the slack or surplus value will be negative. Knowing this can help us to find the violated constraints in an infeasible model. Non-binding constraints, constraints with a slack or surplus value greater than zero, will have positive, nonzero values in this column.

The dual price column in the solution report tells us, the amount that the objective would improve as the right-hand side, or constant term, of the constraint is increased by one unit.

4.4.2.1. Unconstrained Optimization

Unconstrained optimization for TL, HAZ, UW, UH, P and AP responses were carried out separately in order to optimize (in a given data range) the effect of each welding parameters (V, I, F, G) on the welding responses. For optimize one response another responses were not used as a constraint. The program was written to optimize the given welding response in a given data range. The flowchart of the written unconstrained optimization in LINGO 8.0 is given in Figure 4.67.

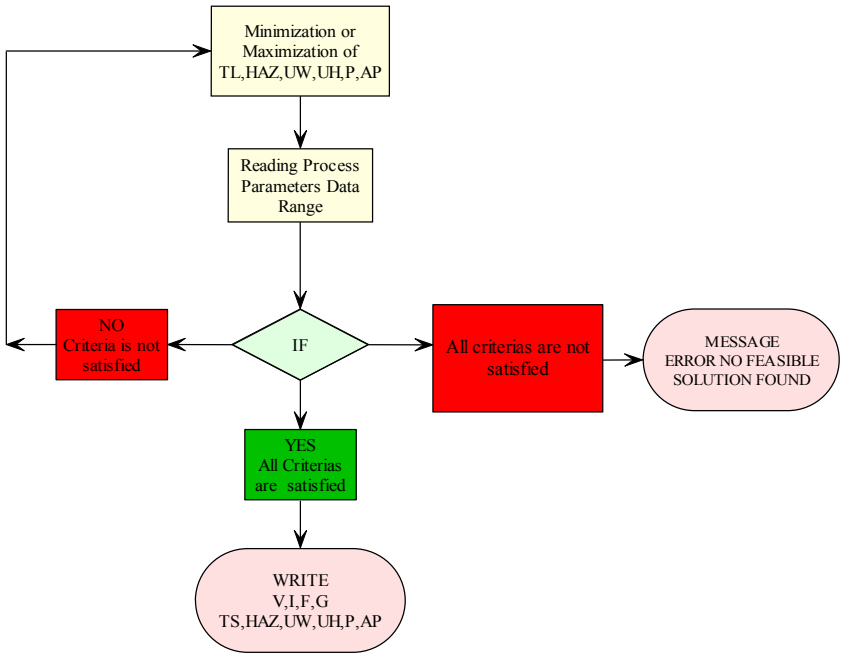

Figure 4.67. Flowchart of the unconstrained optimization

4.4.2.1.1. TL Maximization

As discussed earlier of the study, TIG weld quality is strongly characterized by the weld pool geometry. This is because the weld pool geometry plays an important role in determining the mechanical properties of the weld. Therefore, it is very important to select the welding process parameters for obtaining an optimal weld pool geometry. Usually, the desired welding process parameters are determined based on experience or from a handbook. However, this does not ensure that the selected welding process parameters can produce the optimal or near optimal weld pool geometry for that particular welding machine and environment.

Tensile test is a major selective method used to determine the quality of welding of thin sheet. As studied in this thesis, the quality of welding is affected by the welding parameters that affect the geometry and weld pool quality characteristics such as upper width, upper depth, penetration, and area of penetration.

So far, the formulas related with the effect of welding parameters on the weld pool geometry were derived to analyze each welding parameters on the welding responses such as TL, HAZ, UW, UH, P, AP.

To analyze and compare the results of the optimization method, the program was written to find the maximum transverse tensile load without applying any constraints for other responses. The written program is given in section B1 of Appendix B. Table 4.42 shows the optimization results for TL maximization.

Table 4.42. TL maximization

Objective value: **1330.734**		
Variable	Value	Reduced Cost
V	1.730641	0.000000
I	96.78699	0.000000
F	8.000000	0.000000
G	1.347659	0.000000
TL	1330.734	0.000000
HAZ	7.074831	0.000000
UW	10.07876	0.000000
UH	0.2314239	0.000000
P	1.270529	0.000000
AP	9.922669	0.000000

Row	Slack or Surplus	Dual Price
1	1330.734	1.000000
2	0.6610415	0.000000
3	1.823959	0.000000
4	76.78699	0.000000
5	53.21301	0.000000
6	0.000000	0.7964127E-01
7	4.000000	0.000000
8	0.3476592	0.000000
9	2.652341	0.000000
10	0.000000	0.000000
11	0.000000	0.000000
12	0.000000	0.000000
13	0.000000	0.000000
14	0.000000	0.000000
15	0.000000	0.000000

As indicated in dual price column, the dual price of 0.07964127 on row 6 means that adding one more unit of gas flow rate would cause the objective to improve by 0.07964127, to the TL value from 1330.734 to 1330.735 as shown in Table 4.43. So, it has very small and negligible effect on TL.

Table 4.43. Improved TL maximization

Global Objective value: **1330.735**
Iteration: 42

Variable	Value	Reduced Cost
V	1.730102	0.2628443E-06
I	96.79851	0.000000
F	7.976359	0.000000
G	1.345712	-0.3379232E-06
TL	1330.735	0.000000
HAZ	7.076200	0.000000
UW	10.07989	0.000000
UH	0.2314461	0.000000
P	1.270320	0.000000
AP	9.922461	0.000000

Row	Slack or Surplus	Dual Price
1	1330.735	1.000000
2	0.6605016	0.000000
3	1.824498	0.000000
4	76.79851	0.000000
5	53.20149	0.000000
6	0.5595882E-01	0.002340
7	4.023641	0.000000
8	0.3457122	0.000000
9	2.654288	0.000000
10	0.000000	0.000000
11	0.000000	0.000000
12	0.000000	0.000000
13	0.000000	0.000000
14	0.000000	0.000000
15	0.000000	0.000000

4.4.2.1.2. HAZ Minimization

The heat input rate is one of the most important variables in fusion welding and can strongly affect phase transformations during welding. Because, it governs heating rate, cooling rate and weld pool size. It is also responsible for weld residual stresses and distortion. The metallurgical feature that is directly affected by heat input rate is the grain size in the heat affected zone (HAZ) and in the weld metal. However, in this study by utilizing the HAZ equation derived from the response surface methodology was used to predict the HAZ on the weld samples. The program, given in Appendix B Section B2, was written to find the minimum Heat Affected Zone without applying any constraints.

The results for unconstrained HAZ minimization are shown in Table 4.13. The minimum HAZ value of 1.9243 mm was obtained with iteration number of 1.

Table 4.44. HAZ minimization

Global Objective value: **1.924300**
Iteration: 1

Variable	Value	Reduced Cost
V	3.410221	0.000000
I	20.00000	0.000000
F	12.00000	0.000000
G	1.000000	0.000000
TL	895.7857	0.000000
HAZ	1.924300	0.000000
UW	3.920618	0.000000
UH	0.7995010E-01	0.000000
P	0.8071280	0.000000
AP	4.184371	0.000000

Row	Slack or Surplus	Dual Price
1	1.924300	-1.000000
2	2.340621	0.000000
3	0.1443794	0.000000
4	0.000000	0.4988229E-01
5	130.0000	0.000000
6	4.000000	0.000000
7	0.000000	0.1616154E-01
8	0.000000	0.1207567
9	3.000000	0.000000
10	0.000000	0.000000
11	0.000000	0.000000
12	0.000000	0.000000
13	0.000000	0.000000
14	0.000000	0.000000
15	0.000000	0.000000

As indicated in dual price column above, the dual price of 0.04988 on row 4, 0.01616 on row 7, 0.1207 on row 8 mean that the new adjusted welding parameters according to the Dual price; I=20-0.049=19.951 A, F=12+0.016=12.016 l/min, G=1-0.12=0.88 mm will lower the HAZ value from 1.9243 to 1.9068 with the iteration number of 1 as shown in Table 4.45.

Table 4.45. Improved HAZ minimization

Global Objective value: **1.813022**
Iteration: 1

Variable	Value	Reduced Cost
V	4.805600	0.000000
I	19.95400	0.000000
F	12.13180	0.000000
G	0.8910000	0.000000
TL	420.7712	0.000000
HAZ	2.592148	0.000000
UW	1.813022	0.000000
UH	0.1769689	0.000000
P	0.6074842	0.000000
AP	2.864826	0.000000

Row	Slack or Surplus	Dual Price
1	1.813022	-1.000000
2	3.736000	0.000000
3	0.000000	0.000000
4	0.000000	0.000000
5	130.0460	0.000000
6	4.131800	0.000000
7	0.000000	0.000132
8	0.000000	0.001000
9	3.109000	0.000000
10	0.000000	0.000000
11	0.000000	0.000000
12	0.000000	0.000000
13	0.000000	0.000000
14	0.000000	0.000000
15	0.000000	0.000000

4.4.2.1.3. UW Minimization

As mentioned earlier, upper width is from the quality characteristics of a weldment and it directly affects the transverse tensile strength and the width of the heat affected zone. It is known that, the upper height, upper width, heat affected zone of the weld pool belong to the smaller-the-better quality characteristic. Therefore, their value must be minimized as much as possible. At this point, the program (Appendix B section B3) was written to find the minimum Upper width without applying any constraints. The results for unconstrained UW minimization are shown in Table 4.46.

Table 4.46. UW Minimization

Global Objective value: **3.744488**
Iteration: 1

Variable	Value	Reduced Cost
V	3.554600	0.000000
I	20.00000	0.000000
F	12.00000	0.000000
G	1.000000	0.000000
TL	860.3537	0.000000
HAZ	1.931638	0.000000
UW	3.744488	0.000000
UH	0.8486474E-01	0.000000
P	0.7896342	0.000000
AP	4.056086	0.000000

Row	Slack or Surplus	Dual Price
1	3.744488	-1.000000
2	2.485000	0.000000
3	0.000000	1.251271
4	0.000000	0.4691986E-01
5	130.0000	0.000000
6	4.000000	0.000000
7	0.000000	0.1318040
8	0.000000	0.1095861
9	3.000000	0.000000
10	0.000000	0.000000
11	0.000000	0.000000
12	0.000000	0.000000
13	0.000000	0.000000
14	0.000000	0.000000
15	0.000000	0.000000

The results in Table 4.47 showed that, the dual price of 1.2512 on row 3, 0.046919 on row 4, 0.13180 on row 7 and 0.10958 on row 8 mean that the new adjusted welding parameters according to the Dual price; V= 3.5546+1.2512=4.8056 mm/s, I= 20-0.046=19.954 A, F= 12+0.13180=12.1318 l/min, G= 1-0.109=0.891 mm will much lower the minimized UW value from 3.7444 mm to 1.906814 mm.

Table 4.47. Improved UW minimization

Global Objective value: **1.906814**
Iteration: 1

Variable	Value	Reduced Cost
V	3.409791	0.000000
I	19.95100	0.000000
F	12.01600	0.000000
G	0.8800000	0.000000
TL	894.5187	0.000000
HAZ	1.906814	0.000000
UW	3.902904	0.000000
UH	0.7933493E-01	0.000000
P	0.8092159	0.000000
AP	4.148082	0.000000

Row	Slack or Surplus	Dual Price
1	1.906814	-1.000000
2	2.340191	0.000000
3	0.1448087	0.000000
4	0.000000	0.000000
5	130.0490	0.000000
6	4.016000	0.000000
7	0.000000	0.001235
8	0.000000	0.021500
9	3.120000	0.000000
10	0.000000	0.000000
11	0.000000	0.000000
12	0.000000	0.000000
13	0.000000	0.000000
14	0.000000	0.000000
15	0.000000	0.000000

4.4.2.1.4. UH Minimization

As mentioned previously, upper height is from the smaller the better quality characteristics. Therefore, it needs to be minimized in order to obtain desired weld property. The program (Appendix B section B4) was written to find the minimum Upper Height without applying any constraints. The results for unconstrained UH minimization are shown in Table 4.48.

Table 4.48. UH minimization

Global Objective value: **0.048248**
Iteration: 18

Variable	Value	Reduced Cost
V	2.725442	0.000000
I	20.00000	0.000000
F	8.000000	0.000000
G	1.965282	0.000000
TL	1021.117	0.000000
HAZ	2.243625	0.000000
UW	5.019702	0.000000
UH	0.4824879E-01	0.000000
P	0.8721799	0.000000
AP	5.210986	0.000000

Row	Slack or Surplus	Dual Price
1	0.4824879E-01	-1.000000
2	1.655842	0.000000
3	0.8291578	0.000000
4	0.000000	0.1199715E-02
5	130.0000	0.000000
6	0.000000	0.1083937E-01
7	4.000000	0.000000
8	0.9652825	0.000000
9	2.034718	0.000000
10	0.000000	0.000000
11	0.000000	0.000000
12	0.000000	0.000000
13	0.000000	0.000000
14	0.000000	0.000000
15	0.000000	0.000000

The results showed that, the dual price of 0.0011 on row 4 and 0.0108 on row 6 mean that the new adjusted welding parameters according to the dual price; I= 20-0.00119=19.998 A, F= 8-0.0108=7.98 l/min will lower the minimized UH value from 0.0482 mm to 0.0480 mm. The improved UH value is shown in Table 4.49.

Table 4.49. Improved UH minimization

Global Objective value: **0.0480**
Iteration: 18

Variable	Value	Reduced Cost
V	2.724328	0.000000
I	19.99800	0.000000
F	7.980000	0.000000
G	1.972190	0.000000
TL	1021.042	0.000000
HAZ	2.244901	0.000000
UW	5.021270	0.000000
UH	0.4802911E-01	0.000000
P	0.8720950	0.000000
AP	5.212323	0.000000

Row	Slack or Surplus	Dual Price
1	0.4802911E-01	-1.000000
2	1.654728	0.000000
3	0.8302725	0.000000
4	0.000000	0.000000
5	130.0020	0.000000
6	0.000000	0.000000
7	4.020000	0.000000
8	0.9721899	0.000000
9	2.027810	0.000000
10	0.000000	0.000000
11	0.000000	0.000000
12	0.000000	0.000000
13	0.000000	0.000000
14	0.000000	0.000000
15	0.000000	0.000000

4.4.2.1.5. P Maximization

The Welding Encyclopedia refers to two types of penetrations “weld penetration” also called “fusion” and “heat penetration”. In fusion welding the depth of weld penetration or fusion is generally recognized as the distance below the original surface of the work to which the molten metal progresses. The HAZ refers to the parent metal metallurgically affected by the heat of welding, but not melted. The heat penetration includes the weld penetration as well as HAZ. Weld penetration is referred to as only “penetration” for simplicity.

The importance of proper penetration has been amply demonstrated by many researchers. It is generally recognized that penetration is influenced by polarity, current, arc length and arc-travel rate. It has been seen from the available literature

that the penetration and HAZ are controlled by the rate of heat input, which is a function of arc-travel rate, arc-length polarity and current.

The other factors which influence the penetration are heat conductivity, arc length and arc force. The higher the heat conductivity of a material the lower is the penetration. Longer arc-lengths produce shallower penetration because of the lesser concentration of heat. Too small arc-length may also give rise to poor penetration, if the arc-power is very low.

In this study, welding current affected the transverse tensile load. Lack of penetration which indicates lack of fusion caused low tensile strength. In literature its value must be as high as possible in order to enhance the mechanical properties of the joint. Therefore, its value must be maximized in all kind of welding processes in order to obtain higher strength.

The program in Appendix B section B5 was written to find the maximum Penetration without applying any constraints. The results for unconstrained UH minimization are shown in Table 4.50.

Table 4.50. P maximization

Global Objective value: **1.341610**
Iteration: 19

Variable	Value	Reduced Cost
V	1.069600	0.000000
I	117.7169	0.000000
F	12.00000	0.000000
G	3.076011	0.5413942E-07
TL	1227.896	0.000000
HAZ	9.525150	0.000000
UW	12.10105	0.000000
UH	0.3474763	0.000000
P	1.341610	0.000000
AP	12.47744	0.000000

Row	Slack or Surplus	Dual Price
1	1.341610	1.000000
2	0.000000	0.2110080E-01
3	2.485000	0.000000
4	97.71693	0.000000
5	32.28307	0.000000
6	4.000000	0.000000
7	0.000000	0.3133771E-02
8	2.076011	0.000000
9	0.9239889	0.000000
10	0.000000	0.000000
11	0.000000	0.000000
12	0.000000	0.000000
13	0.000000	0.000000
14	0.000000	0.000000
15	0.000000	0.000000

The results in Table 4.51 showed that, the dual price of 0.0211 on row 2 and 0.003133 on row 7 mean that the new adjusted welding parameters according to the dual price; V= 1.0696-0.0211=1.0485 mm/s, F= 12+0.003133=12.00313 l/min will increase the maximized P value slightly from 1.341 mm to 1.342 mm.

Table 4.51. Improved P maximization

Global Objective value: **1.34206**
Iteration: 20

Variable	Value	Reduced Cost
V	1.048500	0.000000
I	117.6454	0.000000
F	12.00313	0.000000
G	3.090626	0.1178250E-07
TL	1225.275	0.000000
HAZ	9.572681	0.000000
UW	12.12829	0.000000
UH	0.3508092	0.000000
P	1.342060	0.000000
AP	12.51951	0.000000

Row	Slack or Surplus	Dual Price
1	1.342060	1.000000
2	0.000000	0.000235
3	2.506100	0.000000
4	97.64539	0.000000
5	32.35461	0.000000
6	4.003130	0.000000
7	0.000000	0.000000
8	2.090626	0.000000
9	0.9093739	0.000000
10	0.000000	0.000000
11	0.000000	0.000000
12	0.000000	0.000000
13	0.000000	0.000000
14	0.000000	0.000000
15	0.000000	0.000000

4.4.2.1.6. AP Maximization

Area of Penetration is affected by the upper width and penetration. It may also affect the HAZ width. Its value must be maximized to improve the TL value.

The program which is given in Appendix B section B6 was written to find the maximum area of penetration without applying any constraints. The results for unconstrained UH minimization are shown in Table 4.52.

Table 4.52. AP maximization

Global Objective value: **13.92815**
Iteration: 2

Variable	Value	Reduced Cost
V	1.069600	0.000000
I	150.0000	0.000000
F	12.00000	0.000000
G	3.131880	0.000000
TL	1129.787	0.000000
HAZ	10.86175	0.000000
UW	13.63757	0.000000
UH	0.4018942	0.000000
P	1.301633	0.000000
AP	13.92815	0.000000

Row	Slack or Surplus	Dual Price
1	13.92815	1.000000
2	0.000000	2.587861
3	2.485000	0.000000
4	130.0000	0.000000
5	0.000000	0.4088067E-01
6	4.000000	0.000000
7	0.000000	0.1355446E-01
8	2.131880	0.000000
9	0.8681203	0.000000
10	0.000000	0.000000
11	0.000000	0.000000
12	0.000000	0.000000
13	0.000000	0.000000
14	0.000000	0.000000
15	0.000000	0.000000

The results in Table 4.53 indicated that, the dual price of 2.587861 on row 2 and 0.0408 on row 5 and 0.013 on row 7 mean that the new adjusted welding parameters according to the dual price; V=2.587-1.0696=1.5182 mm/s, I=150+0.0408=150.0408 A and F=12+0.0135=12.0135 l/min will increase the maximized AP value from 13.928 mm to 13.930 mm.

Table 4.53. Improved AP maximization

Global Objective value: **13.930**
Iteration: 4

Variable	Value	Reduced Cost
V	1.518200	0.000000
I	150.0408	0.000000
F	12.01350	0.000000
G	3.025243	0.2348713E-08
TL	1165.855	0.000000
HAZ	9.781259	0.000000
UW	12.80980	0.000000
UH	0.3218331	0.000000
P	1.294790	0.000000
AP	12.76590	0.000000

Row	Slack or Surplus	Dual Price
1	12.76590	1.000000
2	0.000000	0.002612
3	2.036400	0.000000
4	130.0408	0.000000
5	0.000000	0.000000
6	4.013500	0.000000
7	0.000000	0.000000
8	2.025243	0.000000
9	0.9747566	0.000000
10	0.000000	0.000000
11	0.000000	0.000000
12	0.000000	0.000000
13	0.000000	0.000000
14	0.000000	0.000000
15	0.000000	0.000000

The results of unconstrained optimization showed that, the effect of dual price on objective parameters (maximization or minimization) is so small. It is about ±0.01 of the actual objective value.

4.4.2.2. Constrained Optimization

Constrained optimization for TL, HAZ, UW, UH, P and AP responses were carried out together in order to optimize (in a given data range) the effect of each welding parameters (V, I, F, G) on the welding responses. For optimize one response another responses were used as a constraint. This is the real case used in practice. The program was written to optimize the given welding response in a given data range and constraints. The flowchart of the written unconstrained optimization in LINGO 8.0 is given in Figure 4.68.

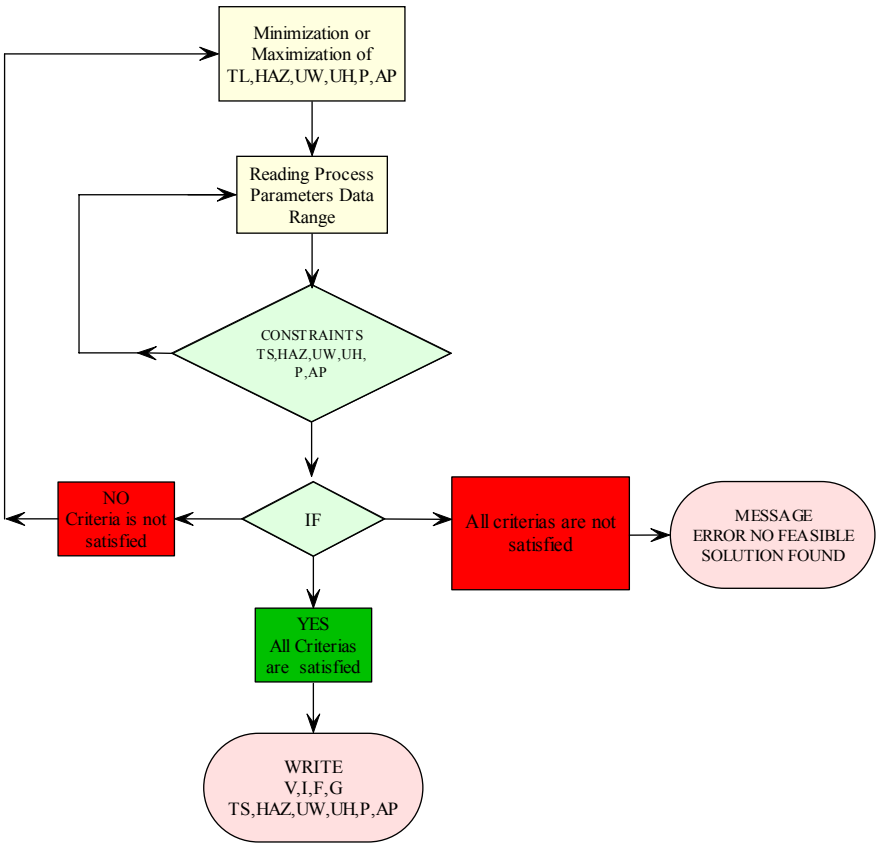

Figure 4.68. Flowchart of the constrained optimization

4.4.2.2.1. Constrained TL Optimization

Constraints are required to satisfy the target value by adopting the responses. The Response Constrained program given in Appendix B section B7 was written to find the maximum TL with applying constraints. In the program responses were chosen as constraint. The results for constrained TL maximization are shown in Table 4.54. TL value of 1330.645 kgf was obtained with the constrained optimization technique. So, only slight negligible difference of 0.088 kgf with the unconstrained optimization was considered.

Table 4.54. Constrained TL optimization

Global Objective value: **1330.645**
Iteration: 23

Variable	Value	Reduced Cost
V	1.751866	0.000000
I	95.98245	0.000000
F	8.139003	0.000000
G	1.346964	0.000000
TL	1330.645	0.000000
HAZ	7.001355	0.000000
UW	10.01017	0.000000
UH	0.2279954	0.000000
P	1.270265	0.000000
AP	9.857532	0.000000

Row	Slack or Surplus	Dual Price
1	1330.645	1.000000
2	0.6822659	0.000000
3	1.802734	0.000000
4	75.98245	0.000000
5	54.01755	0.000000
6	0.1390033	0.000000
7	3.860997	0.000000
8	0.3469641	0.000000
9	2.653036	0.000000
10	0.000000	0.4404222E-01
11	0.1702650	0.000000
12	0.000000	0.000000
13	0.000000	0.000000
14	0.000000	0.000000
15	0.000000	0.000000
16	0.000000	0.000000
17	0.000000	0.000000

4.4.2.2.2. Constrained HAZ Optimization

TL and P were chosen as constraint in the program to satisfy the desired HAZ value. The Response Constrained program given in Appendix D8 was written to find the minimum HAZ with applying constraints. The results for constrained TL maximization are shown in Table 4.55. Constrained optimized value of 4.9190 mm was obtained in this section. The unconstrained HAZ value increased from 1.924 mm to 4.9190 mm when considered all of the responses as a constraint. The increment is 2.995 mm for constrained optimization.

Table 4.55. Constrained HAZ optimization

Global Objective value: **4.919098**
Iteration: 19

Variable	Value	Reduced Cost
V	2.577672	0.000000
I	76.08548	0.000000
F	11.65038	0.000000
G	1.000000	0.000000
TL	1247.988	0.000000
HAZ	4.919098	0.000000
UW	7.646438	0.000000
UH	0.1335872	0.000000
P	1.200000	0.000000
AP	7.517670	0.000000

Row	Slack or Surplus	Dual Price
1	4.919098	-1.000000
2	1.508072	0.000000
3	0.9769278	0.000000
4	56.08548	0.000000
5	73.91452	0.000000
6	3.650375	0.000000
7	0.3496249	0.000000
8	0.000000	0.1051059E-01
9	3.000000	0.000000
10	0.000000	0.2920594E-02
11	0.000000	-11.57168
12	0.000000	0.000000
13	0.000000	0.000000
14	0.000000	0.000000
15	0.000000	0.000000
16	0.000000	0.000000
17	0.000000	0.000000

4.4.2.2.3. Constrained UW Optimization

The Response Constrained program was written to find the minimum UW by applying constraints. Table 4.56 shows solution of the constrained UW optimization. UW value of 7.4428 mm was obtained with 19 iterations when considering the constraints as a whole. The increment in UW value is 3.698 mm for constrained optimization.

Table 4.56. Constrained UW optimization

Global Objective value: **7.4428**
Iteration: 19

Variable	Value	Reduced Cost
V	2.253941	0.000000
I	63.60731	0.000000
F	12.00000	0.000000
G	1.000000	0.000000
TL	1248.819	0.000000
HAZ	4.687479	0.000000
UW	7.442881	0.000000
UH	0.1406728	0.000000
P	1.171031	0.000000
AP	7.441002	0.000000

Row	Slack or Surplus	Dual Price
1	7.442881	-1.000000
2	1.184341	0.000000
3	1.300659	0.000000
4	43.60731	0.000000
5	86.39269	0.000000
6	4.000000	0.000000
7	0.000000	0.4613741E-02
8	0.000000	0.1061598
9	3.000000	0.000000
10	0.000000	0.2016991E-01
11	0.7103147E-01	0.000000
12	0.000000	0.000000
13	0.000000	0.000000
14	0.000000	0.000000
15	0.000000	0.000000
16	0.000000	0.000000
17	0.000000	0.000000

4.4.2.2.4. Constrained UH Optimization

The Response Constrained program was written to find the minimum UH by applying constraints. As shown in Table 4.57 shows the solution of the constrained UH optimization. UH value of 7.4428 mm was obtained with 30 iterations when considering the constraints as a whole. The increment in UH value is 0.07 mm for constrained optimization.

Table 4.57. Constrained UH optimization

Global Objective value: **0.1187**
Iteration: 30

Variable	Value	Reduced Cost
V	2.397302	0.1225735E-07
I	68.15456	0.000000
F	8.000000	0.000000
G	1.920463	0.000000
TL	1262.967	0.000000
HAZ	4.964658	0.000000
UW	7.899717	0.000000
UH	0.1187916	0.000000
P	1.182733	0.000000
AP	7.759485	0.000000

Row	Slack or Surplus	Dual Price
1	0.1187916	-1.000000
2	1.327702	0.000000
3	1.157298	0.000000
4	48.15456	0.000000
5	81.84544	0.000000
6	0.000000	0.2541452E-02
7	4.000000	0.000000
8	0.9204631	0.000000
9	2.079537	0.000000
10	0.000000	0.8463389E-03
11	0.8273308E-01	0.000000
12	0.000000	0.000000
13	0.000000	0.000000
14	0.000000	0.000000
15	0.000000	0.000000
16	0.000000	0.000000
17	0.000000	0.000000

4.4.2.2.5. Constrained P Optimization

The Response Constrained program was written to find the minimum P by applying constraints. As shown in Table 4.58 shows the solution of the constrained P optimization. P value of 1.3216 mm was obtained with 39 iterations when considering the constraints as a whole. The reduction in P value is recorded as 0.01 mm for constrained optimization.

Table 4.58. Constrained P optimization

Global Objective value: **1.3216**
Iteration: 39

Variable	Value	Reduced Cost
V	1.612465	0.000000
I	108.3196	0.000000
F	12.00000	0.000000
G	2.388893	0.000000
TL	1289.816	0.000000
HAZ	7.880538	0.000000
UW	10.73387	0.000000
UH	0.2557629	0.000000
P	1.321672	0.000000
AP	10.86670	0.000000

Row	Slack or Surplus	Dual Price
1	1.321672	1.000000
2	0.5428650	0.000000
3	1.942135	0.000000
4	88.31955	0.000000
5	41.68045	0.000000
6	4.000000	0.000000
7	0.000000	0.3183828E-02
8	1.388893	0.000000
9	1.611107	0.000000
10	0.000000	0.4058603E-03
11	0.1216723	0.000000
12	0.000000	0.000000
13	0.000000	0.000000
14	0.000000	0.000000
15	0.000000	0.000000
16	0.000000	0.000000
17	0.000000	0.000000

4.4.2.2.6. Constrained AP Optimization

The Response Constrained program was written to find the minimum AP by applying constraints. As shown in Table 4.59 shows the solution of the constrained AP optimization. AP value of 10.640 mm^2 was obtained with 11 iterations when considering the constraints as a whole. Mainly, decrease in P value caused a reduction in AP. The reduction in AP value is recorded as 3.288 mm^2 for constrained optimization.

Table 4.59. Constrained AP optimization

Global Objective value: **10.640**
Iteration: 11

Variable	Value	Reduced Cost
V	1.635331	0.000000
I	105.6970	0.000000
F	12.00000	0.000000
G	1.948333	0.000000
TL	1295.837	0.000000
HAZ	7.654247	0.000000
UW	10.48154	0.000000
UH	0.2529978	0.000000
P	1.314249	0.000000
AP	10.64013	0.000000

Row	Slack or Surplus	Dual Price
1	10.64013	1.000000
2	0.5657305	0.000000
3	1.919269	0.000000
4	85.69704	0.000000
5	44.30296	0.000000
6	4.000000	0.000000
7	0.000000	0.2764973E-01
8	0.9483328	0.000000
9	2.051667	0.000000
10	0.000000	0.2652561E-01
11	0.1142490	0.000000
12	0.000000	0.000000
13	0.000000	0.000000
14	0.000000	0.000000
15	0.000000	0.000000
16	0.000000	0.000000
17	0.000000	0.000000

4.4.3. Comparison of the Predicted and Measured Results

The final step in optimization is to compare and verify the effect of TIG welding process parameters on the weld pool geometry of the joints. The effect of the process parameters on the TIG welding of stainless steel with the optimal weld pool geometry has been compared. The optimal weld pool geometry has three smaller-the-better quality characteristics, i.e. the upper width (UW), upper height (UH), heat affected zone (HAZ) and three higher-the-better quality characteristics, i.e. tensile load (TL), penetration (P) and area of penetration (AP).

Table 4.60 shows the comparison of the two optimization method. Results of optimization indicate that welding speed, welding current, gas flow rate and arc gap are the significant welding process parameters affecting the multiple quality characteristics.

Table 4.60. Comparison of optimization methods and optimum welding parameters

		Objective	Constraints	Optimum value				Optimum solution
				V	I	F	G	
LINGO 8.0	One Objective	TL max	$1.06 \leq V \leq 3.55$ $20 \leq I \leq 150$ $8 \leq F \leq 12$ $1 \leq G \leq 4$	1.73	96.78	8.0	1.34	TL= 1330.73 kgf
		HAZ min		3.41	20.00	12.0	1.00	HAZ= 1.924 mm
		UW min		3.55	20.00	12.0	1.00	UW= 3.744 mm
		UH min		2.72	20.00	8.00	1.96	UH= 0.04 mm
		P max		1.07	117.71	12.0	3.07	P= 1.340 mm
		AP max		1.07	150.0	12.0	3.13	AP=13.920 mm^2
	Multi Objective	TL max P max HAZ min		1.73	96.53	8.0	1.34	TL= 1330.73 kgf HAZ= 7.054 mm UW= 10.06 mm UH= 0.23 mm P= 1.260 mm AP= 9.90 mm^2
Design Expert 6.0	One Objective	TL max	$1.06 \leq V \leq 3.55$ $20 \leq I \leq 150$ $8 \leq F \leq 12$ $1 \leq G \leq 4$	1.73	96.77	8.00	1.35	TL= 1330.73 kgf
		HAZ min		3.44	20.50	10.80	3.78	HAZ=2.150 mm
		UW min		3.47	22.40	10.34	1.62	UW= 4.190 mm
		UH min		2.72	20.05	8.00	1.96	UH= 0.04 mm
		P max		1.88	110.44	10.25	2.84	P= 1.30 mm
		AP max		1.39	132.95	9.27	1.66	AP= 12.22 mm^2
	Multi Objective	TL max P max HAZ min		2.41	67.32	9.94	1.01	TL= 1261.55 kgf HAZ= 4.73 mm UW= 7.65 mm UH=0.134 mm P= 1.17 mm AP=7.52 mm^2

Also, experimental results have shown that the upper width, upper height, heat affected zone, tensile strength, penetration and area of penetration of the weld pool in the TIG welding of stainless steel are greatly improved by using this technique.

The results from diagnostic test showed that, the minimum residual obtained from the derived equations is shown in Table 4.61.

Table 4.61. Maximum and minimum residuals obtained from diagnostic test

Residuals	TL	HAZ	UW	UH	P	AP
Minimum	-263.05	-0.81	-0.120	-0.10	-0.13	-2.16
Maximum	229.56	1.13	0.120	0.12	0.13	1.71

Comparisons were made to detect the validity of the developed mathematical formulas. Good agreement was obtained between the predicted values and actual measured values as shown in Table 4.62.

Table 4.62. Comparison of the predicted and measured results

TL	Predicted	1167	**V (mm/s)**	1.06	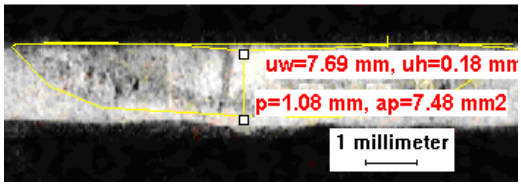
	Measured	1125			
HAZ	Predicted	5.16	**I (A)**	40	
	Measured	5.44			
UW	Predicted	7.30			
	Measured	7.69			
UH	Predicted	0.19	**F (l/min)**	8	
	Measured	0.18			
P	Predicted	1.08			
	Measured	1.08	**G (mm)**	1	
AP	Predicted	7.66			
	Measured	7.48			
TL	Predicted	1135	**V (mm/s)**	1.53	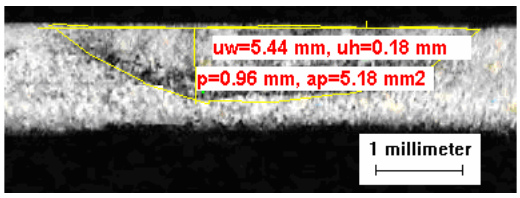
	Measured	1100			
HAZ	Predicted	3.97	**I (A)**	30	
	Measured	4.13			
UW	Predicted	6.52			
	Measured	5.79			
UH	Predicted	0.13	**F (l/min)**	10	
	Measured	0.18			
P	Predicted	1.03			
	Measured	0.96	**G (mm)**	2.5	
AP	Predicted	6.83			
	Measured	5.18			

Continue of Table 4.62

TL	Predicted	1033	**V (mm/s)**	1.06	
	Measured	1000			
HAZ	Predicted	3.85			
	Measured	3.26	**I (A)**	20	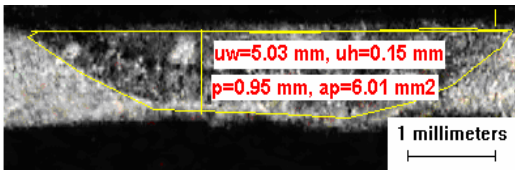
UW	Predicted	5.51			
	Measured	5.03			
UH	Predicted	0.17	**F (l/min)**	12	
	Measured	0.15			
P	Predicted	0.98			
	Measured	0.95	**G (mm)**	1	
AP	Predicted	6.15			
	Measured	6.01			
TL	Predicted	1236	**V (mm/s)**	1.99	
	Measured	1260			
HAZ	Predicted	5.64			
	Measured	5.30	**I (A)**	70	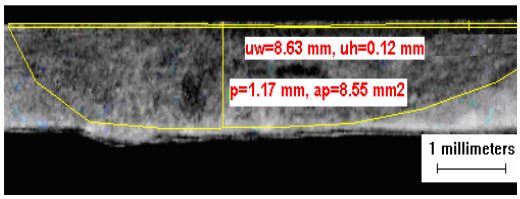
UW	Predicted	8.60			
	Measured	8.63			
UH	Predicted	0.17	**F (l/min)**	12	
	Measured	0.12			
P	Predicted	1.15			
	Measured	1.17	**G (mm)**	4	
AP	Predicted	8.26			
	Measured	8.55			

Furthermore, as indicated in Table 4.63, an attempt was made to compare the optimized welding process parameters with the measured welding process parameters. Here is also close agreement obtained with the actual parameters.

Table 4.63. Comparison of the predicted and optimized welding parameters

TL	Measured	1300	**V (mm/s)**	1.73	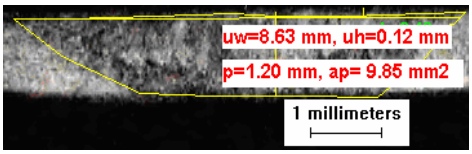
	Optimized	1330			
HAZ	Measured	6.89			
	Optimized	7.07	**I (A)**	95	
UW	Measured	9.53			
	Optimized	10.07			
UH	Measured	0.20	**F (l/min)**	8	
	Optimized	0.23			
P	Measured	1.20			
	Optimized	1.27	**G (mm)**	1.7	
AP	Measured	9.85			
	Optimized	9.92			

4.5. Weld Pool Shape Modeling

4.5.1. Modeling with MATLAB

Weld pool geometry which includes penetration, bead height and bead width are important physical properties of a weldment. It is said that the cooling rate of a weld can be predicted from the weld cross-sectional area and the arc-travel rate. The weld pool cross-sectional area together with its height and width affects the total shrinkage, which determines largely the residual stresses and thus the distortion. When welding brittle materials like cast iron, the shrinkage may give rise to crack formation.

Several welding parameters seem to affect the bead geometry. Since the weld bead results from the solidification of liquid metal, the interfacial tensions play a significant role in determining the ultimate bead geometry. Summarizing, it can be stated that the weld pool geometry and penetration affect the weldment characteristics and are dependent on a number of welding variables.

In the present investigation an attempt was made to study and predict some of the weldment characteristics such as upper height, upper width and penetration, as it was affected by welding parameters like arc length, welding speed rate, welding current, gas flow rate and gap distance.

For a fairly limited number of weld trials it can be concluded that high correlations can be achieved by using prediction program when predicting bead width, bead height, penetration and area of penetration for single butt welds of 1.2 mm AISI 304 stainless steel. The highest correlation for all four output parameters was achieved with MATLAB programming technique.

Knowing the values of these shape parameters may be sufficient for certain applications, but they do not provide an actual predicted weld pool profile. Such a predicted cross-sectional profile would allow for a visual means of assessing the accuracy in the profile predictions and also allow for a visual means of evaluating the effect of process parameters on the weld pool shape. To address this need for predicting the actual weld profiles, a program given in Appendix C was written in MATLAB programming language to convert the predicted shape parameters into a weld profile.

The general run mode of the written MATLAB program is shown in Figure 4.69.

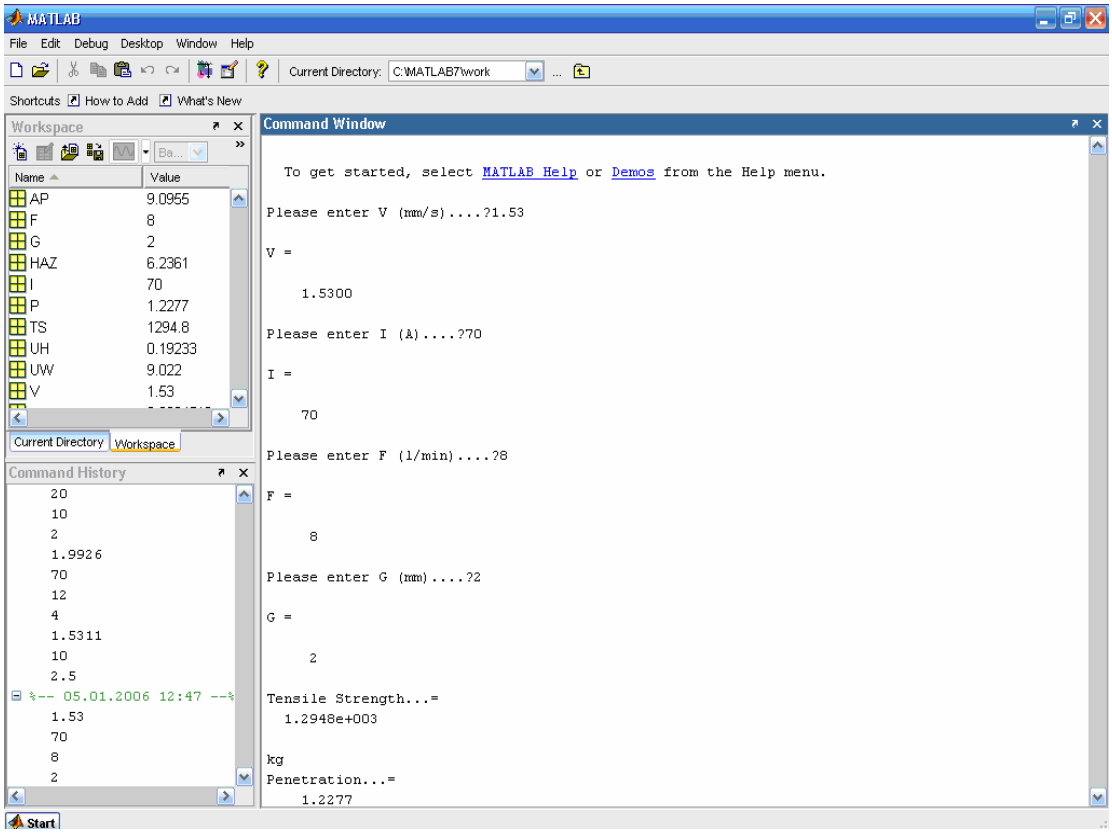

Figure 4.69. Run mode of the program

This program calculates the weld pool parameters (TL, HAZ, UW, UH, P, AP) and draws the predicted shape according to the entering inputs (V, I, F, G) as shown in Figure 4.70.

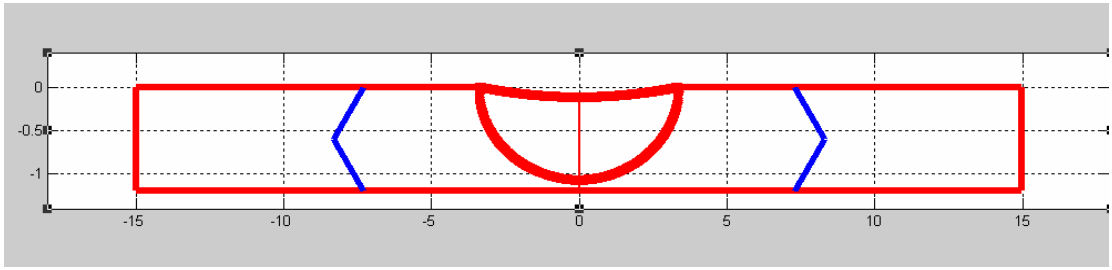

Figure 4.70. Final predicted weld pool shape (end of the MATLAB program)

Comparison was made with the actual weld pool geometry and predicted weld pool geometry to show the visual means of evaluating the effect of process parameter on the weld pool shape. Good agreement was obtained between measured weld profile and predicted weld profile, as shown in Table 4.64.

Table 4.64. Comparison of predicted weld pool profiles

Process Parameters	Pool Properties			Measured Weld Profile Actual	Predicted weld profile MATLAB
	Prop.	**Mea.**	**Calc.**		
V=1.06mm/s I=40A F=8 l/min G=1mm	**TL**	1125	1166.1	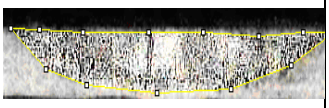	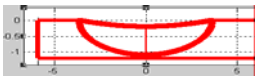
	HAZ	5.44	5.44		
	UW	7.69	7.30		
	UH	0.180	0.193		
	P	1.08	1.0822		
	AP	7.48	7.668		
Process Parameters	**Pool Properties**			**Measured Weld Profile Actual**	**Predicted weld profile MATLAB**
	Prop.	**Mea.**	**Calc.**		
V=1.99mm/s I=70A F=12 l/min G=4mm	**TL**	1260	1236.3	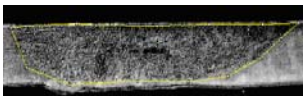	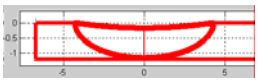
	HAZ	5.30	5.64		
	UW	8.63	8.60		
	UH	0.12	0.16		
	P	1.17	1.150		
	AP	8.56	8.25		
Process Parameters	**Pool Properties**			**Measured Weld Profile Actual**	**Predicted weld profile MATLAB**
	Prop.	**Mea.**	**Calc.**		
V=1.53mm/s I=10A F=10 l/min G=2.5mm	**TL**	750	950	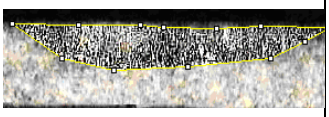	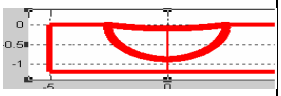
	HAZ	2.55	2.68		
	UW	4.22	5.11		
	UH	0.09	0.09		
	P	0.75	0.88		
	AP	4.60	5.51		

4.5.2. Neural Network Analysis

Neural networks are based on a methodical scheme in which inputs are related to outputs by a system of interconnected nodes. Neural networks are a highly flexible modeling tool with an ability to learn the relationships between input variables and output feature spaces. It has been shown that neural networks are superior to traditional approaches in modeling manufacturing processes with highly non-linear, strongly coupled characteristics. A back-propagation network was considered to construct the relationships between welding process parameters and the features on the weld pool geometry.

In this study, the neurons of the input layer are used to receive the process parameters, i.e., welding speed, welding current, gas flow rate and arc gap. The neurons of the output layer are used to send out six features on the weld pool geometry, i.e., tensile load, heat affected zone, upper width, upper height, penetration and area of penetration. As a result, there are four input variables and six output variables in the back-propagation network. The number of neurons in the hidden layer was determined by trial-and-error experimentation. To establish properly the relationships between welding process parameters and the features on the weld pool geometry, a number of TIG welding experiments as a training data were carried out according to the Table D1 in Appendix D.

Training takes the form of adjusting the weights (connections) between the nodes in the different layers. Once the optimal neural network weights are determined, the process of calculating the outputs from a set of inputs is a rapid and trivial task. Neural network training was carried out with the use of a training data set that contains sets of inputs and corresponding, experimentally determined outputs. The neural network was developed by comparing the predicted output values with the actual outputs and, using an optimization scheme, adjusting the weights to minimize the prediction error.

Through the learning process, which involved thousands of iterations, a complex relationship between the inputs and output evolved. Eventually, the network “learned” a scheme in which outputs were associated with the inputs. In the

present analysis, Qwiknet V2.23 software program was used for the neural network development. Also, MATLAB codes for neural network were written in order to create another alternative for neural network solvers. The written program in MATLAB language is given in Appendix C.

After learning process of the network, the connection weights according to the input and output nodes were found as shown in Table 4.65.

Table 4.65. Connection weights between input, output and hidden layers

Input	**Hidden layer node number**					
layer node	1	2	3	4	5	
Bias	8.98654	1.95867	-0.468343	0.232803	-1.51125	
Velocity	-8.53646	3.49575	-0.003059	-0.81455	2.287120	
Current	-1.87252	2.43242	-0.163630	0.593715	-0.239929	
Gas flow	0.951458	-6.86457	-0.16584	0.117838	-5.46895	
Arc gap	8.25133	-5.41284	-0.61699	-2.88346	-1.32354	
Hidden	**Output node**					
node number	TL	HAZ	UW	UH	P	AP
Bias	-3.60389	-0.905768	1.08144	-5.12274	1.31375	2.06967
1	1.53855	1.49383	3.36355	-2.68354	-0.022030	-2.20858
2	-1.50829	-0.478542	5.70713	-3.16411	1.00531	-0.921646
3	1.8928	2.54372	-4.34028	-2.19703	-1.83259	-0.024737
4	0.34106	2.16982	1.67857	-5.06617	1.69595	-1.43516
5	0.107818	1.86656	2.00923	-3.67969	0.522064	-1.75875

Ninety different experimental welds were made, as listed in Appendix D Table D1. These welds provide a total data set of 90 weld conditions and the corresponding weld pool parameters. For the purpose of identifying the optimal network architecture and testing the adequacy of the network model thirty-eight testing data were prepared as shown in Appendix D Table D2.

The optimum architecture was selected as the one with the minimal predictive error. Figure 4.71 shows the training and predictive errors, averaged over

the 38 training/testing pairs, as a function of the number of hidden nodes. A small predictive error was found for five hidden nodes

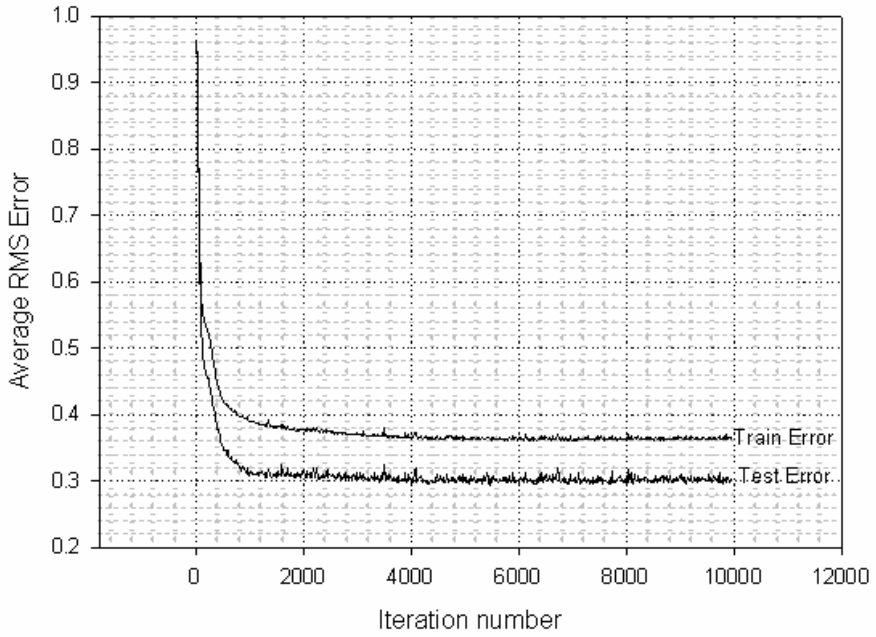

Figure 4.71. Average RMS errors as a function of iteration number for network learning and testing

The predictive capability of the resultant networks was evaluated by predicting the pool parameters for the previously unseen conditions in the test sets. In this way, the predictions were made for conditions that were not used in the training of the networks and therefore represented true predictions.

In many neural network applications, the number of hidden nodes is inappropriately high compared with the amount of data available for training the network. The result is that the network fits the training data very well but its predictive capabilities are poor. This condition is referred to as overfitting. As a rule of thumb, the number of connections between the inputs and the hidden nodes in the neural network should be less than the number of data points available for training. In the present work, the number of data points available for training (90) was enough.

The analysis showed that an optimum neural network, based on a minimum prediction error, contained five hidden nodes. For the four process parameters that were used as input variables and the bias, this corresponds to 61 connection weights.

In this study, neural network modeling appeared to be well suited for predicting weld pool shape, particularly when there is no other predictive capability using theoretical numerical models. The model predictions were shown to be in good agreement with the experimental pool properties. Neural networks are ideally suited for identifying trends and relationships between actual and predicted values and this capability is demonstrated in Figures 4.72-4.77 for prediction of the TIG welding parameters. The full forms of the comparisons Tables are given in Appendix D Table D3.

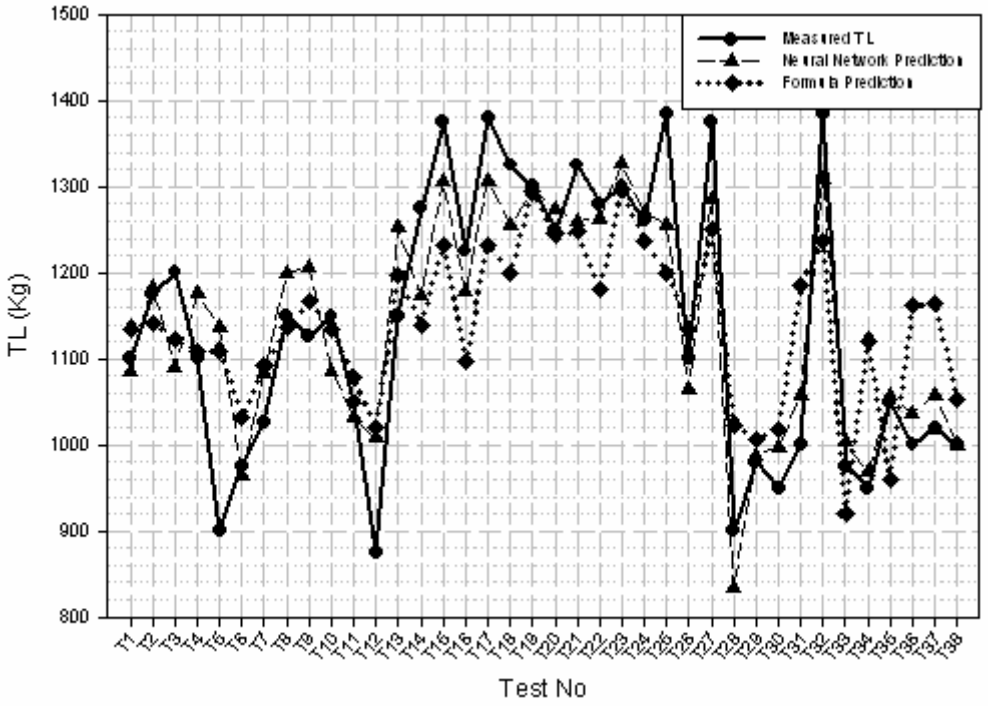

Figure 4.72. Comparison of the results for TL

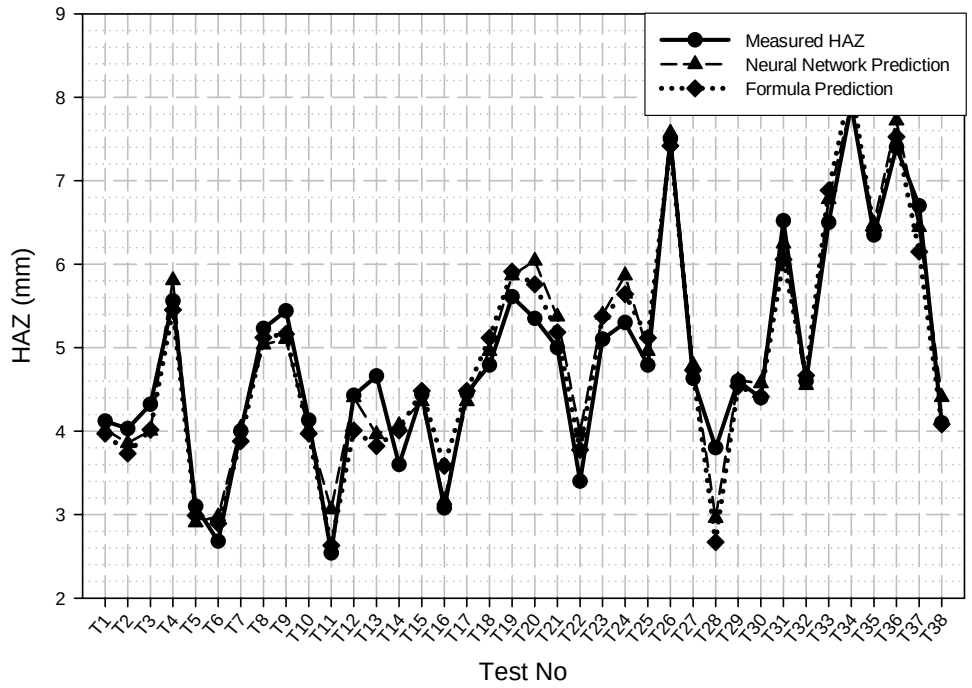

Figure 4.73. Comparison of the results for HAZ

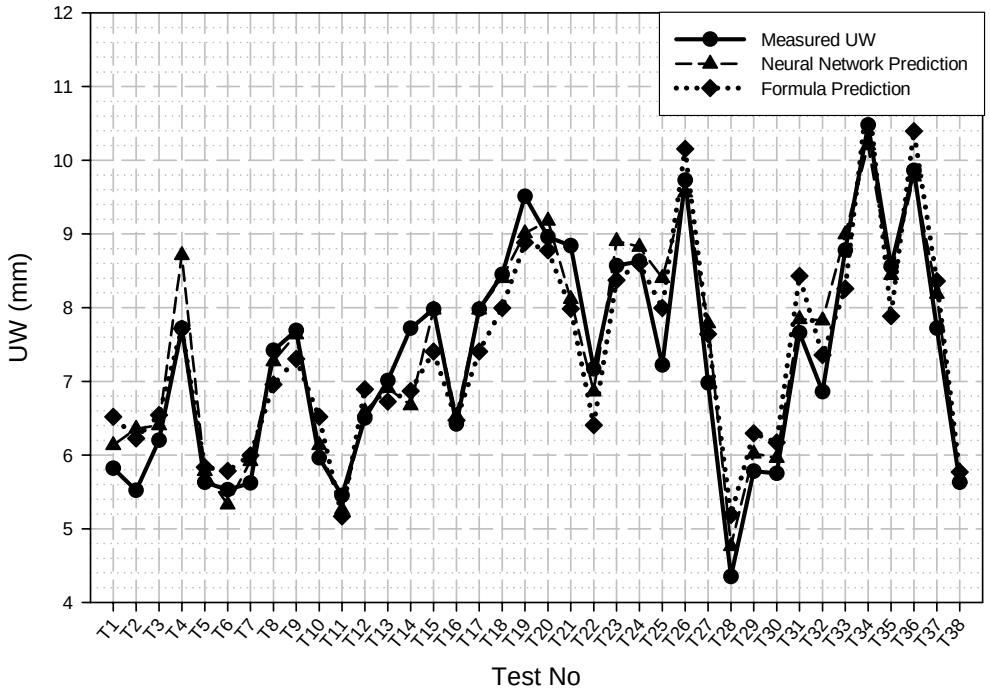

Figure 4.74. Comparison of the results for UW

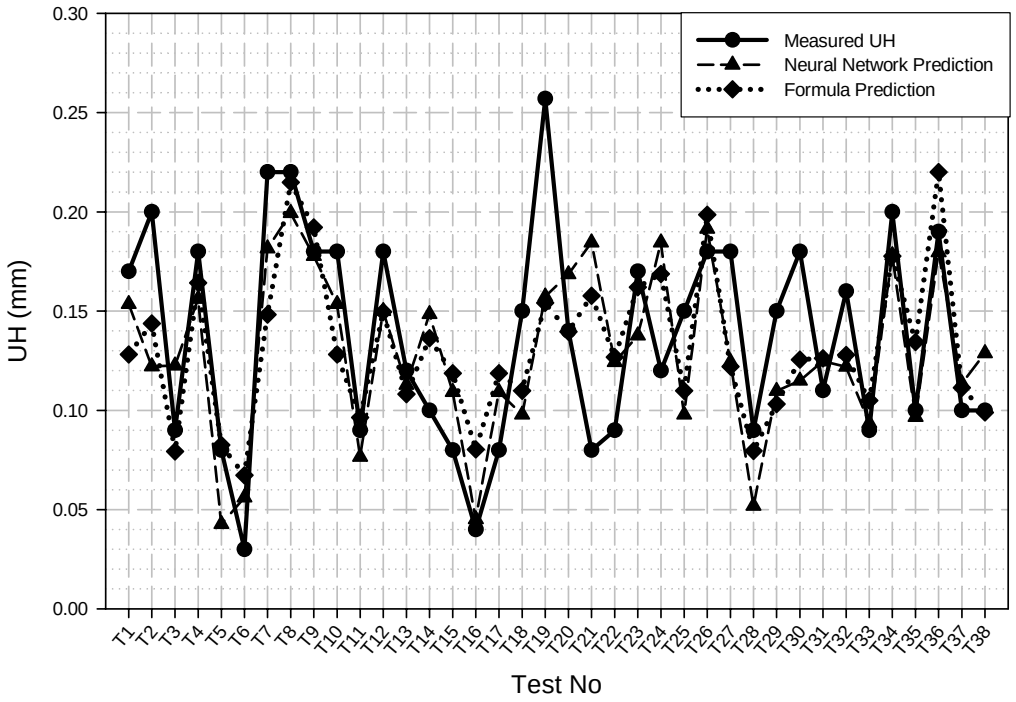

Figure 4.75. Comparison of the results for UH

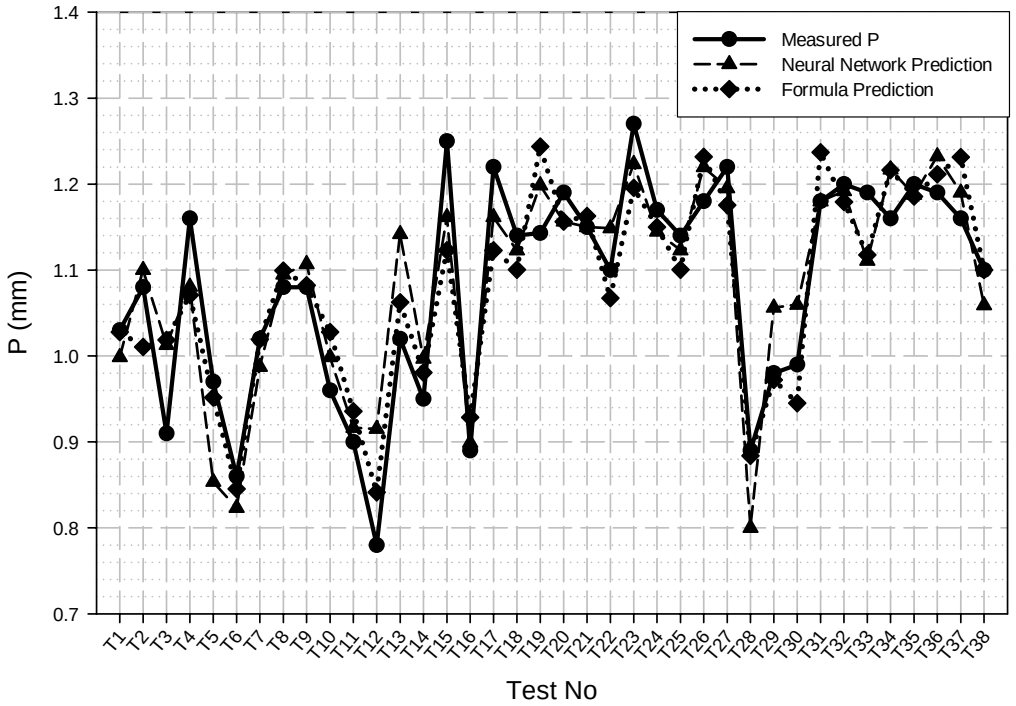

Figure 4.76. Comparison of the results for P

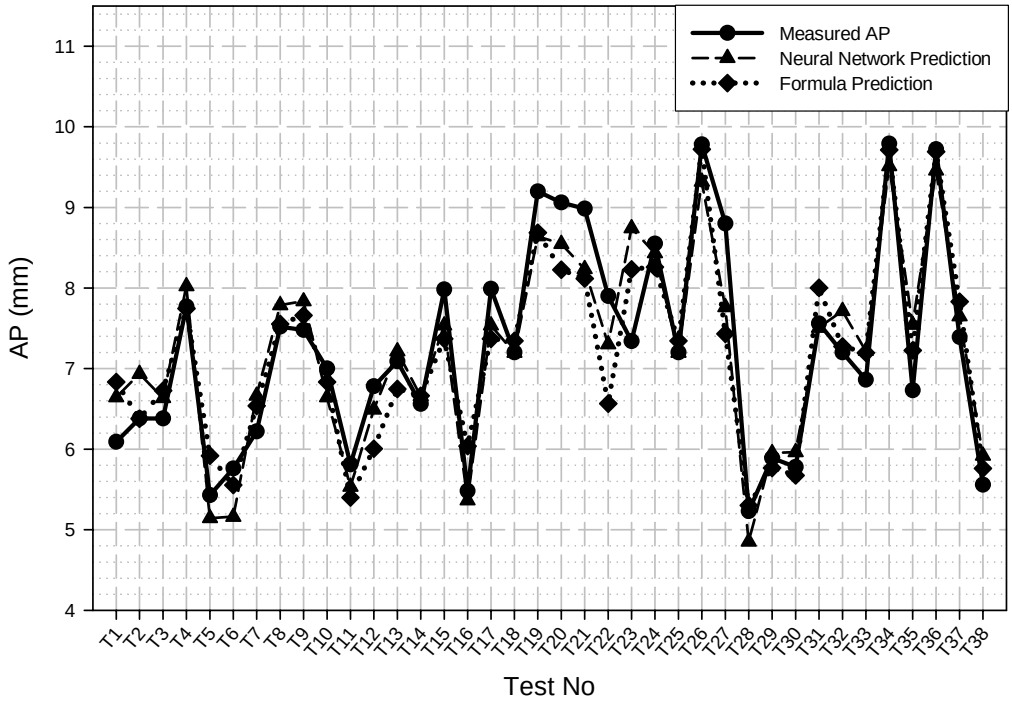

Figure 4.77. Comparison of the results for AP

The present analysis showed that neural network modeling is a viable means for predicting weld pool shape as a function of weld process conditions. Accurate predictions could be achieved after training the network with a limited amount of experimental data. The neural network model indicates that the weld pool geometry is a sensitive function of the input parameters such as welding speed, current, shielding gas flow rate and arc gap.

4.6. Controlling the Applicability of the Mathematical Formulation for Different Thicknesses

The applicability of the mathematical formulations was tested for the same material AISI 304 and thickness of 2mm. The same procedure was applied step by step as follows;

- ✓Choosing the design type as response surface and central composite design

- ✓Design of experiments: lower and upper limits were determined according to the Table E1 in Appendix E
- ✓Their levels were determined (Appendix E Figure E1)
- ✓ Determining the completed response form (Appendix E Figure E2)
- ✓Creating the design layout and recording responses (Appendix E Figure E3)
- ✓Statistical analysis of results
  - o sequential model sum of squares for TL and HAZ separately (Appendix E Table E2-E3)
  - o lack of fit tests for TL and HAZ respectively (Appendix E Table E4-E5)
  - o Model Summary Statistics for TL and HAZ (Appendix E Table E6-E7)
  - o Analysis of variance for TL and HAZ (Appendix E Table E7-E8)

After from these steps the final quadratic mathematical models were constructed according to equation 4.1 given in mathematical modeling section and final mathematical equations were derived for TL and HAZ as follows;

Transverse tensile strength:

$$TL=-1374.16364 - 237.70287 * V + 12.45075 * I + 512.03844 * F + 272.94085 * G -4.00437 * V^2 -0.055744 * I^2 -20.99482 * F^2 -8.36397 * G^2 + 2.51509 * V * I - 6.28773 * V * F - 20.12072 * V * G - 0.31250 * I * F - 0.30303 * I * G - 16.66667 * F * G \quad (4.10)$$

Heat affected zone:

$$HAZ=6.99690 - 1.02651 * V + 0.074079 * I - 0.84935 * F - 0.69361 * G + 0.13748 * V2 - 1.17121E-004 * I2 + 0.041640 * F2 + 0.12470 * G2 - 8.24035E-003 * V * I - 7.54527E-004 * V * F- 1.00604E-003 * V * G + 5.11364E-005 * I * F - 1.43939E-004 * I * G + 4.79167E-003 * F * G \quad (4.11)$$

Here is also optimization was made using Design Expert 6.0 software. Optimization condition and optimization results for AISI 304 2 mm stainless steel sheet is shown in Table 4.66 and 4.67 respectively.

Table 4.66. Optimization conditions for 2mm AISI 304 sheet

Name	Goal	Lower Limit	Upper Limit	Lower Weight	Upper Weight	Importance
V	is in range	1.69	2.93	1	1	3
I	is in range	52	117	1	1	3
F	is in range	9	11	1	1	3
G	is in range	1.75	3.25	1	1	3
TS	maximize	850	1985	1	1	3
HAZ	minimize	1.23	9.28	1	1	3

Ten solutions were found according to the given situation in Table 4.38. The optimized solution is shown in Table 4.67.

Table 4.67. Optimization results for 2 mm AISI 304 stainless steel sheet

Number	V	I	F	G	TS	HAZ	Desirability
1	1.69	52.02	10.35	2.75	1779.04	3.29763	0.780
2	1.69	52.00	10.37	2.67	1778.64	3.29568	0.780
3	1.69	52.01	10.25	2.74	1778.25	3.29468	0.780
4	1.69	52.00	10.25	2.69	1777.86	3.29329	0.780
5	1.70	52.00	10.57	2.72	1776.52	3.29402	0.779
6	1.69	52.00	10.28	3.03	1779.51	3.31442	0.779
7	1.69	54.24	10.23	2.59	1792	3.39937	0.779
8	1.69	52.00	10.31	2.36	1775.37	3.30195	0.778
9	2.93	99.75	10.12	2.21	1840.1	3.83259	0.768
10	2.93	99.43	9.81	2.77	1823.97	3.79812	0.764

In order to compare the optimized values for different thicknesses to show the applicability of the developed formulas, the same optimization conditions were provided (namely discarding UW, UH, P and AP) as indicated in Table 4.38 for 1.2 mm AISI 304 steel. Then, the seven optimization conditions were obtained for maximization TL and minimization HAZ for 1.2 mm thicknesses as shown in Table

4.68. The welding parameters of V=3.55 mm/s, I=134 A, F=9.93 I/min, G=1.94 mm resulted in maximum TL= 1933 kgf and minimum HAZ=3.874 mm just for two constraints (TL and HAZ).

Table 4.68. Optimization results for 1.2 mm AISI 304 stainless steel sheet

Number	V	I	F	G	TL	HAZ	Desirability
1	2.25	50.94	9.09	1.00	1229.08	4.11593	0.746
2	2.25	51.00	9.11	1.00	1229.17	4.1172	0.746
3	2.25	50.75	9.06	1.00	1228.38	4.10595	0.746
4	2.25	51.16	9.14	1.00	1229.54	4.12251	0.746
5	2.25	50.81	8.84	1.00	1228.33	4.10695	0.746
6	2.25	50.97	8.08	1.00	1228.01	4.12551	0.744
7	2.83	94.55	12.00	1.00	1223.27	5.39845	0.642

The welding parameters of V=2.25 mm/s, I=50.8 A, F=9.14 I/min, G=1mm resulted in maximum TL= 1229.54 kgf and minimum HAZ=4.122 mm just for two constraints of TL and HAZ.

The next step is the effect of welding parameters on the responses. The interaction graphs of the parameters were shown in Figure E5-E16 for the responses of transverse tensile strength and heat affected zone. The comments on the interaction effects of welding parameters can be made as explained in the above section (interaction effects of TIG welding parameters).

The obtained result in this section of the study supported that we can apply the same procedure for the different thickness and materials with or without changing the welding procedure.

4.7. Multipass TIG Welding of Stainless Steels

4.7.1. Temperature Distribution in Multipass TIG Welding

In the welding process, the most interesting regions for heat transfer analysis are the fusion zone (FZ) and the heat affected zone (HAZ), where high temperatures are reached. These high temperature levels cause phase transformations,

microstructure, microhardness, alterations in the mechanical properties and residual stresses that will be present in the material after cooling to room temperature. The calculations to estimate the temperature distribution in multiple pass welding is more complex than in the single pass processes, due to superimposed thermal effects of one pass over the previous passes. Thus, very limited experimental data regarding temperature distribution during multipass welding of plates is available in the literature.

Due to the intense concentration of heat in the heat source of welding, the regions near the weld line undergo severe thermal cycles. The thermal cycles cause non-uniform heating and cooling in the material, thus generating inhomogeneous plastic deformation and residual stresses in the weldment. The presence of residual stresses can be detrimental to the performance of the welded product. Tensile residual stresses are generally detrimental, increasing the susceptibility of a weld to fatigue damage, stress corrosion cracking and fracture.

Plates of different thickness are used in the industry and thicker plates are normally joined by multipass welding. In a multipass welding operation, the number of thermal cycles that the material undergoes during welding is same as the number of passes, and with each pass, the residual stress pattern changes. Measurement of temperature distribution in the regions adjoining the weld, after each pass of welding, will be useful in estimating the maximum temperature rise expected in the base plate region during any pass of welding operation, thus enabling optimization of welding procedures.

Welding was carried out in a down-hand position. Weld beads were laid parallel to the weld pad centre line. Thermocouples were used to measure the transient temperatures during welding. The thermocouples were fixed in the middle region of the plate, at mid plane level. Temperatures were measured at different distances from the weld pad centre line on both the left and right side plates of the weld pad. The temperature variations during experiments were recorded using P.A. HILTON multichannel data logger. Four and six passes were applied for 8 mm and 10 mm stainless steel plates.

The temperature distribution obtained on the left and right side plates during welding of 8 mm and 10 mm AISI 304L thick stainless steel plates are shown in Figure 4.78, Figure 4.79, Figure 4.80 and Figure 4.81 respectively.

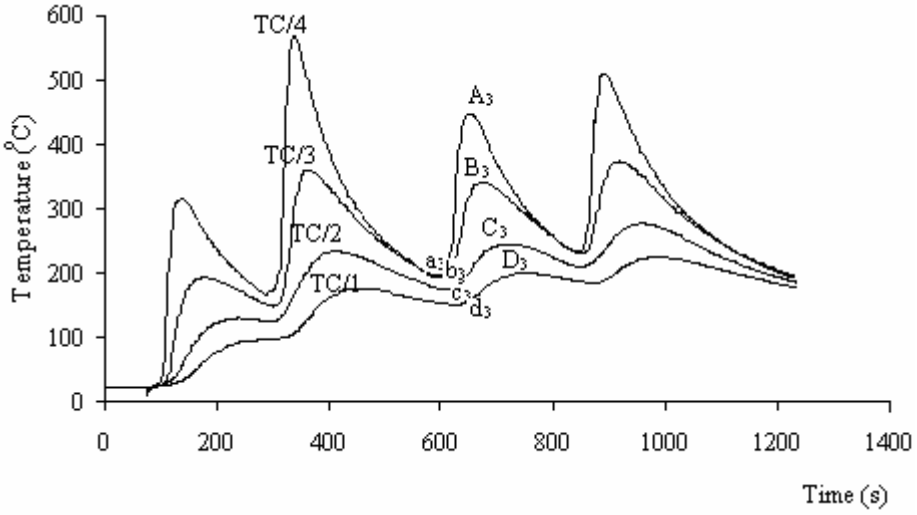

Figure 4.78. Temperature distribution on the left side plate of 304L 8 mm

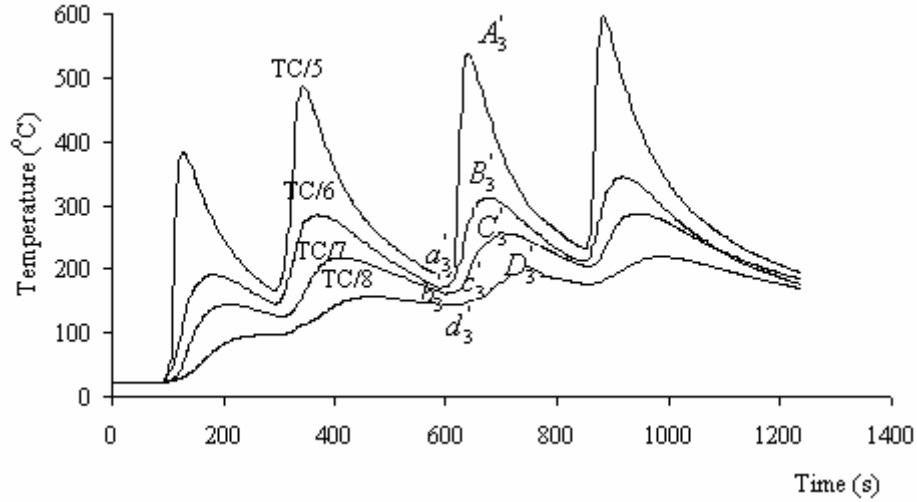

Figure 4.79. Temperature distribution on the right side plate of 304L 8 mm

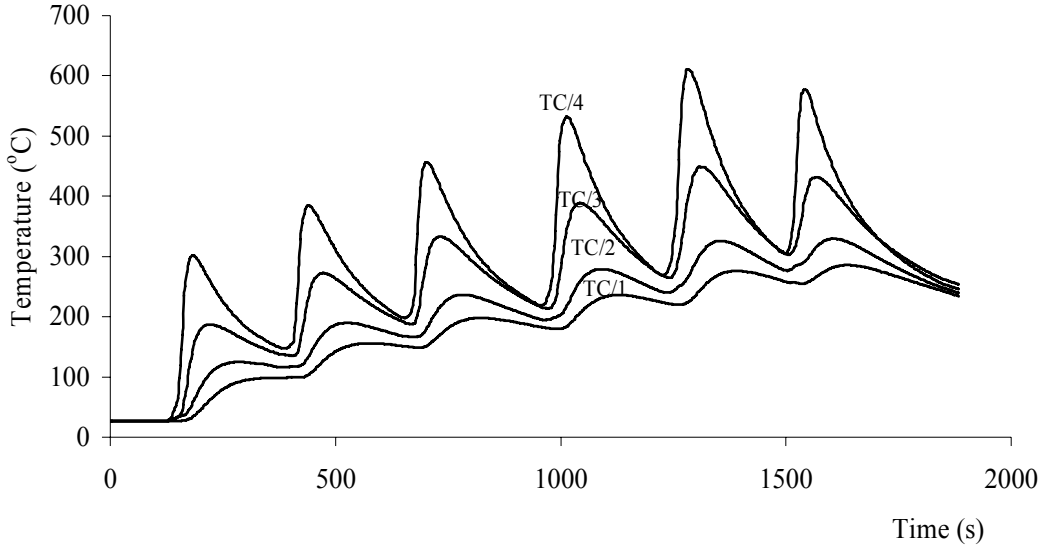

Figure 4.80. Temperature distribution on the left side plate of 304L 10 mm

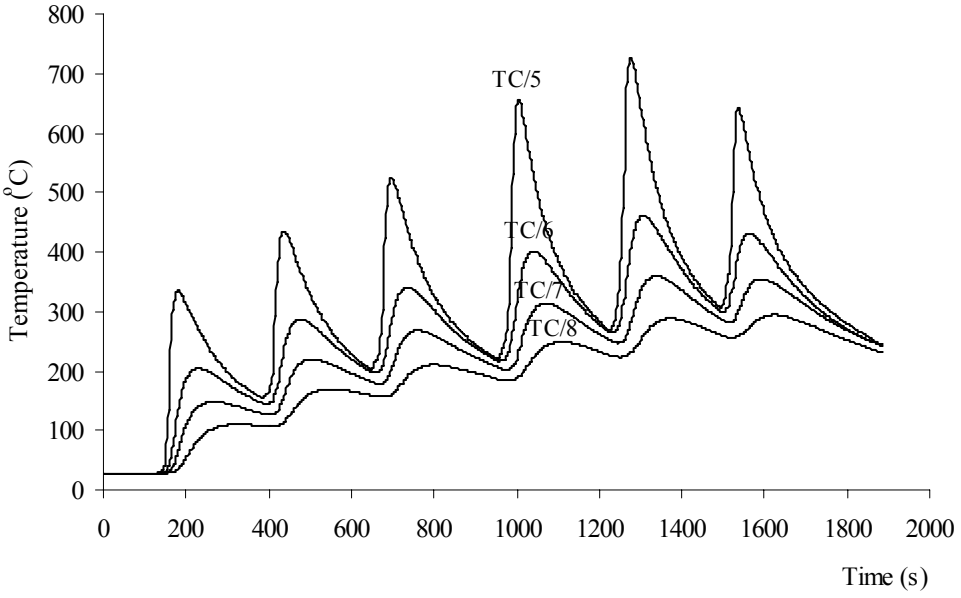

Figure 4.81. Temperature distribution on the right side plate of 304L 10 mm

Similarly, the temperature distribution in 316L stainless steels plates of thicknesses 8 and 10 mm plates are shown in Figure 4.82, Figure 4.83, Figure 4.84 and Figure 4.85.

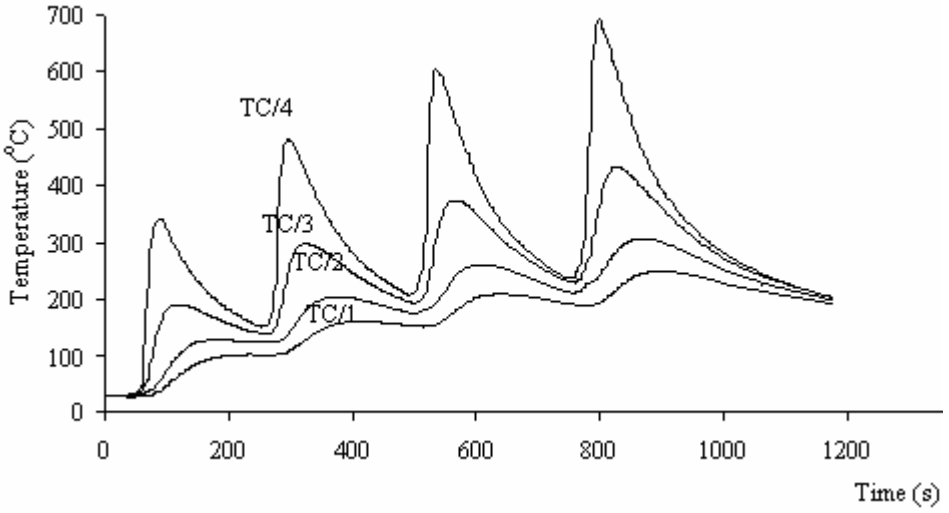

Figure 4.82. Temperature distribution on the left side plate of 316L 8 mm

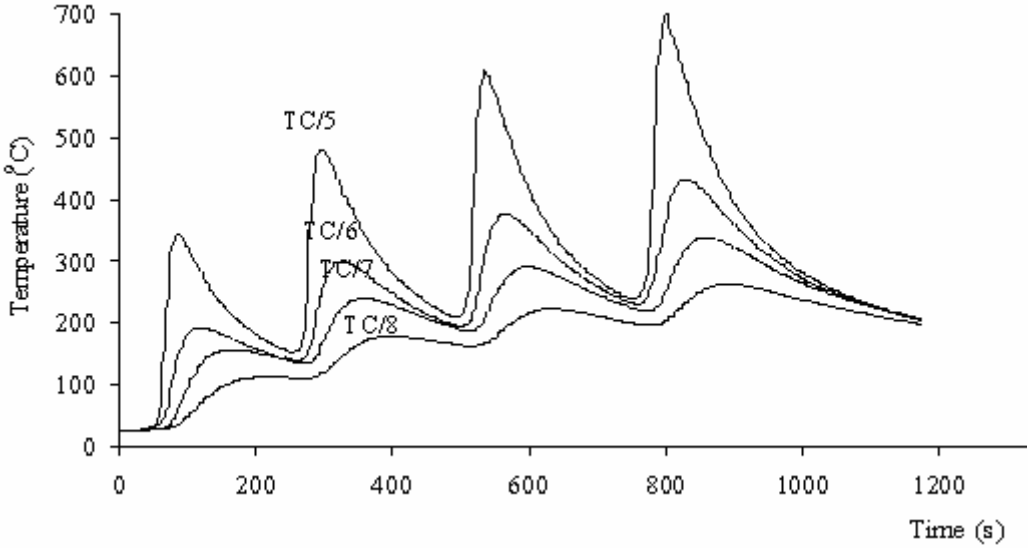

Figure 4.83. Temperature distribution on the right side plate of 316L 8 mm

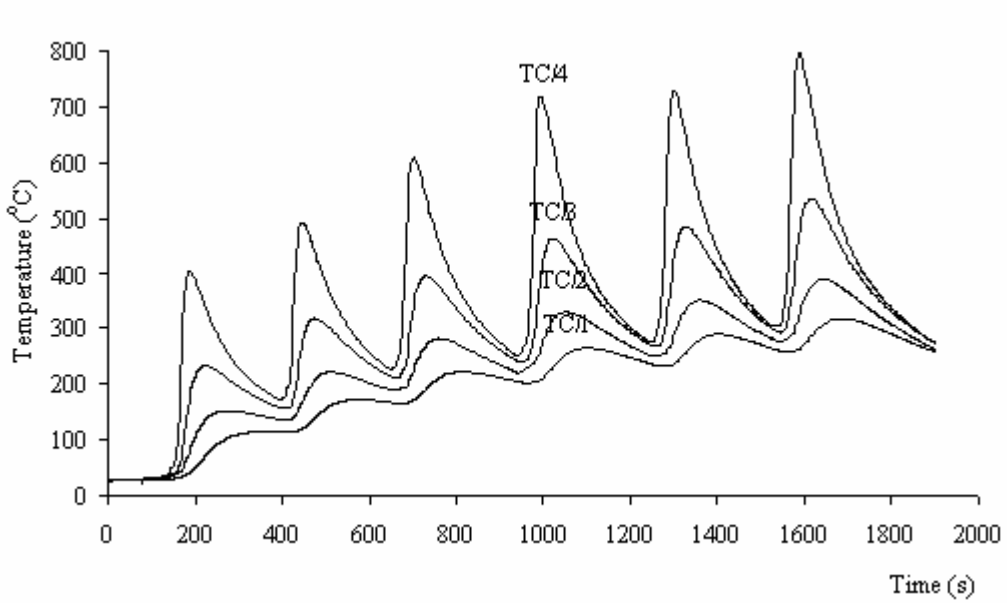

Figure 4.84. Temperature distribution on the left side plate of 316L 10 mm

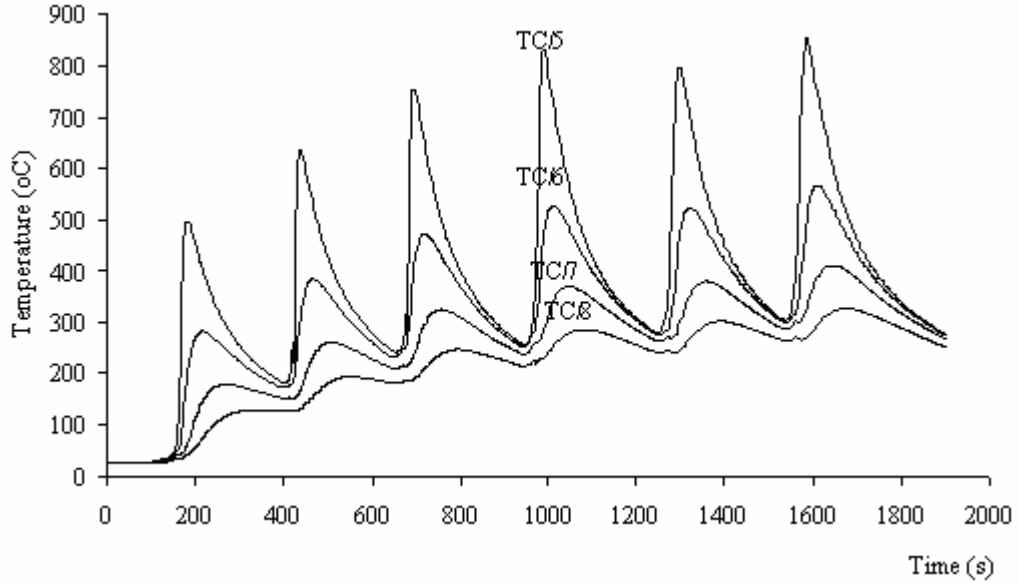

Figure 4.85. Temperature distribution on the right side plate of 316L 10 mm

During each pass of the weld, the temperature at the measuring point increases, reaches a maximum value then decreases. The point that is nearest to the weld pad center line reaches the highest maximum temperature.

In multipass welding, weld passes are laid along different weld lines, parallel to the weld pad center line, in the V-groove joint between the plates. However, in some cases (in industry), the weld pass may be laid closer to the left or right side, to fill V-groove with a filler material. For example, pass no 2 and 3 in 304L 8 mm (left side), Figure 4.78, because of the maximum temperature indicated by the thermocouples located on the left side plated were lower than the temperature measured on the opposite plates for the same pass.

The average maximum temperature rise is the average of maximum and minimum temperature differences for the same pass and same thermocouple locations of left and right side plates. As shown in Figures 4.86-4.89, the average value of maximum temperatures indicated by the thermocouples, for the same pass, located at the same distance from the weld centre line (left or right side of the plate) gave the representative values of the maximum temperatures obtained.

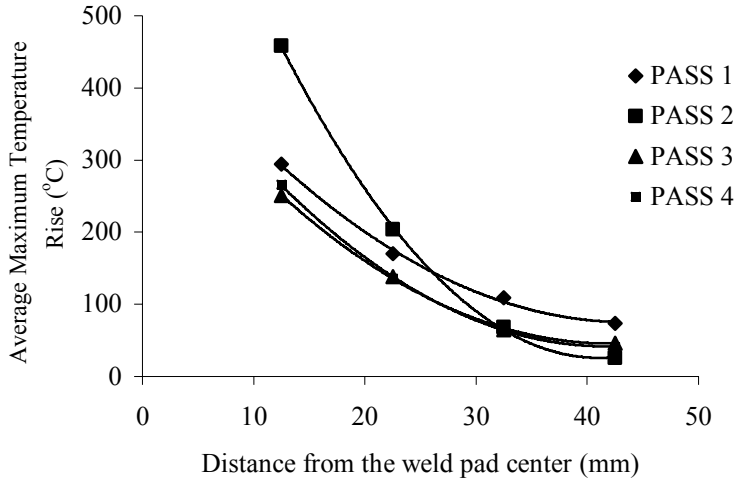

Figure 4.86. Average maximum temperature rise at different points for 304L 8 mm

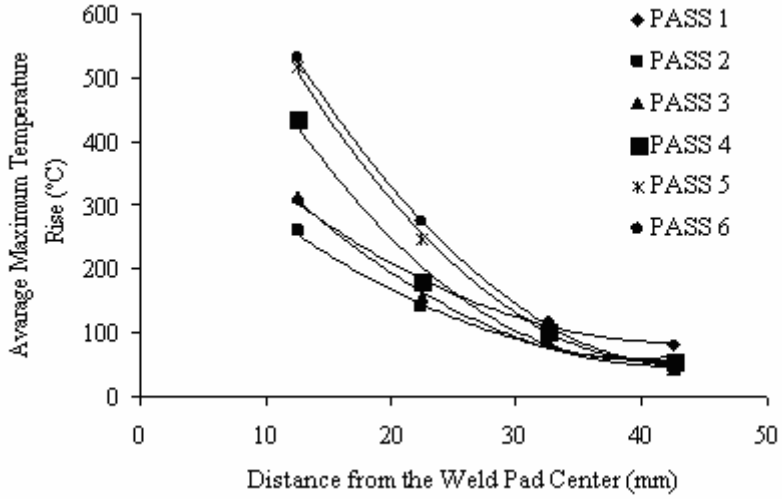

Figure 4.87. Average maximum temperature rise at different points for 304L 10 mm

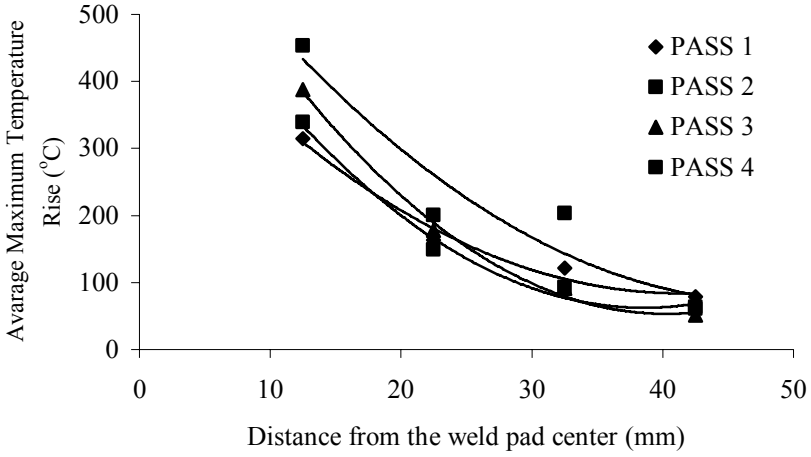

Figure 4.88. Average maximum temperature rise at different points for 316L 8 mm

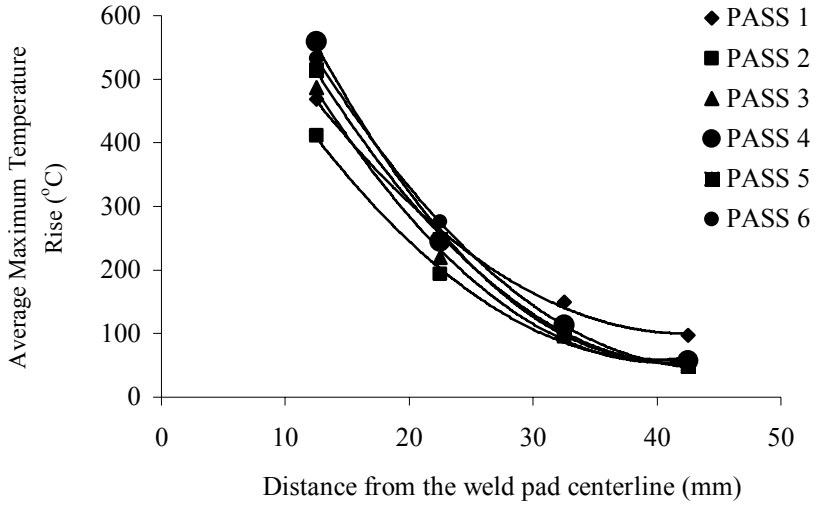

Figure 4.89. Average maximum temperature rise at different points for 316L 10 mm

From these curves, it may be seen that the average maximum temperature rise uniformly varies with the distance from the weld pad centerline. Knowledge of average maximum temperature rises may be useful in the estimation of maximum temperatures attained by different regions of the base plate during multipass welding. Likely changes in the microstructure and consequent degradation in mechanical properties can be estimated from this information.

From the results obtained, the following points can be observed:

1. As expected, during each pass of the weld, the temperature at the measuring point increases, reaches a maximum value and then decreases. The point that is nearest to the weld pad centre line reaches the highest maximum temperature.
2. A time gap of 2 min was given between two passes in the experimental work. It can be seen from the experimental results (for instance, Figure 4.79) that during the cooling phase of any pass, the cooling rate is steep during the initial stage but not as steep in later stages. This time gap of 2 min given in the experimental work is a representative value of the time duration between passes in practical welds.

3. The average value of maximum temperatures indicated by the thermocouples, for a particular pass, located at the same distance from the weld centre line (on the left or right side plate) will give representative values of maximum temperatures at the referred distance during that pass.
4. The distances indicated in the temperature distribution plots (Figures 4.78-4.85) are as measured from the weld pad centre line. However, it can be noted that since the temperatures were measured at a mid-plane level, the distances between the weld fusion point and the points of measurement will be less than these values.
5. The difference between the values highest and lowest values of temperature (A_3-a_3) for the same thermocouple will give the maximum temperature rise attained at the point of measurement during that pass. Likewise, the maximum temperature rise ($A_3^{'} - a_3^{'}$) attained by a measurement point located at the same distance from the weld pad centre line, on the other plate of the weld pad, can be obtained from the experimental results by applying the same procedure.
6. The average value of these two maximum temperature rises will give the "average maximum temperature rise" at the referred measurement point (average of (B_2-b_2) and ($B_2^{'} - b_2^{'}$) and so on).

4.7.2. Effect of Welding Parameters on the Quality of Multipass Welded Joints

There are many parameters which affect the quality of TIG welded joints. These are namely, welding current, welding speed, shielding gas flow rate and gap distance. The effects produced by the most important of these variables on tensile strength, microhardness and microstructure were analyzed through this section of the study.

4.7.2.1. Effect of Electrode Tip Geometry on the Penetration Profile

The shape of the Tungsten electrode is an important process variable in GTAW. Tungsten electrode may be used with a variety of tip preparations. In this study, various electrode geometries of 0^o (or 180^o), 15^o, 30^o, 45^o, 60^o, 75^o, 90^o were used to examine the effect of each tip preparation on the weld pool geometry. To analyze the influence of electrode tip geometry welding speed, welding current, gas flow rate and arc gap were kept constant whereas the tip geometry was changed from 0^o to 90^o.

As shown in Figures 4.90-4.96, results that is for 4 mm AISI 304 stainless steel obtained in this study showed that, as the included angle increases, the weld penetration and weld depth increases until 45^o electrode tip angle, between 60^o and 90^o electrode tip angle the shape of the weld bead geometry changing irregularly and weld penetration decreases. For the 0^o (or 180^o) electrode tip angle the weld bead geometry is V-shaped due to the blunt electrode geometry. However, for the other tip angle configurations the weld bead shapes are drop-shaped.

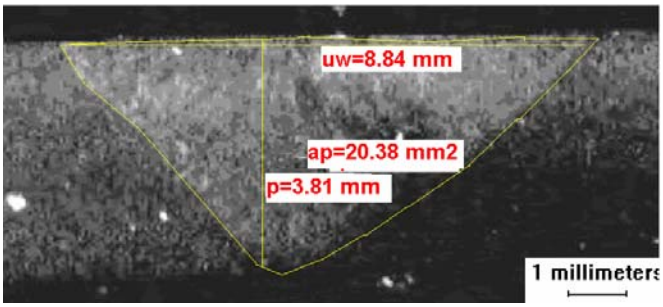

Figure 4.90. 0^o Electrode tip angle (25X)

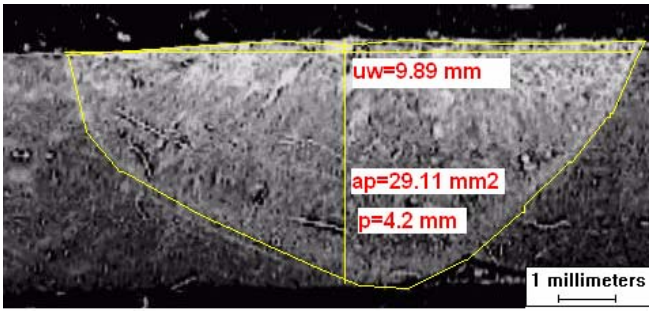

Figure 4.91. 15^o Electrode tip angle (25X)

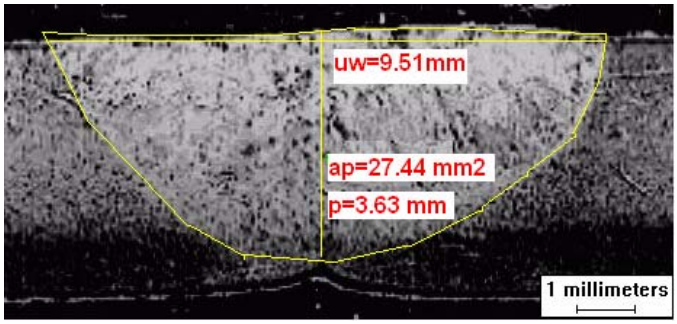

Figure 4.92. 30° Electrode tip angle (25X)

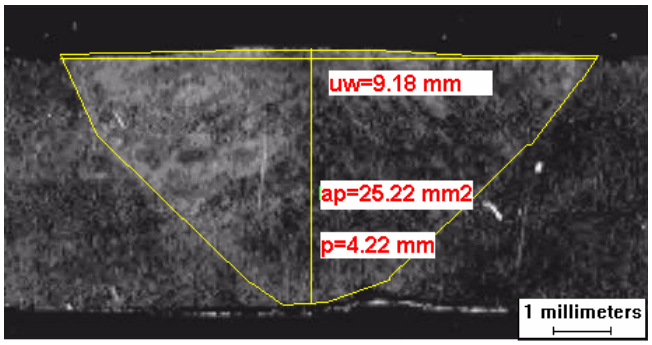

Figure 4.93. 45° Electrode tip angle (25X)

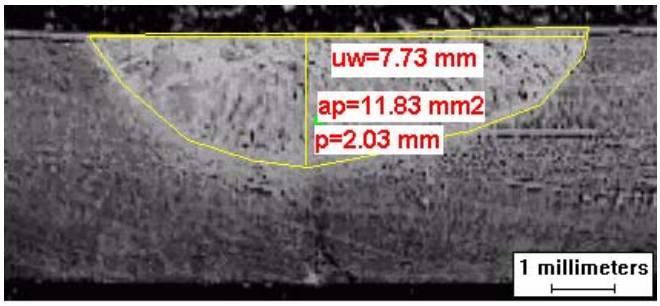

Figure 4.94. 60° Electrode tip angle (25X)

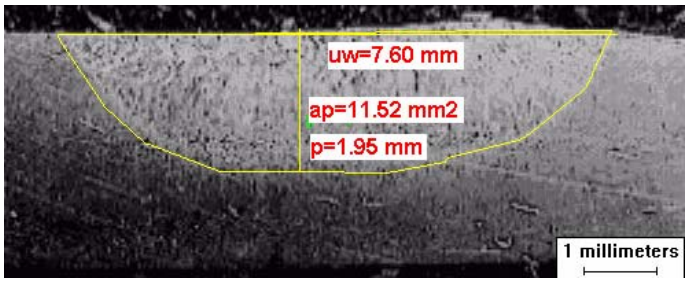

Figure 4.95. 75° Electrode tip angle (25X)

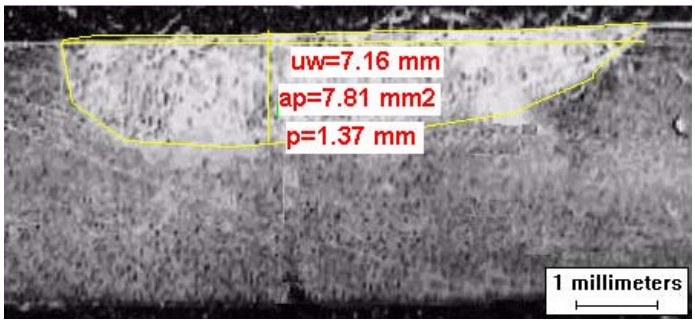

Figure 4.96. 90^{o} Electrode tip angle (25X)

During the experiments the following points were observed.

1. Sharper electrodes resulted in; easy arc starting,
2. Good arc stability but shorter electrode life due to melting of the sharp electrode tip going into the weld pool,
3. With blunter (especially at 0^{o}) electrodes; it was harder to start the arc also had longer electrode life.

It was concluded in this study that, regardless of the electrode tip geometry selected, it is important that a consistent electrode geometry should be used once a welding procedure is established. Changes in electrode geometry significantly influence the weld bead shape and size and hence the joint quality.

4.7.2.1.1. Effect of Electrode Tip Geometry on Microhardness Distribution

When austenitic stainless steels are used in the temperature range between 425 and 870 ^{o}C, carbide precipitation may occur at the material grain boundaries (HAZ). Carbide precipitation changes the microstructure and increases the microhardness. The formation of chromium carbide depends on the working temperature, the grain size and the amount of carbon contained in the steel.

Microhardness profiles of 4 mm AISI 304 stainless steel under different electrode tip geometry is shown in Figure 4.97. For all welding processes the workpiece materials (base material) had a hardness of between 155 and 170 Hardness Vickers (HV_{30}) approximately. We can conclude from the graphs that, larger HAZ zone was obtained on the joints welded with electrode tip angles between

15° and 45° due to the wider weld pool. The hardness profiles obtained on these joints range from 293 to 350 HV_{30}. Workpieces welded with the electrode angles between 0°, 60° and 90°, hardness of which ranges from 300 to 350 $HV_{30,}$ had a smaller HAZ zone due to the narrower weld pool geometry with respect to other tip angles less than 45°. The microhardness taken from HAZ zone of the weldments had higher values. The reason was the carbide precipitation in this region.

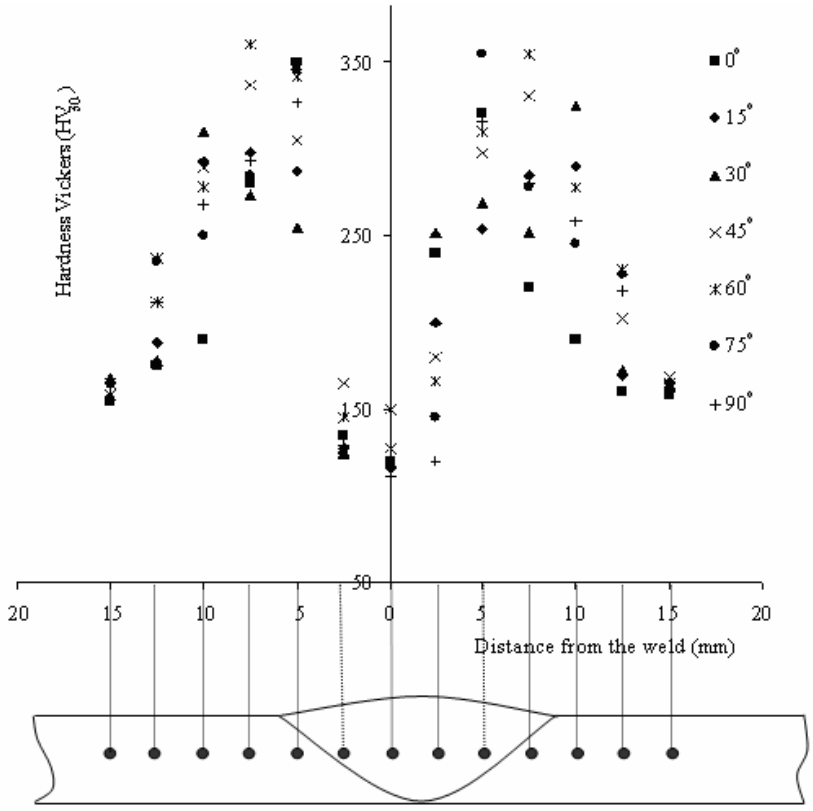

Figure 4.97. Microhardness distribution under varying electrode tip geometry (AISI 304, t= 4mm, V=1.923 mm/s, I=80 A, F=8 I/min, G=2 mm)

4.7.2.2. Welding Current

4.7.2.2.1. Effect of Welding Current on Tensile Load

The results shown in Figure 4.98 were obtained from the multipass welding experiments performed on 5 mm AISI 304L stainless steel. Experiments were performed to examine the effect of each welding parameter on the transverse tensile strength of the joints. In these experiments workpiece and electrode material and

joint type (60^o V-groove joint) were kept constant whereas the other welding parameters (welding current, welding speed, gap distance or arc length, gas flow rate and electrode tip angle) were altered.

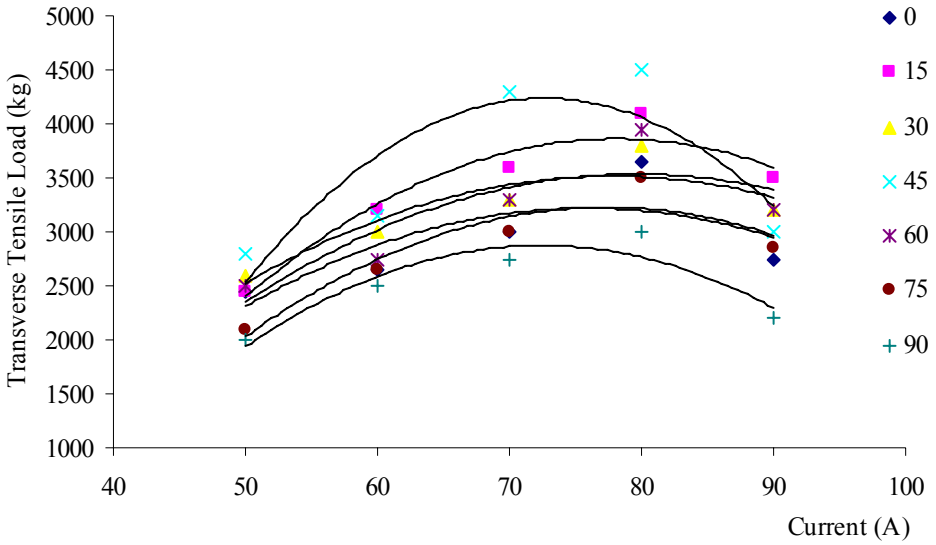

Figure 4.98. Effect of current and electrode tip angle on transverse tensile load (AISI 304L, t=5 mm, V=2.040 mm/s, F= 8 I/min, G=2 mm)

The maximum transverse tensile load of 4500 kgf was obtained for a crosssectional area of 60 mm^2 at 45^o electrode angle, 80 A current 2.040 mm/s torch travel speed, 8 I/min gas flow rate and 2mm arc length for 5 mm AISI 304L stainless steel sheet.

The transverse tensile load increases to a certain current level of 80 A then decreases. This is due to the excessive heating (high heat input rate at constant speed) of the molten weld pool which changes the microstructure and weld bead shape. At high welding currents, tungsten particles transferred to the weld, flat and rough weld bead and electrode deterioration were observed. However, at low welding currents, an uneven high, round weld bead and arc wandering emetically over the end of the electrode were observed.

4.7.2.2.2. Effect of Welding Current on Microhardness

Amount of heat input to the weld pool through adjusting welding current controls the size of heat affected zone directly, e.g. the higher the current applied, the larger heat affected zone is obtained. Microhardness distribution obtained with different welding current is shown in Figure 4.97. In all conditions, hardness values obtained in HAZ (between 178 and 210 HV_{30}) was higher than the hardness values obtained in the fusion zone. This finding is in agreement with Durgutlu (2004) who reported that the hardness of weld metal was lower than the HAZ and base metal. This hardness variation in HAZ was due to different cooling rates in the heat affected zone. Hence, different microstructures were formed under different cooling rates. Therefore heat affected zone was divided into three regions such as fine grained zone, coarse grained zone and partially tempered zone. Generally, coarse grained zone which was occurred near the weld metal zone had the highest hardness for all welding currents.

Increasing current caused high heat input to the base metal and hence this caused longer solidification time for the melt metal. This will much produce carbide precipitation and will increase the microhardness.

At higher current values (80 and 90 A) higher hardness was obtained due to the high heat input formed high carbide precipitation and parallel orientation of the grain size to the heat flow direction. Fusion zone hardness was measured as between 150 and 200 HV_{30}.

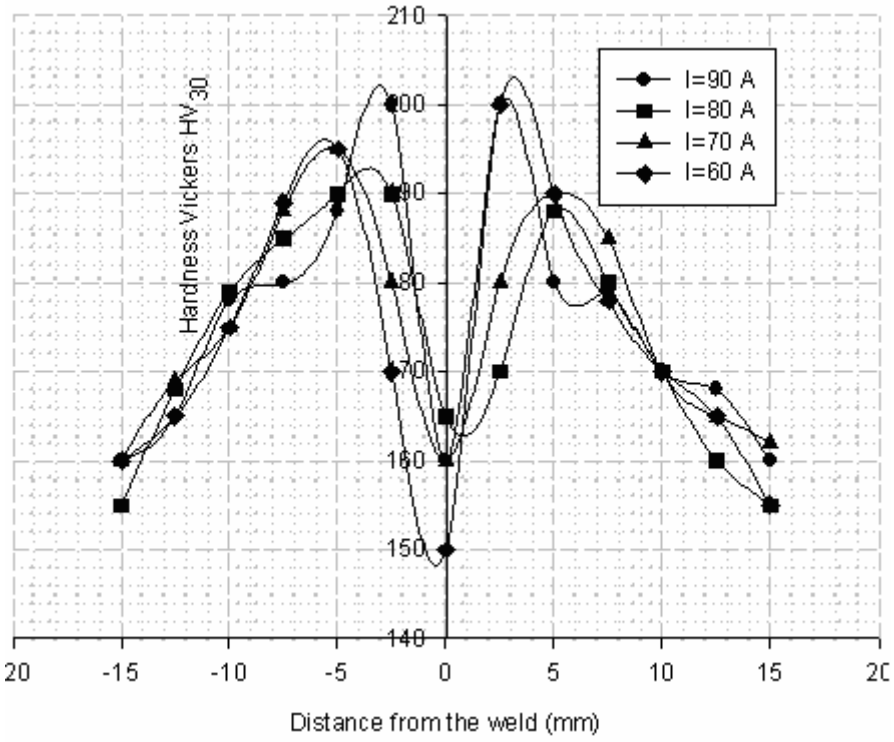

Figure 4.99. Effect of current on microhardness profile
(AISI 304, t= 4 mm, V=1.923 mm/s, F=8 I/min, G=2 mm, θ=45^{o})

4.7.2.2.3. Effect of Welding Current on Microstructure and Pool Shape

Austenitic stainless weldments have often been subject to intergranular attack (IGA). This behavior is particularly prevalent in chloride-bearing aqueous environments, and it is usually typified by accelerated attack in the HAZ. The basis for this attack is related to a phenomenon known as sensitization whereby exposure or slow cooling in the temperature range from 400 to 850 ^{o}C promotes the formation of chromium rich carbides ($M_{23}C_6$) along the austenite grain boundaries. When the austenitic stainless steels are heated up to the sensitization temperature range and if the time within this temperature range is sufficient, then intergranular carbides will nucleate along austenite grain boundaries. The level of precipitation and the associated degree of sensitization are approximately proportional to the carbon content of the austenitic stainless. Conventional austenitic stainless steels can retain a maximum of about 0.02% C in solid solution over their service temperature range

(up to 600 ^{o}C). Thus, as carbon content increases above this level, the driving force for carbide precipitation increases. In this study AISI 304 austenitic stainless steel with the carbon content of 0.08%.

The photomicrographs of the transition zone of the specimens which were welded under the currents of 60 A, 70 A, 80 A and 90 A are given in Figure 4.100. Grains in the weld metal oriented parallel to the heat flow. Durgutlu (2004) also reported similar result. He reported that grains in the weld metal were parallel to the heat flow.

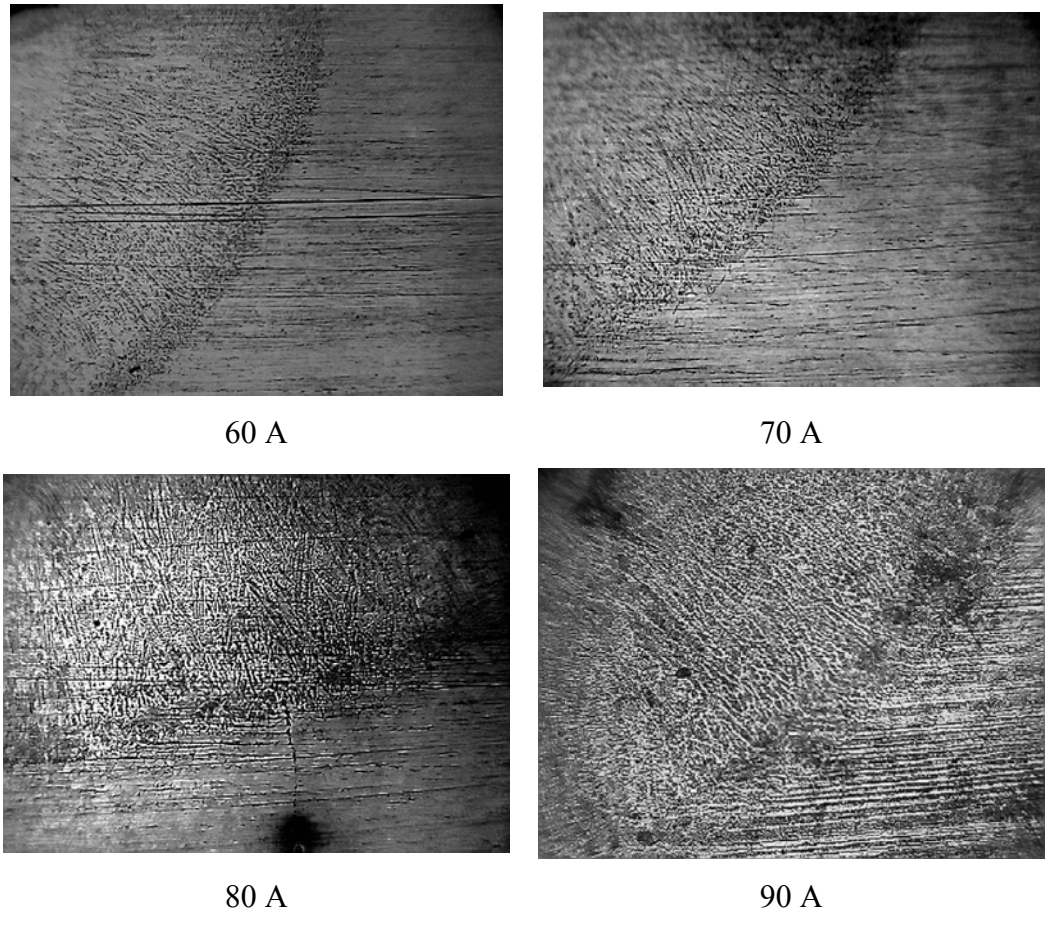

60 A 70 A

80 A 90 A

Figure 4.100. Effect of welding current on microstructure (50X)
(AISI 304L, t=4 mm, V=1.923 mm/s, F=8 I/min, G=2 mm)

Weld metal grains were formed as dendrites. It is a well known fact that increasing current increases the heat input. Increasing heat input to the weld metal causes longer solidification time for the melt metal. Since longer solidification time,

some grain orientations occurred in different directions due to the heat flow in weld. Since more heat input, mean grain size is larger than that of sample welded under low welding currents.

At high welding current (results in high heat input to the workpiece) ferrite transforms into a more brittle sigma phase this causes reduction in ductility, impact strength.

Figure 4.101 shows the effect of current on weld pool geometry. As can be seen from the Figure, arc current controls the weld penetration; the effect is directly proportional to the weld depth because of the heat input to the workpiece from the welding arc. The depth of penetration is linearly increasing and reached maximum value at 80 A. The welds are drop-shaped. Excessive current, 90 A, changed the weld pool shape and caused an irregular change in macrostructure.

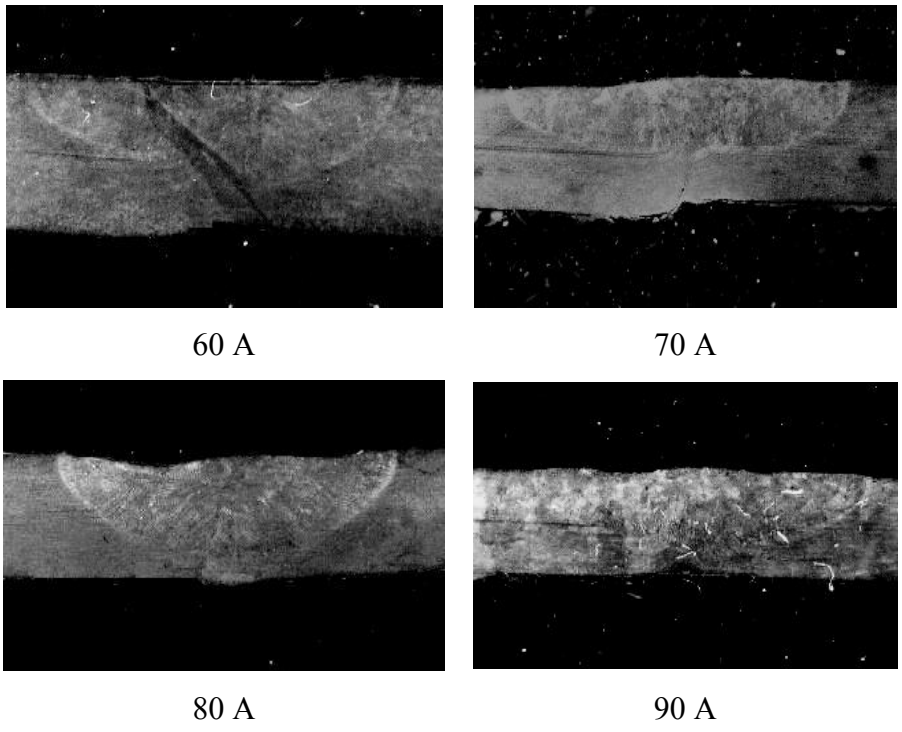

Figure 4.101. Effect of current on weld pool geometry
(AISI 304L, t=4 mm, V=1.923 mm/s, F=8 I/min, G=2 mm)

4.7.2.3. Welding Speed

4.7.2.3.1. Effect of Welding Speed on Tensile Load

Arc penetration is usually inversely proportional to welding speed. As shown in Figure 4.102, at high welding speeds due to the insufficient penetration, low tensile load was observed. However, excessive slow welding speeds caused excessive penetration and flat weld bead. The maximum transverse tensile load of 4500 kgf was obtained for a cross sectional area of 60 mm^2 at 2.040 mm/s welding speed.

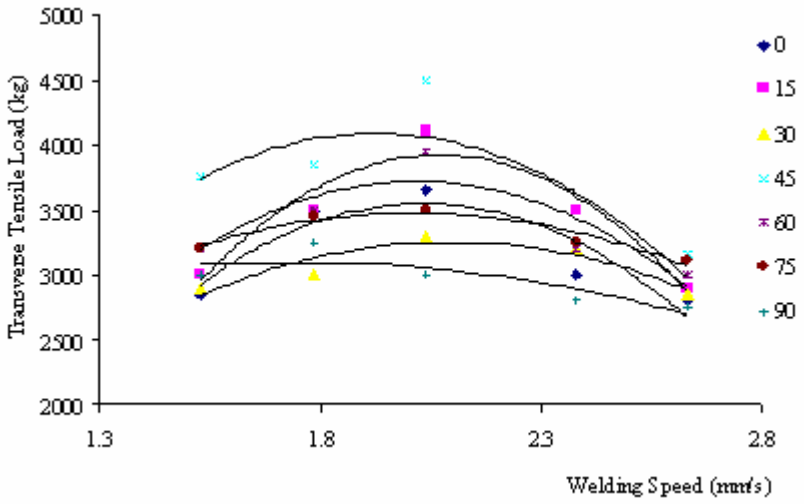

Figure 4.102. Effect of speed and electrode tip angle on transverse tensile load (AISI 304L, t=5 mm, I=80 A, F=8 I/min, G=2 mm)

4.7.2.3.2. Effect of Welding Speed on Microhardness

Figure 4.103 shows the microhardness profile with changing welding speed. At lower speeds, the HAZ zone had the higher hardness between 198 and 280 HV_{30} due to the concentrated heat. Higher speeds caused to decrease in hardness between 175 and 195 HV_{30}. Fusion zone hardness was measured as between 150 and 185 HV_{30}.

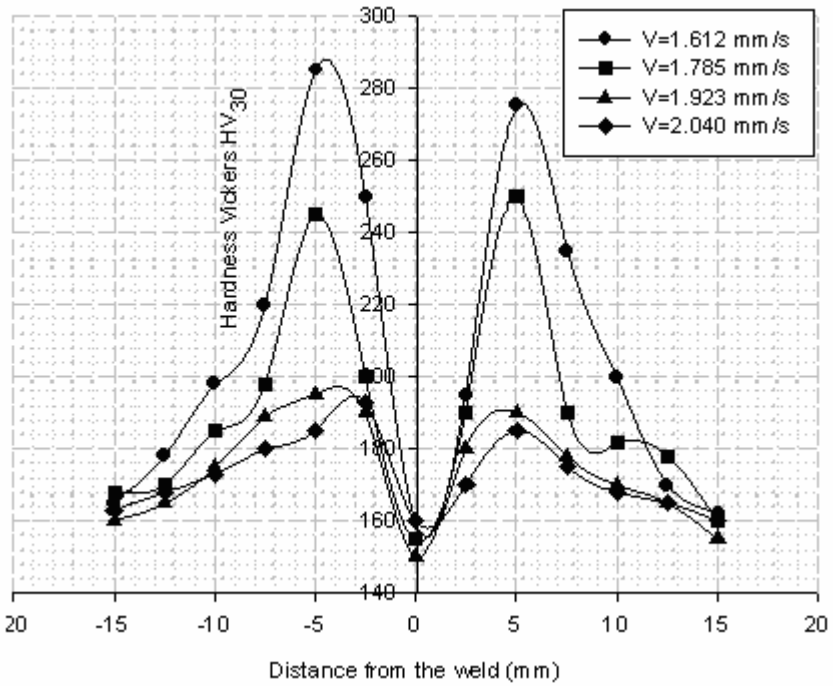

Figure 4.103. Effect of welding speed on microhardness profile (AISI 304, t=4 mm, I=80 A, F=8 I/min, G=2 mm, θ=45^o)

4.7.2.3.3. Effect of Welding Speed on Microstructure and Pool Shape

The heat input and the welding speed can affect the solidification mode of weld metal significantly. Depending on the solidification and welding speed, different structures can be observed in the weld region. The weld has a primary grain structure and each grain has a substructure that results from microsegregations. The type of microstructure observed depends on the form of solidification front, and the solidification parameter, which is equal to the temperature gradient G into the liquid divided by that rate of advance of the solidification front R. The temperature gradient G is equal to the melting temperature (T_m) divided by the distance between the heat source and the rear of the weld pool (x). The solidification parameter is then expressed as:

$$G / R = T_m / Vx \tag{4.12}$$

The solidification mode changes from planar to cellular and dendritic as the ratio G/R decreases. Savage and et al. (1968) stated that when the welding speed increased from 0.85 mm/s to 6.77 mm/s under the constant current of 150 A, weld microstructure changed from cellular to very fine cellular. However, under the same welding speed range and constant current of 450 A, weld microstructure changed to coarse cellular dendritic and severe undercutting was observed.

As shown in Figure 4.104, at low velocities (high solidification parameters) the central part of the weld has grains running longitudinally, and this is associated with a nearly circular weld pool.

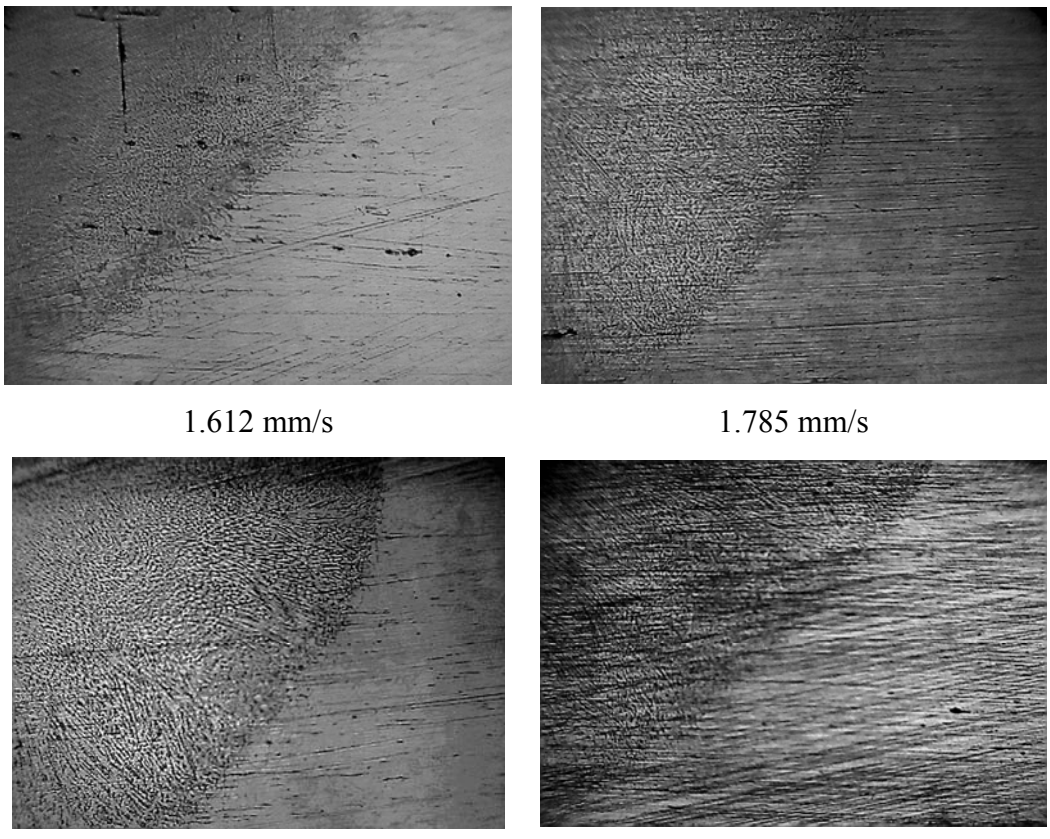

1.612 mm/s 1.785 mm/s

1.923 mm/s 2.040 mm/s

Figure 4.104. Effect of welding speed on microstructure (50X)
(AISI 304L, t=4 mm, I=80 A, F=8 I/min, G=2 mm)

With a higher welding speed, the weld pool becomes more elongated. Grains growing at the fusion boundaries are blocked by the grains growing from the rear of the weld pool. This gives a randomly oriented grain structure. The resulting grain structure of the weld appears to depend on three factors: the composition (solute content), the solidification parameter, and the shape of the weld pool.

Welding speed (torch travel speed) affects both the width and penetration of the joints as seen in Figure 4.105. However, if we compare the speeds of 1.612 and 2.040 mm/s, its effect on width is more pronounced than that on penetration. When the welding speed is increased the penetration decreased gradually.

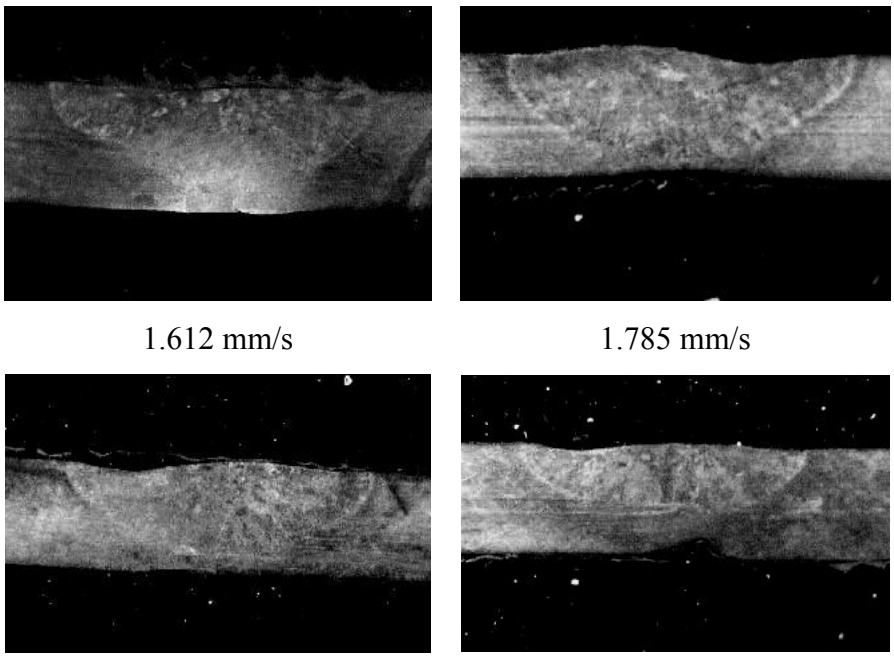

Figure 4.105. Effect of welding speed on weld pool geometry
(AISI 304L, t=4 mm, I=80 A, F=8 l/min, G=2 mm)

4.7.2.4. Gas Flow Rate

4.7.2.4.1. Effect of Gas Flow Rate on Tensile Load

Experimental results of the study, shown in Figure 4.104, showed that excessive gas flow rates caused a decrease in the joint strength due to the turbulence and atmospheric contamination. Low flow rates resulted in a weak strength because of the excessive heat and insufficient cooling rate of the weld pool. The maximum transverse tensile load of 4500 kgf was obtained for a cross sectional area of 60 mm^2 at 8 I/min gas flow rate and 45^o electrode tip angle.

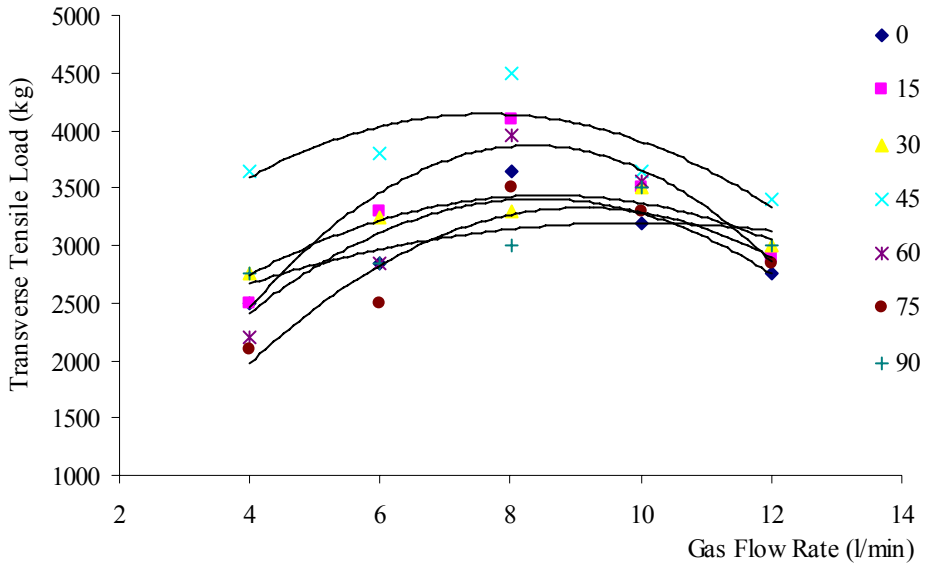

Figure 4.106. Effect of gas flow and electrode tip angle on transverse tensile load (AISI 304L, t=5 mm, V=2.040 mm/s, I=80 A, G=2 mm)

4.7.2.4.2. Effect of Gas Flow Rate on Microhardness

Figure 4.107 shows the microhardness profile with variable 99% argon gas flow rate. Higher flow rates caused rapid solidification and caused higher HAZ hardness between 175 and 218 HV_{30}. Lowering the gas flow rates decreased the HAZ hardness between 160 and 175 HV_{30}. Fusion zone hardness was measured as between 158 and 170 HV_{30}.

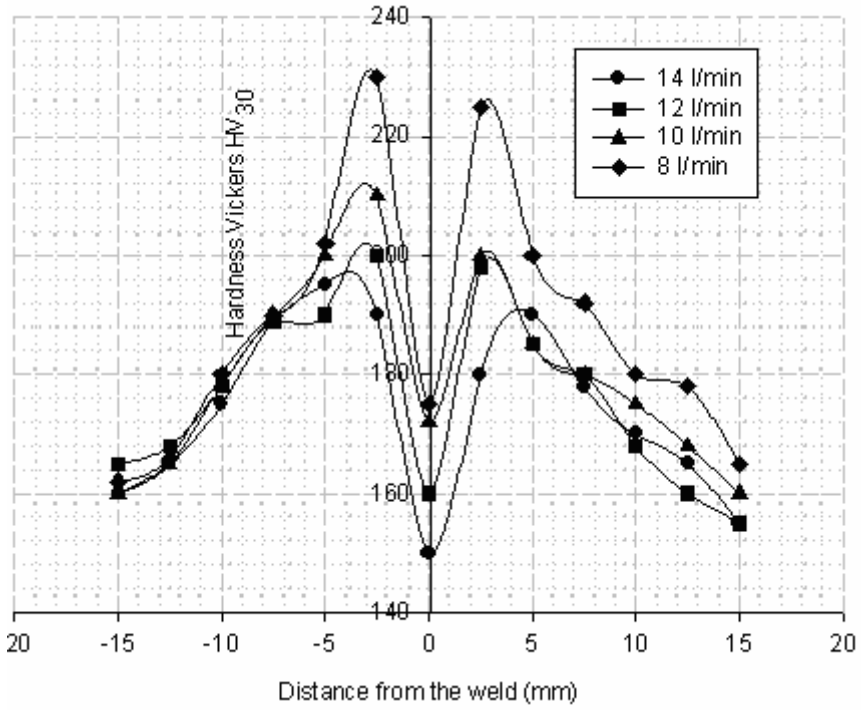

Figure 4.107. Effect of gas flow rate on microhardness profile (AISI 304, t=4 mm, V=1.923 mm/s, I=80 A, G=2 mm, θ=45^{o})

4.7.2.4.3. Effect of Gas Flow Rate on Microstructure and Pool Shape

If the cooling rate is high then the grains will grow at a faster rate and hence cover up more area and leave a smaller equiaxed zone in the top middle of the weld pool. As illustrated in Figure 4.108, larger grain grow was obtained under high flow rates of 12 I/min and 14 I/min due to the rapid solidification rate. The grain structure is getting coarser and more pronounced when the flow rate is increased.

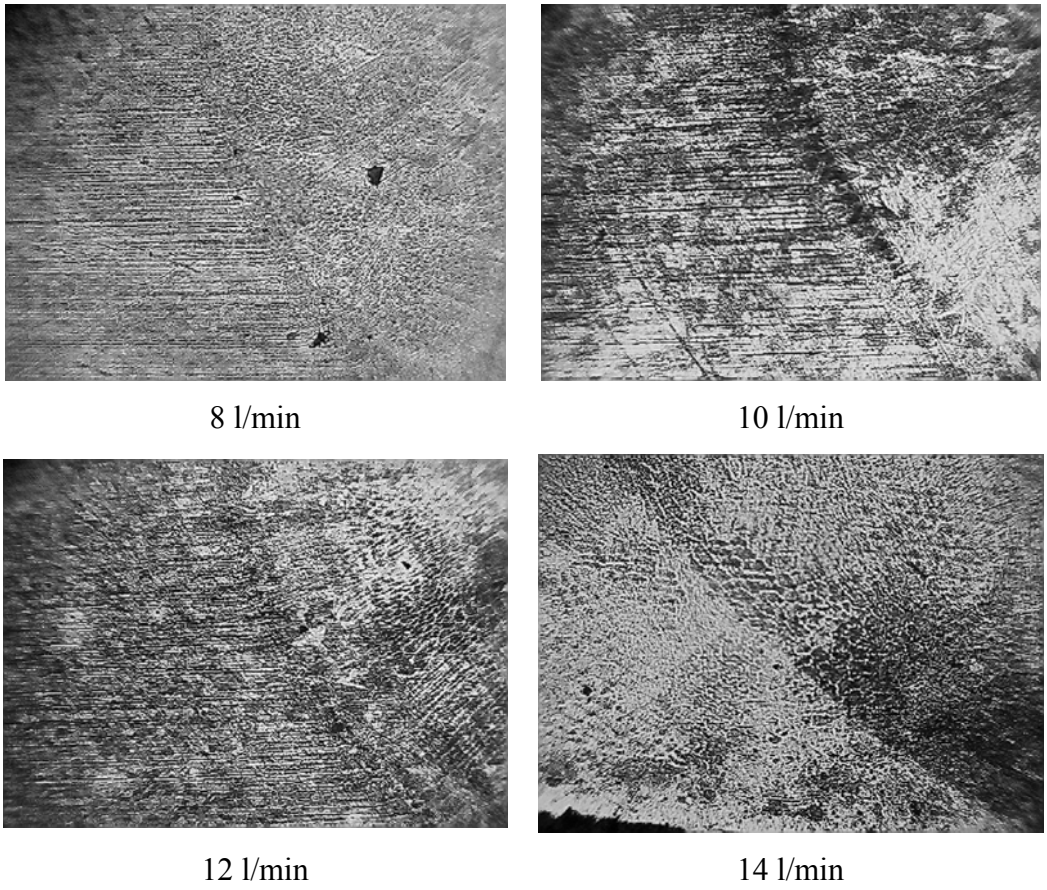

Figure 4.108. Effect of gas flow rate on microstructure (50X)
(AISI 304, t=4 mm, V=1.923 mm/s, I=80 A, G=2 mm, θ=45^{o})

The penetration depth is related to the selected gas and gas flow rate. The minimum shielding gas flow rate is determined by the need for a stiff stream to overcome the heating effects of the arc and cross drafts. As illustrated in Figure 4.109, excessive flow of 14 I/min, caused concave region at the middle of the weld pool due to the high gas pressure and rapid solidification. The optimum result was obtained at a gas flow rate of 8 l/min.

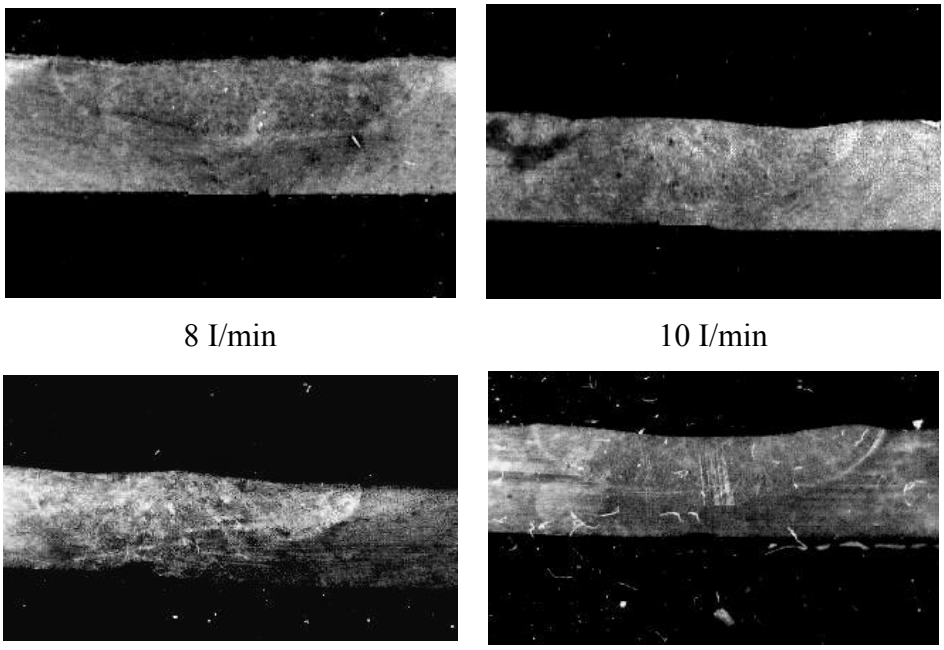

Figure 4.109. Effect of gas flow rate on weld pool geometry
(AISI 304, t=4 mm, V=1.923 mm/s, I=80 A, G=2 mm, θ=45^{o})

4.7.2.5. Gap Distance (Arc Length)

4.7.2.5.1. Effect of Gap Distance on Tensile Load

Figure 4.110 shows the effects of arc length with variable electrode tip angle on the Transverse Tensile load of the TIG welded joints.

We can be concluded from the Figure 4.110 that, arc length is important in this process because it affects the weld pool shape. Since, pool width is proportional to arc length as it increases the tensile load begins to decrease due to the depth (shallower depth) to width (large width) ratio decreases. Of course, recognition needs to be given to the possibility of short circuiting the electrode to the pool if the arc is too short.

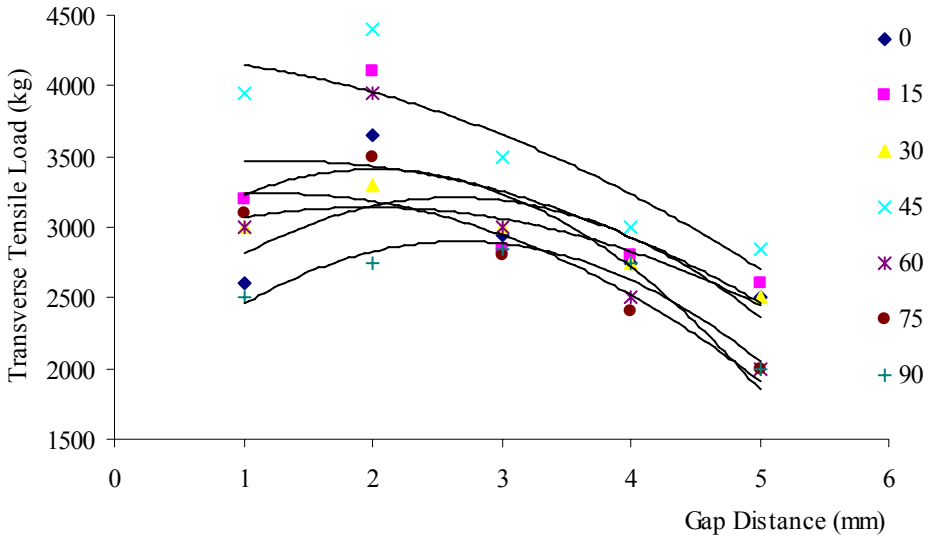

Figure 4.110. Effect of arc length and electrode tip angle on transverse tensile load (AISI 304L, t=5 mm, V=2.040 mm/s, I=80 A, F=8 I/min)

The maximum transverse tensile load of 4500 kgf was obtained for a cross sectional area of 60 mm^2 at a gap distance of 2 mm. Higher gap distances caused a decrease in the weld strength. It can be stated that, the greater the arc length, the higher is the heat leakage to the surrounding atmosphere which results with inefficient welding and smaller depth to width ratio. Whereas the opposite is also true.

4.7.2.5.2. Effect of Gap Distance on Microhardness

Figure 4.111 shows the microhardness profile with changing gap distance (arc length). Increasing gap distance caused higher heat leakage and decreased the HAZ hardness between 160 and 190 HV_{30}. Small distances had higher HAZ hardness values between 178 and 200 HV_{30}. Fusion zone hardness was measured as between 150 and 190 HV_{30}.

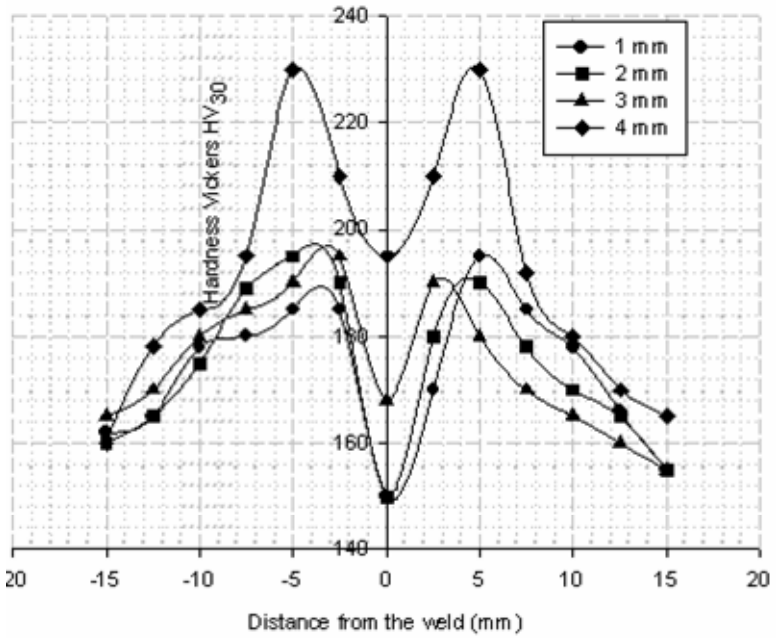

Figure 4.111. Effect of gap distance on microhardness profile (AISI 304, t=4 mm, V=1.92 mm/s, I=80 A, F=8 I/min, θ=45^{o})

4.7.2.5.3. Effect of Gap Distance on Microstructure and Pool Shape

As mentioned earlier, increasing arc gap decreased the heat input due to the heat leakage to the environment and hence microstructure and weld pool shape of the welded samples. Matsunawa and Shinichiro (1994) demonstrated that the plasma shear stress induced by a long arc gap in TIG welding can outweigh both the Lorentz force in the weld pool and the surface tension gradients along the pool surface. They have found that the samples welded at a gap distance of 8 mm produced much wider and shallower weld pool geometry than the samples welded at a gap distance of 2 mm. For a longer and thus wider arc gap, the Lorentz force in the weld pool is smaller because of flatter and wider current density distribution at the pool surface. The surface tension gradients are also smaller because of the flatter and wider power density distribution.

At lower gap distances of 1 mm and 2 mm, the weld pool and grain structure is clear. However, at high gap distances of 3 mm and 4 mm, the weld pool, as shown in Figure 4.112, is less pronounced because of high heat loss to the surrounding from the welding arc.

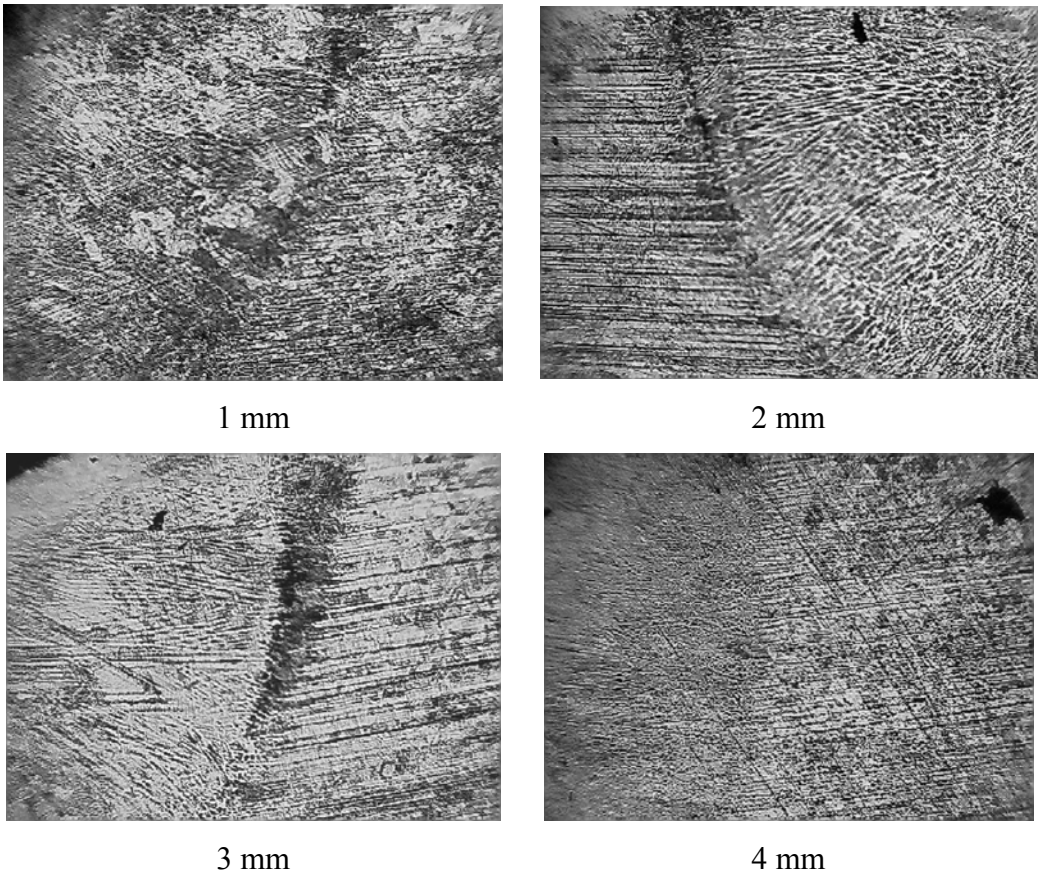

Figure 4.112. Effect of arc length on microstructure (50X)
(AISI 304, t=4 mm, V=1.92 mm/s, I=80 A, F=8 l/min, θ=45^{o})

As indicated in Figure 4.113, the effect of arc gap is more pronounced on both width and depth of penetration. Gap distance less than 1 mm caused electrode sticking and sometimes short circuiting. Increasing arc length caused wider weld depth with shallow penetration. Gap distance of 2 mm gave the maximum penetration, width and optimum result.

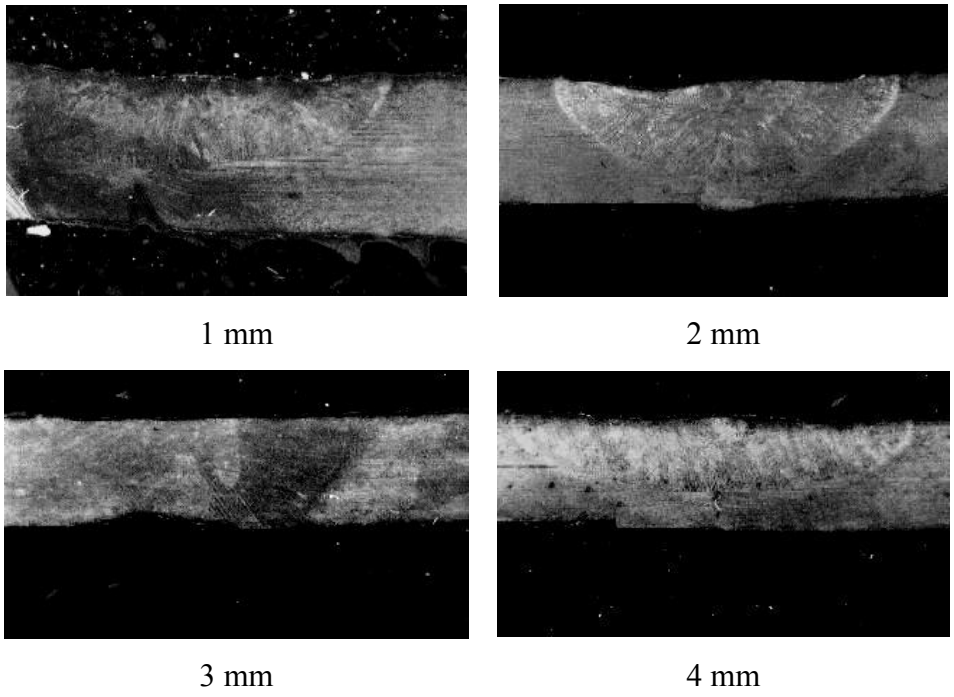

Figure 4.113. Effect of gap distance on weld pool geometry
(AISI 304, t=4 mm, V=1.92 mm/s, I=80 A, F=8 I/min, θ=45^{o})

5. CONCLUSION AND FUTURE STUDIES

5.1. Conclusion

New requirements on high productivity make tungsten inert gas welding an interesting alternative to ordinary arc welding for applications of transport industry, aerospace industry, food industry, machine construction, and the places where the stainless steels are used.

Since the tungsten inert gas welding is a high speed and readily automated process, all welding parameters could be controlled and used in a proper combination to produce an acceptable weld pool geometry in the manufacturing stations.

Weld pool geometry plays an important role in determining the mechanical properties of the weld. Therefore, it is very important to select the welding process parameters for obtaining an optimal weld pool geometry. Usually, the desired welding process parameters are determined based on experience or from a handbook. However, this does not ensure that the selected welding process parameters can produce the optimal or near optimal weld pool geometry for that particular welding machine and environment.

In this work the effect of tungsten inert gas welding parameters on the weld pool geometry and quality of the joint was investigated. The following conclusions were derived after analysis of the experiments carried out in this work.

i. Multipass welding of TIG welded joints;

- ✓ During each pass of the TIG welded thick steel sheet, the temperature at the measuring point increased, reached a maximum value (peak temperature) and then decreased. The point nearest to the weld pad centerline reached the highest maximum temperature
- ✓ The average value of maximum temperatures indicated by the thermocouples, for a particular pass, located at the same

distance from the weld centre line (on the left or right side plate) gave the representative values of maximum temperatures at the referred distance during that pass

- ✓ Approximate temperatures were obtained for the thermocouples that have the same distance from the weld centerline
- ✓ Average maximum temperature rise uniformly varied with the distance from the weld pad centerline
- ✓ Knowledge of average maximum temperature rises may be useful in the estimation of maximum temperatures attained by different regions of the base plate during multipass welding
- ✓ The place of likely microstructural changes and segregations within the heat affected zone can be estimated with the knowledge of temperature distribution during welding process

ii. The effect of electrode tip angle on the penetration profile, microhardness and transverse tensile load;

- ✓ The shape of the tungsten electrode is an important process variable in tungsten inert gas welding
- ✓ Changes in electrode geometry significantly influenced the weld pool geometry and hence the joint quality
- ✓ Sharper electrodes (over 45^{o}) resulted in easy arc starting but shorter electrode life due to melting of the electrode tip going into the weld pool
- ✓ The weld penetration increased until 45^{o} electrode tip angle, between 60^{o} and 90^{o} electrode tip angle the shape of the weld bead geometry changing irregularly and weld with increased.

For the 0^o electrode tip angle the weld bead geometry was V-shaped due to the blunt electrode geometry. However, for the other tip angle configurations the weld bead shapes were drop-shaped

- ✓ For 5 mm AISI 304L stainless steel, the maximum tensile load of 4500 kgf was obtained at 2.040 mm/s welding speed, 80 A current, 8 l/min gas flow rate, 2 mm arc gap and 45^o electrode tip angle
- ✓ The hardness of the base metal was measured as 165 HV_{30} approximately. The width of the heat affected zone increased by increasing tip angle from 15^o to 45^o due to the cone arc shape. For 15^o, 30^o and 45^o electrode angles the wider HAZ width with the hardness of 293~350 HV_{30}, and for 60^o, 75^o, 90^o and 0^o (or 180^o) the narrower HAZ width with the hardness of 300~350 HV_{30} was obtained
- ✓ The welding parameters affected the hardness distribution of the specimens as shown in Table 5.1.

Table 5.1. Effect of welding parameters on microhardness distribution

Welding parameters	**Heat affected zone HV_{30}**	**Fusion zone HV_{30}**
Welding speed (1.612-2.040 mm/s)	175-280	150-180
Welding current (60-90 A)	178-210	160-200
Gas flow rate (8-14 l/min)	175-218	158-170
Gap distance (1-4 mm)	160-190	150-190

iii. The effect of process parameters (welding speed, welding current, gas flow rate and gap distance) on the tensile load, heat affected zone, upper width, upper depth, penetration, area of penetration;

- ✓ **Welding speed (V):** At high welding speeds due to the insufficient penetration, low tensile load was observed. However, excessive slow welding speeds caused excessive penetration and flat weld bead. The maximum transverse tensile load of 1265 kgf was obtained at 2.31 mm/s welding speed. Further increase in welding speed caused sudden decrease in TL due to the insufficient heat input caused low deposition and penetration. When the welding speed was increased the width of the heat affected zone decreased. At low welding speed of 1.07 mm/s, high heat affected zone of 6.51 mm was obtained due to the high heat input rate. Also, at high welding speed of 3.55 mm/s low heat affected zone of 4.83 mm was observed due to the low heat input rate. When heat affected zone increases the upper width also increases. Increasing welding speed decreased the upper height due to the low deposition effect of insufficient heat input. The minimum 7.85 mm and maximum 9.51 mm upper width values were obtained at 3.55 and 1.07 mm/s welding speeds respectively. Also, another negative effect of high welding speed is lowering the upper height. Increasing welding speed decreased the upper height due to insufficient melting rate of the base metal. Minimum 0.10 mm and maximum 0.21 mm upper height values were obtained at 3.55 mm/s and 1.07 mm/s welding speeds respectively. Maximum penetration was obtained at minimum welding speed. Minimum 1.14 mm and maximum 1.22 mm P values were obtained at 3.55 mm/s and 1.07 mm/s welding speeds respectively. As the welding speed increased

the area of penetration decreased gradually because of the decreased penetration and width of the penetration. Maximum value of 10.73 mm^2 and minimum value of 6.45 mm^2 were obtained for AP at 1.07 mm/s and 3.55 mm/s welding speeds.

- ✓ **Welding current (I):** increasing current up to 85 A, caused an increase in tensile load up to 1300 kgf. However, further increase in current (over 85A) reduced the tensile load due to the unsuitable welding speed and current combination caused undercutting along the edges of the weld bead. 1199 kgf and 1225 kgf tensile load values were obtained at minimum 20 A and maximum 150 A respectively. High heat input with unsuitable welding speed increased the upper width. Increasing current from 52 A to 117 A, increased the upper width from 7.20 mm to 10.02 mm. Increasing current from minimum to maximum value increased upper height from 0.11 mm to 0.18 mm. Increasing the welding current from minimum to maximum increased the area of penetration from 6.65 mm^2 to 9.13 mm^2 respectively.
- ✓ **Gas flow rate (F):** slight change in tensile load of 1260 kgf and 1276 kgf was observed when flow rate is increased from 9 I/min to 11 I/min. Increasing gas flow rate from minimum to maximum value slightly reduced the width of the heat affected zone from 5.51 mm to 5.43 mm due to the cooling effect of the shielding gas. Increasing flow rate also slightly decreased the upper width from 8.81 mm to 8.72 mm. The effect of gas flow rate on upper height is again least pronounced. Increasing gas flow rate slightly increased the upper height from 0.14 mm to 0.15 mm. Changing gas flow rate from minimum to maximum value was not changed the penetration so much. 1.18 mm and 1.19 mm penetration was obtained for minimum and maximum flow rates respectively. Slight change in area of penetration

from 8.58 mm^2 to 8.55 mm^2 was observed under minimum and maximum gas flow rates respectively.

- ✓ **Gap distance (G):** Tensile load started to increase to a gap distance of 2 mm (1273 kgf) than followed by decreasing toward the 4 mm (1248 kgf). This is due to the not concentrated heat, and increasing heat leakage to the base metal with increasing arc gap. As the arc gap increased from 1 mm to 4 mm, the heat affected zone also increased from 5.40 mm to 5.57 mm respectively. The increase in the width of the heat affected zone is due to the cone shape of the arc. Further increase in arc gap decreases the heat affected zone due to the low heat input and high heat leakage. Minimum 8.65 mm and maximum 8.87 mm upper width was obtained with increasing gap distance from 1 mm to 4 mm respectively. When the gap distance increases the arc voltage increases and hence the overall efficiency of the welding process decreases. Increase in arc gap decreased the upper height from 0.15 mm to 0.14 mm. Increasing arc gap decreased the penetration remarkably. When the arc gap increased from minimum to maximum value it decreased from 1.19 to 1.16 mm respectively. Hence the area of penetration is dependent on the penetration and upper width, the same trend with the penetration was observed for area of penetration. It increased to 8.42 mm^2 with the arc gap of 2.5 mm. The minimum and maximum values were obtained as 7.92 mm^2 and 7.90 mm^2 for 1mm and 4 mm arc lengths respectively.

iv. The following results were obtained for the interaction effects of weld parameters on welding responses of 1.2 mm AISI 304 stainless steel;

- ✓ **Tensile load (TL):** When welding current was 117 A increasing the welding speed caused an increase in tensile

load from 1174 kgf to 1199 kgf, however when the current decreased to 52 A, increasing welding speed decreased the tensile load from 1210 kgf to 1123 kgf (*decreasing rate of 7.19%*). When gas flow rate was 11 I/min, increasing welding speed increased tensile load slightly from 1226 kgf to 1245 kgf (*increasing rate of 1.55%*). However, when the gas flow rate decreased to 9 I/min, increasing welding speed decreased the tensile load slightly to 1215 kgf (*decreasing rate of 2.40%*). When welding speed was 1.69 mm/s, increasing gap distance caused a slight decrease in tensile load from 1260 kgf to 1226 kgf (*decreasing rate of 2.70%*). However, when the welding speed increased to 2.93 mm/s, increasing gap distance slightly increased the tensile load from 1205 kgf to 1219 kgf (*increasing rate of 1.16%*). When gas flow was 11 I/min, increasing the welding current up to 85 A increased the tensile load from 1199 kgf to 1275 kgf (*increasing rate of 6.33%*), however when the gas flow rate decreased to 9 I/min, increasing welding current up to 85 A increased the tensile load to 1257 kgf further increase in welding current decreased the tensile load. When gap distance was 1.75 mm, increasing welding current up to 85 A caused an increase in tensile load from 1205 kgf to 1275 kgf (*increasing rate of 5.80%*). However, when the gap distance increased to 3.25 mm, increasing the welding current up to 85 A increased the tensile load from 1187 kgf to 1240 kgf (*increasing rate of 4.46%*). Further increase in welding current decreased the tensile load.

- ✓ **Heat affected zone (HAZ):** At the welding current of 117 A, increasing welding speed decreased the heat affected zone from 8.16 mm to 5.95 mm (*decreasing rate of 27.08%*). However, when the current decreased to 52.5 mm, increasing

the welding speed also decreased the heat affected zone from 4.76 mm 3.60 mm (*decreasing rate of 24.36%*). The intersection of the two curves can be reached approximately at 4.5 mm/s. When gap distance was 3.25 mm, increasing the welding speed decreased the heat affected zone from 6.60 mm to 4.94 mm (*decreasing rate of 25.15%*), however, when the gap distance decreased to 1.75 mm, increasing welding speed caused a decrease in heat affected zone from 6.46 mm to 4.75 mm (*decreasing rate of 26.47%*). When the gap distance was 3.25 mm, increasing welding current increased the heat affected zone from 4.06 mm to 6.98 mm (*increasing rate of 71.92%*). However, when the gap distance is decreased to 1.75 mm, increasing current caused an increase in heat affected zone from 3.94 mm to 6.77 mm (*increasing rate of 71.82%*).

- ✓ **Upper width (UW):** When gas flow rate was 9 I/min, increasing welding speed caused a significant decrease in upper width from 9.58 mm to 7.84 mm (*decreasing rate of 18.16%*). At the gas flow rate of 11 I/min, increasing welding speed decreased upper width from 9.40 to 7.84 mm (*decreasing rate of 16.59%*). When the gap distance was 3.25 mm, increasing welding current increased the upper width from 7.28 mm to 10.14 mm (*increasing rate of 39.28%*). However, when the gap distance was decreased to 1.75 mm, increasing welding current caused an increase in upper width from 7.10 mm to 9.88 mm (*increasing rate of 39.15%*).
- ✓ **Upper height (UH):** When welding current was 117 A, increasing the welding speed caused a decrease in upper height from 0.25 mm to 0.13 mm (*decreasing rate of 48%*), however, when the current decreased to 52 A, increasing welding speed decreased the upper height from 0.15 mm to

0.09 mm (*decreasing rate of 40%*). When gap distance was 3.25 mm, increasing the welding speed decreased the upper height from 0.19 mm to 0.12 mm (*decreasing rate of 36.84%*), however, when the gap distance decreased to 1.75 mm, increasing welding speed caused a decrease in upper height from 0.20 mm to 0.12 mm (*decreasing rate of 40%*). When gas flow rate was 9 I/min, increasing welding current significantly increased upper height from 0.10 mm to 0.18 mm (*increasing rate of 80%*). However, when gas flow rate increased to 11 I/min, increasing welding current caused an increase in upper height from 0.11 mm to 0.17 mm (*increasing rate of 54.54%*). When the gap distance was 3.25 mm, increasing welding current increased the upper height from 0.11 mm to 0.17 mm . However, when the gap distance was decreased to 1.75 mm, increasing welding current caused an increase in upper width from 0.11 mm to 0.19 mm (*increasing rate of 72.72%*). When gap distance was 3.25 mm, increasing gas flow rate slightly increased upper height from 0.142 mm to 0.149 mm (*increasing rate of 4.92%*). However, when gap distance decreased to 1.75 mm, increasing gas flow rate caused a decrease in upper height from 0.151 mm to 0.153 mm (*increasing rate of 1.32%*).

- ✓ **Penetration (P):** When the welding current was 117 A, increasing welding speed decreased the penetration from 1.28 mm to 1.21 mm (*decreasing rate of 5.46%*).. However, when the welding current decreased to 52 A, increasing welding speed resulted a decrease in upper width from 1.10 mm to 1.00 (*decreasing rate of 9.09%*). When gas flow rate was 9 I/min, increasing welding speed significantly decreased penetration from 1.19 mm to 1.16 mm (*decreasing rate of 2.52%*). However, when gas flow rate increased to 11 I/min

mm, increasing welding speed caused a decrease in penetration from 1.23 mm to 1.14 mm (*decreasing rate of 7.31%*). When gap distance was 3.25 mm, increasing the welding speed significantly decreased the penetration from 1.22 mm to 1.11 mm (*decreasing rate of 9.01%*), however, when the gap distance decreased to 1.75 mm, increasing welding speed caused a decrease in penetration from 1.23 mm to 1.16 mm (*decreasing rate of 5.69%*). When gas flow rate was 9 I/min, increasing welding current significantly increased penetration from 0.98 mm to 1.15 mm (*increasing rate of 17.34%*). However, when gas flow rate increased to 11 I/min, increasing welding current caused an increase in penetration from 1.05 mm to 1.23 mm (*increasing rate of 17.14%*). When the gap distance was 3.25 mm, increasing welding current increased the penetration from 1.02 mm to 1.23 mm (*increasing rate of 20.58%*). However, when the gap distance was decreased to 1.75 mm, increasing welding current caused an increase in penetration from 1.07 mm to 1.25 mm (*increasing rate of 16.82%*)..

- ✓ **Area of Penetration (AP):** When welding current was 117 A, increasing the welding speed caused a decrease in area of penetration from 10.5 mm^2 to 7.87 mm^2 (*decreasing rate of 25.04%*), however when the current decreased to 52 A, increasing welding speed decreased the area of penetration from 7.46 mm^2 to 6.01 mm^2 (*decreasing rate of 19.43%*). When gas flow rate was 9 I/min, increasing welding speed significantly decreased area of penetration from 9.13 mm^2 to 7.01 mm^2 (*decreasing rate of 14.45%*). However, when gas flow rate increased to 11 I/min mm, increasing welding speed caused a decrease in area of penetration from 8.98 mm^2 to 7.01 mm^2 (*decreasing rate of 21.93%*). When gap distance

was 3.25 mm, increasing the welding speed significantly decreased the area of penetration from 9.03 mm^2 to 6.98 mm^2 (*decreasing rate of 22.70%*), however, when the gap distance decreased to 1.75 mm, increasing welding speed caused a decrease in area of penetration from 9.03 mm^2 to 6.33 mm^2 (*decreasing rate of 29.90%*). When gas flow rate was 9 I/min, increasing welding current significantly increased area of penetration from 6.71 mm^2 to 9.21 mm^2 (*increasing rate of 37.25%*). However, when gas flow rate increased to 11 I/min, increasing welding current caused an increase in area of penetration from 6.64 mm^2 to 9.08 mm^2 (*increasing rate of 36.74%*). When the gap distance was 3.25 mm, increasing welding current increased area of penetration from 6.66 mm^2 to 9.12 mm^2 (*increasing rate of 36.93%*). However, when the gap distance was decreased to 1.75 mm, increasing welding current caused an increase in area of penetration from 6.60 mm^2 to 8.98 mm^2 (*increasing rate of 36.06%*). When gap distance was 3.25 mm, increasing gas flow rate slightly decreased area of penetration from 8.01 mm^2 to 7.88 mm^2 (*decreasing rate of 1.62%*). However, when gap distance decreased to 1.75 mm, increasing gas flow rate caused an increase in penetration from 7.65 mm^2 to 7.88 mm^2 (*increasing rate of 3%*).

v. Prediction and optimization of weld pool geometry;

- ✓ The mathematical models developed are useful for selecting correct process parameters to achieve the desired weld pool quality and to predict weld pool quality for the given process parameters

- ✓ The mathematical models furnished can be used to predict the weld bead geometry by substituting the values of the respective process parameters. Also, the values of the control factors can be obtained by substituting the value of the desired bead geometry
- ✓ Close agreement was obtained between the actual and predicted values of the welding parameters and responses
- ✓ For a fairly limited number of weld trials it can be concluded that high correlations can be achieved by using prediction program when predicting bead width, bead height, penetration and area of penetration for single butt welds, 1.2 mm, in AISI 304 stainless steel. In converting the predicted shape parameters into a weld profile the highest correlation for all four output parameters was achieved with MATLAB programming technique
- ✓ Both two optimization programs (LINGO 8.0 and Design Expert 6.0) provided the close values for the weld parameters and responses. Optimized values for AISI 304 1.2 mm stainless steel is given in Table 5.2.

Table 5.2. Optimized values for 1.2 mm AISI 304 stainless steel

		Objective	Constraints	Optimum value				Optimum solution
				V	I	F	G	
LINGO 8.0	One Objective	TL max	1.06 ≤ V ≤ 3.55 20 ≤ I ≤ 150 8 ≤ F ≤ 12 1 ≤ G ≤ 4	1.73	96.78	8.0	1.34	TL= 1330.73 kgf
		HAZ min		3.41	20.00	12.0	1.00	HAZ= 1.924 mm
		UW min		3.55	20.00	12.0	1.00	UW= 3.744 mm
		UH min		2.72	20.00	8.00	1.96	UH= 0.04 mm
		P max		1.07	117.71	12.0	3.07	P= 1.34 mm
		AP max		1.07	150.0	12.0	3.13	AP=13.92 mm^2
	Multi Objective	TL max P max HAZ min		1.73	96.53	8.0	1.34	TL= 1330.73 kgf HAZ= 7.054 mm UW= 10.06 mm UH= 0.23 mm P= 1.26 mm AP= 9.90 mm^2
Design Expert 6.0	One Objective	TL max	1.06 ≤ V ≤ 3.55 20 ≤ I ≤ 150 8 ≤ F ≤ 12 1 ≤ G ≤ 4	1.73	96.77	8.00	1.35	TL= 1330.73 kgf
		HAZ min		3.44	20.50	10.80	3.78	HAZ=2.15 mm
		UW min		3.47	22.40	10.34	1.62	UW= 4.19 mm
		UH min		2.72	20.05	8.00	1.96	UH= 0.04 mm
		P max		1.88	110.44	10.25	2.84	P= 1.30 mm
		AP max		1.39	132.95	9.27	1.66	AP= 12.22 mm^2
	Multi Objective	TL max P max HAZ min		2.41	67.32	9.94	1.01	TL= 1261.55 kgf HAZ= 4.73 mm UW= 7.65 mm UH=0.134 mm P= 1.17 mm AP=7.52 mm^2

v. Neural network analysis;

- ✓ The present analysis showed that neural network (NN) modeling with back propagation (BP) is a viable means for predicting weld pool shape as a function of weld process conditions.
- ✓ Close and accurate predictions was achieved after training the network with a limited amount of experimental data
- ✓ The neural network model indicated that the weld pool geometry is a sensitive function of the input parameters (welding speed, current, flow rate, arc gap)

5.2. Future Studies

This study has been concentrated on the effect of tungsten inert gas (TIG) welding parameters (welding speed, welding current, shielding gas flow rate, gap distance or arc length and electrode tip angle) on tensile load (TL), heat affected zone (HAZ), upper width (UW), upper height (UH), penetration (P) and area of penetration (AP) for 1.2 mm AISI 304 stainless steel sheet.

In Future, the following considerations could be improved;

- The effect of such welding parameters could be the same for various materials. The difference is only on the welding responses. Therefore, these parameters may be prepared and attempted on various types of materials for tensile load and residual stress measurements.
- Fatique behaviour of the TIG welded joints,
- Statistical models of TIG welded joints,
- Electrothermal analysis of TIG welding process by 3D finite element method.

On a longer perspective a lot could be done with respect to TIG welding control. Today, to achieve a high quality weld, the machine settings have to be adjusted by an experienced operator, and also, the task of performing the weld is very difficult. The adjustment of the machine could be performed by the machine itself if more “intelligence” is included on the machine. Also, more machine “intelligence” could improve the quality and ease the task of performing a weld. Such “improved intelligence” must be based on further research.

REFERENCES

ADAMS, C.M., (1958), Cooling Rates and Peak Temperatures in Fusion Welding, Welding Journal, 37 (5): 210-215.

ALBERRY, P.J., (1989), Sensitivity Analysis of Half Bead and Alternative GTAW Techniques, Welding Journal, 442-451.

ALLEN, T.T. and et al., (2002), Statistical Process Design for Robotic GMA Welding of Sheet Metal, 69-77.

AMES, N.D. and JOHNSON, M.Q., (2003), Effect of GTAW Flux on the Microstructure and Properties of Austenitic, Super Austenitic and Super Duplex Stainless Steel Welds, OSU-Welding Engineering Program, 1-6.

ANDERSEN K., (1992), Studies and Implementation of Stationary Models of the Gas Tungsten Arc Welding Process, M.S. Thesis, Vanderbilt University.

ANDERSEN, K. (1993), Synchronous Weld Pool Oscillation for Monitoring and Control, Ph.D. Dissertation, Vanderbilt University.

ANDERSEN, K. and et al., (1990), Artificial Neural Networks Applied to Arc Welding Process Modeling and Control, IEEE Transactions on Industry Applications, 26(5): 824.

ANDERSON, P. and WIKTOROWICZ, C., (1999), A-TIG Welding the Effects of the Shielding Gas, TWI Welding Institute, USA.

ARENAS, F.M. and ACOFF, L.V., (2002), The Effect of Postweld Heat Treatment on Gas Tungsten Arc Welded Gamma Titanium Aluminide, Scripta Materiala, 46:241-246.

ASM, (1998), Metals Handbook 9th edition, Welding, Brazing and Soldering, American Society for Metal Press.

ASM, (2002), Metals Handbook, Tenth Edition, ASM International Handbook Committee, Materials Park Vol. 1.

ATAMAN, E., (2001), Effect of GTAW Parameters on Mechanical and Microstructural Properties of Weld Joints of Low Alloy AISI 4130 Steel, MSc Thesis, METU, Ankara, Turkey.

ATKINS, G. and et al., (2002), Welding Process Effects in Weldability Testing of Steels, Welding Journal, 61-68.

AWANG, M., (2002), The Effects of Process Parameters on Steel Welding Response in Curved Plates, MSc Thesis, College of Engineering and Mineral Resources West Virginia University, Morgantown, West Virginia.

AWS, (1976), Heat Flow in Welding, Welding Handbook, Volume 3.

AWS, (1980), American Welding Society Committee Recommended Practices for GTAW, American Welding Society Press.

AWS, (1991) A5.32-9X Standard, Specification for Shielding Gases

AWS, (1991), Welding Handbook 8th edition, Volume 2: 74-107.

BENEDETTI, V.A. and et al., (2000), Effect of Welding on the Microstructure and electrochemical Corrosion of AL-Zn-Mg-Fe Alloys, Electrochimica Acta, 45:2187-2195.

BICKNELL, A., SMITH, S. and LUCAS, J., (1994), Infrared Sensor for Top Face Monitoring of Weld Pools, Measurement Science and Technology, 5: 371-378.

BIRCH, R.S. and ALVES, M., (2000), Dynamic Failure of Structural Joint Systems, Thin-Walled Structures, 36, 137-154.

BRAINMAKER, (1993), Simulated Biological Intelligence, California Scientific Software, Nevada City, California.

BROOKS, J.A. and GARRISON, J., (1999), Weld Microstructure Development and Properties of Precipitation-Strengthened Martensitic Stainless Steels, Welding Research Supplement, August, 280-291.

BYRD, T., (1993), Inverter Power Sources, an Efficient Alternative, Welding Journal, 2, 37-40.

CHON, L. and TSO, C.M., (1986), Heat Flow in Fusion Welding, ASM Handbook, Welding Brazing and Soldering, 6: 7-18.

CHRISTENSEN, N., (1965), Distribution of Temperatures in Arc Welding, Welding Journal, 12: 54-75.

COOK, G.E., (1981), Feedback and adaptive control in automated arc welding systems, Metal Construction, 13(9): 551.

COOK, G.E., ANDERSEN, K., BARNETT, R.J., (1990), Feedback and Adaptive Control in Welding, Recent Trends in Welding Science and Technology, Eds.:S.A. David and J.M. Vitek, ASM International, Materials Park, OH, 891.

COOK, H.C. and ROTHSCHILD, (1954), Carbon Steel Electrodes for Use with Inert Gas Shields, Welding Journal, 33(3), 201.

DAE-CHEOL, K. and et al., (1999), Application of Artificial Neural Network and Taguchi Method to Perform design in Metal Forming considering Workability, International Journal of Machine Tools & Manufacture, 39:771-785.

DESIGN EXPERT 6.0.10, (2003), Software Manual Handbook for Design Expert 6.0.10 Evaluation.

DORNFELD, D.A., TOMIZUKA, M. and LANGARI, G., 1982, Modeling and Adaptive Control of Arc Welding Processes, ASME Special Publication: Measurement and Control for Batch Manufacturing.

DURGUTLU, A., (2004), Experimental Investigation of the Effect of Hydrogen in Argon as a Shielding Gas on TIG Welding of Austenitic Stainless Steel, Materials & Design, 25:19-23.

DURGUTLU, A., (2004), Experimental Investigation of the Effect of Hydrogen in Argon as a Shielding Gas on TIG Welding of Austenitic Stainles steel, Materials and Design, 25:19-23.

DYE, D., HUNZIKER, O. and REED, R.C., (2001), Numerical Analysis of the Weldability of Superalloys, Acta Materialia, 49:683–697.

EAGAR, T.W., (1986a), Energy Sources Used For Fusion Welding, ASM Handbook, Welding Brazing and Soldering, 6: 3-6.

EAGAR, T.W., (1986b), The Physics and Chemistry of Welding Processes, Advances in Welding Science and Technology, S.A. David, Metals Park, Ohio, ASM International.

ERASLAN, A.H., ZACHARIA, T., AIDUN, D.K., WELDER, 1986, A Computer Code for Simulating Fast-Transient, Three-Dimensional, Three-Phase, Flow, Temperature and Material Composition Conditions During Welding, Department of MIE, Clarkson University, Potsdam, NY, Report MIE-142.

ERICSSON, M., (2002), Simulation of Robotic TIG-Welding, Lund Institute of Technology Department of Mechanical Engineering, Sweeden.

EROĞLU, M., AKSOY, M. and ORHAN, N., (1999), Effect of Coarse Initial Grain Size on Microsturcture and Mechanical Properties of Weld Metal and HAZ of a Low Carbon Steel, Materials Science and Engineering, (A269), 59-66.

FAN, G.H., TSAI, L.H. and NA, J.S., (2001), Heat Transfer and Fluid Flow in A Partially or Fully Penetrated Weld Pool in as Tungsten Arc Welding, International Journal of Heat and Mass Transfer, 44:417-428.

FENGGUI and et al, (2004), Modelling and Finite Element Analysis on GTAW Arc and Weld Pool, Computational Materials Science, 29, 371-378.

FLINTHAM, E., (1949), All Weld Metal Tensile Tests, Welding Journal, 17(4).

GAN, J. and WU, C., (2001), Extracting Weld Penetration Information in Tungsten Inert Gas Welding, Institute of Materials Joining, Shandong University China.

GAO, J. and WU, C., (2001), Experimental Determination of Weld Pool Geometry in Gas Tungsten arc Welding, Science and Technology of Welding and Joining, (6)5:288-292.

GAYLEY, C.T. and WILLIS, J.G., (1944), Ductile Weld Metal, Welding Journal, 23(1), 8.

GARCIA, D. A., and DONT, P., (1995), Principles of Experimental Design and Analysis, Chapman and Hall.

GEORGE, C. and et al., (2001), Neural Network Systems Techniques in Weld Modelling and Control, Manufacturing System Processes, Chapter 7.

GLICKSTEIN, S.S., (1985), Arc Weld Pool Interactions, Department of Energy Research and Development, USA.

GOODARZI, M., CHOO, R., and TOGURI, M.J., (1997), The Effect of the Cathode Tip Angle on the GTAW Arc and Weld Pool: I. Mathemical Model of the Arc, Journal of Physics D, 30: 2744-2756.

GRAVILLE, B.A., (1973), Weld Cooling Rates and Heat Affected Zone Hardness in Carbon Steel, Welding Journal, 52(9), 377-385.

GROSSBECK, M.L. and et al. (1998), Development of Techniques for Welding V-Cr-Ti Alloys, Journal of Nuclear Materials, 1369-1374.

GROSSBECK, M.L., KING, F.J. and HOELZER, T.D., (2000), Impurity Effects on Gas Tungsten Arc Welds in V-Cr-Ti Alloys, Journal of Nuclear Materials, (283-287): 1356-1360.

HALLAM, N. J., HOPGOOD, A. A., and WOODCOCK, N., (1990), Defect Classification in Welds Using a Feedforward Network within A Blackboard System, International Neural Network Conference (INNC'90), Paris,1, 353-356.

HARRISON, P.L. and HART, P.H.M., (1990), Relationship between HAZ Microstructure and CTOD Transition Behavior in Multipass C-Mn Steel Welds, Recent Trends in Welding Science and Technology, ASM International.

HAZE, T. and AIHARA, S., (1988), Influence of Toughness and Size of Local Brittle Zones on HAZ Toughness of HSLA Steels, 7th Int. Conference on Offshore Mechanics and Engineering, Houston.

HE, X., FUERSCHBACH, W.P. and DEBROY, T., (2003) Heat Transfer and Fluid During Laser Spot Welding of 304 Stainless Steel, 36:1388-1398.

HELLINGA, M.C. and et al., (1997), Identifying Weld Pool Dynamics for GMA Fillet Welds, Liburdi Engineering Corporation Department of Mechanical Engineering.

HENRY, O.H., CLAUSSEN, G.E., (1998), Welding Metallurgy,AWS press,Vol I-II.

HICKEN, G.K. and JACKSON, C.E., (1966), Applied Magnetic Fields on Welding Arcs, Welding Journal, 45: 515-524.

HONG, K., WECKMAN, C.D. and STRONG, B.A.,(1998), The Influence of Thermofluids Phenomena in Gas Tungsten Arc Welds in High and Low Thermal Conductivity Metals, Canadian Metallurgical Quarterly, 37(3-4): 293-303.

HONG, L. and et al. (2000), Vision Based GTA Weld Pool Sensing and Control Using Neurofuzzy Logic, Automated Material Processing Group, Automation Technology Division, 1-7.

INTERNATIONAL INSTITUTE OF WELDING, (1988), Guide to the Light Microscope Examination of Ferritic Steel Welds, Doc No: IX-153388.

JACKSON, C.E. and SHRUBSALL, A.E., (1953), Control of Penetration and Melting Ratio with Welding Technique, Welding Journal, 32(4): 172s.

JACKSON, C.E., (1980),The Science of Arc Welding, Welding Journal,39: 225-230.

JARMAI, K. and FARKAS, J., (1999), Cost calculation and optimisation of welded steel structures, Journal of Constructional Steel Research 50:115–135.

JEFFUS, L., (2004), Welding Principles and Applications Fifth Edition, Thomson Delmar Learning.

JONES, B. and et al., (1996), Statistical Process Control Applied to Gas Metal Arc Welding, Computers & Industrial Engineering, 31(2), 253-256.

KAMOUN, A. and et al., (1999), Apllication of a Rotatable Orthogonal Central Composite Design to the Optimization of the Formulation and Utilization of an Useful Plasticizer for Cement, 27:91-96.

KEY, J.F., (1982), Process Parameters Effects on Arc Physics and Heat Flow in GTAW, Proc. Im. Conf. on welding Technology for Energy Applications, 179-199.

KEY, J.F., CHAN, J.W., (1999), Process Variable Influence on Arc Temperature Distribution, Welding Journal, 62, 179-184.

KEY, J.R., (1980), Anode/Cathode Geometry and Shielding Gas interrelationship in GTAW, Welding Journal, 59, 364-370.

KIM, H.W. and NA, J.S., (1998), Heat and Fluid Flow in Pulsed Current GTA Weld Pool, International Journal of Heat and Mass Transfer, 41, 3213-3227.

KODAMA, M., KAWANO, T. and IWABUCHI, H., (2001), Automatic TIG Welding for Raised Edges of Tank Corners on Membrane LNG Tanks, Mitsubishi Heavy Industries Technical Review, 38(2), 52-56.

KOU, S., (1987), Welding Metallurgy Second Edition, John Wiley & Sons.

KOVACEVIC, R. and ZHANG, (1996a), Y.M., Real-Time Image Processing for Monitoring of Free Weld Pool Surface, ASME Transactions, Journal of Engineering for Industry, 4, 118.

KOVACEVIC, R. and ZHANG, Y.M, (1996d), Apparatus and method for Measuring 3D Weld Pool Shape, United States Patent, #5.481.085.

KOVACEVIC, R., CAO Z.N. and ZHANG Y.M., (1996c), Role of Welding Parameters in Determining the Geometrical Appearance of Weld Pool, ASME Transactions, Journal of Engineering Materials and Technology, 3, 118.

KOVACEVIC, R., ZHANG and Y.M., RUAN S., (1995), Sensing and Control of Weld Pool Geometry for Automated GTA Welding, Transactions of the ASME, Journal of Engineering for Industry, 117(2), 210.

KOVACEVIC, R., ZHANG, Y.M. and LI, L., (1996b), Monitoring of Weld Joint Penetration Based on Weld Pool Geometrical Appearance, Welding Journal, 317.

KRYSRAK, K.F. and BHANIHA, P.M., (1990), Shielding Gas Purification Improves Weld Quality, Welding Journal, 47-49.

LANCASTER, J.F., (1988), The Physics of Welding 2nd edition, International Institute of Welding, USA.

LANCASTER, J.F., (1993), Metallurgy of Welding, 5th edition, Chapman and Hall Press, Great Britain.

LARSON, N.E. and MEREDITH, W.F., (1990), Shielding Gas Selection Manual, Union Carbide Industrial Gases Tech., 10-11.

LATHABAI, S., JARVIS, L.B. and BARTON, J.K., (2001), Comparison of Keyhole and Conventional Gas Tungsten Arc Welds in Commercially Pure Titanium, Materials Science and Engineering, A299, 81-93.

LEBACQ, C. and et al., (2002), Selection of joining Methods in Mechanical Design, Materials and Design, 23:405-416.

LI, P. and ZHANG, Y.M., (2001), Robust Sensing of Arc Length, IEEE Transactions on Instrumentation and measurement, 50(3): 697-704.

LI, Y.Z. and WU, S.C., (1997), Analysis of the Transport Phenomena in the Interfacial Region between TIG Arcs and Weld Pools, Computational Materials Science, 8, 243-250.

LIN, M.L. and EAGAR, T.W., (1984), Influence of Surface Depression and Convection on Arc Weld Pool Geometry, Transport Phenomena in Materials Processing, ASME, 63.

LIPPMANN, R. P., (1987), An Introduction to Computing with Neural Nets, IEEE ASSP Magazine, 4-22.

LOTHONGKUM, G., CHAUMBAI, P. and BHANDHUBANYONG, P., (1999), TIG Pulse Welding of 304L Austenitic Stainless steel in Flat, Vertical and Overhead Positions, Journal of Materials Processing Technology , 89(90): 410-414.

LOTHONGKUM, G., VIYANIT, E. and BHANDHUBANYONG, P., (2001), Study on the Effects Pulsed TIG Welding Parameters on delta-Ferrite Content, Shape Factor and Bead Quality in Orbital Welding of AISI 316L Stainless Steel Plate, Journal of Materials Processing Technology, 110:233-238.

LU, F. and et al., (2004), Modeling and Finite Element Analysis on GTAW Arc and Weld Pool, 29:371-378.

LUO, H. and et al. (2002), Vision Based Neurofuzzy Logic Control of Weld Pool Geometry, Science Technology of Welding and Joining, 7(5): 321-325.

LUO, H. and et al., (2002), Vision Based Neurofuzzy Logic Control of Weld Pool Geometry, Science and Technology of Welding and Joining, 7(5), 321-325.

MAROPOULOS, G.P. and et al., (2000), An Integrated Design and Planning Environment for Welding Part 2: Product Planning, 107:9-14.

MAROPOULOS, G.P., and et al., (2000), An Integrated Design and Planning Environment for Welding Part 1: Product Modelling, Journal of Materiasl Processing Technology, 107:3-8.

MATSUDA, F., HASHIMOTO, T., SENDA, T., (1969), Trans. Nat. Res. Inst. Met., 11: 43.

MCGLONE, J.C., (1982), Weld Bead Geometry Prediction-A Review, Metal Construction, 14(7): 378.

MEE, V., MEELKER, H. and SCHELDE, R., (1999), How To Control hydrogen Level in (Super) Duplex Stainless Steel Weldments Using the GTAW or GMAW Process, AWS Welding Research Supplement, 7-14.

MENDEZ and EAGAR, (2000), estimation of the Characteristic Properties of the Weld Pool During High Productivity Arc Welding, Mathematical Modelling of Weld Phenomena 5: 1-8.

MILLS, K.C. and et al., (1990), Factors Effecting Variable Weld Penetration, International Materials Review, 35(4).

MODENESI, J.P., APOLINARIO, R.E., and PEREIRA, M.I., (2000), TIG Welding With Single-Component Fluxes, Journal of Materials Processing Technology, 99:260-265.

MOHANDAS, T. and et al., (1999), A Comparative Evaluation of Gas Tungsten and Shielded Metal Arc Welds of a Ferritic Stainless Steel, Journal of Materials Processing Technology, 94:133-140.

MUNITZ, A. and et al., (2001), Mechanical Properties and Microstructure of Gas Tungsten Arc Welded Magnesium AZ91D Plates, Materials Science and Engineering, A302, 68-73.

MURUGAN, S. and KUMAR, P.V., (1998), Temperature Distribution during Multipass Welding of Plates, Int. Journal of Pressure Vessels and Piping, 75: 891-905.

MURUGAN, S. and et al., (2001), Temperature Distribution and Residual Stresses due to Multipass Welding in type 304 Stainless Steel and Low Carbon Steel Weld Pads, International Journal of Pressure Vessels and Piping, 78(4): 307-317.

MYERS, T., (1992), Why the Growing Interests in GTAW, The Fabricator,22,38-39.

NAGESH, S.D. and DATTA, L.G., (2002), Prediction of Weld Bead Geometry and Penetration in Shielded Metal-Arc Welding Using Artificial Neural Networks, Journal of Materials Processing Technology, 123:303-312.

NILES, R.W. and JACKSON, C.E., (1975), Weld Thermal Efficiency of the GTAW, Welding Journal, 54: 25-32.

NORMAN, F.A., DRAZHNER, V. and PRANGNELL, B.P., (1999), Effect of Welding Parameters on the Solidification Microstructure of Autogenous TIG Welds in an A1-Cu-Mg-Mn Alloy, Materials Science and Engineering, (A259): 53-64.

NUNES, J.A.C., (1983), An Extended Rosenthal Weld Model, Welding Journal, 165.

ONOE, H. and TANAKA, J., (1979), Japanese LNG Tanker Constructed Using a New Welding Process, Metal Construction, 26-31.

OWEN, R.A. and et al., (2003), Neutron and Synchrotron Measurements of Residual Strain in TIG Welded Aluminium Alloy 2024, Materials Science and Engineering A346:159-167.

PATRICIO, F. and et al, (1999), Humping Formation in High GTA Welding, Massachusetts Institute of Technology, Cambridge, UK.

PFAID, K.J., (1990), Automatic Contour Welding of Tube and Pipe, Tube Pipe Q., 3 (4): 58-62.

POORHAYDARI, B.K. and et al., (2005), Estimation of Cooling rate in the Welding of Plates with Intermediate Thickness, Welding journal, October, 149-155.

ROKHLIN, S.I. and GUU, (1993), A.C., A Study of Arc Force, Pool Depression, and Weld Penetration During Gas Tungsten Arc Welding, Welding Journal, 72(8): 381.

ROSENBLATT, F., (1988), The Perceptron: A Probabilistic Model for Information Storage and Organization in the Brain, Psychological Review, 65: 6.

ROSENTHAL, D., (1941), Mathematical Theory of Heat Distribution during Welding and Cutting, Welding Journal, 20(5): 220.

ROSS, P.J., (1995), Taguchi Techniques for Quality Engineering, Second Edition, McGraw-Hill, Singapore.

RUMELHART, D. E., HINTON, G. E., and WILLIAMS, R. J., (1986), Learning Internal Representations by Error Propagation, in Parallel Distributed Processing: Explorations in the Microstructures of Cognition, vol. 1, Rumelhart, D. E. and McClelland, J. L. (Eds.), MIT Press.

SAEED, G., LOU, M. and ZHANG, Y.M., (2002), Computation of 3D Weld Pool Surface from the Slope Field and Point Tracking of Laser Beams, Center for Manufacturing and Department of Electrical and Computer Engineering Lexington, KY 40506, USA.

SACKS, R.J. and BOHNART, E.R., (2005), Welding Principles and Practices Third Edition, McGraw Hill.

SAITO, S. and et al., (2002) Neutron Irradiation Effect on the Mechanical Properties of Type 316L SS Welded Joints, Journal of Nuclear Materials 307(311):1573-1577.

SAVAGE, W.F., (1980), Weld World, 18: 89-113.

SHANKAR, K. and WU, W., (2001), Effect of Welding and Weld Repair on Crack Propagation Behaviour in Aluminium Alloy 5083 Plates, Materials and Design, 23(2): 201-208.

SIEWERT, T.A., (1988), Ferrite Number Prediction to 100 FN in Stainless Steel Weld Metal, Welding Journal, 289-298.

SINGH, P.J. and et al., (2003), Fatigue Life Prediction of Gas Tungsten Arc Welded AISI 304L Cruciform Joints with Different LOP Sizes, International Journal of Fatigue 25:1-7.

SMART, H.B., (1986), Heat Transfer in GTAW, ASM Metals/Materials Technology and Welding Congress, USA.

SMOLIK, R.G. and al., (2001), Oxidation and Volatilization from Tungsten Brush High Heat Flux Armor During Steam Exposure, 54:583-591.

STOUT, R.D., (1987), Weldability of Steels, Welding Research Council, 4th edition, USA.

SUBAN, M., TUSEK, J. and URAN, M., (2001), Use of Hydrogen in Welding Engineering in Former Times and Today, Journal of Materials Processing Technology, 119:193-198.

SUZUKI, A., HARDT D.E. and VALVANI, L., (1991), Application of Adaptive Control Theory to On-Line GTA Weld Geometry Regulation, Journal of Dynamic Systems Measurement and Control, 113: 93.

TARNG, Y.S. and et al., (1999), Intelligent Modelling and Optimization of the Gas Tungsten Arc Welding Process, Journal of Intelligent Manufacturing, 10:73-79.

TAY, M.K. and BUTLER, C., (1997), Modelling and Optimizing of a Mig Welding Process-A Case Study Using Experimental Design and Neural-Networks, 13:61-70.

TENG, L.T. and LIN, C.C., (1998), Effect of Welding conditions on Residual Stresses Due to Butt Welds, International Journal of Pressure Vessels and Piping, 75:857-864.

TENG, L.T., CHANG, H.P., and TSENG, C.W., (2003), Effect of Welding Sequences on Residual Stresses, Computers and Structures, 81:273-286.

TIMOFEEV, T.B. and et al., (1999), Facture Toughness of Austenitic Welded Joints, International Journal of Pressure Vessels and Piping, 76:393-400.

TSAI, C.I., (1980), Modeling of Casting and Welding Processes II, Engineering Foundation Meeting, New England.

TSAI, N., 1983, Heat Distribution and Weld Bead Geometry in Arc Welding, Ph.D. Thesis, M.I.T.

TUSEK, J., and SUBAN, M., (2000), Experimental Research of the Effect of Hydrogen in Argon as a Shielding Gas in Arc Welding of High-Alloy Stainless Steel, International Journal of Hydrogen Energy, 25:369-376.

URENA, A., ESCALERA, D.M. and GIL L., (2000), Influence of Interface Reactions on Fracture Mechanisms in TIG Arc-Welded Aluminium Matrix Composites, Composites Science and Technology, 60:613-622.

VITEK, M.J. and et al., (2001), Weld Shape Prediction in Plasma Augmented Laser Welded Steel, (6) 5, 305-314.

WAHAB, A.M., and SAKANO, M., (2001), Experimental Study Corrosion Fatigue Behaviour of Welded Steel Structures, Journal of Materials Processing Technology, 118:117-122.

WENDELSTORF, J. and et al., (1996), TIG and Plasma arc modeling: a Survey, Mathematical Modelling of Weld Phenomena 3, The Institute of Materials, 1-46.

WIKLE, C.H., ZEE, H.R. and CHIN, A.B., (1999), A Sensing System for Weld Process Control, Journal of Materials Processing Technology, (89-90): 254-259.

WILLIS, M. J. and et al., (1991), Artificial Neural Networks in Process Engineering, IEE Proceedings-D, 138, 256-266.

WU, C.S. and et al. (2003), Vision-Based Measurement of Weld Pool Geometry in Constant-Current Gas Tungsten Arc Welding, Journal of Engineering Manufacture, 217, 879-882.

WU, C.S. and GAO, J.Q., (2002), Analysis of the heat flux distribution at the anode of a TIG welding arc, Computational Materials Science 24:323–327.

WU, S.C., USHIO, M. and TANAKA., (1999), Analysis of the TIG Welding Arc Behavior, Journal of Engineering Manufacture 7:308-314.

WU, W., (2000), Influence of Vibration Frequency on Solidification of Weldments, Scripta Materiala, 42:661-665.

YASUO, S. and et al., (1999), Measurement of Molten pool Shape and Penetration Control Applying Neural Network in TIG Welding of Thin Steel Plates, ISIJ International, 39(10):1075-1080.

YURI, T. and et al., (2000), Effect of Welding Structure and Delta-Ferrite on Fatigue Properties for TIG Welded Austenitic Stainless Steels at Cryogenic Temperatures, Cryogenics, 40:251-259.

ZACHARIA, T., ERASLAN, A.H. and AIDUN, D.K., (1988a), Modeling of Autogenous Welding, Welding Journal, 67(3): 53.

ZACHARIA, T., ERASLAN, A.H., AIDUN, D.K., (1988b), Modeling of Non-Autogenous Welding, Welding Journal, 67(1): 18.

ZENG, X.M., LUCAS, J. and FANG M.T.C., (1993), Use of Neural Networks for Parameter Prediction and Quality Inspection in TIG Welding, Transactions of the Institute of Measurement and Control, 15(2):87.

ZHANG, M. and KOVACEVIC., R., (1998), Neurofuzzy Model-Based Predictive Control of Weld Fusion Zone Geometry, IEEE Transactions on Fuzzy Systems, (6)3:389-401.

ZHANG, Y.M. and et al., (1993), Determining Joint Penetration in GTAW with Vision Sensing of Weld Face Geometry, Welding Journal, 72(10): 463.

ZHANG, Y.M. and JIANG, M., (2002), Keyhole Double-Sided Arc Welding Process, Welding Journal, Journal of Manufacturing Science and Technology, 124: 249-255.

ZHANG, Y.M. and ZHANG, S.B., (1999), Welding Aluminium Alloy 6061 with the Opposing Dual-Torch GTAW Process, Welding Research Supplement, 202-206.

ZHAO, D.B. and et al., (2001), Intelligent Control for the Shape of the weld Pool in Pulsed GTAW with Filler Metal, AWS Welding Research Supplement, 253-260.

ZHAO, P.C., WU, C.S. and ZHANG, Y.M., (2004), Numerical Simulation of the Dynamic characteristics of Weld Pool Geometry with Step-Changes of Welding Parameters, Modelling and Simulation in Materials Science and Engineering, 12:765-780.

ZHU, K.X., and CHAO, J.Y., (2002), Effects of Temperature-Dependent Material Properties on Welding Simulation, Computers and Structures, 80:967-976.

CURRICULUM VITAE

Uğur EŞME was born in Adana on 6th May of 1973. After being graduated from Adana Erkek High School, he enrolled in the Çukurova University Engineering and Architecture Faculty Department of Mechanical Engineering. He graduated from Çukurova University as a Mechanical Engineer on September 1999. He started his Master of Science (MSc) education in Çukurova University Institute of Natural and Applied Sciences Mechanical Engineering Department Construction & Manufacture Division in 1999. He completed MSc education in February of 2002 and he started Doctor of Philosophy (PhD) education in the same department and year. He has been working as a Research Assistant in the same department since 1999. He has been married since 2002.

APPENDIX A

A1. The FORTRAN Program used to convert data from mV to ^{o}C

```
      DIMENSION VERI(20),tempre(17),volt(20), amper(20)

    character*45 dummy
    character*1 d1

    open(5, file='d:\welding\s31681',status='old')
    open(6, file='d:\welding\out\s31681son.out')

C     ********Reading First Raw Data********

      DO 11 J=1,9
      READ(5,*)dummy

 11   CONTINUE

      n=0
      min=0

     DO WHILE (.NOT. EOF(5))

C     ********Reading and Dividing the Time Period********

 read(5,55)d1,nh,d1,nm,d1,ns,dummy
```

```
 55   format(a1,i2,a1,i2,a1,i2,a45)

  if(n.eq.0) then
       nho=nh
                 nmo=nm
                 nso=ns
 endif

  if(ns.lt.nso) then
                 nm=nm-1
                 ns=ns+60
  endif
  nsf=ns-nso
   if(nm.lt.nmo) then
                 nh=nh-1
                 nm=nm+60
  endif
 nmf=nm-nmo

   if(nh.eq.0) then
                 nh=nh+24
   endif
 nhf=nh-nho
  mintek=nhf*3600+nmf*60+nsf
   min=min+mintek

C      ********Reading Necessary Data********

   DO 10 I=1,8
  read(5,*)VERI(I)
```

```
10          CONTINUE

C    ….Calculation Temperature....

           DO 15 i=1,8
                tempre(i)=24.711*veri(i)+0.1909

 15         CONTINUE

C     ********Calculation of Volt and Ampere********

       write(6,9) n,min,(tempre(I),I=1,8)

9           format(2i6,8f9.4)

            nso=ns
            nmo=nm
            nho=nh

            n=n+1

     END DO
          close(5)
          close(6)
          stop
          end
```

APPENDIX B

B1. TL Maximization

MAX=630.03049 + 238.03487 * V + 8.10260 * I + 25.05345 * F + 4.03510 * G - 75.10057 * V^2 - 0.039932 * I^2 -1.78092 * F^2 - 7.09131 * G^2 - 0.059916 * V * I + 3.34043 * V * F + 0.73102 * V * G - 0.041339 * I * F + 0.045711 * I * G + 1.17361 * F * G;

1.0696<=V;
V<=3.5546;
20<=I;
I<=150;
8<=F;
F<=12;
1<=G;
G<=4;

HAZ=4.25726-2.25321 * V + 0.078141 * I + 0.027766 * F + 0.19755 * G + 0.35202 * V^2 - 1.17845E-004 * I^2 - 1.38373E-003 * F^2 - 0.021331 * G^2 - 6.77070E-003 * V * I - 1.03468E-003 * V * F + 1.07815E-004 * V * G - 1.26837E-004 * I * F + 1.06672E-003 * I * G - 4.65278E-003 * F * G;

UW=3.30265 + 0.44806 * V + 0.089617 * I + 0.20048 * F + 0.074331 * G - 0.21720 * V^2 - 1.28410E-004 * I^2 - 0.015592 * F^2 - 4.65626E-003 * G^2 - 0.011222 * V * I +8.07090E-003 * V * F - 0.027623 * V * G +1.30514E-004 * I * F + 7.62815E-004 * I * G + 0.010625 * F * G;

UH=0.083160 - 0.14708 * V + 4.27108E-003 * I + 0.026577 * F - 0.039542 * G + 0.029239 * V^2 - 1.23691E-006 * I^2 -9.02466E-004 * F^2 + 2.98197E-003 * G^2 - 7.67366E-004 * V * I - 1.10081E-003 * V * F + 6.03239E-003 * V * G -8.54959E-005 * I * F - 1.25432E-004 * I * G + 1.73611E-003 * F * G;

P=0.64397 + 0.066087 * V + 6.96690E-003 * I + 0.018256 * F + 0.087894 * G - 0.019590 * V^2 - 3.88930E-005 * I^2 -5.51306E-004 * F^2 - 0.014174 * G^2 + 5.02410E-004 * V * I - 3.32300E-003 * V * F - 0.020984 * V * G + 5.22375E-005 * I * F + 3.33420E-004 * I * G - 1.45833E-003 * F * G;

AP=3.94256 - 0.19505 * V + 0.084155 * I + 0.21323 * F + 0.46969 * G - 0.019710 * V^2 - 1.26140E-004 * I^2 -0.012660 * F^2 - 0.10079 * G^2 - 0.013011 * V * I - 0.020638 * V * F - 0.048323 * V * G + 5.88725E-004 * I * F + 4.53258E-004 * I * G + 0.012111 * F * G;

B2. HAZ Minimization

MİN=4.25726-2.25321 * V + 0.078141 * I + 0.027766 * F + 0.19755 * G + 0.35202 * V^2 - 1.17845E-004 * I^2 - 1.38373E-003 * F^2 - 0.021331 * G^2 - 6.77070E-003 * V * I - 1.03468E-003 * V * F + 1.07815E-004 * V * G - 1.26837E-004 * I * F + 1.06672E-003 * I * G - 4.65278E-003 * F * G;

1.0696<=V;
V<=3.5546;
20<=I;
I<=150;
8<=F;
F<=12;
1<=G;
G<=4;

HAZ=4.25726-2.25321 * V + 0.078141 * I + 0.027766 * F + 0.19755 * G + 0.35202 * V^2 - 1.17845E-004 * I^2 - 1.38373E-003 * F^2 - 0.021331 * G^2 - 6.77070E-003 * V * I - 1.03468E-003 * V * F + 1.07815E-004 * V * G - 1.26837E-004 * I * F + 1.06672E-003 * I * G - 4.65278E-003 * F * G;

UW=3.30265 + 0.44806 * V + 0.089617 * I + 0.20048 * F + 0.074331 * G - 0.21720 * V^2 - 1.28410E-004 * I^2 - 0.015592 * F^2 - 4.65626E-003 * G^2 - 0.011222 * V * I +8.07090E-003 * V * F - 0.027623 * V * G +1.30514E-004 * I * F + 7.62815E-004 * I * G + 0.010625 * F * G;

UH=0.083160 - 0.14708 * V + 4.27108E-003 * I + 0.026577 * F - 0.039542 * G + 0.029239 * V^2 - 1.23691E-006 * I^2 -9.02466E-004 * F^2 + 2.98197E-003 * G^2 - 7.67366E-004 * V * I - 1.10081E-003 * V * F + 6.03239E-003 * V * G -8.54959E-005 * I * F - 1.25432E-004 * I * G + 1.73611E-003 * F * G;

P=0.64397 + 0.066087 * V + 6.96690E-003 * I + 0.018256 * F + 0.087894 * G - 0.019590 * V^2 - 3.88930E-005 * I^2 -5.51306E-004 * F^2 - 0.014174 * G^2 + 5.02410E-004 * V * I - 3.32300E-003 * V * F - 0.020984 * V * G + 5.22375E-005 * I * F + 3.33420E-004 * I * G - 1.45833E-003 * F * G;

AP=3.94256 - 0.19505 * V + 0.084155 * I + 0.21323 * F + 0.46969 * G - 0.019710 * V^2 - 1.26140E-004 * I^2 -0.012660 * F^2 - 0.10079 * G^2 - 0.013011 * V * I - 0.020638 * V * F - 0.048323 * V * G + 5.88725E-004 * I * F + 4.53258E-004 * I * G + 0.012111 * F * G;

B3. UW Minimization

MİN=3.30265 + 0.44806 * V + 0.089617 * I + 0.20048 * F + 0.074331 * G - 0.21720 * V^2 - 1.28410E-004 * I^2 - 0.015592 * F^2 - 4.65626E-003 * G^2 - 0.011222 * V * I +8.07090E-003 * V * F - 0.027623 * V * G +1.30514E-004 * I * F + 7.62815E-004 * I * G + 0.010625 * F * G;

1.0696<=V;
V<=3.5546;
20<=I;
I<=150;
8<=F;
F<=12;
1<=G;
G<=4;

HAZ=4.25726-2.25321 * V + 0.078141 * I + 0.027766 * F + 0.19755 * G + 0.35202 * V^2 - 1.17845E-004 * I^2 - 1.38373E-003 * F^2 - 0.021331 * G^2 - 6.77070E-003 * V * I - 1.03468E-003 * V * F + 1.07815E-004 * V * G - 1.26837E-004 * I * F + 1.06672E-003 * I * G - 4.65278E-003 * F * G;

UW=3.30265 + 0.44806 * V + 0.089617 * I + 0.20048 * F + 0.074331 * G - 0.21720 * V^2 - 1.28410E-004 * I^2 - 0.015592 * F^2 - 4.65626E-003 * G^2 - 0.011222 * V * I +8.07090E-003 * V * F - 0.027623 * V * G +1.30514E-004 * I * F + 7.62815E-004 * I * G + 0.010625 * F * G;

UH=0.083160 - 0.14708 * V + 4.27108E-003 * I + 0.026577 * F - 0.039542 * G + 0.029239 * V^2 - 1.23691E-006 * I^2 -9.02466E-004 * F^2 + 2.98197E-003 * G^2 - 7.67366E-004 * V * I - 1.10081E-003 * V * F + 6.03239E-003 * V * G -8.54959E-005 * I * F - 1.25432E-004 * I * G + 1.73611E-003 * F * G;

P=0.64397 + 0.066087 * V + 6.96690E-003 * I + 0.018256 * F + 0.087894 * G - 0.019590 * V^2 - 3.88930E-005 * I^2 -5.51306E-004 * F^2 - 0.014174 * G^2 + 5.02410E-004 * V * I - 3.32300E-003 * V * F - 0.020984 * V * G + 5.22375E-005 * I * F + 3.33420E-004 * I * G - 1.45833E-003 * F * G;

AP=3.94256 - 0.19505 * V + 0.084155 * I + 0.21323 * F + 0.46969 * G - 0.019710 * V^2 - 1.26140E-004 * I^2 -0.012660 * F^2 - 0.10079 * G^2 - 0.013011 * V * I - 0.020638 * V * F - 0.048323 * V * G + 5.88725E-004 * I * F + 4.53258E-004 * I * G + 0.012111 * F * G;

B4. UH Minimization

MİN=0.083160 - 0.14708 * V + 4.27108E-003 * I + 0.026577 * F - 0.039542 * G + 0.029239 * V^2 - 1.23691E-006 * I^2 -9.02466E-004 * F^2 + 2.98197E-003 * G^2 - 7.67366E-004 * V * I - 1.10081E-003 * V * F + 6.03239E-003 * V * G -8.54959E-005 * I * F - 1.25432E-004 * I * G + 1.73611E-003 * F * G;

1.0696<=V;
V<=3.5546;
20<=I;
I<=150;
8<=F;
F<=12;
1<=G;
G<=4;

HAZ=4.25726-2.25321 * V + 0.078141 * I + 0.027766 * F + 0.19755 * G + 0.35202 * V^2 - 1.17845E-004 * I^2 - 1.38373E-003 * F^2 - 0.021331 * G^2 - 6.77070E-003 * V * I - 1.03468E-003 * V * F + 1.07815E-004 * V * G - 1.26837E-004 * I * F + 1.06672E-003 * I * G - 4.65278E-003 * F * G;

UW=3.30265 + 0.44806 * V + 0.089617 * I + 0.20048 * F + 0.074331 * G - 0.21720 * V^2 - 1.28410E-004 * I^2 - 0.015592 * F^2 - 4.65626E-003 * G^2 - 0.011222 * V * I +8.07090E-003 * V * F - 0.027623 * V * G +1.30514E-004 * I * F + 7.62815E-004 * I * G + 0.010625 * F * G;

UH=0.083160 - 0.14708 * V + 4.27108E-003 * I + 0.026577 * F - 0.039542 * G + 0.029239 * V^2 - 1.23691E-006 * I^2 -9.02466E-004 * F^2 + 2.98197E-003 * G^2 - 7.67366E-004 * V * I - 1.10081E-003 * V * F + 6.03239E-003 * V * G -8.54959E-005 * I * F - 1.25432E-004 * I * G + 1.73611E-003 * F * G;

P=0.64397 + 0.066087 * V + 6.96690E-003 * I + 0.018256 * F + 0.087894 * G - 0.019590 * V^2 - 3.88930E-005 * I^2 -5.51306E-004 * F^2 - 0.014174 * G^2 + 5.02410E-004 * V * I - 3.32300E-003 * V * F - 0.020984 * V * G + 5.22375E-005 * I * F + 3.33420E-004 * I * G - 1.45833E-003 * F * G;

AP=3.94256 - 0.19505 * V + 0.084155 * I + 0.21323 * F + 0.46969 * G - 0.019710 * V^2 - 1.26140E-004 * I^2 -0.012660 * F^2 - 0.10079 * G^2 - 0.013011 * V * I - 0.020638 * V * F - 0.048323 * V * G + 5.88725E-004 * I * F + 4.53258E-004 * I * G + 0.012111 * F * G;

B5. P Maximization

MAX=0.64397 + 0.066087 * V + 6.96690E-003 * I + 0.018256 * F + 0.087894 * G - 0.019590 * V^2 - 3.88930E-005 * I^2 -5.51306E-004 * F^2 - 0.014174 * G^2 + 5.02410E-004 * V * I -3.32300E-003 * V * F - 0.020984 * V * G + 5.22375E-005 * I * F + 3.33420E-004 * I * G - 1.45833E-003 * F * G;

1.0696<=V;
V<=3.5546;
20<=I;
I<=150;
8<=F;
F<=12;
1<=G;
G<=4;

HAZ=4.25726-2.25321 * V + 0.078141 * I + 0.027766 * F + 0.19755 * G + 0.35202 * V^2 - 1.17845E-004 * I^2 - 1.38373E-003 * F^2 - 0.021331 * G^2 - 6.77070E-003 * V * I - 1.03468E-003 * V * F + 1.07815E-004 * V * G - 1.26837E-004 * I * F + 1.06672E-003 * I * G - 4.65278E-003 * F * G;

UW=3.30265 + 0.44806 * V + 0.089617 * I + 0.20048 * F + 0.074331 * G - 0.21720 * V^2 - 1.28410E-004 * I^2 - 0.015592 * F^2 - 4.65626E-003 * G^2 - 0.011222 * V * I +8.07090E-003 * V * F - 0.027623 * V * G +1.30514E-004 * I * F + 7.62815E-004 * I * G + 0.010625 * F * G;

UH=0.083160 - 0.14708 * V + 4.27108E-003 * I + 0.026577 * F - 0.039542 * G + 0.029239 * V^2 - 1.23691E-006 * I^2 -9.02466E-004 * F^2 + 2.98197E-003 * G^2 - 7.67366E-004 * V * I - 1.10081E-003 * V * F + 6.03239E-003 * V * G -8.54959E-005 * I * F - 1.25432E-004 * I * G + 1.73611E-003 * F * G;

P=0.64397 + 0.066087 * V + 6.96690E-003 * I + 0.018256 * F + 0.087894 * G - 0.019590 * V^2 - 3.88930E-005 * I^2 -5.51306E-004 * F^2 - 0.014174 * G^2 + 5.02410E-004 * V * I - 3.32300E-003 * V * F - 0.020984 * V * G + 5.22375E-005 * I * F + 3.33420E-004 * I * G - 1.45833E-003 * F * G;

AP=3.94256 - 0.19505 * V + 0.084155 * I + 0.21323 * F + 0.46969 * G - 0.019710 * V^2 - 1.26140E-004 * I^2 -0.012660 * F^2 - 0.10079 * G^2 - 0.013011 * V * I - 0.020638 * V * F - 0.048323 * V * G + 5.88725E-004 * I * F + 4.53258E-004 * I * G + 0.012111 * F * G;

B6. AP Maximization

MAX=3.94256 - 0.19505 * V + 0.084155 * I + 0.21323 * F + 0.46969 * G - 0.019710 * V^2 - 1.26140E-004 * I^2 -0.012660 * F^2 - 0.10079 * G^2 - 0.013011 * V * I - 0.020638 * V * F - 0.048323 * V * G + 5.88725E-004 * I * F + 4.53258E-004 * I * G + 0.012111 * F * G;
1.0696<=V;

V<=3.5546;
20<=I;
I<=150;
8<=F;
F<=12;
1<=G;
G<=4;

HAZ=4.25726-2.25321 * V + 0.078141 * I + 0.027766 * F + 0.19755 * G + 0.35202 * V^2 - 1.17845E-004 * I^2 - 1.38373E-003 * F^2 - 0.021331 * G^2 - 6.77070E-003 * V * I - 1.03468E-003 * V * F + 1.07815E-004 * V * G - 1.26837E-004 * I * F + 1.06672E-003 * I * G - 4.65278E-003 * F * G;

UW=3.30265 + 0.44806 * V + 0.089617 * I + 0.20048 * F + 0.074331 * G - 0.21720 * V^2 - 1.28410E-004 * I^2 - 0.015592 * F^2 - 4.65626E-003 * G^2 - 0.011222 * V * I +8.07090E-003 * V * F - 0.027623 * V * G +1.30514E-004 * I * F + 7.62815E-004 * I * G + 0.010625 * F * G;

UH=0.083160 - 0.14708 * V + 4.27108E-003 * I + 0.026577 * F - 0.039542 * G + 0.029239 * V^2 - 1.23691E-006 * I^2 -9.02466E-004 * F^2 + 2.98197E-003 * G^2 - 7.67366E-004 * V * I - 1.10081E-003 * V * F + 6.03239E-003 * V * G -8.54959E-005 * I * F - 1.25432E-004 * I * G + 1.73611E-003 * F * G;

P=0.64397 + 0.066087 * V + 6.96690E-003 * I + 0.018256 * F + 0.087894 * G - 0.019590 * V^2 - 3.88930E-005 * I^2 -5.51306E-004 * F^2 - 0.014174 * G^2 + 5.02410E-004 * V * I - 3.32300E-003 * V * F - 0.020984 * V * G + 5.22375E-005 * I * F + 3.33420E-004 * I * G - 1.45833E-003 * F * G;

AP=3.94256 - 0.19505 * V + 0.084155 * I + 0.21323 * F + 0.46969 * G - 0.019710 * V^2 - 1.26140E-004 * I^2 -0.012660 * F^2 - 0.10079 * G^2 - 0.013011 * V * I - 0.020638 * V * F - 0.048323 * V * G + 5.88725E-004 * I * F + 4.53258E-004 * I * G + 0.012111 * F * G;

B7. Constrained TL Maximization

MAX=630.03049 + 238.03487 * V + 8.10260 * I + 25.05345 * F + 4.03510 * G - 75.10057 * V^2 - 0.039932 * I^2 -1.78092 * F^2 - 7.09131 * G^2 - 0.059916 * V * I + 3.34043 * V * F + 0.73102 * V * G - 0.041339 * I * F + 0.045711 * I * G + 1.17361 * F * G;

1.0696<=V;
V<=3.5546;
20<=I;
I<=150;
8<=F;
F<=12;
1<=G;
G<=4;

!TL CONSTRAINT; 630.03049 + 238.03487 * V + 8.10260 * I + 25.05345 * F + 4.03510 * G - 75.10057 * V^2 - 0.039932 * I^2 -1.78092 * F^2 - 7.09131 * G^2 - 0.059916 * V * I + 3.34043 * V * F + 0.73102 * V * G - 0.041339 * I * F + 0.045711 * I * G + 1.17361 * F * G>=1330.734;

!HAZ CONSTRAINT; 4.25726-2.25321 * V + 0.078141 * I + 0.027766 * F + 0.19755 * G + 0.35202 * V^2 - 1.17845E-004 * I^2 - 1.38373E-003 * F^2 - 0.021331 * G^2 - 6.77070E-003 * V * I - 1.03468E-003 * V * F + 1.07815E-004 * V * G - 1.26837E-004 * I * F + 1.06672E-003 * I * G - 4.65278E-003 * F * G<=1.9243;

!UW CONSTRAINT; 3.30265 + 0.44806 * V + 0.089617 * I + 0.20048 * F + 0.074331 * G - 0.21720 * V^2 - 1.28410E-004 * I^2 - 0.015592 * F^2 - 4.65626E-003 * G^2 - 0.011222 * V * I +8.07090E-003 * V * F - 0.027623 * V * G +1.30514E-004 * I * F + 7.62815E-004 * I * G + 0.010625 * F * G<=3.7448;

!UH CONSTRAINT; 0.083160 - 0.14708 * V + 4.27108E-003 * I + 0.026577 * F - 0.039542 * G + 0.029239 * V^2 - 1.23691E-006 * I^2 -9.02466E-004 * F^2 + 2.98197E-003 * G^2 - 7.67366E-004 * V * I - 1.10081E-003 * V * F + 6.03239E-003 * V * G -8.54959E-005 * I * F - 1.25432E-004 * I * G + 1.73611E-003 * F * G<=0.048;

!P CONSTRAINT; 0.64397 + 0.066087 * V + 6.96690E-003 * I + 0.018256 * F + 0.087894 * G - 0.019590 * V^2 - 3.88930E-005 * I^2 -5.51306E-004 * F^2 - 0.014174 * G^2 + 5.02410E-004 * V * I -3.32300E-003 * V * F - 0.020984 * V * G + 5.22375E-005 * I * F + 3.33420E-004 * I * G - 1.45833E-003 * F * G>=1.2;

!AP CONSTRAINT; 3.94256 - 0.19505 * V + 0.084155 * I + 0.21323 * F + 0.46969 * G - 0.019710 * V^2 - 1.26140E-004 * I^2 -0.012660 * F^2 - 0.10079 * G^2 - 0.013011 * V * I - 0.020638 * V * F -0.048323 * V * G + 5. 88725E-004 * I * F + 4.53258E-004 * I * G + 0.012111 * F * G>=13.92;

HAZ=4.25726-2.25321 * V + 0.078141 * I + 0.027766 * F + 0.19755 * G + 0.35202 * V^2 - 1.17845E-004 * I^2 - 1.38373E-003 * F^2 - 0.021331 * G^2 - 6.77070E-003 * V * I - 1.03468E-003 * V * F + 1.07815E-004 * V * G - 1.26837E-004 * I * F + 1.06672E-003 * I * G - 4.65278E-003 * F * G;

UW=3.30265 + 0.44806 * V + 0.089617 * I + 0.20048 * F + 0.074331 * G - 0.21720 * V^2 - 1.28410E-004 * I^2 - 0.015592 * F^2 - 4.65626E-003 * G^2 - 0.011222 * V * I +8.07090E-003 * V * F - 0.027623 * V * G +1.30514E-004 * I * F + 7.62815E-004 * I * G + 0.010625 * F * G;

UH=0.083160 - 0.14708 * V + 4.27108E-003 * I + 0.026577 * F - 0.039542 * G + 0.029239 * V^2 - 1.23691E-006 * I^2 -9.02466E-004 * F^2 + 2.98197E-003 * G^2 - 7.67366E-004 * V * I - 1.10081E-003 * V * F + 6.03239E-003 * V * G -8.54959E-005 * I * F - 1.25432E-004 * I * G + 1.73611E-003 * F * G;

P=0.64397 + 0.066087 * V + 6.96690E-003 * I + 0.018256 * F + 0.087894 * G - 0.019590 * V^2 - 3.88930E-005 * I^2 -5.51306E-004 * F^2 - 0.014174 * G^2 + 5.02410E-004 * V * I - 3.32300E-003 * V * F - 0.020984 * V * G + 5.22375E-005 * I * F + 3.33420E-004 * I * G - 1.45833E-003 * F * G;

AP=3.94256 - 0.19505 * V + 0.084155 * I + 0.21323 * F + 0.46969 * G - 0.019710 * V^2 - 1.26140E-004 * I^2 -0.012660 * F^2 - 0.10079 * G^2 - 0.013011 * V * I - 0.020638 * V * F - 0.048323 * V * G + 5.88725E-004 * I * F + 4.53258E-004 * I * G + 0.012111 * F * G;

B8. Constrained HAZ Minimization

MIN=4.25726-2.25321 * V + 0.078141 * I + 0.027766 * F + 0.19755 * G + 0.35202 * V^2 - 1.17845E-004 * I^2 - 1.38373E-003 * F^2 - 0.021331 * G^2 - 6.77070E-003 * V * I - 1.03468E-003 * V * F + 1.07815E-004 * V * G - 1.26837E-004 * I * F + 1.06672E-003 * I * G - 4.65278E-003 * F * G;

1.0696<=V;
V<=3.5546;
20<=I;
I<=150;
8<=F;
F<=12;
1<=G;
G<=4;

!TL CONSTRAINT; 630.03049 + 238.03487 * V + 8.10260 * I + 25.05345 * F + 4.03510 * G - 75.10057 * V^2 - 0.039932 * I^2 -1.78092 * F^2 - 7.09131 * G^2 - 0.059916 * V * I + 3.34043 * V * F + 0.73102 * V * G - 0.041339 * I * F + 0.045711 * I * G + 1.17361 * F * G>=1330.734;

!HAZ CONSTRAINT; 4.25726-2.25321 * V + 0.078141 * I + 0.027766 * F + 0.19755 * G + 0.35202 * V^2 - 1.17845E-004 * I^2 - 1.38373E-003 * F^2 - 0.021331 * G^2 - 6.77070E-003 * V * I - 1.03468E-003 * V * F + 1.07815E-004 * V * G - 1.26837E-004 * I * F + 1.06672E-003 * I * G - 4.65278E-003 * F * G<=1.9243;

!UW CONSTRAINT; 3.30265 + 0.44806 * V + 0.089617 * I + 0.20048 * F + 0.074331 * G - 0.21720 * V^2 - 1.28410E-004 * I^2 - 0.015592 * F^2 - 4.65626E-003 * G^2 - 0.011222 * V * I +8.07090E-003 * V * F - 0.027623 * V * G +1.30514E-004 * I * F + 7.62815E-004 * I * G + 0.010625 * F * G<=3.7448;

!UH CONSTRAINT; 0.083160 - 0.14708 * V + 4.27108E-003 * I + 0.026577 * F - 0.039542 * G + 0.029239 * V^2 - 1.23691E-006 * I^2 -9.02466E-004 * F^2 + 2.98197E-003 * G^2 - 7.67366E-004 * V * I - 1.10081E-003 * V * F + 6.03239E-003 * V * G -8.54959E-005 * I * F - 1.25432E-004 * I * G + 1.73611E-003 * F * G<=0.048;

!P CONSTRAINT; 0.64397 + 0.066087 * V + 6.96690E-003 * I + 0.018256 * F + 0.087894 * G - 0.019590 * V^2 - 3.88930E-005 * I^2 -5.51306E-004 * F^2 - 0.014174 * G^2 + 5.02410E-004 * V * I -3.32300E-003 * V * F - 0.020984 * V * G + 5.22375E-005 * I * F + 3.33420E-004 * I * G - 1.45833E-003 * F * G>=1.2;

!AP CONSTRAINT; 3.94256 - 0.19505 * V + 0.084155 * I + 0.21323 * F + 0.46969 * G - 0.019710 * V^2 - 1.26140E-004 * I^2 -0.012660 * F^2 - 0.10079 * G^2 - 0.013011 * V * I - 0.020638 * V * F -0.048323 * V * G + 5. 88725E-004 * I * F + 4.53258E-004 * I * G + 0.012111 * F * G>=13.92;

HAZ=4.25726-2.25321 * V + 0.078141 * I + 0.027766 * F + 0.19755 * G + 0.35202 * V^2 - 1.17845E-004 * I^2 - 1.38373E-003 * F^2 - 0.021331 * G^2 - 6.77070E-003 * V * I - 1.03468E-003 * V * F + 1.07815E-004 * V * G - 1.26837E-004 * I * F + 1.06672E-003 * I * G - 4.65278E-003 * F * G;

UW=3.30265 + 0.44806 * V + 0.089617 * I + 0.20048 * F + 0.074331 * G - 0.21720 * V^2 - 1.28410E-004 * I^2 - 0.015592 * F^2 - 4.65626E-003 * G^2 - 0.011222 * V * I +8.07090E-003 * V * F - 0.027623 * V * G +1.30514E-004 * I * F + 7.62815E-004 * I * G + 0.010625 * F * G;

UH=0.083160 - 0.14708 * V + 4.27108E-003 * I + 0.026577 * F - 0.039542 * G + 0.029239 * V^2 - 1.23691E-006 * I^2 -9.02466E-004 * F^2 + 2.98197E-003 * G^2 - 7.67366E-004 * V * I - 1.10081E-003 * V * F + 6.03239E-003 * V * G -8.54959E-005 * I * F - 1.25432E-004 * I * G + 1.73611E-003 * F * G;

P=0.64397 + 0.066087 * V + 6.96690E-003 * I + 0.018256 * F + 0.087894 * G - 0.019590 * V^2 - 3.88930E-005 * I^2 -5.51306E-004 * F^2 - 0.014174 * G^2 + 5.02410E-004 * V * I - 3.32300E-003 * V * F - 0.020984 * V * G + 5.22375E-005 * I * F + 3.33420E-004 * I * G - 1.45833E-003 * F * G;

AP=3.94256 - 0.19505 * V + 0.084155 * I + 0.21323 * F + 0.46969 * G - 0.019710 * V^2 - 1.26140E-004 * I^2 -0.012660 * F^2 - 0.10079 * G^2 - 0.013011 * V * I - 0.020638 * V * F - 0.048323 * V * G + 5.88725E-004 * I * F + 4.53258E-004 * I * G + 0.012111 * F * G;

B9. Constrained UW Minimization

MIN=3.30265 + 0.44806 * V + 0.089617 * I + 0.20048 * F + 0.074331 * G - 0.21720 * V^2 - 1.28410E-004 * I^2 - 0.015592 * F^2 - 4.65626E-003 * G^2 - 0.011222 * V * I +8.07090E-003 * V * F - 0.027623 * V * G +1.30514E-004 * I * F + 7.62815E-004 * I * G + 0.010625 * F * G;

1.0696<=V;
V<=3.5546;
20<=I;
I<=150;
8<=F;
F<=12;
1<=G;
G<=4;

!TL CONSTRAINT; 630.03049 + 238.03487 * V + 8.10260 * I + 25.05345 * F + 4.03510 * G - 75.10057 * V^2 - 0.039932 * I^2 -1.78092 * F^2 - 7.09131 * G^2 - 0.059916 * V * I + 3.34043 * V * F + 0.73102 * V * G - 0.041339 * I * F + 0.045711 * I * G + 1.17361 * F * G>=1330.734;

!HAZ CONSTRAINT; 4.25726-2.25321 * V + 0.078141 * I + 0.027766 * F + 0.19755 * G + 0.35202 * V^2 - 1.17845E-004 * I^2 - 1.38373E-003 * F^2 - 0.021331 * G^2 - 6.77070E-003 * V * I - 1.03468E-003 * V * F + 1.07815E-004 * V * G - 1.26837E-004 * I * F + 1.06672E-003 * I * G - 4.65278E-003 * F * G<=1.9243;

!UW CONSTRAINT; 3.30265 + 0.44806 * V + 0.089617 * I + 0.20048 * F + 0.074331 * G - 0.21720 * V^2 - 1.28410E-004 * I^2 - 0.015592 * F^2 - 4.65626E-003 * G^2 - 0.011222 * V * I +8.07090E-003 * V * F - 0.027623 * V * G +1.30514E-004 * I * F + 7.62815E-004 * I * G + 0.010625 * F * G<=3.7448;

!UH CONSTRAINT; 0.083160 - 0.14708 * V + 4.27108E-003 * I + 0.026577 * F - 0.039542 * G + 0.029239 * V^2 - 1.23691E-006 * I^2 -9.02466E-004 * F^2 + 2.98197E-003 * G^2 - 7.67366E-004 * V * I - 1.10081E-003 * V * F + 6.03239E-003 * V * G -8.54959E-005 * I * F - 1.25432E-004 * I * G + 1.73611E-003 * F * G<=0.048;

!P CONSTRAINT; 0.64397 + 0.066087 * V + 6.96690E-003 * I + 0.018256 * F + 0.087894 * G - 0.019590 * V^2 - 3.88930E-005 * I^2 -5.51306E-004 * F^2 - 0.014174 * G^2 + 5.02410E-004 * V * I -3.32300E-003 * V * F - 0.020984 * V * G + 5.22375E-005 * I * F + 3.33420E-004 * I * G - 1.45833E-003 * F * G>=1.2;

!AP CONSTRAINT; 3.94256 - 0.19505 * V + 0.084155 * I + 0.21323 * F + 0.46969 * G - 0.019710 * V^2 - 1.26140E-004 * I^2 -0.012660 * F^2 - 0.10079 * G^2 - 0.013011 * V * I - 0.020638 * V * F -0.048323 * V * G + 5. 88725E-004 * I * F + 4.53258E-004 * I * G + 0.012111 * F * G>=13.92;

HAZ=4.25726-2.25321 * V + 0.078141 * I + 0.027766 * F + 0.19755 * G + 0.35202 * V^2 - 1.17845E-004 * I^2 - 1.38373E-003 * F^2 - 0.021331 * G^2 - 6.77070E-003 * V * I - 1.03468E-003 * V * F + 1.07815E-004 * V * G - 1.26837E-004 * I * F + 1.06672E-003 * I * G - 4.65278E-003 * F * G;

UW=3.30265 + 0.44806 * V + 0.089617 * I + 0.20048 * F + 0.074331 * G - 0.21720 * V^2 - 1.28410E-004 * I^2 - 0.015592 * F^2 - 4.65626E-003 * G^2 - 0.011222 * V * I +8.07090E-003 * V * F - 0.027623 * V * G +1.30514E-004 * I * F + 7.62815E-004 * I * G + 0.010625 * F * G;

UH=0.083160 - 0.14708 * V + 4.27108E-003 * I + 0.026577 * F - 0.039542 * G + 0.029239 * V^2 - 1.23691E-006 * I^2 -9.02466E-004 * F^2 + 2.98197E-003 * G^2 - 7.67366E-004 * V * I - 1.10081E-003 * V * F + 6.03239E-003 * V * G -8.54959E-005 * I * F - 1.25432E-004 * I * G + 1.73611E-003 * F * G;

P=0.64397 + 0.066087 * V + 6.96690E-003 * I + 0.018256 * F + 0.087894 * G - 0.019590 * V^2 - 3.88930E-005 * I^2 -5.51306E-004 * F^2 - 0.014174 * G^2 + 5.02410E-004 * V * I - 3.32300E-003 * V * F - 0.020984 * V * G + 5.22375E-005 * I * F + 3.33420E-004 * I * G - 1.45833E-003 * F * G;

AP=3.94256 - 0.19505 * V + 0.084155 * I + 0.21323 * F + 0.46969 * G - 0.019710 * V^2 - 1.26140E-004 * I^2 -0.012660 * F^2 - 0.10079 * G^2 - 0.013011 * V * I - 0.020638 * V * F - 0.048323 * V * G + 5.88725E-004 * I * F + 4.53258E-004 * I * G + 0.012111 * F * G;

B10. Constrained UH Minimization

MIN=0.083160 - 0.14708 * V + 4.27108E-003 * I + 0.026577 * F - 0.039542 * G + 0.029239 * V^2 - 1.23691E-006 * I^2 -9.02466E-004 * F^2 + 2.98197E-003 * G^2 - 7.67366E-004 * V * I - 1.10081E-003 * V * F + 6.03239E-003 * V * G -8.54959E-005 * I * F - 1.25432E-004 * I * G + 1.73611E-003 * F * G;

1.0696<=V;
V<=3.5546;
20<=I;
I<=150;
8<=F;
F<=12;
1<=G;
G<=4;

!TL CONSTRAINT; 630.03049 + 238.03487 * V + 8.10260 * I + 25.05345 * F + 4.03510 * G - 75.10057 * V^2 - 0.039932 * I^2 -1.78092 * F^2 - 7.09131 * G^2 - 0.059916 * V * I + 3.34043 * V * F + 0.73102 * V * G - 0.041339 * I * F + 0.045711 * I * G + 1.17361 * F * G>=1330.734;

!HAZ CONSTRAINT; 4.25726-2.25321 * V + 0.078141 * I + 0.027766 * F + 0.19755 * G + 0.35202 * V^2 - 1.17845E-004 * I^2 - 1.38373E-003 * F^2 - 0.021331 * G^2 - 6.77070E-003 * V * I - 1.03468E-003 * V * F + 1.07815E-004 * V * G - 1.26837E-004 * I * F + 1.06672E-003 * I * G - 4.65278E-003 * F * G<=1.9243;

!UW CONSTRAINT; 3.30265 + 0.44806 * V + 0.089617 * I + 0.20048 * F + 0.074331 * G - 0.21720 * V^2 - 1.28410E-004 * I^2 - 0.015592 * F^2 - 4.65626E-003 * G^2 - 0.011222 * V * I +8.07090E-003 * V * F - 0.027623 * V * G +1.30514E-004 * I * F + 7.62815E-004 * I * G + 0.010625 * F * G<=3.7448;

!UH CONSTRAINT; 0.083160 - 0.14708 * V + 4.27108E-003 * I + 0.026577 * F - 0.039542 * G + 0.029239 * V^2 - 1.23691E-006 * I^2 -9.02466E-004 * F^2 + 2.98197E-003 * G^2 - 7.67366E-004 * V * I - 1.10081E-003 * V * F + 6.03239E-003 * V * G -8.54959E-005 * I * F - 1.25432E-004 * I * G + 1.73611E-003 * F * G<=0.048;

!P CONSTRAINT; 0.64397 + 0.066087 * V + 6.96690E-003 * I + 0.018256 * F + 0.087894 * G - 0.019590 * V^2 - 3.88930E-005 * I^2 -5.51306E-004 * F^2 - 0.014174 * G^2 + 5.02410E-004 * V * I -3.32300E-003 * V * F - 0.020984 * V * G + 5.22375E-005 * I * F + 3.33420E-004 * I * G - 1.45833E-003 * F * G>=1.2;

!AP CONSTRAINT; 3.94256 - 0.19505 * V + 0.084155 * I + 0.21323 * F + 0.46969 * G - 0.019710 * V^2 - 1.26140E-004 * I^2 -0.012660 * F^2 - 0.10079 * G^2 - 0.013011 * V * I - 0.020638 * V * F -0.048323 * V * G + 5. 88725E-004 * I * F + 4.53258E-004 * I * G + 0.012111 * F * G>=13.92;

HAZ=4.25726-2.25321 * V + 0.078141 * I + 0.027766 * F + 0.19755 * G + 0.35202 * V^2 - 1.17845E-004 * I^2 - 1.38373E-003 * F^2 - 0.021331 * G^2 - 6.77070E-003 * V * I - 1.03468E-003 * V * F + 1.07815E-004 * V * G - 1.26837E-004 * I * F + 1.06672E-003 * I * G - 4.65278E-003 * F * G;

UW=3.30265 + 0.44806 * V + 0.089617 * I + 0.20048 * F + 0.074331 * G - 0.21720 * V^2 - 1.28410E-004 * I^2 - 0.015592 * F^2 - 4.65626E-003 * G^2 - 0.011222 * V * I +8.07090E-003 * V * F - 0.027623 * V * G +1.30514E-004 * I * F + 7.62815E-004 * I * G + 0.010625 * F * G;

UH=0.083160 - 0.14708 * V + 4.27108E-003 * I + 0.026577 * F - 0.039542 * G + 0.029239 * V^2 - 1.23691E-006 * I^2 -9.02466E-004 * F^2 + 2.98197E-003 * G^2 - 7.67366E-004 * V * I - 1.10081E-003 * V * F + 6.03239E-003 * V * G -8.54959E-005 * I * F - 1.25432E-004 * I * G + 1.73611E-003 * F * G;

P=0.64397 + 0.066087 * V + 6.96690E-003 * I + 0.018256 * F + 0.087894 * G - 0.019590 * V^2 - 3.88930E-005 * I^2 -5.51306E-004 * F^2 - 0.014174 * G^2 + 5.02410E-004 * V * I - 3.32300E-003 * V * F - 0.020984 * V * G + 5.22375E-005 * I * F + 3.33420E-004 * I * G - 1.45833E-003 * F * G;

AP=3.94256 - 0.19505 * V + 0.084155 * I + 0.21323 * F + 0.46969 * G - 0.019710 * V^2 - 1.26140E-004 * I^2 -0.012660 * F^2 - 0.10079 * G^2 - 0.013011 * V * I - 0.020638 * V * F - 0.048323 * V * G + 5.88725E-004 * I * F + 4.53258E-004 * I * G + 0.012111 * F * G;

B11. Constrained P Maximization

MAX=0.64397 + 0.066087 * V + 6.96690E-003 * I + 0.018256 * F + 0.087894 * G - 0.019590 * V^2 - 3.88930E-005 * I^2 -5.51306E-004 * F^2 - 0.014174 * G^2 + 5.02410E-004 * V * I -3.32300E-003 * V * F - 0.020984 * V * G + 5.22375E-005 * I * F + 3.33420E-004 * I * G - 1.45833E-003 * F * G;

1.0696<=V;
V<=3.5546;
20<=I;
I<=150;
8<=F;
F<=12;
1<=G;
G<=4;

!TL CONSTRAINT; 630.03049 + 238.03487 * V + 8.10260 * I + 25.05345 * F + 4.03510 * G - 75.10057 * V^2 - 0.039932 * I^2 -1.78092 * F^2 - 7.09131 * G^2 - 0.059916 * V * I + 3.34043 * V * F + 0.73102 * V * G - 0.041339 * I * F + 0.045711 * I * G + 1.17361 * F * G>=1330.734;

!HAZ CONSTRAINT; 4.25726-2.25321 * V + 0.078141 * I + 0.027766 * F + 0.19755 * G + 0.35202 * V^2 - 1.17845E-004 * I^2 - 1.38373E-003 * F^2 - 0.021331 * G^2 - 6.77070E-003 * V * I - 1.03468E-003 * V * F + 1.07815E-004 * V * G - 1.26837E-004 * I * F + 1.06672E-003 * I * G - 4.65278E-003 * F * G<=1.9243;

!UW CONSTRAINT; 3.30265 + 0.44806 * V + 0.089617 * I + 0.20048 * F + 0.074331 * G - 0.21720 * V^2 - 1.28410E-004 * I^2 - 0.015592 * F^2 - 4.65626E-003 * G^2 - 0.011222 * V * I +8.07090E-003 * V * F - 0.027623 * V * G +1.30514E-004 * I * F + 7.62815E-004 * I * G + 0.010625 * F * G<=3.7448;

!UH CONSTRAINT; 0.083160 - 0.14708 * V + 4.27108E-003 * I + 0.026577 * F - 0.039542 * G + 0.029239 * V^2 - 1.23691E-006 * I^2 -9.02466E-004 * F^2 + 2.98197E-003 * G^2 - 7.67366E-004 * V * I - 1.10081E-003 * V * F + 6.03239E-003 * V * G -8.54959E-005 * I * F - 1.25432E-004 * I * G + 1.73611E-003 * F * G<=0.048;

!P CONSTRAINT; 0.64397 + 0.066087 * V + 6.96690E-003 * I + 0.018256 * F + 0.087894 * G - 0.019590 * V^2 - 3.88930E-005 * I^2 -5.51306E-004 * F^2 - 0.014174 * G^2 + 5.02410E-004 * V * I -3.32300E-003 * V * F - 0.020984 * V * G + 5.22375E-005 * I * F + 3.33420E-004 * I * G - 1.45833E-003 * F * G>=1.2;

!AP CONSTRAINT; 3.94256 - 0.19505 * V + 0.084155 * I + 0.21323 * F + 0.46969 * G - 0.019710 * V^2 - 1.26140E-004 * I^2 -0.012660 * F^2 - 0.10079 * G^2 - 0.013011 * V * I - 0.020638 * V * F -0.048323 * V * G + 5. 88725E-004 * I * F + 4.53258E-004 * I * G + 0.012111 * F * G>=13.92;

HAZ=4.25726-2.25321 * V + 0.078141 * I + 0.027766 * F + 0.19755 * G + 0.35202 * V^2 - 1.17845E-004 * I^2 - 1.38373E-003 * F^2 - 0.021331 * G^2 - 6.77070E-003 * V * I - 1.03468E-003 * V * F + 1.07815E-004 * V * G - 1.26837E-004 * I * F + 1.06672E-003 * I * G - 4.65278E-003 * F * G;

UW=3.30265 + 0.44806 * V + 0.089617 * I + 0.20048 * F + 0.074331 * G - 0.21720 * V^2 - 1.28410E-004 * I^2 - 0.015592 * F^2 - 4.65626E-003 * G^2 - 0.011222 * V * I +8.07090E-003 * V * F - 0.027623 * V * G +1.30514E-004 * I * F + 7.62815E-004 * I * G + 0.010625 * F * G;

UH=0.083160 - 0.14708 * V + 4.27108E-003 * I + 0.026577 * F - 0.039542 * G + 0.029239 * V^2 - 1.23691E-006 * I^2 -9.02466E-004 * F^2 + 2.98197E-003 * G^2 - 7.67366E-004 * V * I - 1.10081E-003 * V * F + 6.03239E-003 * V * G -8.54959E-005 * I * F - 1.25432E-004 * I * G + 1.73611E-003 * F * G;

P=0.64397 + 0.066087 * V + 6.96690E-003 * I + 0.018256 * F + 0.087894 * G - 0.019590 * V^2 - 3.88930E-005 * I^2 -5.51306E-004 * F^2 - 0.014174 * G^2 + 5.02410E-004 * V * I - 3.32300E-003 * V * F - 0.020984 * V * G + 5.22375E-005 * I * F + 3.33420E-004 * I * G - 1.45833E-003 * F * G;

AP=3.94256 - 0.19505 * V + 0.084155 * I + 0.21323 * F + 0.46969 * G - 0.019710 * V^2 - 1.26140E-004 * I^2 -0.012660 * F^2 - 0.10079 * G^2 - 0.013011 * V * I - 0.020638 * V * F - 0.048323 * V * G + 5.88725E-004 * I * F + 4.53258E-004 * I * G + 0.012111 * F * G;

B12. Constrained AP Maximization

MAX=3.94256 - 0.19505 * V + 0.084155 * I + 0.21323 * F + 0.46969 * G - 0.019710 * V^2 - 1.26140E-004 * I^2 -0.012660 * F^2 - 0.10079 * G^2 - 0.013011 * V * I - 0.020638 * V * F - 0.048323 * V * G + 5. 88725E-004 * I * F + 4.53258E-004 * I * G + 0.012111 * F * G;

1.0696<=V;
V<=3.5546;
20<=I;
I<=150;
8<=F;
F<=12;
1<=G;
G<=4;

!TL CONSTRAINT; 630.03049 + 238.03487 * V + 8.10260 * I + 25.05345 * F + 4.03510 * G - 75.10057 * V^2 - 0.039932 * I^2 -1.78092 * F^2 - 7.09131 * G^2 - 0.059916 * V * I + 3.34043 * V * F + 0.73102 * V * G - 0.041339 * I * F + 0.045711 * I * G + 1.17361 * F * G>=1330.734;

!HAZ CONSTRAINT; 4.25726-2.25321 * V + 0.078141 * I + 0.027766 * F + 0.19755 * G + 0.35202 * V^2 - 1.17845E-004 * I^2 - 1.38373E-003 * F^2 - 0.021331 * G^2 - 6.77070E-003 * V * I - 1.03468E-003 * V * F + 1.07815E-004 * V * G - 1.26837E-004 * I * F + 1.06672E-003 * I * G - 4.65278E-003 * F * G<=1.9243;

!UW CONSTRAINT; 3.30265 + 0.44806 * V + 0.089617 * I + 0.20048 * F + 0.074331 * G - 0.21720 * V^2 - 1.28410E-004 * I^2 - 0.015592 * F^2 - 4.65626E-003 * G^2 - 0.011222 * V * I +8.07090E-003 * V * F - 0.027623 * V * G +1.30514E-004 * I * F + 7.62815E-004 * I * G

+ 0.010625 * F * G<=3.7448;
!UH CONSTRAINT; 0.083160 - 0.14708 * V + 4.27108E-003 * I + 0.026577 * F - 0.039542 * G + 0.029239 * V^2 - 1.23691E-006 * I^2 -9.02466E-004 * F^2 + 2.98197E-003 * G^2 - 7.67366E-004 * V * I - 1.10081E-003 * V * F + 6.03239E-003 * V * G -8.54959E-005 * I * F - 1.25432E-004 * I * G + 1.73611E-003 * F * G<=0.048;

!P CONSTRAINT; 0.64397 + 0.066087 * V + 6.96690E-003 * I + 0.018256 * F + 0.087894 * G - 0.019590 * V^2 - 3.88930E-005 * I^2 -5.51306E-004 * F^2 - 0.014174 * G^2 + 5.02410E-004 * V * I -3.32300E-003 * V * F - 0.020984 * V * G + 5.22375E-005 * I * F + 3.33420E-004 * I * G - 1.45833E-003 * F * G>=1.2;

!AP CONSTRAINT; 3.94256 - 0.19505 * V + 0.084155 * I + 0.21323 * F + 0.46969 * G - 0.019710 * V^2 - 1.26140E-004 * I^2 -0.012660 * F^2 - 0.10079 * G^2 - 0.013011 * V * I - 0.020638 * V * F -0.048323 * V * G + 5. 88725E-004 * I * F + 4.53258E-004 * I * G + 0.012111 * F * G>=13.92;

HAZ=4.25726-2.25321 * V + 0.078141 * I + 0.027766 * F + 0.19755 * G + 0.35202 * V^2 - 1.17845E-004 * I^2 - 1.38373E-003 * F^2 - 0.021331 * G^2 - 6.77070E-003 * V * I - 1.03468E-003 * V * F + 1.07815E-004 * V * G - 1.26837E-004 * I * F + 1.06672E-003 * I * G - 4.65278E-003 * F * G;

UW=3.30265 + 0.44806 * V + 0.089617 * I + 0.20048 * F + 0.074331 * G - 0.21720 * V^2 - 1.28410E-004 * I^2 - 0.015592 * F^2 - 4.65626E-003 * G^2 - 0.011222 * V * I +8.07090E-003 * V * F - 0.027623 * V * G +1.30514E-004 * I * F + 7.62815E-004 * I * G + 0.010625 * F * G;

UH=0.083160 - 0.14708 * V + 4.27108E-003 * I + 0.026577 * F - 0.039542 * G + 0.029239 * V^2 - 1.23691E-006 * I^2 -9.02466E-004 * F^2 + 2.98197E-003 * G^2 - 7.67366E-004 * V * I - 1.10081E-003 * V * F + 6.03239E-003 * V * G -8.54959E-005 * I * F - 1.25432E-004 * I * G + 1.73611E-003 * F * G;

P=0.64397 + 0.066087 * V + 6.96690E-003 * I + 0.018256 * F + 0.087894 * G - 0.019590 * V^2 - 3.88930E-005 * I^2 -5.51306E-004 * F^2 - 0.014174 * G^2 + 5.02410E-004 * V * I - 3.32300E-003 * V * F - 0.020984 * V * G + 5.22375E-005 * I * F + 3.33420E-004 * I * G - 1.45833E-003 * F * G;

AP=3.94256 - 0.19505 * V + 0.084155 * I + 0.21323 * F + 0.46969 * G - 0.019710 * V^2 - 1.26140E-004 * I^2 -0.012660 * F^2 - 0.10079 * G^2 - 0.013011 * V * I - 0.020638 * V * F - 0.048323 * V * G + 5.88725E-004 * I * F + 4.53258E-004 * I * G + 0.012111 * F * G;

APPENDIX C

C1. Weld Pool Shape Prediction Program written in MATLAB

```
V=input ('Please enter V (mm/s)... (1.0696~3.55)…?')
I=input ('Please enter I (A).... (20~150)…?')
F=input ('Please enter F (l/min)... (8~12)….?')
G=input ('Please enter G (mm)... (1~4)…?')

TL=630.03049 + 238.03487 * V + 8.10260 * I + 25.05345 * F + 4.03510 * G - 75.10057 * V^2 - 0.039932 * I^2 -1.78092 * F^2 - 7.09131 * G^2 - 0.059916 * V * I + 3.34043 * V * F + 0.73102 * V * G - 0.041339 * I * F  + 0.045711 * I * G + 1.17361 * F * G;

HAZ=4.25726-2.25321 * V + 0.078141 * I + 0.027766 * F + 0.19755 * G + 0.35202 * V^2 - 1.17845E-004 * I^2 - 1.38373E-003 * F^2 - 0.021331 * G^2 - 6.77070E-003 * V * I - 1.03468E-003 * V * F + 1.07815E-004 * V * G - 1.26837E-004 * I * F + 1.06672E-003 * I * G - 4.65278E-003 * F * G;

UW=3.30265 + 0.44806 * V + 0.089617 * I + 0.20048 * F + 0.074331 * G - 0.21720 * V^2 - 1.28410E-004 * I^2 - 0.015592 * F^2 - 4.65626E-003 * G^2 - 0.011222 * V * I +8.07090E-003 * V * F - 0.027623 * V * G +1.30514E-004 * I * F + 7.62815E-004 * I * G + 0.010625 * F * G;

UH=0.083160 - 0.14708 * V + 4.27108E-003 * I + 0.026577 * F - 0.039542 * G + 0.029239 * V^2 - 1.23691E-006 * I^2 -9.02466E-004 * F^2 + 2.98197E-003 * G^2 - 7.67366E-004 * V * I - 1.10081E-003 * V * F + 6.03239E-003 * V * G -8.54959E-005 * I * F - 1.25432E-004 * I * G + 1.73611E-003 * F * G;

P=0.64397 + 0.066087 * V + 6.96690E-003 * I + 0.018256 * F + 0.087894 * G - 0.019590 * V^2 - 3.88930E-005 * I^2 -5.51306E-004 * F^2 - 0.014174 * G^2 + 5.02410E-004 * V * I -3.32300E-003 * V * F - 0.020984 * V * G + 5.22375E-005 * I * F + 3.33420E-004 * I * G - 1.45833E-003 * F * G;

AP=3.94256 - 0.19505 * V + 0.084155 * I + 0.21323 * F + 0.46969 * G - 0.019710 * V^2 - 1.26140E-004 * I^2 -0.012660 * F^2 - 0.10079 * G^2 - 0.013011 * V * I - 0.020638 * V * F -0.048323 * V * G + 5.88725E-004 * I * F + 4.53258E-004 * I * G + 0.012111 * F * G;

%disp('TL');disp(TL);disp('kg')
%disp('HAZ');disp(HAZ);disp('mm')
```

```
%disp('UW');disp(UW);disp('mm')
%disp('UH');disp(UH);disp('mm')
%disp('P');disp(P);disp('mm')
%disp('AP');disp(AP);disp('mm2')
xmin=-UW/2;
xmax=UW/2;
r=UW/2;
a=4*(UH)/(UW^2);
%ymin=-UW/2;
%ymax=0;
x=xmin:0.01:xmax;
y1=-P/r*(sqrt(r^2-x.^2));
y2=a*x.^2-UH;
plot(x,y1,'r+:',x,y2,'r+:','linewidth',3);
axis([-18 18 -1.4 0.4]);
line([-15,15],[-1.2,-1.2],'color','r','linewidth',5);
%line([-12,12],[0,0],'color','r','linewidth',5);
line([15,15],[0,-1.2],'color','r','linewidth',5);
line([-15,-15],[-1.2,0],'color','r','linewidth',5);
line([-15,-r],[0,0],'color','r','linewidth',5);
line([r,15],[0,0],'color','r','linewidth',5);
line([-r-HAZ,-r-HAZ-1],[0,-0.6],'color','b','linewidth',5);
line([-r-HAZ-1,-r-HAZ],[-0.6,-1.2],'color','b','linewidth',5);
line([r+HAZ,r+HAZ+1],[0,-0.6],'color','b','linewidth',5);
line([r+HAZ+1,r+HAZ],[-0.6,-1.2],'color','b','linewidth',5);
line([0,0],[-UH,-1.2],'color','r','linewidth',2);
%plot(x,y2);
%plot(x,y2)
grid on
%disp(xmin)
%disp(xmax)
```

```
%disp(ymin)
%disp(ymax)
%disp(r)
%disp(x)
disp('Tensile Strength...='),disp(TL),disp('kg')
disp('Penetration...='),disp(P),disp('mm')
disp('Upper Width...='),disp(UW),disp('mm')
disp('Upper Height...='),disp(UH),disp('mm')
disp('Heat Aaffected Zone...='),disp(HAZ),disp('mm')
disp('Area of Penetration...='),disp(AP),disp('mm2')
```

APPENDIX D

Table D1. Training data used for the construction of the neural network model

Train No	V (mm/s)	I (A)	F (I/min)	G (mm)	TL (kgf)	HAZ (mm)	UW (mm)	UH (mm)	P (mm)	AP (mm^2)
1	2.3101	85	10	2.5	1100	4.12	5.78	0.18	1.06	6.58
2	1.5311	10	10	2.5	750	2.55	4.22	0.09	0.75	4.6
3	2.3101	85	10	2.5	1100	4.14	5.82	0.19	1.06	6.55
4	1.0696	20	8	1	950	3.4	5.14	0.1	0.98	6.08
5	1.0696	20	8	4	1000	3.8	5.33	0.09	0.94	6.11
6	0.6081	30	10	2.5	1150	5.96	8.56	0.12	1.06	8.38
7	2.3101	85	10	2.5	1100	4.12	5.82	0.17	1.03	6.09
8	1.5311	30	10	0.5	1175	4.03	5.52	0.2	1.08	6.38
9	1.5311	30	6	2.5	1200	4.32	6.2	0.09	0.91	6.38
10	1.0696	40	8	4	1100	5.56	7.72	0.18	1.16	7.77
11	2.4541	30	10	2.5	900	3.1	5.63	0.08	0.97	5.43
12	1.9926	20	8	4	975	2.68	5.53	0.03	0.86	5.76
13	1.5311	30	14	2.5	1025	4	5.62	0.22	1.02	6.22
14	1.0696	40	12	1	1150	5.23	7.42	0.22	1.08	7.52
15	1.0696	40	8	1	1125	5.44	7.69	0.18	1.08	7.48
16	2.3101	85	10	2.5	1150	4.13	5.96	0.18	0.96	7
17	1.9926	20	12	1	1050	2.54	5.45	0.09	0.9	5.81
18	1.5311	30	10	5.5	875	4.43	6.5	0.18	0.78	6.78
19	1.9926	40	8	1	1150	4.66	7.01	0.12	1.02	7.09
20	2.3101	85	10	2.5	1050	4.14	5.78	0.16	1.06	6.23
21	1.0696	40	12	4	1125	5.53	7.89	0.2	1.12	7.82
22	1.5311	50	10	2.5	1250	5.32	7.23	0.28	1.1	7.11
23	1.9926	40	12	1	1025	4.73	7.02	0.16	1.05	7.12
24	1.9926	40	12	4	1050	4.89	7.22	0.13	0.98	7.23
25	1.0696	20	12	1	1000	3.26	5.03	0.15	0.95	6.01
26	1.9926	40	8	4	1000	4.94	7.28	0.13	1.03	7.26
27	2.3101	85	10	2.5	1100	4.13	5.79	0.18	0.96	6.18
28	1.0696	20	12	4	1025	3.53	5.22	0.19	0.9	5.98
29	1.9926	20	8	1	1100	2.55	5.48	0.09	0.92	5.53
30	1.9926	20	12	4	1000	2.78	5.64	0.1	0.89	5.63
31	1.9926	40	8	4	1230	3.79	9.08	0.09	0.94	7.87
32	2.5606	70	8	1	1227	4.63	9.02	0.18	1.17	8.801
33	1.9926	70	12	1	1265	5.1	8.12	0.11	1.24	8.607
34	2.2766	55	14	2.5	1287	4.45	7.12	0.08	1.23	7.1
35	2.2766	55	6	2.5	1237	4.43	7.88	0.06	1.18	7.03
36	2.3101	85	10	2.5	1375	4.45	7.98	0.07	1.25	7.97
37	2.2766	55	10	5.5	1245	4.52	8.53	0.15	0.98	4.887
38	2.5606	70	12	1	1265	4.6	8.26	0.16	1.2	7.2
39	2.8446	55	10	2.5	1230	3.2	7.86	0.09	1.06	5.54
40	2.5606	70	12	4	1212	4.78	8.39	0.17	1	8
41	2.2766	55	10	0.5	1320	4.39	6.36	0.14	1.11	5.8
42	1.9926	40	8	1	1275	3.35	8.36	0.1	1.13	8.3
43	2.2766	25	10	2.5	1050	2.54	5.9	0.02	0.8	5.3
44	2.3101	85	10	2.5	1380	4.45	7.99	0.08	1.25	7.98
45	2.3101	85	10	2.5	1375	4.44	7.98	0.08	1.23	7.95
46	2.3101	85	10	2.5	1375	4.45	8	0.07	1.25	7.98
47	2.5606	40	12	1	1300	2.98	5.98	0.04	0.95	5.02
48	2.5606	40	12	4	1235	3.06	6.54	0.08	0.87	5.63
49	2.5606	40	8	1	1300	2.99	5.9	0.03	0.93	5.42
50	1.9926	40	12	4	1275	3.6	7.72	0.1	0.95	6.56
51	2.3101	85	10	2.5	1375	4.44	7.98	0.08	1.25	7.98

Continue of Table D1

Train No	V (mm/s)	I (A)	F (I/min)	G (mm)	TL (kgf)	HAZ (mm)	UW (mm)	UH (mm)	P (mm)	AP (mm^2)
52	2.5606	40	8	4	1225	3.08	6.42	0.04	0.89	5.48
53	2.3101	85	10	2.5	1380	4.46	7.98	0.08	1.22	7.99
54	2.5606	70	8	4	1325	4.79	8.45	0.15	1.14	7.2
55	2.2766	85	10	2.5	1300	5.61	9.51	0.257	1.143	9.198
56	1.9926	70	8	4	1250	5.35	8.96	0.14	1.19	9.061
57	1.7086	55	10	2.5	1325	5	8.84	0.08	1.15	8.984
58	1.9926	40	12	1	1280	3.4	7.17	0.09	1.1	7.9
59	1.9926	70	8	1	1300	5.1	8.57	0.17	1.27	7.34
60	1.9926	70	12	4	1260	5.3	8.63	0.12	1.17	8.55
61	2.3101	85	10	2.5	1000	6.5	7.66	0.11	1.18	7.56
62	4.0516	110	10	2.5	1150	4.82	7.21	0.15	1.1	7.63
63	2.3101	85	10	2.5	1020	6.44	7.66	0.11	1.18	7.56
64	3.0576	110	10	0.5	1030	5.2	6.86	0.19	1.21	7.62
65	2.5606	150	12	4	1050	7.8	10.56	0.18	1.21	9.69
66	2.3101	85	10	2.5	1100	6.43	7.66	0.11	1.18	7.56
67	3.5546	150	8	4	1000	6.8	8.87	0.08	1.18	6.98
68	3.0576	190	10	2.5	980	8.2	11.12	0.22	1.22	10.48
69	2.5606	70	8	4	1385	4.79	7.22	0.15	1.14	7.2
70	2.5606	150	12	1	1100	7.5	9.73	0.18	1.18	9.78
71	2.5606	70	8	1	1375	4.63	6.98	0.18	1.22	8.801
72	3.0576	30	10	2.5	900	3.8	4.35	0.09	0.89	5.23
73	3.5546	70	8	4	980	4.6	5.78	0.15	0.98	5.89
74	3.5546	70	12	4	950	4.4	5.75	0.18	0.99	5.78
75	2.3101	85	10	2.5	1000	6.52	7.66	0.11	1.18	7.56
76	2.5606	70	12	1	1385	4.6	6.86	0.16	1.2	7.2
77	3.5546	150	12	4	975	6.5	8.78	0.09	1.19	6.86
78	2.5606	150	8	4	950	7.9	10.48	0.2	1.16	9.79
79	3.5546	150	8	1	1050	6.35	8.56	0.1	1.2	6.73
80	2.5606	150	8	1	1000	7.4	9.86	0.19	1.19	9.72
81	3.0576	110	6	2.5	1020	6.7	7.72	0.1	1.16	7.39
82	3.5546	70	12	1	1000	4.1	5.63	0.1	1.1	5.56
83	3.0576	110	10	5.5	975	7.2	8.23	0.09	0.98	6.98
84	3.5546	150	12	1	1050	6.3	8.5	0.09	1.21	6.79
85	3.0576	110	14	2.5	1020	6.2	7.21	0.14	1.19	7.67
86	2.3101	85	10	2.5	1050	6.5	7.66	0.11	1.18	7.56
87	2.5606	70	12	4	1385	4.78	7.23	0.17	1	7.98
88	2.0636	110	10	2.5	1250	6.8	9.93	0.18	1.21	7.88
89	3.5546	70	8	1	950	4.3	5.68	0.08	1.18	5.63
90	2.3101	85	10	2.5	1050	6.45	7.66	0.11	1.18	7.56

Table D2. Training data used in neural network study

Test No	V (mm/s)	I (A)	F (I/min)	G (mm)	TL (kgf)	HAZ (mm)	UW (mm)	UH (mm)	P (mm)	AP (mm^2)
1	2.3101	85	10	2.5	1100	4.12	5.82	0.17	1.03	6.09
2	1.5311	30	10	0.5	1175	4.03	5.52	0.20	1.08	6.38
3	1.5311	30	6	2.5	1200	4.32	6.20	0.09	0.91	6.38
4	1.0696	40	8	4	1100	5.56	7.72	0.18	1.16	7.77
5	2.4541	30	10	2.5	900	3.10	5.63	0.08	0.97	5.43
6	1.9926	20	8	4	975	2.68	5.53	0.03	0.86	5.76
7	1.5311	30	14	2.5	1025	4.00	5.62	0.22	1.02	6.22
8	1.0696	40	12	1	1150	5.23	7.42	0.22	1.08	7.52
9	1.0696	40	8	1	1125	5.44	7.69	0.18	1.08	7.48
10	2.3101	85	10	2.5	1150	4.13	5.96	0.18	0.96	7.00
11	1.9926	20	12	1	1050	2.54	5.45	0.09	0.90	5.81
12	1.5311	30	10	5.5	875	4.43	6.50	0.18	0.78	6.78
13	1.9926	40	8	1	1150	4.66	7.01	0.12	1.02	7.09
14	1.9926	40	12	4	1275	3.60	7.72	0.10	0.95	6.56
15	2.3101	85	10	2.5	1375	4.44	7.98	0.08	1.25	7.98
16	2.5606	40	8	4	1225	3.08	6.42	0.04	0.89	5.48
17	2.3101	85	10	2.5	1380	4.46	7.98	0.08	1.22	7.99
18	2.5606	70	8	4	1325	4.79	8.45	0.15	1.14	7.20
19	2.3101	85	10	2.5	1300	5.61	9.51	0.25	1.14	9.19
20	1.9926	70	8	4	1250	5.35	8.96	0.14	1.19	9.06
21	1.7086	55	10	2.5	1325	5.00	8.84	0.08	1.15	8.98
22	1.9926	40	12	1	1280	3.4	7.17	0.09	1.10	7.9
23	1.9926	70	8	1	1300	5.10	8.57	0.17	1.27	7.34
24	1.9926	70	12	4	1260	5.30	8.63	0.12	1.17	8.55
25	2.5606	70	8	4	1385	4.79	7.22	0.15	1.14	7.20
26	2.5606	150	12	1	1100	7.50	9.73	0.18	1.18	9.78
27	2.5606	70	8	1	1375	4.63	6.98	0.18	1.22	8.80
28	3.0576	30	10	2.5	900	3.80	4.35	0.09	0.89	5.23
29	3.5546	70	8	4	980	4.60	5.78	0.15	0.98	5.89
30	3.5546	70	12	4	950	4.40	5.75	0.18	0.99	5.78
31	2.3101	85	10	2.5	1000	6.52	7.66	0.11	1.18	7.56
32	2.5606	70	12	1	1385	4.60	6.86	0.16	1.20	7.20
33	3.5546	150	12	4	975	6.50	8.78	0.09	1.19	6.86
34	2.5606	150	8	4	950	7.90	10.48	0.20	1.16	9.79
35	3.5546	150	8	1	1050	6.35	8.56	0.10	1.20	6.73
36	2.5606	150	8	1	1000	7.40	9.86	0.19	1.19	9.72
37	3.0576	110	6	2.5	1020	6.70	7.72	0.10	1.16	7.39
38	3.5546	70	12	1	1000	4.10	5.63	0.10	1.10	5.56

Table D3. Comparison of predicted and measured results for AISI 304 1.2 mm stainless steel

MEASURED VALUES						PREDICTIONS WITH NEURAL NETWORK						PREDICTIONS WITH FORMULA					
TL	HAZ	UW	UH	P	AP	PRETL	PREHAZ	PREUW	PREUH	PREP	PREAP	PRETL	PREHAZ	PREUW	PREUH	PREP	PREAP
1100	4.12	5.82	0.17	1.03	6.09	1086.133	4.020259	6.134462	0.153586	0.998672	6.645271	1135.337	3.969817	6.519137	0.12817	1.027909	6.834221
1175	4.03	5.52	0.2	1.08	6.38	1182.138	3.855284	6.355611	0.122109	1.100173	6.934335	1141.361	3.731426	6.22473	0.143693	1.010583	6.37814
1200	4.32	6.2	0.09	0.91	6.38	1090.892	4.004773	6.404029	0.122539	1.012847	6.635174	1121.868	4.015397	6.543763	0.07926	1.018834	6.726179
1100	5.56	7.72	0.18	1.16	7.77	1175.314	5.808832	8.711871	0.156176	1.080635	8.024091	1108.844	5.452643	7.71598	0.164246	1.070928	7.745944
900	3.1	5.63	0.08	0.97	5.43	1136.824	2.906194	5.781773	0.042678	0.853616	5.143583	1109.658	2.988172	5.833778	0.082477	0.951668	5.919421
975	2.68	5.53	0.03	0.86	5.76	963.406	2.978616	5.329385	0.056095	0.82334	5.161005	1032.649	2.894043	5.786002	0.067302	0.845376	5.555364
1025	4	5.62	0.22	1.02	6.22	1083.501	4.039884	5.917451	0.181581	0.987365	6.664321	1091.816	3.879958	5.995566	0.148201	1.019341	6.537142
1150	5.23	7.42	0.22	1.08	7.52	1200.264	5.034888	7.271892	0.199324	1.094938	7.78514	1137.222	5.120306	6.957403	0.214837	1.099406	7.55319
1125	5.44	7.69	0.18	1.08	7.48	1206.488	5.103472	7.637089	0.177802	1.106944	7.835713	1167.11	5.163272	7.30493	0.192171	1.082179	7.658728
1150	4.13	5.96	0.18	0.96	7	1086.133	4.020259	6.134462	0.153586	0.998672	6.645271	1135.337	3.969817	6.519137	0.12817	1.027909	6.834221
1050	2.54	5.45	0.09	0.9	5.81	1031.333	3.061019	5.258035	0.076604	0.916486	5.534313	1077.386	2.631738	5.169038	0.096439	0.935516	5.400319
875	4.43	6.5	0.18	0.78	6.78	1007.987	4.405106	6.59098	0.150006	0.915273	6.491129	1019.931	4.00744	6.890902	0.149614	0.841287	6.006492
1150	4.66	7.01	0.12	1.02	7.09	1252.093	3.963318	6.908962	0.112951	1.141901	7.214643	1197.68	3.820998	6.724376	0.108166	1.062452	6.745629
1275	3.6	7.72	0.1	0.95	6.56	1173.498	4.071211	6.673866	0.148488	0.996885	6.657316	1137.966	4.008047	6.868709	0.13638	0.980555	6.662637
1375	4.44	7.98	0.08	1.25	7.98	1306.046	4.35763	7.971872	0.109263	1.161663	7.536239	1231.355	4.483079	7.403477	0.118655	1.12294	7.368768
1225	3.08	6.42	0.04	0.89	5.48	1177.582	3.171151	6.533555	0.045136	0.899039	5.363768	1097.893	3.582957	6.470661	0.080291	0.928609	6.038097
1380	4.46	7.98	0.08	1.22	7.99	1306.046	4.35763	7.971872	0.109263	1.161663	7.536239	1231.355	4.483079	7.403477	0.118655	1.12294	7.368768
1325	4.79	8.45	0.15	1.14	7.2	1256.053	4.960385	8.402303	0.097846	1.122833	7.19628	1200.157	5.115752	7.996227	0.109823	1.10041	7.342691
1300	5.61	9.51	0.257	1.143	9.198	1295.389	5.864779	9.009017	0.157301	1.198561	8.640996	1293.653	5.911888	8.88259	0.154127	1.243587	8.685617
1250	5.35	8.96	0.14	1.19	9.061	1273.579	6.041993	9.179316	0.168524	1.156575	8.545555	1244.722	5.758835	8.775728	0.139553	1.156337	8.22534
1325	5	8.84	0.08	1.15	8.984	1260.372	5.371657	8.117585	0.18453	1.149918	8.234041	1248.009	5.183313	7.984588	0.157671	1.162723	8.116478
1280	3.4	7.17	0.09	1.1	7.9	1263.374	3.97968	6.862245	0.124374	1.148658	7.300301	1180.125	3.774211	6.406647	0.126768	1.06741	6.563896
1300	5.1	8.57	0.17	1.27	7.34	1326.852	5.396143	8.903917	0.137758	1.223276	8.739944	1296.85	5.373161	8.372512	0.162063	1.195684	8.231137
1260	5.3	8.63	0.12	1.17	8.55	1269.272	5.865713	8.825079	0.184528	1.144723	8.432028	1236.29	5.640995	8.60116	0.168729	1.150064	8.259586
1385	4.79	7.22	0.15	1.14	7.2	1256.053	4.960385	8.402303	0.097846	1.122833	7.19628	1200.157	5.115752	7.996227	0.109823	1.10041	7.342691
1100	7.5	9.73	0.18	1.18	9.78	1064.501	7.575304	9.563515	0.191529	1.219739	9.318608	1133.216	7.419355	10.15321	0.198508	1.231767	9.72135
1375	4.63	6.98	0.18	1.22	8.801	1285.179	4.794983	7.788079	0.124417	1.195238	7.763706	1251.04	4.729895	7.640081	0.122054	1.175515	7.43083
900	3.8	4.35	0.09	0.89	5.23	833.554	2.961122	4.763924	0.051983	0.800137	4.852788	1023.681	2.670622	5.185565	0.079537	0.883771	5.303125
980	4.6	5.78	0.15	0.98	5.89	988.632	4.610945	6.019562	0.109755	1.056313	5.951055	1005.565	4.536914	6.294871	0.103193	0.972124	5.767453
950	4.4	5.75	0.18	0.99	5.78	998.046	4.573512	5.962062	0.114985	1.059756	5.962608	1018.003	4.412609	6.17073	0.125491	0.945089	5.672752
1000	6.52	7.66	0.11	1.18	7.56	1058.136	6.246326	7.844431	0.124689	1.179764	7.506276	1186.066	6.057745	8.428716	0.126183	1.236889	8.001794
1385	4.6	6.86	0.16	1.2	7.2	1308.239	4.551814	7.82652	0.121984	1.191829	7.714681	1236.113	4.665537	7.356351	0.127895	1.179192	7.272855
975	6.5	8.78	0.09	1.19	6.86	1003.003	6.779854	8.992428	0.093635	1.110882	7.221378	921.312	6.884033	8.258291	0.104979	1.117636	7.195395
950	7.9	10.48	0.2	1.16	9.79	968.771	7.911805	10.20347	0.178139	1.216896	9.511072	1121.459	8.166171	10.9344	0.177691	1.21629	9.711576
1050	6.35	8.56	0.1	1.2	6.73	1057.277	6.485934	8.442715	0.096649	1.187589	7.544709	959.8342	6.406734	7.883817	0.134386	1.185613	7.22516
1000	7.4	9.86	0.19	1.19	9.72	1036.311	7.721124	9.780086	0.179621	1.232348	9.457374	1161.371	7.5243	10.39518	0.220025	1.211373	9.690933
1020	6.7	7.72	0.1	1.16	7.39	1057.135	6.444974	8.188277	0.113534	1.190037	7.648114	1165.429	6.150231	8.362297	0.111353	1.231389	7.831376
1000	4.1	5.63	0.1	1.1	5.56	1000.472	4.407393	5.680814	0.128742	1.05915	5.918386	1052.623	4.082263	5.769456	0.0989	1.100268	5.759659

APPENDIX E

Table E1. Lower and upper values of experimental parameters

Factors	Units	Minimum Value	Maximum Value	Low Level (-1)	High Level (+1)
Welding Speed	mm/s	1.0696	3.5546	1.690	2.930
Current	A	20	150	52	117
Gas flow rate	l/min	8	12	9	11
Gap	mm	1	4	1.75	3.25

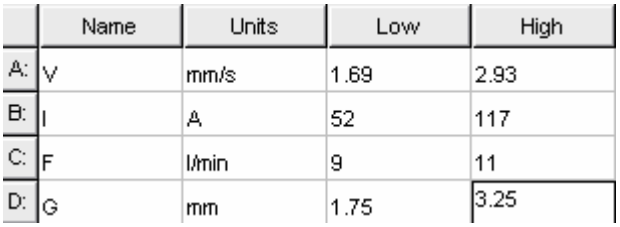

	Name	Units	Low	High
A:	V	mm/s	1.69	2.93
B:	I	A	52	117
C:	F	l/min	9	11
D:	G	mm	1.75	3.25

Figure E1. Design expert response surface design tab

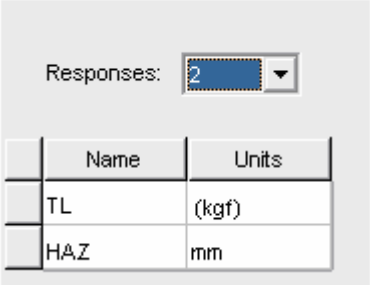

Figure E2. Completed response form

Std	Run	Block	Factor 1 A:V mm/s	Factor 2 B:I A	Factor 3 C:F l/min	Factor 4 D:G mm	Response 1 TL kgf	Response 2 HAZ mm
4	1	Block 1	3.55	150.00	8.00	1.00	1725	4.67
28	2	Block 1	2.31	95.00	10.00	2.50	1900	4.48
30	3	Block 1	2.31	95.00	10.00	2.50	1925	4.47
19	4	Block 1	2.31	15.00	10.00	2.50	850	1.23
18	5	Block 1	4.80	95.00	10.00	2.50	1800	2.8
24	6	Block 1	2.31	95.00	10.00	5.50	1875	4.48
20	7	Block 1	2.31	205.00	10.00	2.50	1925	5.34
8	8	Block 1	3.55	150.00	12.00	1.00	1875	4.52
26	9	Block 1	2.31	95.00	10.00	2.50	1900	4.47
3	10	Block 1	1.07	150.00	8.00	1.00	1725	9.22
27	11	Block 1	2.31	95.00	10.00	2.50	1975	4.47
10	12	Block 1	3.55	40.00	8.00	4.00	1000	1.79
15	13	Block 1	1.07	150.00	12.00	4.00	1700	9.27
21	14	Block 1	2.31	95.00	6.00	2.50	1375	4.5
17	15	Block 1	0.17	95.00	10.00	2.50	1925	5.33
14	16	Block 1	3.55	40.00	12.00	4.00	1100	1.76
11	17	Block 1	1.07	150.00	8.00	4.00	1875	9.28
7	18	Block 1	1.07	150.00	12.00	1.00	1800	9.25
5	19	Block 1	1.07	40.00	12.00	1.00	1800	4.15
6	20	Block 1	3.55	40.00	12.00	1.00	1050	1.69
12	21	Block 1	3.55	150.00	8.00	4.00	1875	4.48
9	22	Block 1	1.07	40.00	8.00	4.00	1850	4.18
16	23	Block 1	3.55	150.00	12.00	4.00	1250	4.66
22	24	Block 1	2.31	95.00	14.00	2.50	1825	4.46
25	25	Block 1	2.31	95.00	10.00	2.50	1900	4.47

Figure E3. Some part of design layout (Partially shown)

Table E2. Summary of sequential model sum of squares for TL

Response: TL

Sequential Model Sum of Squares

Source	Sum of Squares	DF	Mean Square	F Value	Prob > F	
Mean	8.496E+007	1	8.496E+007			
Linear	1.285E+006	4	3.213E+005	3.87	0.0139	Suggested
2FI	5.680E+005	6	94661.46	1.19	0.3509	
Quadratic	7.038E+005	4	1.760E+005	3.29	0.0399	Suggested
Cubic	7.712E+005	9	85688.77	16.98	0.0013	Aliased
Residual	30270.83	6	5045.14			
Total	8.832E+007	30	2.944E+006			

Table E3. Summary of sequential model sum of squares for HAZ

Response: HAZ

Sequential Model Sum of Squares

Source	Sum of Squares	DF	Mean Square	F Value	Prob > F	
Mean	638.12	1	638.12			
Linear	5.61	4	1.40	1.82	0.176E	
2FI	5.08	6	0.85	0.94	0.4905	
Quadratic	113.96	4	28.49	32.07	< 0.0001	Suggested
Cubic	11.52	9	1.28	992.24	< 0.0001	Aliased
Residual	7.740E-003	6	1.290E-003			
Total	774.29	30	25.81			

Table E4. Lack of fit test for TL

Lack of Fit Tests

Source	Sum of Squares	DF	Mean Square	F Value	Prob > F	
Linear	2.066E+006	20	1.033E+005	66.45	< 0.0001	Suggested
2FI	1.498E+006	14	1.070E+005	68.83	< 0.0001	
Quadratic	7.937E+005	10	79369.89	51.07	0.0002	Suggested
Cubic	22500.00	1	22500.00	14.48	0.0126	Aliased
Pure Error	7770.83	5	1554.17			

Table E5. Lack of fit test for HAZ

Lack of Fit Tests

Source	Sum of Squares	DF	Mean Square	F Value	Prob > F	
Linear	11.53	10	1.15	69161.31	< 0.0001	
2FI	17.13	14	1.22	73423.66	< 0.0001	
Quadratic	22.21	20	1.11	66636.37	< 0.0001	Suggested
Cubic	7.656E-003	1	7.656E-003	459.38	< 0.0001	Aliased
Pure Error	8.333E-005	5	1.667E-005			

Table E6. Model summary statistics for TL

Model Summary Statistics

Source	Std. Dev.	R-Squared	Adjusted R-Squared	Predicted R-Squared	PRESS	
Linear	287.98	0.3827	0.2839	0.1043	3.008E+006	Suggested
2FI	281.47	0.5518	0.3159	-0.1391	3.826E+006	
Quadratic	231.15	0.7614	0.5386	-0.4324	4.811E+006	Suggested
Cubic	71.03	0.9910	0.9564		+	Aliased

Table E7. Model summary statistics for HAZ

Model Summary Statistics

Source	Std. Dev.	R-Squared	Adjusted R-Squared	Predicted R-Squared	PRESS	
Linear	0.88	0.9153	0.8363	0.4842	70.24	
2FI	0.95	0.8742	0.8080	0.6612	46.14	
Quadratic	0.94	0.8369	0.8108	0.7446	34.78	Suggested
Cubic	0.036	0.9999	0.9997		+	Aliased

Table E8. ANOVA table for quadratic model of TL

Source		Sum of Squares	DF	Mean Square	F Value	Prob > F	
Model		2.557E+006	14	1.827E+005	3.42	0.0121	significant
	A	*5.952E+005*	*1*	*5.952E+005*	*11.14*	*0.0045*	
	B	*9.169E+005*	*1*	*9.169E+005*	*17.16*	*0.0009*	
	C	*3750.00*	*1*	*3750.00*	*0.070*	*0.7947*	
	D	*5401.19*	*1*	*5401.19*	*0.10*	*0.7549*	
	A^2	*864.05*	*1*	*864.05*	*0.016*	*0.9005*	
	B^2	*5.432E+005*	*1*	*5.432E+005*	*10.17*	*0.0061*	
	C^2	*1.994E+005*	*1*	*1.994E+005*	*3.73*	*0.0725*	
	D^2	*6391.94*	*1*	*6391.94*	*0.12*	*0.7342*	
	AB	*4.727E+005*	*1*	*4.727E+005*	*8.85*	*0.0095*	
	AC	*3906.25*	*1*	*3906.25*	*0.073*	*0.7905*	
	AD	*22500.00*	*1*	*22500.00*	*0.42*	*0.5262*	
	BC	*18906.25*	*1*	*18906.25*	*0.35*	*0.5608*	
	BD	*10000.00*	*1*	*10000.00*	*0.19*	*0.6714*	
	CD	*40000.00*	*1*	*40000.00*	*0.75*	*0.4005*	

Table E9. ANOVA table for quadratic model of HAZ

Source		Sum of Squares	DF	Mean Square	F Value	Prob > F	
Model		124.64	14	8.90	11.59	< 0.0001	significant
	A	*48.99*	*1*	*48.99*	*63.75*	*< 0.0001*	
	B	*69.13*	*1*	*69.13*	*89.96*	*< 0.0001*	
	C	*2.042E-004*	*1*	*2.042E-004*	*2.657E-004*	*0.9872*	
	D	*0.067*	*1*	*0.067*	*0.087*	*0.7722*	
	A^2	*1.02*	*1*	*1.02*	*1.33*	*0.2677*	
	B^2	*2.40*	*1*	*2.40*	*3.12*	*0.0977*	
	C^2	*0.78*	*1*	*0.78*	*1.02*	*0.3283*	
	D^2	*1.42*	*1*	*1.42*	*1.85*	*0.1940*	
	AB	*5.07*	*1*	*5.07*	*6.60*	*0.0214*	
	AC	*5.625E-005*	*1*	*5.625E-005*	*7.320E-005*	*0.9933*	
	AD	*5.625E-005*	*1*	*5.625E-005*	*7.320E-005*	*0.9933*	
	BC	*5.063E-004*	*1*	*5.063E-004*	*6.588E-004*	*0.9799*	
	BD	*2.256E-003*	*1*	*2.256E-003*	*2.936E-003*	*0.9575*	
	CD	*3.306E-003*	*1*	*3.306E-003*	*4.302E-003*	*0.9486*	

Table E10. Diagnostic case statistics for TL

Standard Order	Measured Value	Predicted Value	Residual	%Error	Leverage	Run Order
1	1875	1579.89	295.11	18.68	0.62	28
2	1100	1018.18	81.82	8.04	0.615	29
3	1725	1772	-47	-2.65	0.609	10
4	1725	1897.8	-172.8	-9.11	0.604	1
5	1800	1804.89	-4.89	-0.27	0.62	19
6	1050	1180.68	-130.68	-11.07	0.615	20
7	1800	1859.5	-59.5	-3.20	0.609	18
8	1875	1922.8	-47.8	-2.49	0.604	8
9	1850	1772.33	77.67	4.38	0.606	22
10	1000	1060.62	-60.62	-5.72	0.6	12
11	1875	1864.44	10.56	0.57	0.592	17
12	1875	1840.23	34.77	1.89	0.585	21
13	1850	1797.33	52.67	2.93	0.606	30
14	1100	1023.12	76.88	7.51	0.6	16
15	1700	1751.94	-51.94	-2.96	0.592	13
16	1250	1665.23	-415.23	-24.94	0.585	23
17	1925	2151.56	-226.56	-10.53	0.48	15
18	1800	1541.86	258.14	16.74	0.652	5
19	850	1230.68	-380.68	-30.93	0.358	4
20	1925	1633.4	291.6	17.85	0.694	7
21	1375	1529.88	-154.88	-10.12	0.603	14
22	1825	1579.88	245.12	15.52	0.603	24
23	1875	1879.05	-4.05	-0.22	0.308	26

Continue of Table E10

Standard Order	Measured Value	Predicted Value	Residual	%Error	Leverage	Run Order
24	1875	1782.95	92.05	5.16	0.71	6
25	1900	1890.79	9.21	0.49	0.154	25
26	1900	1890.79	9.21	0.49	0.154	9
27	1975	1890.79	84.21	4.45	0.154	11
28	1900	1890.79	9.21	0.49	0.154	2
29	1985	1890.79	94.21	4.98	0.154	27
30	1925	1890.79	34.21	1.81	0.154	3
			%Average Error*	7.53		

$$\%Error^{*} = \frac{Measured\ value - predicted\ value}{\Pr edicted\ value} * 100$$

Table E11. Diagnostic case statistics for HAZ

Standard Order	Measured Value	Predicted Value	Residual	%Error	Leverage	Run Order
1	4.13	3.82	0.31	8.12	0.62	28
2	1.7	2.01	-0.31	-15.42	0.615	29
3	9.22	8.58	0.64	7.46	0.609	10
4	4.67	4.52	0.15	3.32	0.604	1
5	4.15	3.78	0.37	9.79	0.62	19
6	1.69	1.96	-0.27	-13.78	0.615	20
7	9.25	8.56	0.69	8.06	0.609	18
8	4.52	4.5	0.025	0.44	0.604	8
9	4.18	3.71	0.47	12.67	0.606	22
10	1.79	1.89	-0.1	-5.29	0.6	12
11	9.28	8.42	0.86	10.21	0.592	17
12	4.48	4.35	0.13	2.99	0.585	21
13	4.16	3.72	0.44	11.83	0.606	30
14	1.76	1.9	-0.14	-7.37	0.6	16
15	9.27	8.46	0.81	9.57	0.592	13
16	4.66	4.38	0.28	6.39	0.585	23
17	5.33	7.52	-2.19	-29.12	0.48	15
18	2.8	2.26	0.54	23.89	0.652	5
19	1.23	0.97	0.26	26.80	0.358	4
20	5.34	6.56	-1.22	-18.60	0.694	7
21	4.5	5.03	-0.53	-10.54	0.603	14
22	4.46	5.02	-0.56	-11.16	0.603	24
23	4.48	4.93	-0.45	-9.13	0.308	26
24	4.48	5.36	-0.88	-16.42	0.71	6
25	4.47	4.36	0.11	2.52	0.154	25
26	4.47	4.36	0.11	2.52	0.154	9
27	4.47	4.36	0.11	2.52	0.154	11
28	4.48	4.36	0.12	2.75	0.154	2
29	4.47	4.36	0.11	2.52	0.154	27
30	4.47	4.36	0.11	2.52	0.154	3
			%Average Error*	9.79		

$$\%Error^{*} = \frac{Measured\ value - predicted\ value}{\Pr edicted\ value} * 100$$

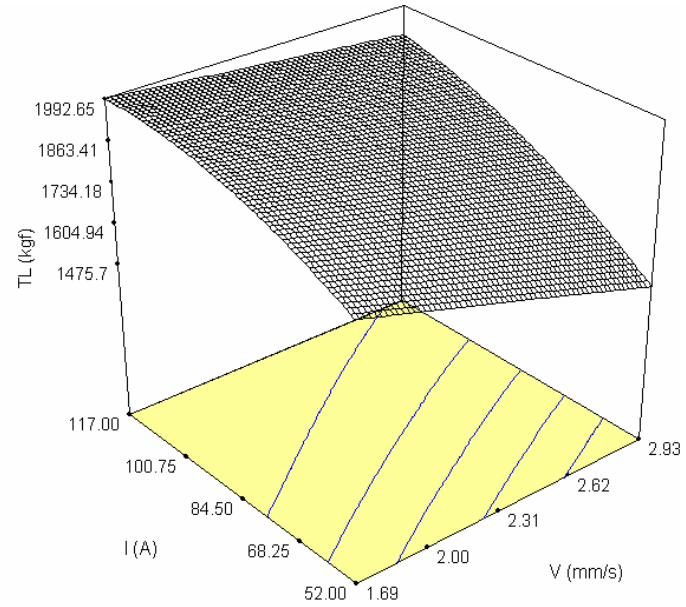

Figure E4. Interaction effects of V and I on TL (t=2mm, F=10 I/min, G= 2.5 mm)

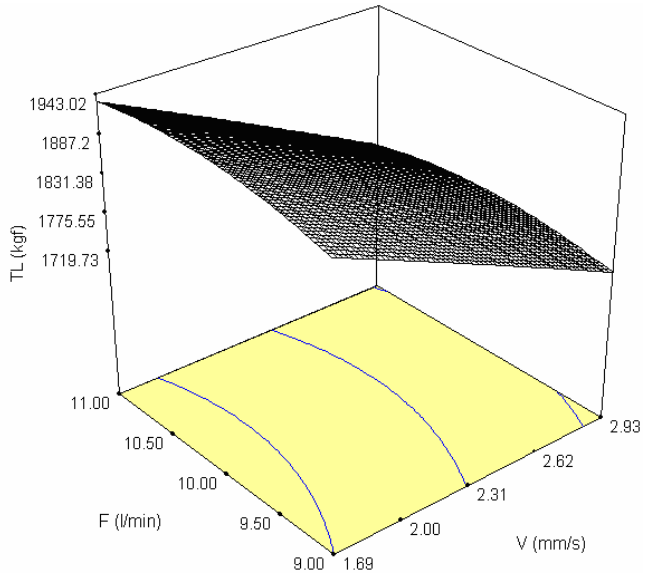

Figure E5. Interaction effects of V and F on TL (t=2mm, I=95 A, G= 2.5 mm)

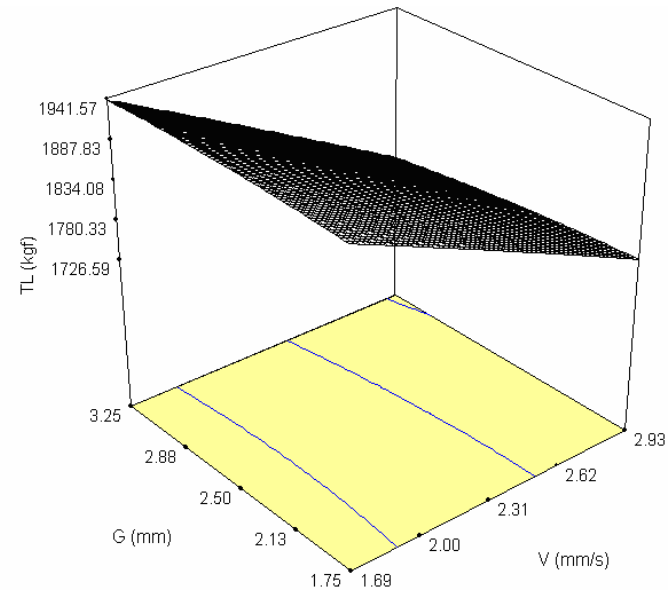

Figure E6. Interaction effects of G and V on TL (t=2mm, F=10 I/min, I=95 A)

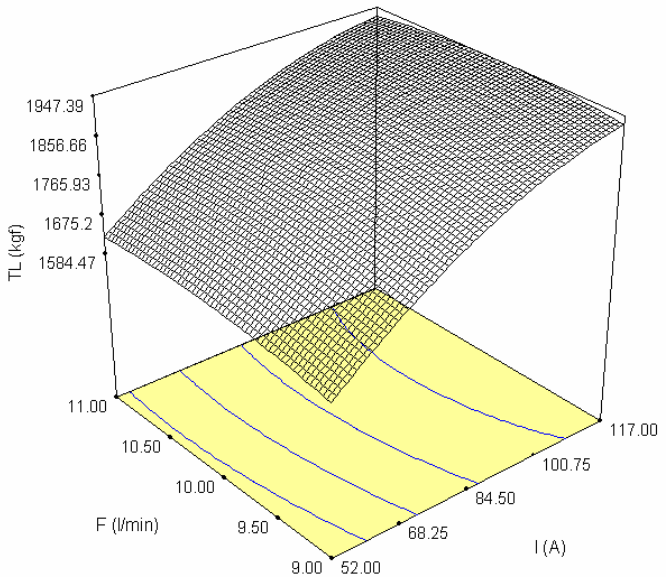

Figure E7. Interaction effects of F and I on TL (t=2mm, V=2.31 mm/s, G= 2.5 mm)

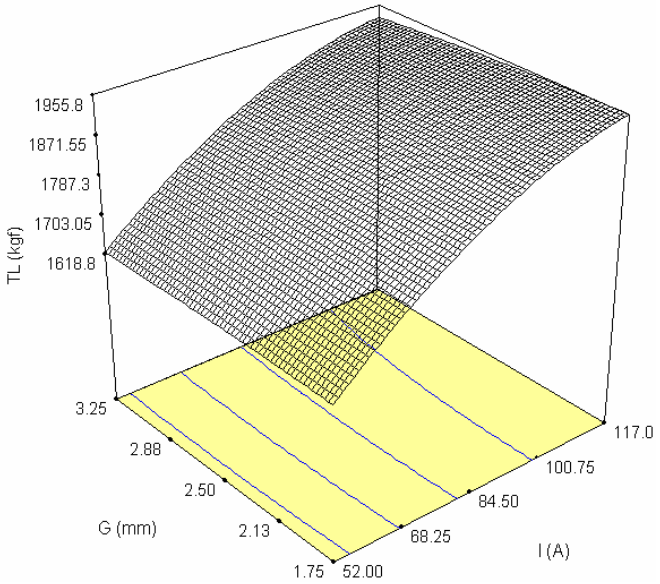

Figure E8. Interaction effects of I and G on TL (t=2mm, F=10 I/min, V=2.31 mm/s)

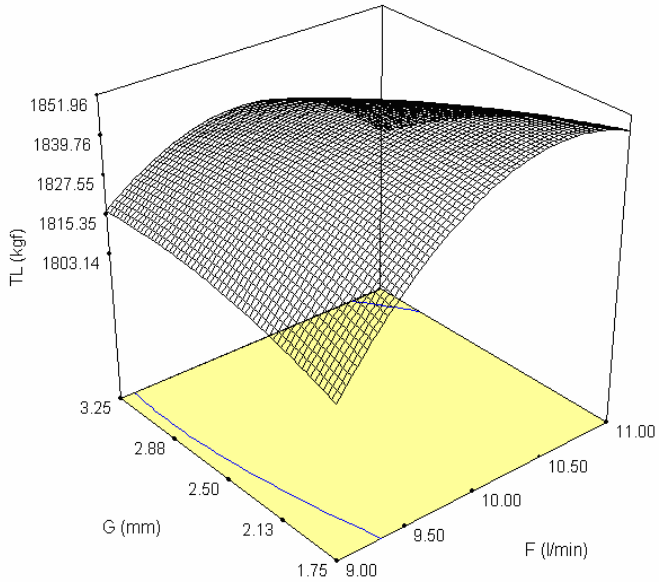

Figure E9. Interaction effects of G and F on TL (t=2mm, I=95 A, V=2.31 mm/s)

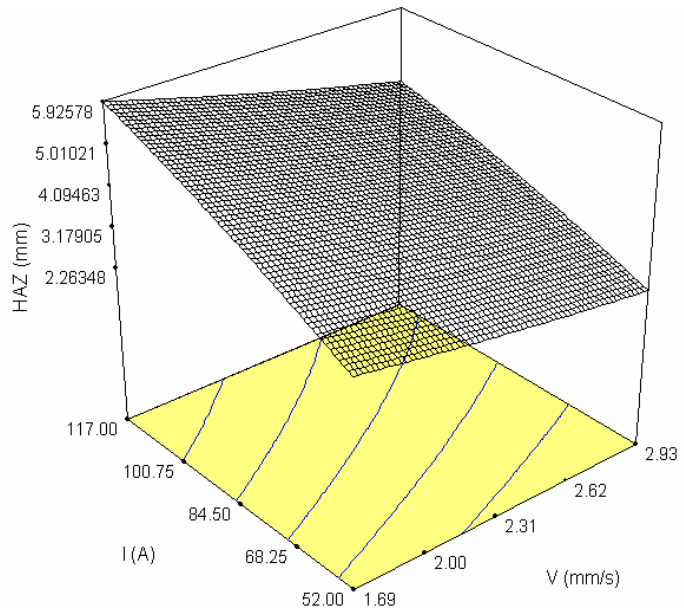

Figure E10. Interaction effects of V and I on HAZ (t=2mm, F=10 I/min,G= 2.5 mm)

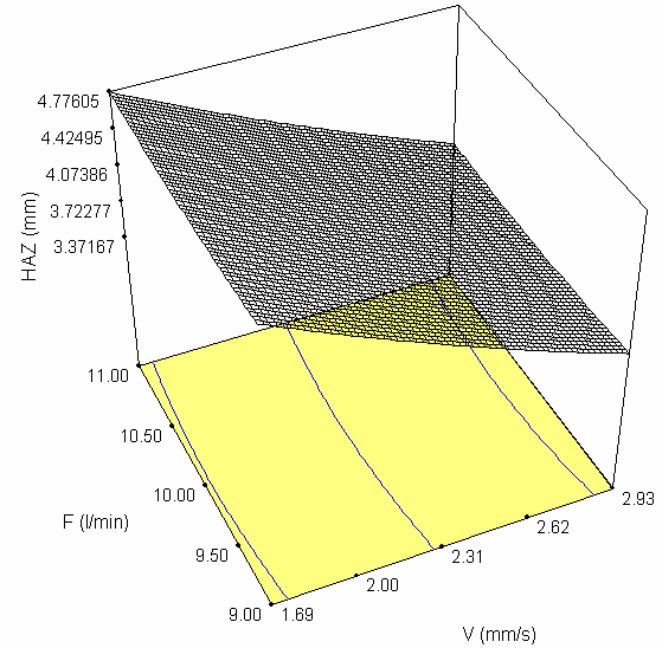

Figure E11. Interaction effects of V and F on HAZ (t=2mm, I=95 A, G= 2.5 mm)

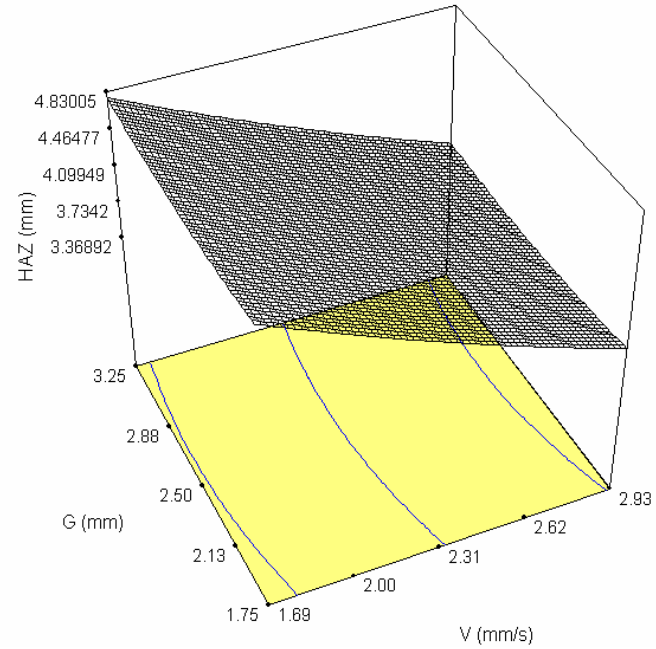

Figure E12. Interaction effects of G and V on HAZ (t=2mm, F=10 I/min, I=95 A)

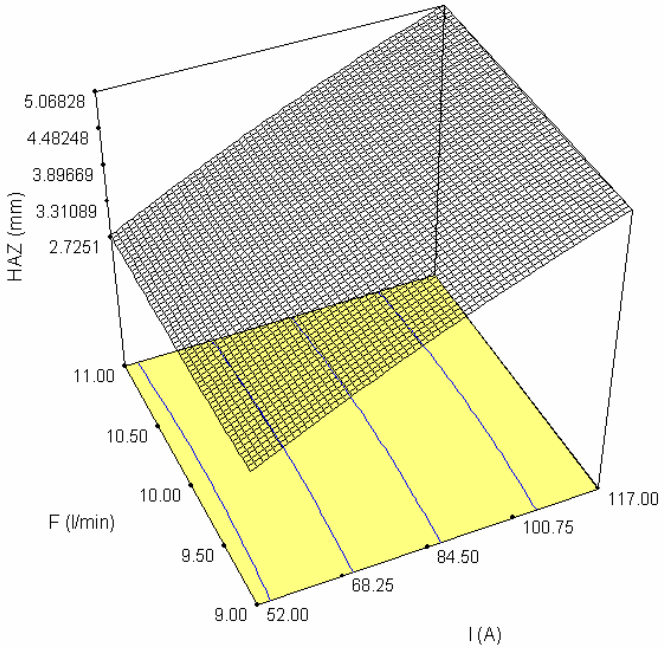

Figure E13. Interaction effects of F and I on HAZ (t=2mm,V=2.31mm/s, G=2.5mm)

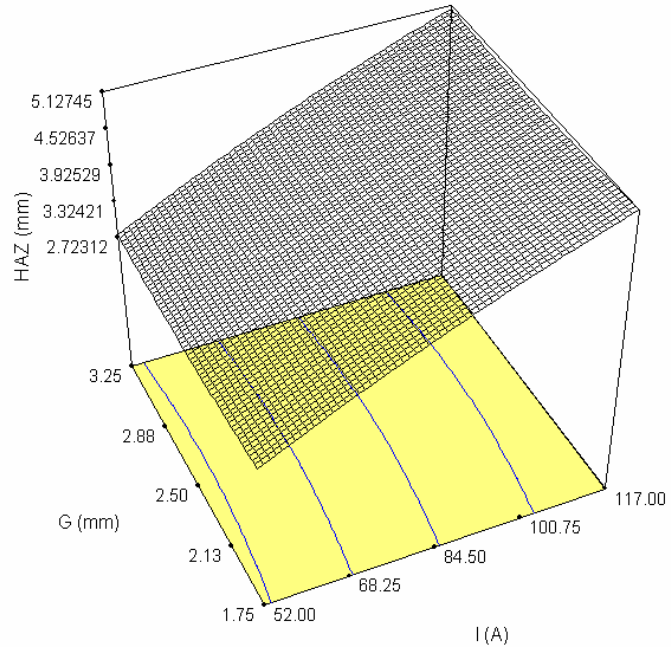

Figure E14. Interaction effects of I and G on HAZ (t=2mm,F=10I/min,V=2.31mm/s)

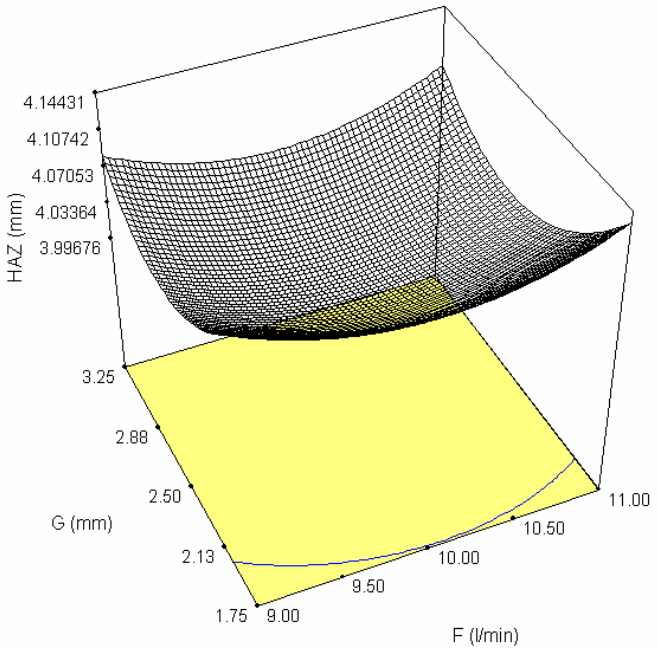

Figure E15. Interaction effects of G and F on HAZ (t=2mm, I=95 A, V=2.31 mm/s)